Modelling, Simulation and Fabrication of Surface Acoustic Wave Motors Employing Dual Friction-drive

A thesis submitted

for the award of the degree of

DOCTOR OF PHILOSOPHY

By

BASUDEBA BEHERA

DEPARTMENT OF ELECTRONICS AND ELECTRICAL ENGINEERING

INDIAN INSTITUTE OF TECHNOLOGY GUWAHATI

GUWAHATI-781039, ASSAM, INDIA

OCTOBER 2016

Modelling, Simulation and Fabrication of Surface Acoustic Wave Motors Employing Dual Friction-drive

Basudeba Behera

"Inventing is a combination of brains and materials.

The more brains you use, the less material you need."

Charles Kettering

To my

Parents, *Abirama, Prafulla*

Brothers, *Debasish, Subhasish*

Sisters, *Harapriya, Lakshmi*

Wife, *Chinmayee*

Certificate

This is to certify that the thesis entitled "**Modelling, Simulation and Fabrication of Surface Acoustic Wave Motors Employing Dual Friction-drive**", submitted by Basudeba Behera (10610216), a research scholar in the Department of Electronics and Electrical Engineering, Indian Institute of Technology Guwahati, for the award of the degree of Doctor of Philosophy, is a record of an original research work carried out by him under our supervision and guidance. The thesis has fulfilled all requirements as per the regulations of the Institute and in our opinion has reached the standard needed for submission. The results embodied in this thesis have not been submitted to any other University or Institute for the award of any degree or diploma.

Dated

Guwahati.

Dr. Harshal B. Nemade

Professor

Department of Electronics and Electrical Engineering

Indian Institute of Technology Guwahati

Guwahati - 781 039, Assam, India

Abstract

Surface acoustic wave (SAW) devices are widely used in sensors, actuators, filters, and telecommunication systems. SAWs are elastic waves launched on a piezoelectric substrate when an electrical signal is applied to metallic comb-like electrodes called as interdigital transducers (IDTs) patterned on the surface of the substrate. A SAW motor consists of a piezoelectric substrate with IDTs as the stator that generates Rayleigh SAW on its surface and displaces a movable part called as a slider placed in contact with the substrate. The operation of a SAW linear motor is based on the frictional drive generating high tangential force on the slider at the contact points with the stator, as the SAW travels on the surface of the stator.

Conventionally the slider in a SAW motor is held tightly in contact with the surface of the stator and the preload is applied from the top through a lubricated guide rail to reduce friction at the top side of the slider while increasing friction between the stator and the bottom surface of the slider. To achieve the conflicting friction-related requirements at the two sides of the slider, normally heavy and bulky lubricated guide rails are used causing a major impediment in the commercialization of SAW motors. The research work presented in the thesis proposes a dual friction-drive (DFD) technique where an additional stator replaces the bulky guide rail to drive the slider from two sides and greatly simplifies the operating mechanism.

This thesis mainly focuses on the research work carried out on the modelling, finite element simulation, fabrication, and demonstration of the proposed DFD SAW motor, where a slider/ rotor is placed between two identical stators.

Initially, modelling of single point contact is carried out where the parameters like force, preload and contact length are derived, followed by modelling of multi-contact points normally prevalent in the case of sliders having projections. The modelling is extended for DFD SAW motor using the cuboid slider with projections and cylindrical slider where parameters for line contact are derived.

The system based on DFD technique is simulated using finite element method in COMSOL Multiphysics. Initially, the conventional SAW motors using a spherical slider and cuboid slider are simulated. The simulation of cuboid slider includes sliders without projections and with different shapes of projections. Subsequently, the simulation is extended for DFD SAW motors using cuboid sliders for translational motion. Finally, the simulation for DFD SAW motor using cylindrical shaft is carried out for both translational and rotational motions.

The stators for different operating frequencies are designed and fabricated using microfabrication facility. A large number of sliders having projections of different shapes and spacing using silicon substrate are fabricated. All the fabricated devices are characterised and tested. Conventional SAW motor having single stator is tested. The stators are arranged in DFD assembly and tested for translational motion of cylindrical shaft. The experimental observation is captured through the digital video camera to analyse the results.

Acknowledgement

I feel it as a great privilege in expressing my deepest and most sincere gratitude to my thesis supervisor Prof. Harshal B. Nemade for his excellent guidance throughout my study. His kindness, dedication, hard work, and attention to detail have been a great inspiration to me. I am grateful to him for the unlimited support and infinite patience he has shown to me. He is the man from whom I learnt the inner technical aspects of MEMS. His unwavering support, invaluable guidance and suggestions in accomplishing this research are extraordinary. His guidance helped me in all the time of preparing research manuscripts and writing of this thesis.

I am thankful to my doctoral committee members Prof. R Bhattacharjee, Prof. S. K. Dwivedi and Prof. Roy Paily for sparing their precious time to evaluate the progress of my work. They have boosted my confidence every time. I would like to thank them for all the support they gave me during my stay in IIT Guwahati. I am also thankful to Prof. R Bhattacharjee, head of the centre for providing the facility to carry out the research work. My special thanks to the technical staff of EEE Department, IIT Guwahati, Sonowal, Sanjeev Das, P J Goswami, without their help I could not have completed this thesis. I would also like extend my thanks to office staff in ECE Department, IIT Guwahati.

I am fortunate to have an opportunity to present my research work at IEEE International Ultrasonic Symposium 2016 at Tours, France, and meet Prof. M. K. Kurosawa from Tokyo Institute of Technology, Japan who is the pioneer in the field of SAW motors and his published research work inspired me to take up research in this area in the early stage of my PhD work. I am thankful to Prof. M. K. Kurosawa, for appreciating my research work at the conference and the conversation with him was greatly encouraging.

I am obliged to Indian Nanoelectronics User Program (INUP), and Centre for Excellence in Nanoelectronics (CENSE), IISc., Bangalore for providing the fabrication facility to carry out the major part of my fabrication work. I would like to thank all faculty coordinators of INUP, In particular, I would like to thank Dr. Sanjeev Srivastava, INUP coordinator for his tremendous help and support in carrying out my work in IISc., Bangalore. Most importantly I would like to give my gratitude to the INUP staff at CENSE, IISc., Bangalore especially Dr. Prabhakara Rao for helping me with most of the fabrication work.

I am extremely thankful to Mrs. Leena Nemade madam for her care shown and support is given to me during my stay at IIT Guwahati.

My special thanks to my SAW group member the guys who are always with me, Dr. Ramakrishnan, presently Senior Lecturer at Monash University, Malaysia Campus, Dr. Ashish Kumar Namdeo, presently Lead Engineer at Samsung R&D Institute Noida, Sai Krishna, Jitendra Kumar, Vivek Lukose, Mandar, Sushanta and Shyam, for their care, support, and extreme cooperation during my stay in IIT Guwahati.

For day-to-day lab support, I would like to express my thanks to my friends, Dr. D G Pradhan, Dr. Sanjoy Mandal, Dr. Bajrangbali, Dr. Reena, Madhulika, Nabanita, Vinay, Gargi, Saurav, Tousif, Arghya, Uddi, Karnika and Trushna. My work in this remote place definitely would not be possible without their love and care that helped me to enjoy my new life in this IIT Guwahati. Special thanks to my friends Dr. Prakash, Dr. Vikash, Satish and Sai from Dept. of Design for guiding me to see this world from the design perspective and implement in real life. My work in this remote place definitely would not be possible without their love and care that helped me to enjoy my hostel life in this IIT Guwahati.During these four years at IIT Guwahati, I have had several friends that have helped me in several ways, I would like to say a big thank you to all of them for their friendship and support.

My deepest gratitude goes to my parents, grandparents, brothers and sisters for their continuous love and support throughout my studies. Especially I want to thank my father for the opportunities he has given me and his unlimited love and support are the reasons where I am and what I have accomplished so far. Finally, I want to thank my beloved wife for supporting whole-heartedly to complete the final stages of my PhD thesis work.

My hearty thanks to the researcher community, with the support of their available research work in terms of patents, Journals, and articles, I am able to carry out my present research work.

Finally, I believe this research experience will greatly benefit my career in the future.

Basudeba Behera

Contents

List of Figures

List of Tables

List of Acronyms

APM	Acoustic Plate Mode
COM	Coupling of Mode
DFD	Dual Friction-drive
DI	De-ionized
DOF	Degrees of Freedom
FEM	Finite Element Method
FESEM	Field Emission Scanning Electron Microscope
GUI	Graphical User Interface
HAR	High Aspect Ratio
IDT	Interdigital Transducer
MEMS	Microelectromechanical Systems
PDE	Partial Differential Equation
RF	Radio Frequency
SAW	Surface Acoustic Wave
SEM	Scanning Electron Microscope
SH	Shear Horizontal
TEM	Transmission Electron Microscope
TSM	Thickness Shear Mode
UV	Ultraviolet

List of Symbols

T	Time period
p	IDT finger pitch
t	Time
v	SAW phase velocity
v_0	Free surface SAW phase velocity in substrate
λ	SAW wavelength
f_r	Synchronous or resonance frequency
f_b	3dB bandwidth of SAW device
h_a	Air gap
h_e	Electrode height
k	wave number
N	Number of IDT finger pairs
N_r	Number of reflector strips
r_s	Reflection coefficient of one strip
A_n	Amplitude of impulse
ω	Angular frequency
a_0	Amplitude of step response
K_R	Electromechanical coupling coefficient of Rayleigh wave
C_1	Capacitance per pair of IDT fingers and per unit length
P_R	Mean power density of transported by the wave
$\|U\|$	Amplitude of applied input signal
θ	Periodic section transit angle
R_0	Mechanical impedance
C_s	Electrode capacitance per electrode (static)
j	Imaginary unit

E_n	Electric potential equivalent to F_n (n stands for number of electrodes)
I_n	Equivalent electric current
ϕ	Turns ratio of an acoustic-to-electric circuit transformer
C_T	Total capacitance of IDT
G_a	Radiation conductance
B_a	Susceptance
α	Transduction coefficient
ε	Permittivity
R_f	Thin film resistance in one transduction unit
C_f	Interdigital capacitance in one transduction period
κ	Reflection parameter
F_n	Acoustic terminal force(n stands for number of electrodes)
P_{11} and P_{22}	Reflections coefficients of IDT in P-Matrix
P_{12} and P_{21}	Transmission coefficients of IDT in P-Matrix
P_{13} and P_{23}	Excitation coefficients of IDT in P-Matrix
P_{31} and P_{32}	Current generated by the wave arriving at acoustic ports of IDT
P_{33}	Admittance of IDT in P-matrix
S	Strain
T	Stress
V_{in}	Input electric potential to IDT
V	Scalar electric potential
$\mathbf{u}$	SAW particle displacement
u'_i	Particle velocity of SAW along i direction
$T_{ij(mech)}$	Stress due to mechanical strain
$T_{ij(elec)}$	Stress due to electric field

ε_{ij}	Permittivity tensor of dielectric medium
c_{ijkl}^{E}	Stiffness tensor for constant electric field
S_{jk}	Strain components
ε_{ij}^{s}	Permittivity tensor for constant stress
E_{j}	Electric field vector
ρ	Material density
δ	Edge length
B	Magnetic field
E	Electric field
X, Y, and Z	Crystal lattice direction
k and β	Wave number of the surface wave
U_{left}, *and* V_{left}	Displacements and potentials at left side of boundaries
U_{right} *and* V_{right}	Displacements and potentials at right side of boundaries
f_{sc-}	Lower edge frequency called as resonance frequency
f_{sc+}	Upper edge frequency called as antiresonance frequency
Γ_{L}	Denotes left side boundary of the SAW resonator geometry
Γ_{R}	Denotes right side boundary of the SAW resonator geometry
d	IDT electrode width
η	Normalized frequency
f_0	Free surface resonance frequency
Q_r	Quality factor at resonance frequency
Δf	Bandwidth at half of the peak-conductance
γ	Capacitance ratio
f_a	Antiresonance frequency

B_L, B_R and B_B	Critical damping at the edge of the transmitter, receiver, and bottom of the substrate
$\lvert\kappa_p\rvert$	Absolute value of the reflection coefficient per period
K_{eff}^2	Effective electromechanical coupling coefficient
h_s	Depth of the piezo-substrate
α_p	Transaction coefficient per period of fingers
γ_p	Attenuation per period of IDT fingers
G_r	Conductance at resonance frequency
v_f	Free surface SAW phase velocity of the device
v_m	Metallized surface SAW phase velocity of the device
S_{11}	Scattering parameter (return loss)
K^2	Electromechanical coupling coefficient
I	Cross-section moment of inertia
i_n	Current equivalent to particle velocity for a single pair of electrode of IDT
x_i	Co-ordinate axis (i = 1, 2, 3)
ξ	Damping ratio
ς	Piezoelectric constant used in mason equivalent circuit
Z_o	Acoustic impedance
$\mathbf{Z}$	Rayleigh damping matrix
x_i	Co-ordinate axis (i = 1, 2, 3)
φ_a	Phase offset of the gratings of IDT
φ_t	Phase offset in the potential
V_{in}	Input voltage to IDT
V_o	Output voltage from IDT

A_{dM}	Mass proportional damping parameter
B_{dk}	Stiffness proportional damping parameter
$\hat{z}_{st}$	Amplitudes of wave in normal directions
$\hat{x}_{st}$	Amplitudes of wave in translational directions
F_l	Preload
R	Radius of the slider
F_n	Normal Force
F_t	Tangential force
a	Contact length
h	The parameter deciding stick and slip of slider
z_{sl}	Normal position of the slider
E_{sl}	Young's modulus of the slider
E_{st}	Young's modulus of the stator
ν_{sl}	Poisson's ratio of the slider
ν_{st}	Poisson's ratio of the stator
R_{sl}	Radius of slider
R_{st}	Radius of stator
P_{max}	Maximum contact pressure
m	Slider mass
μ_d	Coefficient of friction
ρ	Sheet resistance of metal sheet
L	Length of the cylindrical shaft

1

Introduction to Ultrasonic Motors

1.1 Introduction

Micro-electro-mechanical system (MEMS) is a batch-fabricated integrated microscale system that may involve motional, electromagnetic, radiating energy and optical microdevices/ microstructures, driving/ sensing circuitry, controlling/ processing ICs, and requires multi-disciplinary process technology to create tiny integrated devices or structures that combine mechanical, electrical, and electronics components [1], [2]. MEMS devices are usually made using microfabrication techniques or using integrated circuit (IC) batch processing techniques on a single chip and can range in size from a few micrometres

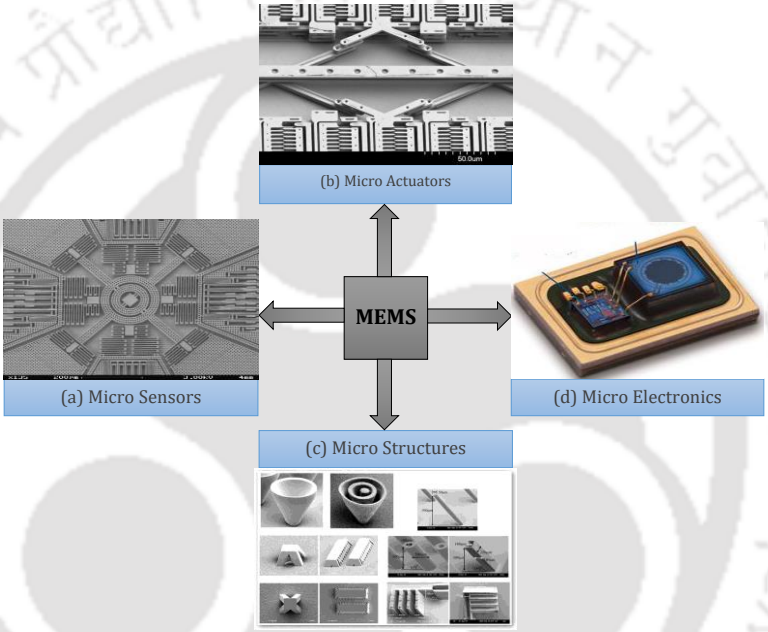

Figure 1.1: Micro-electro-mechanical system components.
Source: Adapted from (a) http://www.geekmomprojects.com/gyroscopes-and-accelerometers-on-a-chip/, (b) http://www.bacteria-world.com/high-force-mems-actuator.htm, (c) http://www.eetimes.com/ document.asp? mc= RSS_EET_EDT& doc_id=1324827, (d) http://tzjwinfcha.pixnet.net/ blog/post/25040588.

to millimetres [3], [4]. Though MEMS have the ability to sense, control and actuate at the micro/nanoscale, they have far-reaching effects extending into large scale [2].

Based on applications, MEMS are divided into four functional elements, viz. microstructures, microsensors, microactuators, and integrated microelectronics as shown in Figure 1.1. Microsensors and Microactuators are categorised as "transducers." Generally, MEMS microsensors convert a mechanical signal to be measured into an electrical signal and are engineered to measure physical quantities such as temperature, pressure, radiation, magnetic field, and chemical detections [5].

An actuator is a type of motor for displacing or controlling a system or mechanism [6]. Generally, an actuator operates with an input typically in the form of an electric current or voltage, hydraulic pressure or pneumatic pressure, and converts the input energy into motion [7]. Microactuator is a mechanism in the microscopic domain that supplies and transmits energy for the operation of a secondary system or mechanism. The four main types of actuation options available in MEMS are electrostatic, thermal, magnetic, and piezoelectric [2]. The choice of actuation depends on the nature of the application, ease of integration with the fabrication process, the specifics of the system around it, and economic justification. The desired features for microactuators are large travel, high precision, fast switching, low power consumption, power-free force sustainability, micro-structurality, and integrability [3].

Popular microactuators developed include microresonators, micropumps to develop fluid pressure, microvalves for control of gas and liquid flows, optical switches and mirrors to

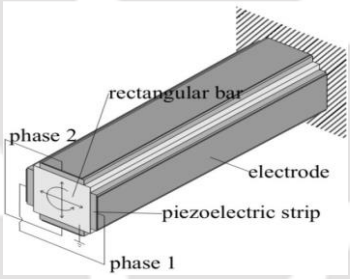

Figure 1.2: Piezoelectric motor
Source: Adapted from (a) Williams *et al.*[8]

redirect light beams, interferometric modulation based displays, RF switches and others [5].

In 1948 Williams *et al.*[8] developed a piezoelectric motor consisted of four piezoelectric rectangle elements bonded to the four faces of a square bar as shown in Figure 1.2. The bending modes of the rectangular bar were excited by 90° out-of-phase signals resulting in a vibratory movement of a piezoelectric crystal element translated into rotary motion at one end of the bar with respect to the other end.

A piezoelectric motor was introduced by Lavrinenko in 1965 [9] as shown in Figure 1.3. The motor was made up of a piezoelectric plate pressed against a rotor and was unidirectional, i.e. only one mode on a vibrator is excited. One, or multiple, elastic vibration couplers oriented obliquely and attached either on a spinning element or a vibrating element transfer the vibration to the rotating element. In the previous structures, circular piezoelectric plates were used along with the rectangular piezoelectric plates, of which

longitudinal modes were excited, to convert radial vibratory motion into tangential motion via angularly-attached lamina [10] as shown in Figure 1.3 (b). The advance investigations of piezoelectric motors led to a recognition of fundamental design principles that following structures could be operated bi-directional [9].

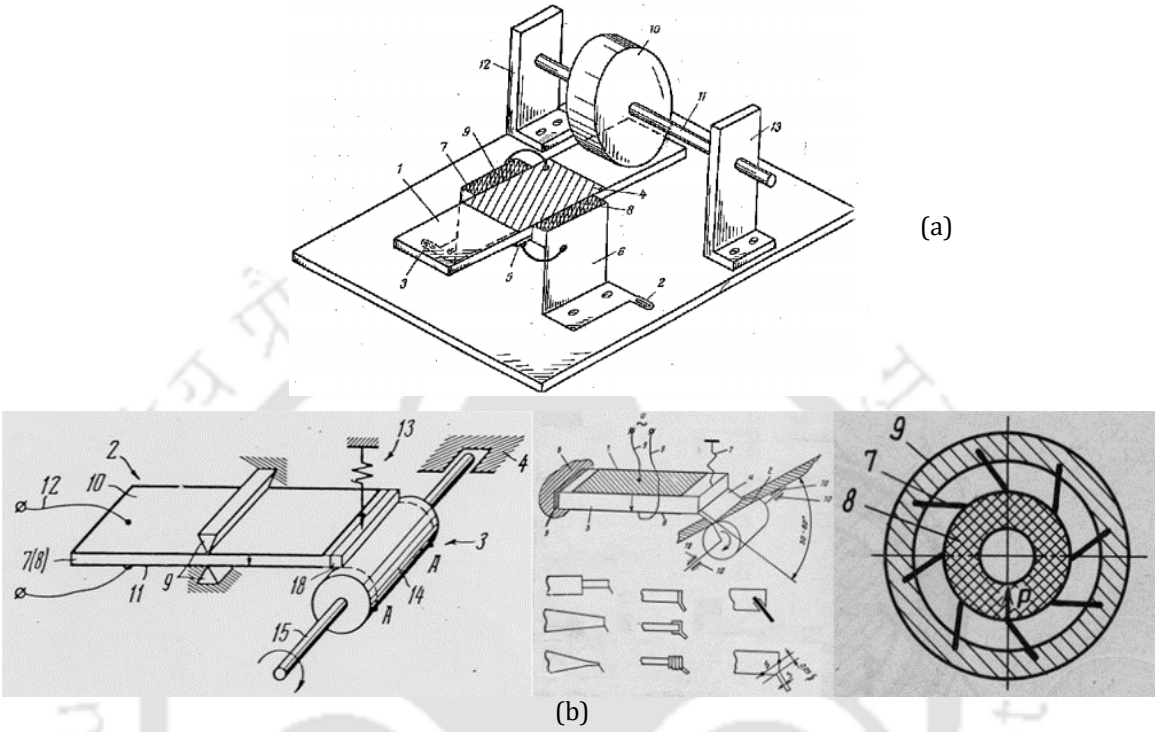

Figure 1.3: Piezoelectric motor introduced by (a) V. Lavrinenko[9]**, (b) Wischnewskiy** [11].

In 1988 Uchino *et al.*[12] invented a π-shaped linear motor equipped with a multilayer piezoelectric actuator and fork-shaped metallic legs as shown in Figure 1.4 (a). A minor difference in the mechanical resonance frequency between the two legs, the phase difference between the bending vibrations of both legs can be controlled by changing the drive frequency. The walking slider moves in a way similar to a horse using its fore and hind legs when trotting.

In 2000 Koc *et al.* developed a piezoelectric micromotor known as windmill motor [13], in which uniformly electrode piezoelectric ring bonded to a metal ring is used as the stator as shown in Figure 1.4 (b). Four inward arms at the inner circumference of the metal ring transfer radial displacements into tangential displacements. The rotor ends in a truncated cone shape and touches the tips of the arms. A rotation takes place by exciting coupled modes of the stator element, such as a radial mode and a second bending mode of the arms.

The real potential of MEMS is in microelectronics where the micro– sensors, actuators, and structures can be integrated with circuits on a common silicon substrate. While the electronics are fabricated using integrated circuit (IC) process sequences, the

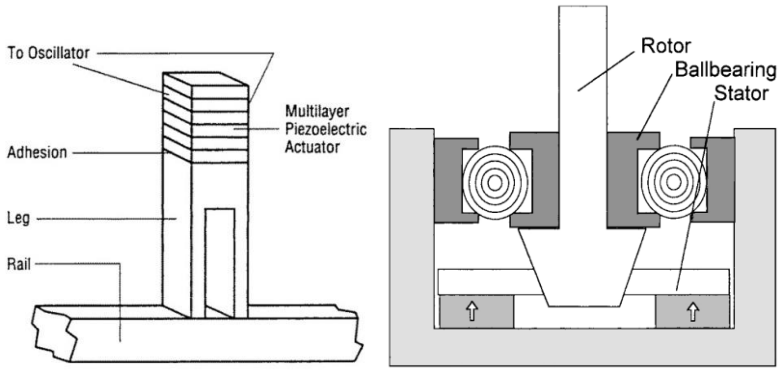

Figure 1.4: (a) π-shaped linear motor (b) Windmill motor

Source: Adapted from (a) K Uchino *et al.*[12], (b) Koc *et al.*[13].

micromechanical components are fabricated using compatible "micromachining" processes that carefully etch away unwanted parts of the silicon wafer or adjoin new structural layers to form the mechanical and electromechanical devices [5].

This thesis mainly focuses on the research work carried out in the design, development, and analysis of the proposed dual friction-drive surface acoustic wave (SAW) motors, in which a slider is sandwiched between two piezoelectric stators producing surface waves that drive the slider with frictional force. The design, simulation, fabrication, and results of experiments on the linear and rotational types of proposed SAW motors with sliders with different shapes are presented in this thesis.

1.2 Ultrasonic Motors

Ultrasonic motors have been developed with a novel concept of utilising the surface deformation of an elastic body known as a stator in the ultrasonic frequency band using the reverse piezoelectric effect in piezoelectric materials [14], [15]. The mechanical movement and torque are usually obtained by means of the frictional contact force between the vibrating stator and the rotor/slider [16]. The demand of micro and nano-scale motors is high as the motions are aiming at accurately controlled manipulation like in microsurgery, assembly processes of micro-robotic applications, optical instruments such as cameras, mobile phones and in printers [17].

The ultrasonic motor is a class of motor which uses tiny elastic vibrations to generate macroscopic rotations or translations of a rotor or a slider respectively [18]. The frequency of the microscopic vibrations is ultrasonic, i.e. higher than the upper limit of the human

hearing range about 20 kHz. The conversion between vibration and resulting motion is based on friction (Ueha, 1993).

An ultrasonic motor is a group of motor which uses microscopic elastic vibrations at an ultrasonic frequency to produce large translations in a slider or rotations in a rotor. Various forms of ultrasonic motors and their working mechanisms have been reported till date [15].

1.3 Types of Ultrasonic Motors

Ultrasonic motors (USMs) are classified into various categories depending on different working principles, some of them are discussed below with their history and working principle.

Table 1. 1: Classification of Ultrasonic Motors.

Source: Adapted from Zhao, [15]**.**

Viewing perspective	Types
Wave propagation method	Travelling wave, Standing wave
Movement output way	Rotational, Linear
Contact state between the stator and rotor/Slider	Contact, Non-contact
Excitation conditions of stator by piezoelectric	Resonant, Non-resonant
Rotary conditions	Unidirectional, Bidirectional
Displacement of operating mode in direction	Out of plane, In-plane
Geometry shape of stators	Disk, Ring, Bar and Shell
Number of degree of freedom (DOF) of the rotor	Single-DOF, Multi-DOF

As time progresses, various form of USMs developed in different part of the world by various Universities through the dedicated works by researchers. Classifications of USMs from a different angle of viewing are given in Table 1. 1.

USMs are divided into two categories: a standing and travelling wave types. The standing wave type directly utilises the modes (standing wave) of an elastic body. Whereas the second one works on the rotation mode (travelling wave) synthesised by two particular standing waves. The standing wave occurs due to mechanical vibration of the subject and the travelling wave due to anelastic wave of the subject [15].

1.3.1 Standing wave

When two plane waves with the same amplitude transmitting from opposite directions are superposed forms a standing wave. By superposing two travelling waves with the same frequency and amplitude moving from opposite directions forms the standing wave, where

certain points in the elastic body stationary at any time and whereas the amplitude of other points is twice as much as the amplitude of the travelling wave at any time as shown in Figure 1.6.

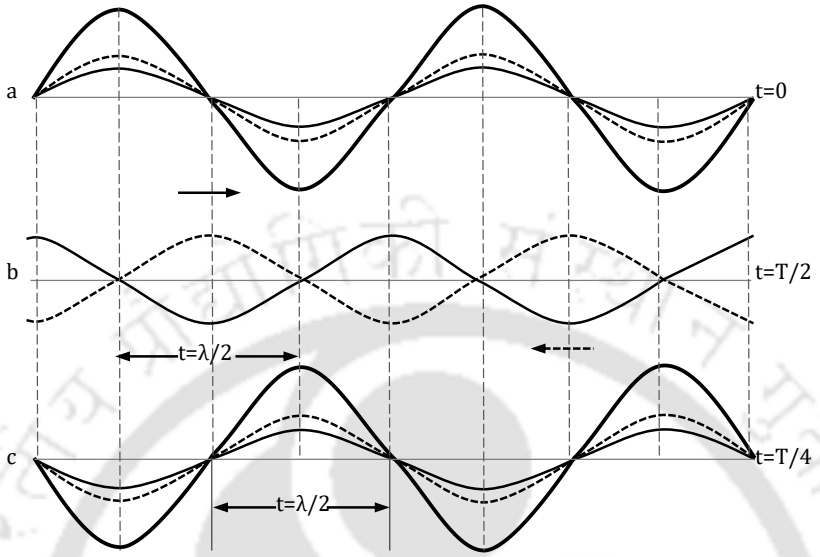

Figure 1.6: Formation of standing waves.

Source: Adapted from Zhao, [15]**.**

In 1973 Barth [19] presented a USM where the rotor was pressed against the horns as shown in Figure 1.5 (a). The rotor was driven in a clockwise direction by exciting horn 1 and in reverse direction by exciting horn 2 (The horns vibrated in the axial direction). T. Sashida [4] proposed a standing-wave type or vibratory-coupler type motor, where the vibratory piece is connected to a piezoelectric driver, and the tip portion generates flat-elliptical movement. The excited vibration displacement of the piezoelectric vibrator

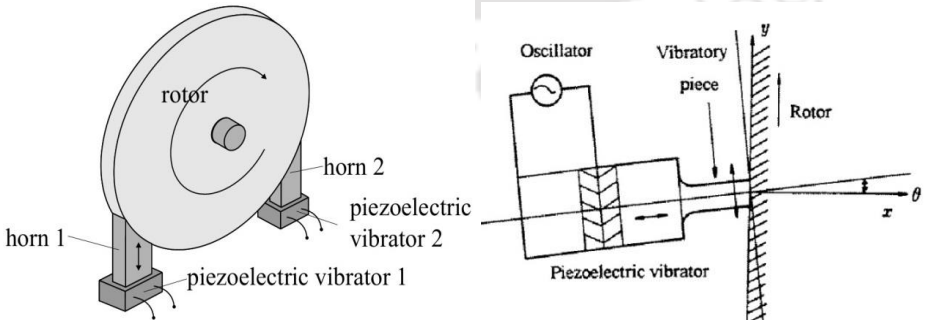

(a) (b)

Figure 1.5: (a) The vibrating horns type motor (b) Vibratory coupler type motor

Source: Adapted from (b) Barth [19], (c) Sashida [4].

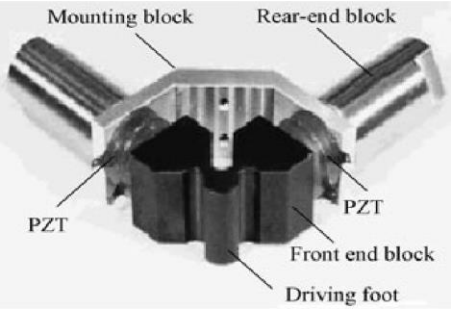

Figure 1.7: Linear USM. Source: Adapted from Kurosawa *et al.*[20].

generates bending because of restriction by the rotor so that the tip moves along the rotor face is shown in Figure 1.5 (b).

In 1998 Kurosawa *et al.*[20] and [21], proposed a linear USM with higher drive efficiency using the composite mode of two longitudinal vibrations as shown in Figure 1.7. The experiment proved that the no-load maximum speed was 3.5 m/s. The output force was 39 N at the driving voltage of 500 Vrms and the preload of 150 N.

1.3.2 Traveling wave

Standing waves are usually generated in the limited elastic body, and travelling waves can be produced by following special conditions: Travelling wave generated by vibrator and absorber [16-18].

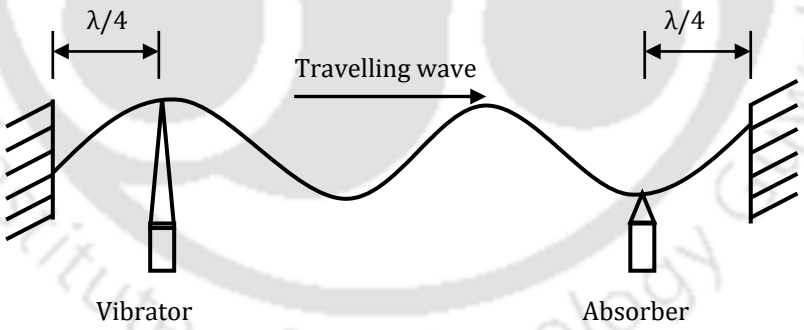

Figure 1. 8: Method of producing travelling waves by a vibrator and an absorber.

Sashida proposed a simple method to generate travelling waves, as shown in Figure 1. 8. It is known from the figure that two actuators (Langevin vibrators) are employed: one is employed to produce a vibration and the other to absorb the vibration. In other words, the vibrator in the left end of the elastic body produces vibration which continues to move towards the right side, forming the travelling wave. In order to prevent the reflection of the traveling wave from the right end of the elastic body, the absorber is applied to consume the

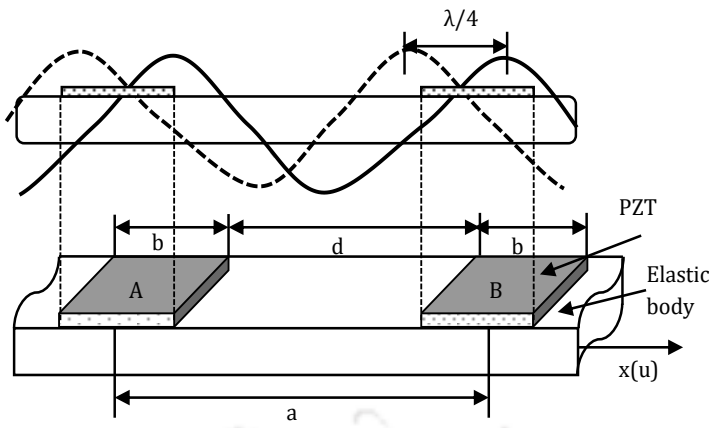

Figure 1.9: Excitation of bending travelling wave.

Source: Adapted from Zhao, [3].

energy of the travelling wave. This method was used in the linear motor developed by Sashida in 1983.

A travelling wave can be excited in a limited elastic body in particular conditions, as shown in Figure 1.9. PZT pieces A and B are affixed to a uniform beam simply supported. The corresponding resonance mode is excited at the certain resonance frequency of the beam. When the elastic body is excited by the PZT pieces A and B, we obtain a composing wave. Only the wave that moves towards left is obtained (retrogressive wave). A travelling wave can be generated by superimposing two standing waves whose phases differ by 90°from each other both in time and in space.

Sashida[22], proposed a travelling wave USM as shown in Figure 1.10 (a), a travelling wave was generated in the elastic ring, which drove the rotor by means of friction. The driving direction reversed by changing the sign of the phase. Sashida[15] presented a travelling wave linear USM (straight beam types) as shown in Figure 1.10 (b) having two Langevin

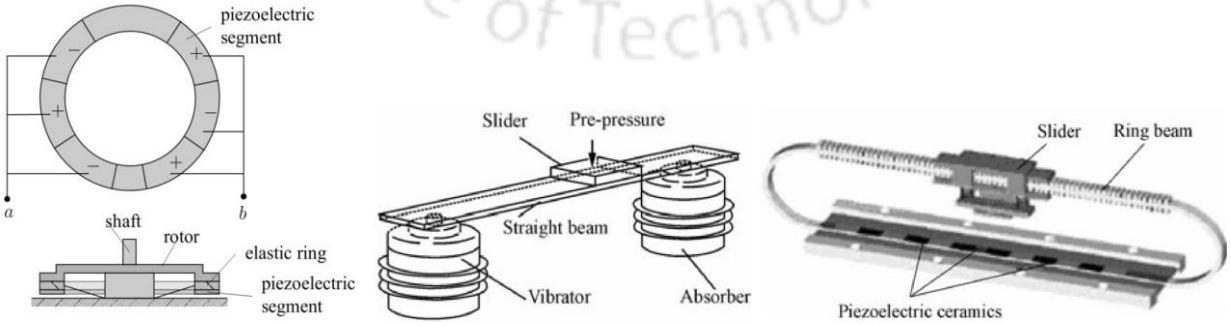

(a) (b) (c)

Figure 1.10: (a) Travelling USM, (b) Straight beam type USM, (c) Ring beam type USM.

Source: Adapted from (a) Sashida [22]**, (b) Sashida** [15]**, (c) Hermann et al.** [15]**.**

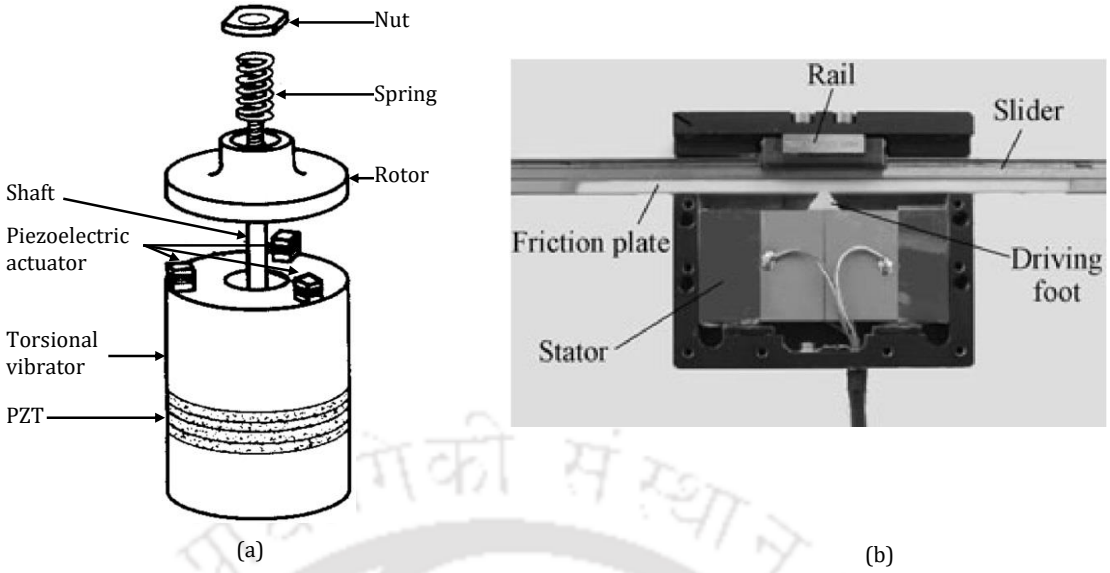

Figure 1.11: (a) Schematic of a hybrid transducer type USM, (b) Piezoelectric actuator. Source: Adapted from Kurosawa *et al.*, [23].

vibrators, where one was used as a vibrator, and the other was used as an absorber to prevent the reflection of the travelling wave. The travelling wave on the beam was produced to drive the slider and would move in an opposite direction when the role of two vibrators was exchanged. Hermann et al. [15] developed a ring beam type linear USM Figure 1.10 (c), the slider makes linear motion when it was pressed on the linear portion of the ring beam where traveling wave on the surface of the ring beam was excited by the piezoelectric ceramic pieces bonded inside of the ring beam.

Kurosawa et *al.*[23] proposed a hybrid type USM as shown in Figure 1.11(a) consisting of a torsional vibrator to drive the rotor by frictional contact and Figure 1.11(b) a piezoelectric actuator operating in a normal direction to control the contact duration. During the forward stroke, the torsional vibrator turns the rotor through the frictional force enhanced by expanding the piezoelectric actuators. During retraction, the actuators contract and the rotor is detached from the torsional vibrator.

1.3.3 Surface acoustic wave

Surface acoustic waves (SAW) can be generated on the free surface of an elastic solid, and the phenomenon has been exploited for electronic analogue signal processing with the development of host devices or systems [24]. The SAW devices have been popular for applications in electronic industries, instrumentation, signal processing and communications that includes satellite receivers, remote control units, keyless entry system, radio frequency identification (RFID), television sets, mobile phones, actuators, and sensors due to their compactness, versatility, efficiency in controlling and processing

electrical signals [25], [26]. Normally SAW devices are made of piezoelectric substrates such as lithium niobate ($LiNbO_3$ or LN), lithium tantalite ($LiTaO_3$), langasite ($La_3Ga_5SiO_{14}$), and lead zirconate titanate (PZT). The metal electrodes arranged in comb structure known as interdigital transducers (IDT) on a piezoelectric substrate are used to convert an electrical signal into acoustic waves through the electromechanical coupling and vice versa. With the application of input power to IDT, SAW is generated on the surface of the piezoelectric substrate. In a SAW device, the most of the acoustic energy is confined to one wavelength depth of the piezoelectric substrate and SAW amplitude decays exponentially with the substrate depth [27]. Since the phase velocity of SAW is about five orders lower than the electromagnetic wave, signal processing in the acoustic domain is possible in real time in a single compact device [28]. SAW devices are used as microactuators such as SAW motors with nano and sub-nano steps resolution and SAW micropumps [29].

The generation of travelling or standing waves on an elastic medium occurs when the particles in the medium are displaced from their equilibrium positions by an external force together with the elastic restoring forces [30]. The three possible trajectories of the particles in motion on the elastic medium are linear, elliptical, and circular polarisation[28],[30]. The motion of the particles can be resolved into two components, namely longitudinal component and shear component.

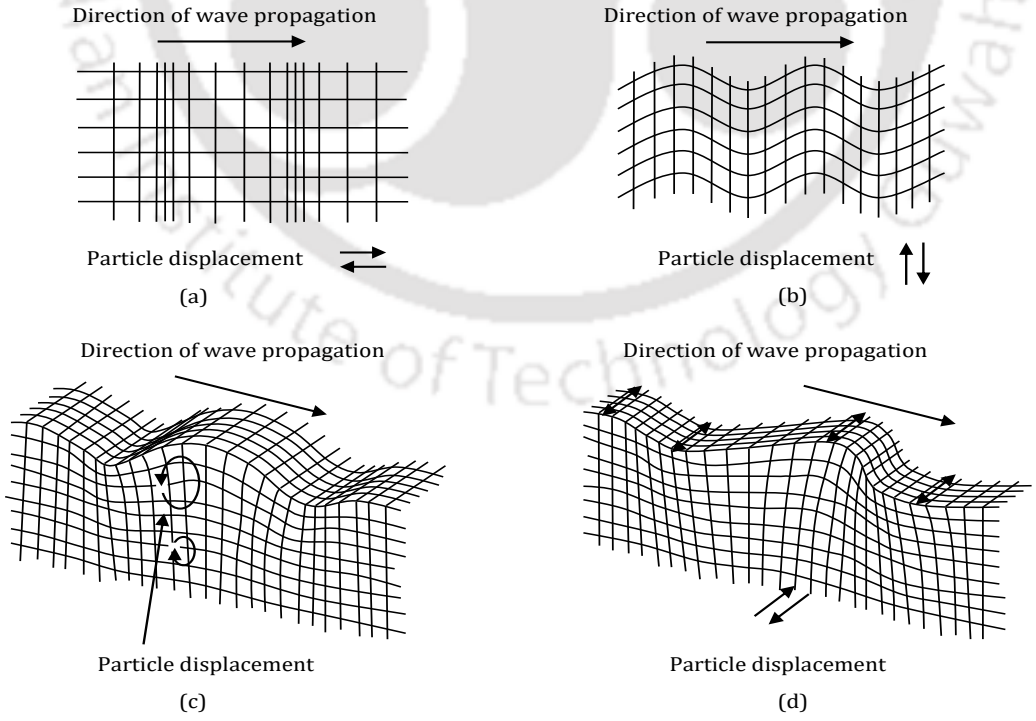

Figure 1.12: Schematic of acoustic wave propagation for (a) Longitudinal or compressional wave, (b) Shear or transverse wave, (c) Rayleigh wave, and (d) Shear horizontal (SH) wave.

In longitudinal or compressional waves, the particle displacement is parallel to the direction of wave propagation as shown in Figure 1.12 (a). In the shear or transverse waves, the particle displacement is normal to the direction of wave propagation as shown in Figure 1.12 (b). Additional types of acoustic waves are generated in a piezoelectric medium as determined by the properties of the piezoelectric material, such as the thickness of the elastic medium, crystal cut (and therefore orientation), and the pattern of IDT [28], [4]. Different types of acoustic waves used in SAW devices are Rayleigh wave, shear horizontal (SH) wave, acoustic plate mode (APM) wave, flexural plate mode (FPM) wave, and Love wave [4], [31].

In 1885, English scientist Lord Rayleigh published a research paper on surface acoustic wave entitled “On wave propagation along the plane surface of an elastic solid" based on his study of seismic waves. The particle displacement in elastic Rayleigh wave has both surface normal and surface parallel components with respect to the direction of wave propagation. Figure 1.12 (c) shows the movement of the particle at the top surface of the elastic medium taking the elliptical path in an anti-clockwise direction that reduces in magnitude and

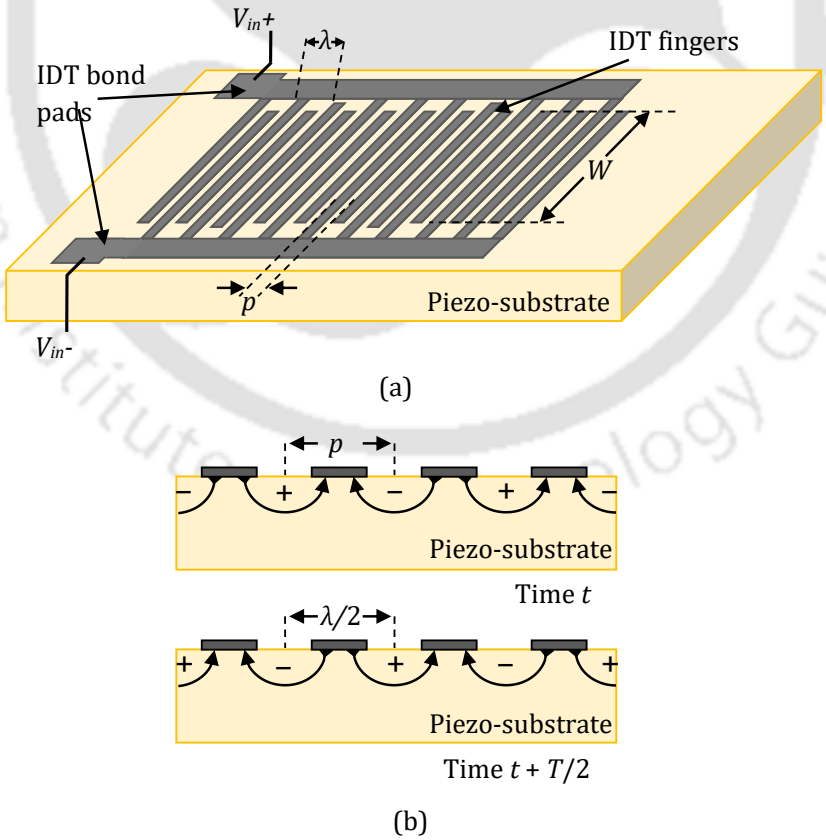

Figure 1.13:(a) Interdigital transducer (IDT) with bond pads on a piezo-substrate. (b) Polarities of applied potentials on IDT fingers at time *t* and at time *t* + *T*/2.

changes to the clockwise direction of motion at about one wavelength depth inside the medium [32].

The particle displacement of shear wave is mostly parallel to the plane of the surface and transverse to the direction of wave propagation as shown in Figure 1.12 (d). The SH-APM is similar to Rayleigh waves but the substrate thickness is of a few acoustic wavelengths and wave reflects between the surfaces as in plates. FPM is similar to Rayleigh wave where the velocity varies with the variation of the thickness and material of the substrate. The Love waves are SAWs that propagate in a waveguide deposited on a substrate whose thickness is much greater than the waveguide layer [25]. These waves are transverse, bring the only shear stresses into action, and the amplitude decays exponentially with depth. The energy of Love wave is concentrated mostly in the waveguide layer and close to the interface.

1.3.3.1 Generation of surface acoustic waves

The metallic electrodes patterned in comb-like structure over the surface of a piezo substrate in a SAW device is called as interdigital transducer (IDT) [28]. The metal used for fabricating IDT can be gold, silver or aluminium depending on the conducting and physical properties, but IDT is usually made of aluminium (Al) using photolithography [32]. An IDT with bond pads for electrical connection fabricated on a piezo substrate is shown in Figure 1.13(a).The electrical potential applied to the IDT electrodes produces an electric field which will cut the piezo substrate as illustrated in Figure 1.13(b) and generate stresses at the surface of the piezo substrate. Application of sine wave excitation results in series of alternate compression and expansion regions propagating on the surface of the substrate on both sides of the IDT [32] as SAW.

When the applied potential is sinusoidal with period T, the vibrations add constructively if the center-to-center distance between IDT fingers p is equal to the half of the acoustic wavelength λ for the excitation frequency as shown in Figure 1.13(a) [32]. Figure 1.13 (b)

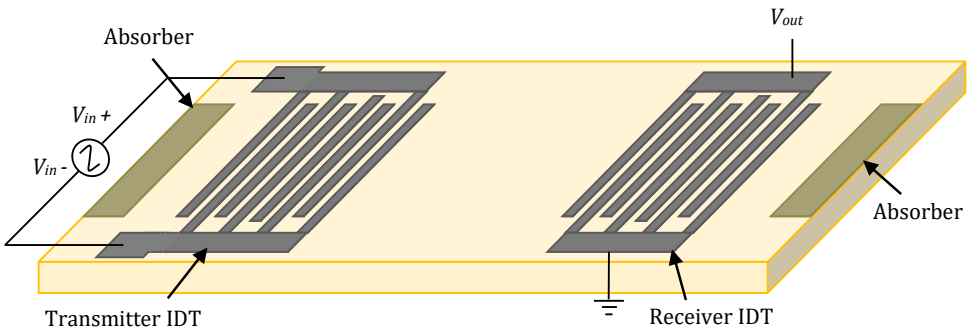

Figure 1.14: Schematic diagrams of the SAW delay line device.

illustrates the constructive generation of SAW on a piezo substrate. The stress wave generated at time t by a pair of IDT fingers travels a distance of half acoustic wavelength ($\lambda/2$) in the time interval of half period ($T/2$) with the speed of SAW phase velocity c.As shown in Figure 1.13 (b), at time $t + T/2$, the generated stress wave reaches the neighbour IDT finger pair where it adds constructively to the stress wave produced during the next half cycle of the input sinusoid [32].

The stress waves generated by each finger pair add constructively with the stress waves generated by other finger pairs in the subsequent cycles of input excitation resulting in resonance. The resonance frequency or the synchronous frequency f_0 is related to the pitch p of the IDT fingers and SAW phase velocity c as given in equation (1.1) and equation (1.2).

$$f_0 = \frac{c}{\lambda} \tag{1.1}$$

$$\lambda = 2p \tag{1.2}$$

whereλ is the acoustic wavelength. The bandwidth of the SAW device is determined by the number of finger pairs of the IDT. The 3 dB bandwidth f_b of a SAW device with N number of IDT finger pairs can be estimated [33] as given in equation (3).

$$f_b = \frac{0.88 f_0}{N} \tag{1.3}$$

The IDTs are fabricated on piezo-substrate using photolithography techniques well established in semiconductor industries [32].

1.3.3.2Basic configurations of SAW devices

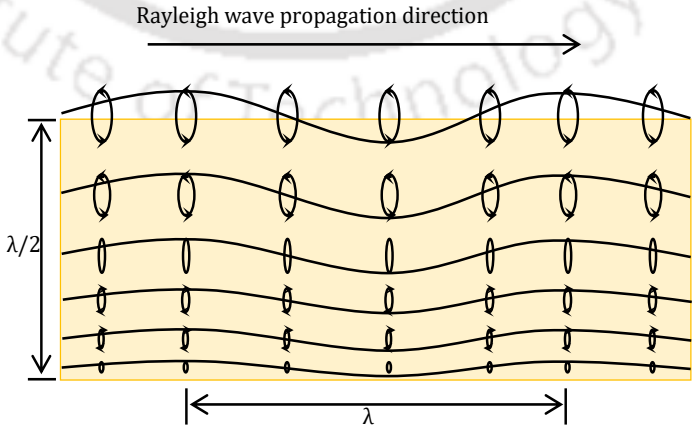

Figure 1.15: Schematic of motion trajectories of points in the substrate during propagation of Rayleigh SAW.

The SAW devices are generally operated in two different ways: resonator and delay line. A SAW delay line type device is a two port device as shown in Figure 1.14, where an IDT is fabricated at either end of the substrate separated by a distance of a few wavelengths [34]. One IDT called as a transmitter IDT, on electrical excitation, generates SAW that propagates towards the other IDT called as a receiver IDT which converts the SAW in electrical output. Figure 1.15 shows the schematic of the motion trajectories of the points when SAW propagates on the free surface of a semi-infinite elastic body. A Rayleigh wave travelling from left to right results in anticlockwise elliptical motion of the points on the surface of the stator as shown in Figure 1.15 [35]. The amplitude of SAW falls exponentially with the depth inside the substrate. The SAW resonator devices are divided into two types: one port resonator and two port resonator as shown in Figure 1.16. In resonators, SAW of the specific frequency generated by the IDT propagates within the substrate block such that the wave is reflected back and forth within the confinement causing resonance.

In one-port SAW resonator, a bidirectional IDT is fabricated with a set of reflectors on

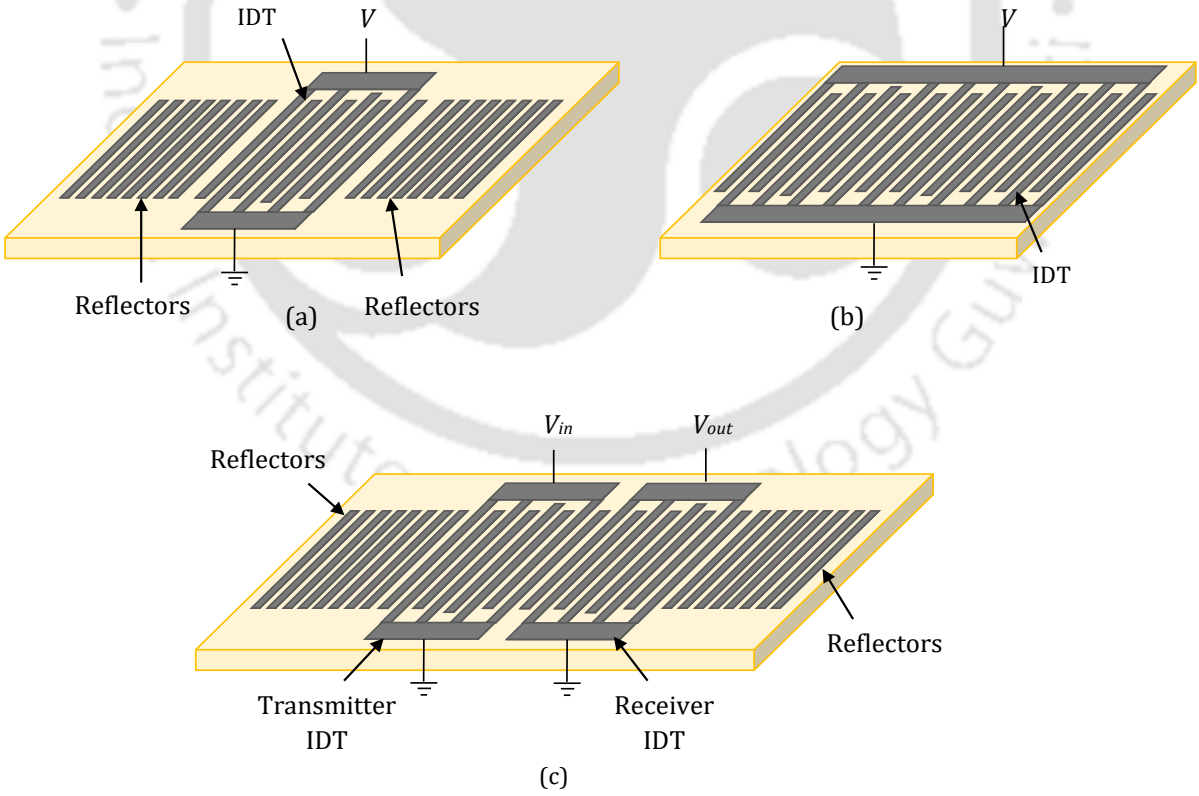

Figure 1.16: Schematic diagrams of SAW devices, (a) One-port SAW resonator with reflectors, (b) One-port SAW resonators with long IDT, (c) Two-port SAW resonator with reflectors.

either side as shown in Figure 1.16 (b) [28].

The reflectors could be made of shorted metal strips or grooves. At the Bragg frequency, the periodicity of the reflector electrodes is equal to half the wavelength, so that the reflections from individual fingers are in phase and add coherently. Strong reflections are obtained when N|rs|>1, where N is the number of reflector fingers and rs is the reflection coefficient of a finger. Typically, |rs| is about 2 % and N is 200 or more [28].

A one-port SAW resonator can also be made by using a large number of IDT fingers without reflectors. In this device, multiple reflections within the IDT lead to standing waves and the device resonates at a particular frequency. In the case of the two-port resonator, a set of reflectors is fabricated on each outer side of the pair of adjacent IDTs. Two port resonators are used in high stability oscillators [28].

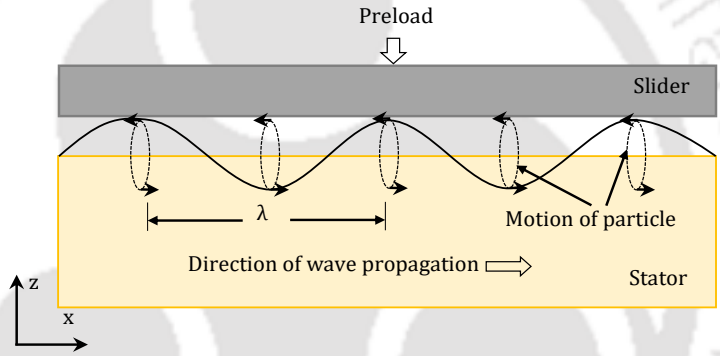

Figure 1.17: Schematic diagram to explain the interaction of Rayleigh wave with the slider in a SAW motor.

In chapter 2, the conventional SAW devices are discussed in detail and simulated based on finite element simulation method (FEM) using COMSOL Multiphysics [14].

1.4 Surface Acoustic Wave Motors

A SAW motor consists of a movable part called as a slider placed in contact with a stator made of a piezoelectric substrate that generates SAW on its surface and drives the slider in

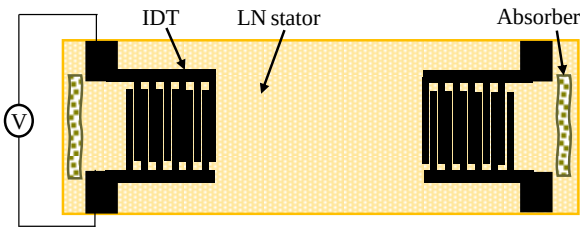

Figure 1.18: Schematic diagram of the LN stator used for SAW motor.

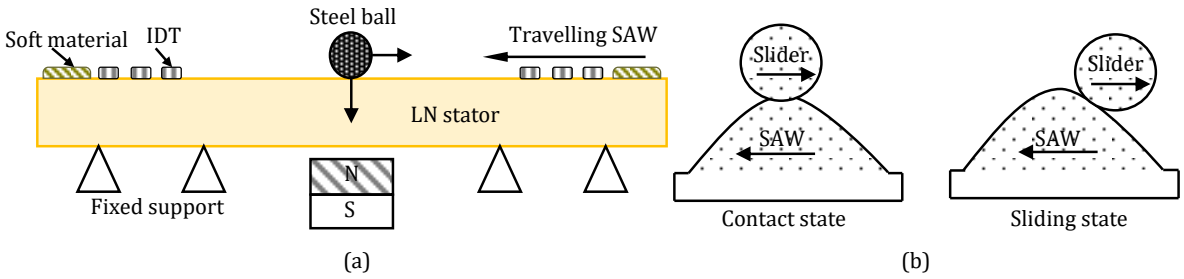

Figure 1.19: (a) Controlling preload, (b) Contact and sliding condition.

Source: Adapted from Morita et al., [36].

translational motion [36]. The operation of a SAW linear motor is based on the frictional drive generating high tangential force on the slider at the contact points with the stator as the Rayleigh wave travels on the surface of the stator [37].

The stator in SAW linear motors is normally made of 128°-rotated Y-cut X-propagated lithium niobate ($LiNbO_3$ or LN) substrate. Comb-shaped aluminium (Al) electrodes known as IDTs [38], are fabricated on the surface of the LN substrate [39] at either end of the substrate and separated by a distance of a few wavelengths. The Rayleigh SAW [30] is generated when a sinusoidal voltage excitation is applied to the IDT, and the wave propagates on the surface of the stator. A Rayleigh wave travelling on the surface of the stator results in elliptical motion of the points on the surface as shown in Figure 1.15.

In 1994 Kurosawa *et al.* demonstrated the operation of a surface acoustic wave (SAW) motor using the stator shown in Figure 1.18 and a steel ball slider held in contact with the stator by a magnetic force as shown in Figure 1.19 (a). The SAW motor goes through two states viz., contact state and sliding state as illustrated in Figure 1.19 (b).

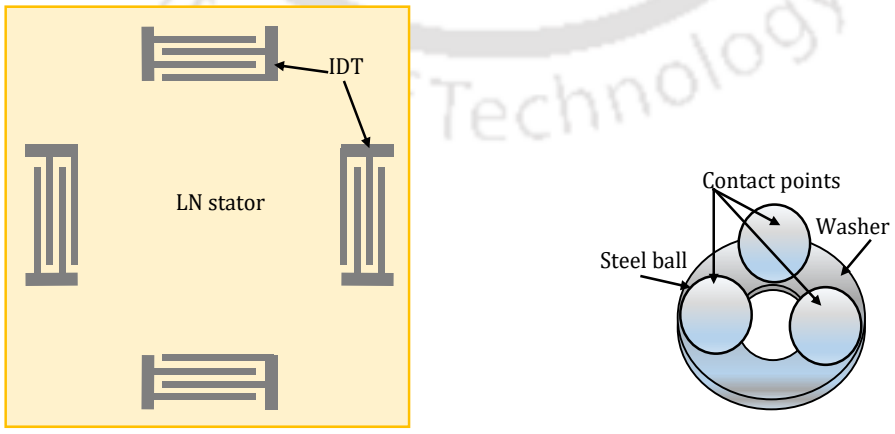

Figure 1.20: The view of the slider kept upside down indicating multiple contacts.

Source: Adapted from Kurosawa et al., [40].

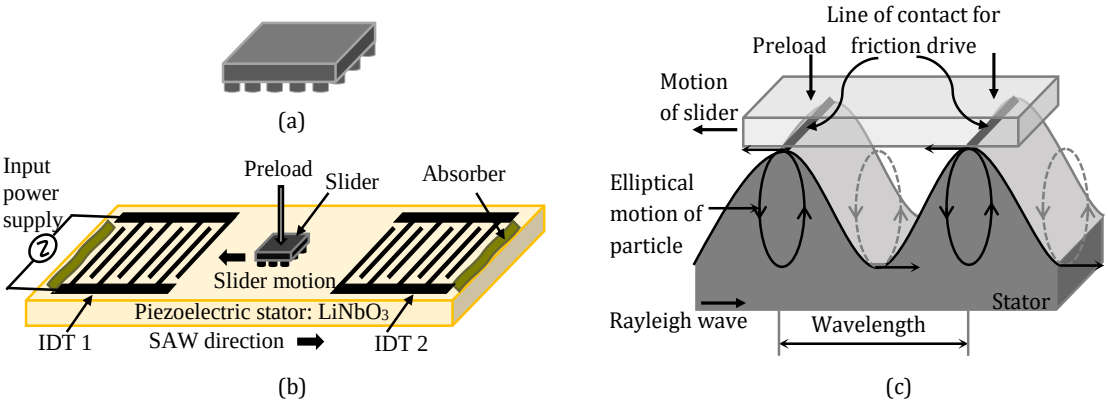

Figure 1.21: (a) SAW linear motor, (b) Multi-contact-point slider using tiny steel balls. Source: Adapted from Shigematsu et al., [26], [41].

During contact state, the tangential frictional force moves the slider, and during non-contact state, there is no driving force on the slider. Further, Morita *et al.* [36] using Hertz contact theorem calculated contact force between the slider and the stator, frictional force, normal position of the slider, and tangential position of the slider by dynamic simulation of the SAW motor and reported a method to obtain optimum preload.

Kurosawa *et al.*[40] made a SAW motor using a slider made of 3 steel balls as shown in Figure 1.20 (a) with LN stator having an additional pair of IDTs as shown in Figure 1.20 (b) to enable two degrees of freedom. The planar motion of the slider was obtained by two

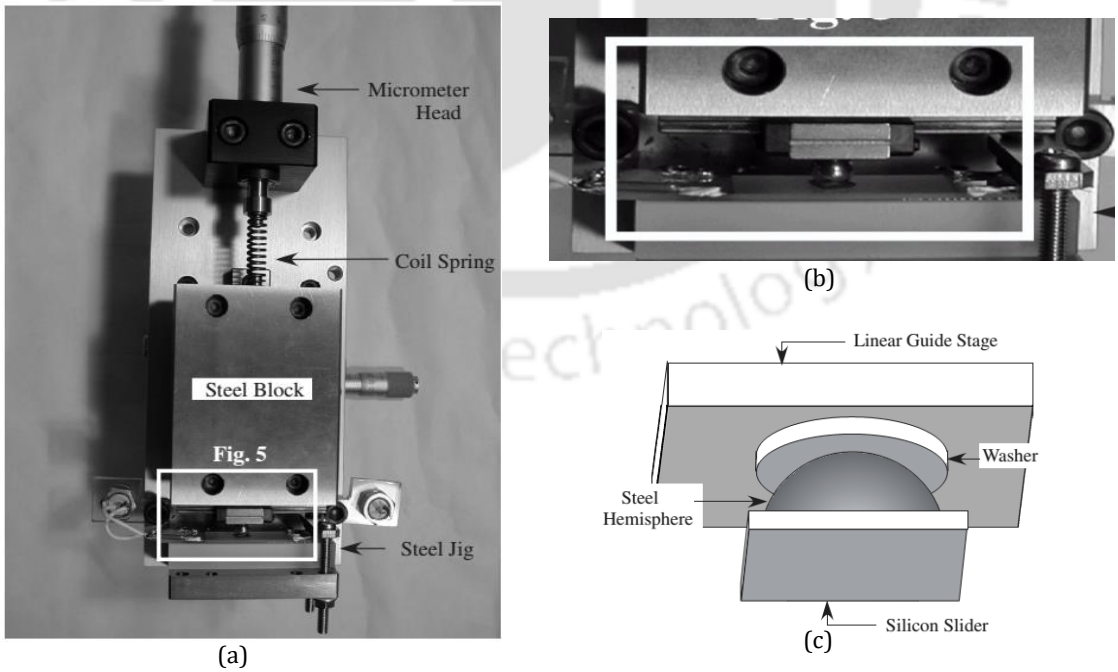

Figure 1.22: The assembly of a SAW motor adopted by Shigematsu [26]**. (a) Entire SAW motor assembly (b) a small part of the assembly magnified to show the stator and slider (c) a hemispherical pivot placed on the slider to delink preload assembly while allowing preload to act on the slider. Source: Adapted from Shigematsu** [26]**.**

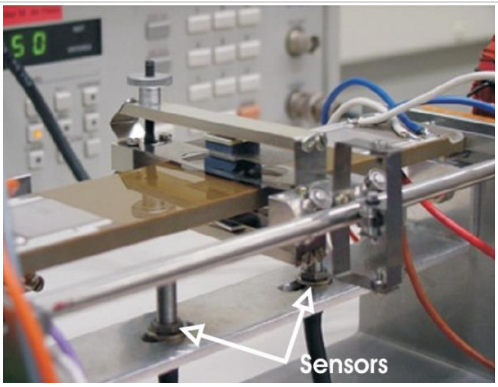

Figure 1.23: SAW motor using two sliders preloaded against each other and utilising end-of-stroke sensors.
Source: Adapted from Feenstra *et al.*

orthogonal SAWs excited by IDTs.

A slider having multiple contact points as shown in Figure 1.21 (a) is proposed by Kurosawa *et al.*[41]. The slider enlarges contact area while solving the problem of the sticky slider due to pre-pressure between the stator and the slider. The principle of operation of a linear SAW motor is explained in Figure 1.21 (c), where the particles of the surface of the stator make elliptical trajectory around their mean position [26] as the Rayleigh SAW propagates. The stator makes contact with the slider at the wave crests where the particles have maximum horizontal velocity component. The particle motion is transmitted to the slider through frictional force.

Shigematsu *et al.*[26], [42] have presented a SAW motor with high resolution stepping motions of nano to the sub-nanometer range, and the step displacement controlled in the nanometer to centimetre range by adjusting the number of cycles of driving waves. To generate high contact friction force at the interface of the slider and the stator, high preload is required, and the guide rail mechanism to provide preload makes the device cumbersome and bulky as shown in Figure 1.22. The spring-loaded steel block provides the preload, and

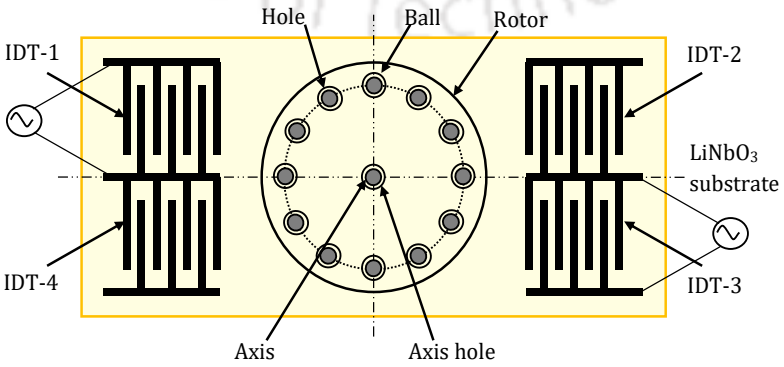

Figure 1.24: SAW rotary motor using two opposite SAWs.
Source: Adapted from Cheng *et al.* [43].

a lubricated guide rail is necessary to reduce friction at the top side of the slider and guide the slider movement in a predetermined path.

Using the results of the experimental work of Kurosawa-related to single point contact SAW motor, Feenstra *et al.*[44] have developed a mathematical model which they extended for the case of multi-point contact. For verification of the mathematical model, they assembled a SAW motor using two sliders preloaded against each other with the stators placed in between as shown in Figure 1.23. However, they omitted the sandwich construction, as the use of two sliders often generated a difference (e.g. amplitude) between the top and bottom SAWs of the stator and adopted SAW motor using thesingle slider which produced more precise experimental results.

Figure 1.24 shows a rotary type SAW USM developed by Cheng *et al.*[43], [45]. Two pairs of IDTs on stator excite two SAWs parallel to each other with opposite direction to drive a slider. The rotor pivoted at the centre and is supported on the ring-shaped arrangement of balls which are in contact with the stator. The frictional forces acting in the opposite directions in the two halves of the rotor produce torque that sets the rotor revolving.

A SAW USM using the liquid as the driving medium was developed by Sano *et al.*[46] as shown in Figure 1.25. When Rayleigh wave strikes liquid, it radiates a longitudinal wave into the liquid and damps. If the liquid amount is small as in a droplet, it moves the droplet in the direction of SAW propagation. If a small solid object is placed with the small water droplet, the SAW moves the object along the direction of the wave.

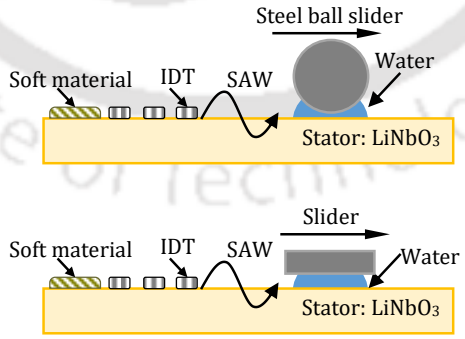

Figure 1.25: Driving principle of SAW streaming manipulator.
Source: Adapted from Shiokawa et al., [46].

Yosuke Fujii *et al.*[47] applied segment-structured diamond-like carbon (S-DLC) film either on the slider or the stator of the SAW linear motor. As S-DLC film is recognised as a wear resistant material, it is used for wear resistant coating in the friction drive of the SAW linear

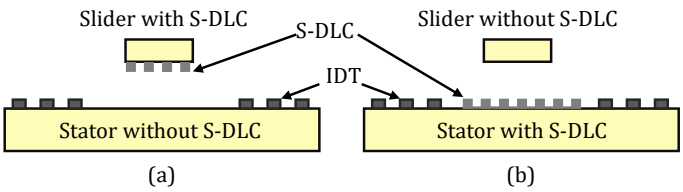

Figure 1.26: SAW linear motor with anS-DLC film deposited (a) on the slider, and (b) on the stator. Source: Adapted from Yosuke Fujii et al., [47]**.**

motor. Figure 1.26 illustrates the two types, (a) the S-DLC film deposited on the slider surface, and (b) the film deposited on the LN stator.

Huan-Huan et al. [48] carried out research on non-contact SAW linear motors shown in Figure 1.27, in which the slider is placed in a pool of liquid on the surface of the stator carrying SAW. The SAW converts into leaky SAW at the liquid and solid interface. Further, at

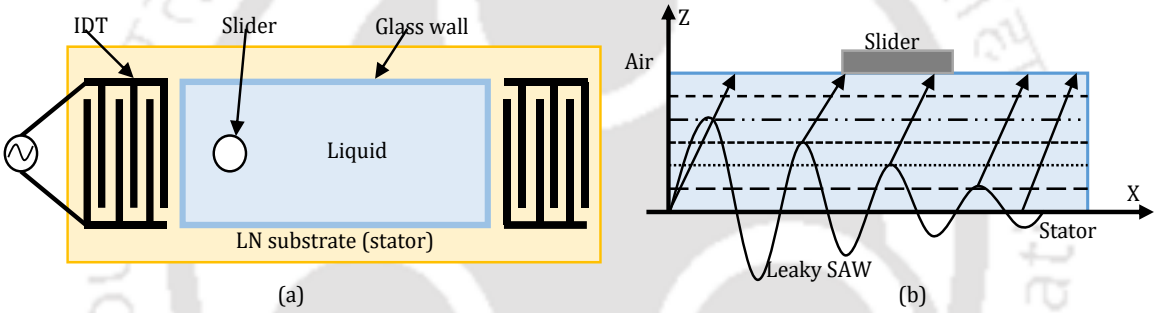

Figure 1.27: (a) Sketch, (b) Principle of non-contact SAW linear motor. Source: Adapted from Huan-Huan GU et al., [48]**.**

the interface, leaky SAW produces longitudinal wave into the liquid which drives the slider in the direction of SAW propagation. Their experimental results show that the slider velocity is proportional to the driving voltage of the SAW and decreases almost exponentially with the increase in the thickness of the liquid layer.

Sakano *et al.*[49], [50] presented a flat-plane slider as shown in Figure 1. 28 for a SAW

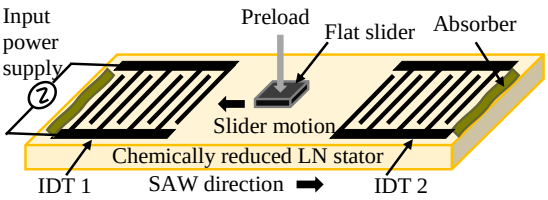

Figure 1. 28: Schematic view of a SAW motor with a chemically reduced stator and flat plane slider. Source: Adapted from Sakano et al., [49]**.**

motor that could provide stable drive by using chemically reduced LN stator. This stator has higher electric conductivity and prevents charge build-up at the contact area. As the contact area of the flat-plane slider is larger than that of the slider with projections, the flat-plane slider can drive faster than a slider with projections, however under a higher preload. The advantage of the flat-plane slider is that it does not require silicon micromachining processes.

1.5 Problem Definition

In a conventional SAW linear motor, the slider is held tightly in contact with the surface of the stator with required preload is applied from the top through a lubricated guide rail to reduce friction at the top side of the slider while increasing friction between the stator and the bottom surface of the slider [26] as shown in Figure 1.29. To achieve the conflicting friction-related requirements at the two sides of the slider and to guide the slider to move in

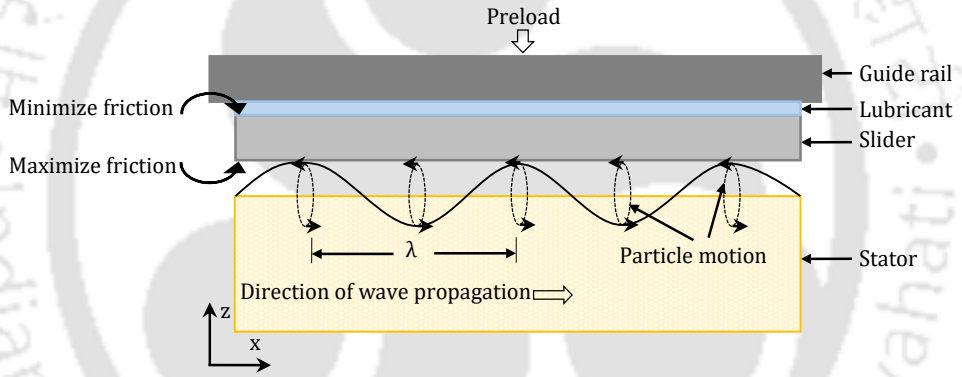

Figure 1.29: Schematic diagram of conventional SAW linear motor.

the predefined path, usually heavy and bulky lubricated guide rails, described in the previous section, are used. Thecumbersomeancillary, in fact, has become the major impediment in the commercialization of SAW motors.

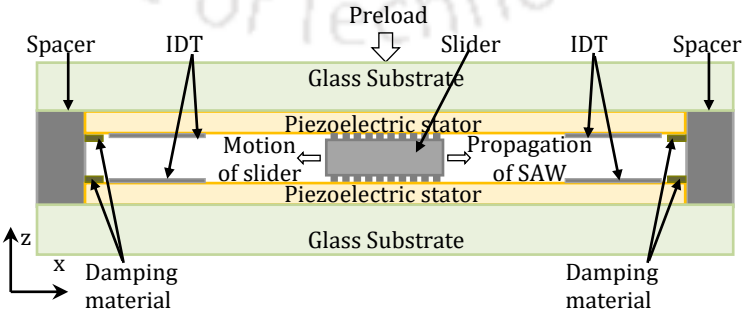

Figure 1.30: Schematic of dual friction-drive SAW linear motor with a slider having a uniform array of projections.

The research work presented in the thesis is aimed at achieving a compact design which is convenient to use and suitable for commercialization. The necessary restructuring of a SAW linear motor with the guide rail replaced by an additional stator to drive the slider simplifies the operating mechanism. The assembly of the proposed SAW motor is shown in Figure 1.30 where a slider with a uniform array of projections on both the contact surfaces is sandwiched between two identical stators aligned to generate SAWs that drive the slider from top and bottom.

The glass substrates provide support to the piezoelectric stators while supplying preload. In each stator, SAW propagating on the surface of the stator interacts with the slider at the contact points and the frictional force acts on the slider in the direction opposite to the propagation of SAW. By applying simultaneous excitation to two IDTs on one side of the motor, one each from the top and bottom stators, the Rayleigh waves propagates on the

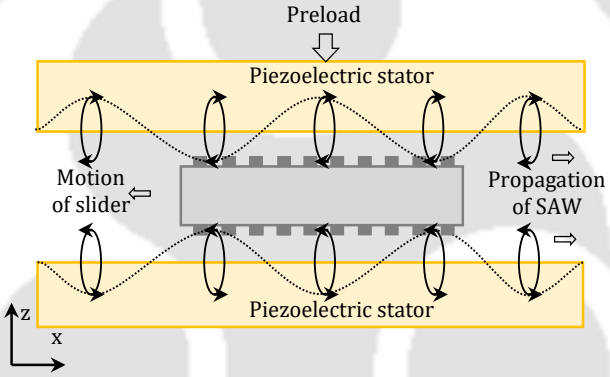

Figure 1.31: Schematic diagram of proposed principle of working for the dual friction-drive SAW linear motor.

stator surfaces and deliver a frictional force on the surface of the slider at the contact points is represented in Figure 1.31. Since the waves propagate in the same direction on the two stator surfaces facing each other, the elliptical motion of the points on the surfaces of the stators generates frictional forces on the two contact surfaces of the slider which results in driving the slider towards the activated IDTs. The direction of motion of the slider can be changed by switching the excitation to the IDT pair on the respective side of the motor, thus forward or reverse translational motion is possible. The proposed DFD technique SAW linear motor could overcome the limitations mentioned above for the conventional SAW linear motor.

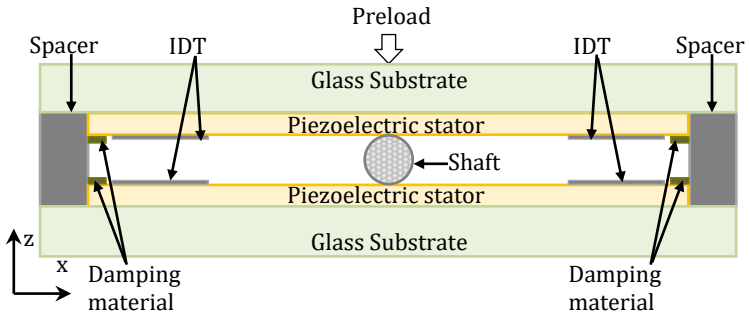

Figure 1.32: Schematic diagram of dual friction-drive SAW motor with a cylindrical shaft.

The assembly of the proposed SAW motor is shown in Figure 1.32 where a cylindrical shaft is sandwiched between two identical stators aligned to generate SAWs that drive the slider from top and bottom. The glass substrates provide support to the piezoelectric stators while

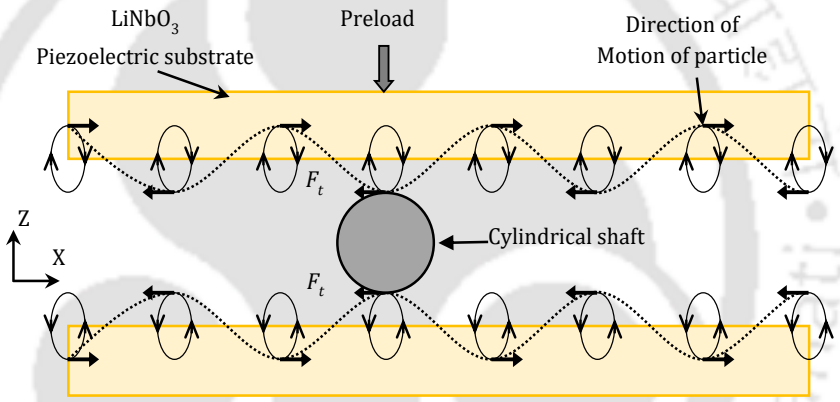

Figure 1. 33: Schematic diagram of proposed principle for dual-drive SAW motor as a linear motor.

supplying preload. Each stator has an IDT fabricated on the piezoelectric substrate on either side of the shaft. In each stator, SAW propagating on the surface of the stator interacts with the shaft at the contact points and the frictional force acts on the shaft in the direction opposite to the propagation of SAW. The proposed SAW motor is capable of making both translational and rotational motion in forward and reverses directions.

When electrical excitation is applied in a synchronised way to the one side of the stators each of top and bottom stator, Rayleigh SAW is generated that propagates in the the +X direction in both the stators. Since the two stators are kept facing each other, for the SAW travelling in a +X direction, the particles at the surface of the bottom stator make anticlockwise elliptical motion, and the particles on the surface of the top stator make clockwise elliptical motion as drawn in Figure 1. 33. The preload applied to the shaft generates high frictional force on the cylindrical shaft in –X direction at both the contact

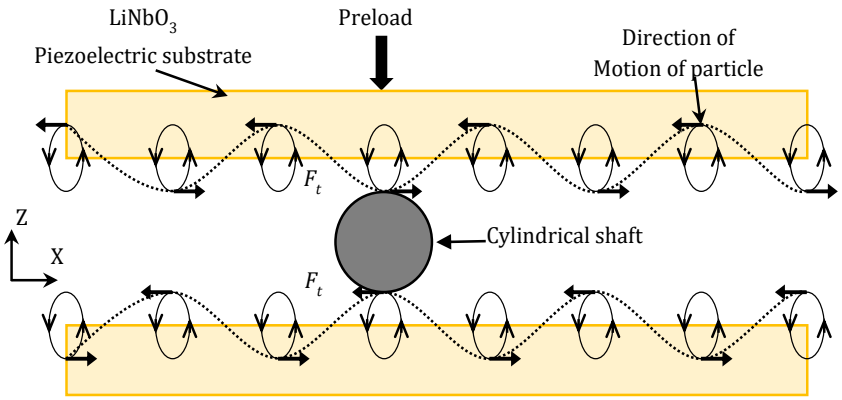

Figure 1.34: Schematic of proposed principle of working for dual friction-drive SAW motor as a rotational motor.

points and the shaft performsatranslational motion in –X direction. Similarly, if IDTs present at other side are activated instead of present activated IDTs, the shaft will perform atranslational motion in the opposite direction i.e. in the +X direction.

When electrical excitation is applied in a synchronised way to the IDTs present on each of top, and bottom stator disposed of crosswise as shown in Figure 1.32, Rayleigh SAW is generated that propagates in the +X direction in the bottom stator and in –X direction in the top stator. With the above arrangement, for the SAW traveling in +X direction, the particles at the surface of the bottom stator make anticlockwise elliptical motion and for the SAW traveling in –X direction the particles at the surface of the top stator make clockwise elliptical motion as drawn in Figure 1.34. The applied preload generates high frictional force on the shaft in –X direction at both the contact points and the shaft performs a rotational motion in a clockwise direction. Similarly, if IDTs on the other side are activated instead of present activated IDTs, the shaft will perform a rotational motion in the opposite direction i.e. in an anticlockwise direction. Thus the shaft can make a rotational motion in both clockwise and anticlockwise directions. By applying alternate excitations for translational and rotational motions through time multiplexing repeatedly, a simultaneous translational and rotational motion is achieved.

1.6 Scope of the Thesis

In this thesis, two types of SAW motor configurations are presented: 1. Dual friction drive SAW linear motor with cuboid slider making only translational motion, 2. Dual friction drive SAW motor with cylindrical shaft making both translational and rotational motion.

The scope of the thesis includes the following.

- Study and simulation of conventional SAW devices such as one-port SAW resonator with an infinite number of IDT fingers and SAW delay line device, using COMSOL Multiphysics based on FEM.
- Study and simulation of conventional SAW motor with the spherical ball and cuboid slider with and without projections, to verify the previous results using COMSOL Multiphysics based on FEM and MATLAB.
- Simulation of the proposed SAW motor; study of various aspects pertinent to the proposed SAW devices that include effects of preload, the coefficient of friction and supplied power.
- Methodology to fabricate the proposed SAW motors and measurements of fabricated SAW devices using a network analyser. Experimental validation of the proposed SAW motors.

1.7 Thesis Outline

The thesis work has been organised into eight chapters, and the contents are briefly outlined as follows.

- Chapter 1 gives a brief introduction to SAW and presents the generation of SAW by an IDT, basic configuration of SAW devices, and literature survey on SAW motors followed by problem definition.
- Chapter 2 describes various modelling and simulation techniques for SAW devices.
- Chapter 3 is devoted to the mathematical modelling of conventional SAW motors and their finite element simulation through COMSOL Multiphysics.
- Chapter 4 explains the proposed DFD technique and presents the mathematical modelling of SAW motors based on DFD technique. The results of FE simulation of various configurations of the DFD based SAW motor are included.
- Chapter 5 presents mathematical modelling and FE simulation of DFD based SAW motor with the cylindrical shaft.
- Chapter 6 describes the design and process flow for the fabrication of the stators and sliders of the proposed DFD SAW motor.
- Chapter 7 presents details of characterization and testing of the fabricated devices using a network analyser. Assembly of the DFD SAW motor is described. The motion of the slider is observed by applying voltage excitations.
- Chapter 8 lists the conclusions of the research work and recommendations for future work.

2

Modelling and Simulation of SAW Devices

A brief introduction and literature survey on ultrasonic motors (USMs) and surface acoustic wave (SAW) motors are presented in chapter 1. We have discussed the working principles and their pros and cons of different types of SAW motors developed by various research groups and different research persons. This chapter deals with the modelling and simulation of surface acoustic wave devices. Different techniques of modelling of SAW devices are discussed along with finite element simulation of resonator and delay line. A surface acoustic wave motor operates using Rayleigh surface acoustic waves (SAW). In the next chapter, the design and working principle of SAW motor depending on Rayleigh wave is explained. Hence it is mandatory to go through the modelling of interdigital transducers (IDTs) including characteristics, principles and generation of surface waves.

2.1 Generation of Surface Acoustic Waves

The aim of the stator used in SAW motor is to generate Rayleigh waves with a large amplitude. SAW devices consisting of IDTs fabricated on the surface of piezoelectric substrates to generate Rayleigh SAW can be modeled, and the functions of IDT can be described using feasible techniques such as delta function method or discrete source, impulse response method, coupling of mode (COM) method, piezoelectric permittivity method, matrix representation, numerical techniques using equations, and equivalent circuit method [51], [34]. The finite element method (FEM) is a numerical technique that allows simulating the devices with any number of IDT fingers and easy visualisation of the device response to the applied boundary conditions [34], [25]. This chapter mainly describes the simulations of conventional SAW devices such as one-port SAW resonators and SAW delay line devices by FEM using COMSOL Multiphysics. Brief descriptions of the modelling techniques used for SAW devices are given in the following sections.

Early researchers relied on experiments to design and develop SAW devices. There were numerous discrepancies in actual function of devices. The basic design of SAW transducers has to be optimised with the help of modelling techniques. Nowadays computer aided simulation helps in designing SAW devices and studying the characteristics of these devices made on new piezoelectric substrates. Simulations of SAW devices assist in estimating and visualising the SAW device response before fabricating these devices.

2.1.1 Delta function model

Delta function model is one of the first and simplest methods to analyse the shape of the IDT and design devices [51]. To analyse through this method, non-reflective uniform

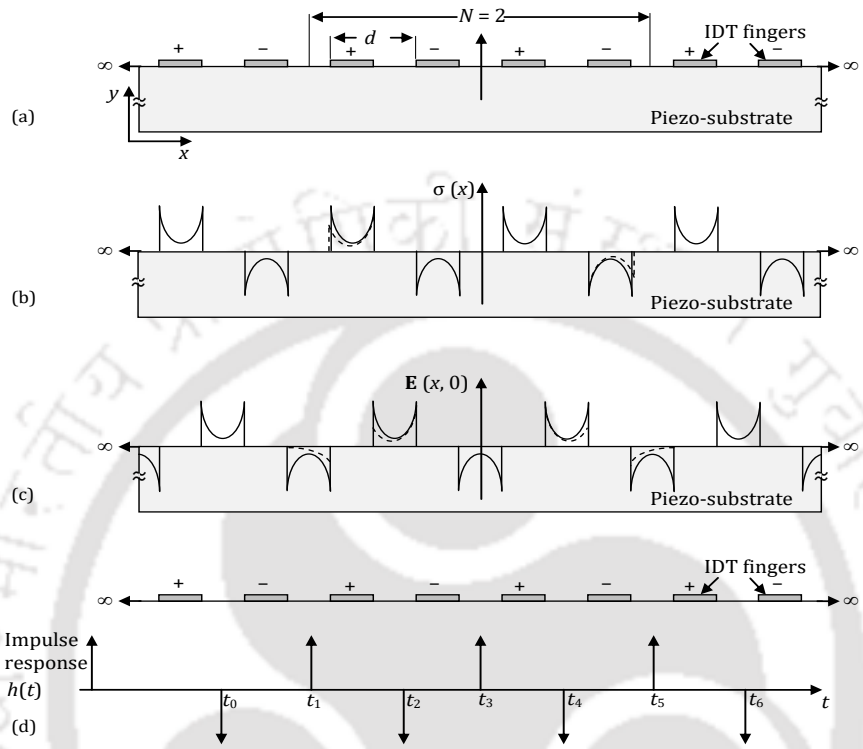

Figure 2. 1: (a) Schematic of IDT fabricated on piezo-substrate. (b) Spatial distribution of charge density at the surface of piezo-substrate. (c) Spatial distribution of electric field at the surface of piezo-substrate. (d) An array of discrete sources at the centres of the interval between IDT fingers.

Note: Solid line shows aspatial distribution with N = ∞, and the broken line shows deviation in the spatial distribution for N = 2.

transducers are considered where propagation loss and diffraction conditions are ignored. It does not consider energy, capacitance, and the electromechanical coupling coefficient of the material used in the device. The discrete source model is derived from the examination of the spatial distribution of charge density or electric field at the surface of the piezoelectric substrate. The delta function method associates either two electric field spikes of the same sign to each IDT interval or two charge spikes of the same sign to each IDT finger [51]. The spatial distributions of charge density and the electric field of two pairs of IDT fingers and infinite pairs of IDT fingers are shown in Figure 2. 1 (b) and (c), respectively. The broken line demonstrates the deviation in the spatial distributions of charge density and electric field for two pairs of IDT fingers. The end effects of IDTs in a

significant number of IDT pairs can be neglected. Thus the electrical quantities are assumed periodic in Figure 2. 1 (b) and (c). As per the delta function method, two charge density or electric field spikes normal to the piezo substrate from IDT fingers are assumed as two delta function sources are equivalent to one delta function source [51].

Each delta function source has an amplitude *A* proportional to the corresponding aperture *W* of the IDT and the sign depends on the polarity of the charge density or electric field. Figure 2. 1 (d) shows an array of delta function sources at the centre of the IDT finger intervals. The input is voltage, and output is mechanical displacement. The frequency response of IDT with delta function source method can now be expressed as,

$$H(\omega)=\sum_{n=0}^{N-1} s_n A_n e^{-i\omega t_n} \tag{2.1}$$

where, s_n= (-1)is a sign, when the direction of the electric field reverses at each IDT interval,ω is the angular frequency and N is the number of finger pairs in IDT. The expression is given in the equation (2.1) can be approximated as a sync function. The detailed description of this method is presented in [51].

2.1.2 Impulse response method

The impulse response method calculates the absolute amplitude, hence the power of SAW by considering the energy of the wave [4]. If V_{in} = 1-U(t), where U(t) is unit step, is applied as input to the IDT, the output for t>0 is given by $a_u(t)$ in equation (2.2). A unit step signal is applied to the IDT fabricated on the piezosubstrate, and the output response is shown in Figure 2.2 (b). If the IDT electrodes are short-circuited for t < 0, the response of the device with unit step signal for duration of N/f_0 can be expressed as

$$a_u(t)=\begin{cases} -a_0 \sin(2\pi f_0 t) & \text{for } 0<t<N/f_0 \\ 0 & \text{for } t>N/f_0 \end{cases} \tag{2.2}$$

$$a_0 = K_R\sqrt{f_0 C_1/2} \tag{2.3}$$

where f_0 is the resonance frequency, C_1 is the capacitance per pair per unit length of IDT fingers. Thus the impulse response from (2.2) and (2.3) can be expressed as

$$h(t)=\pi\sqrt{2}K_R C_1^{1/2} f_0^{3/2}\cos(2\pi f_0 t), \qquad \text{for } 0<t<N/f_0 \tag{2.4}$$

If a sinusoidal signal with unit amplitude is applied to the input, the mean power density transported by the wave can be expressed as,

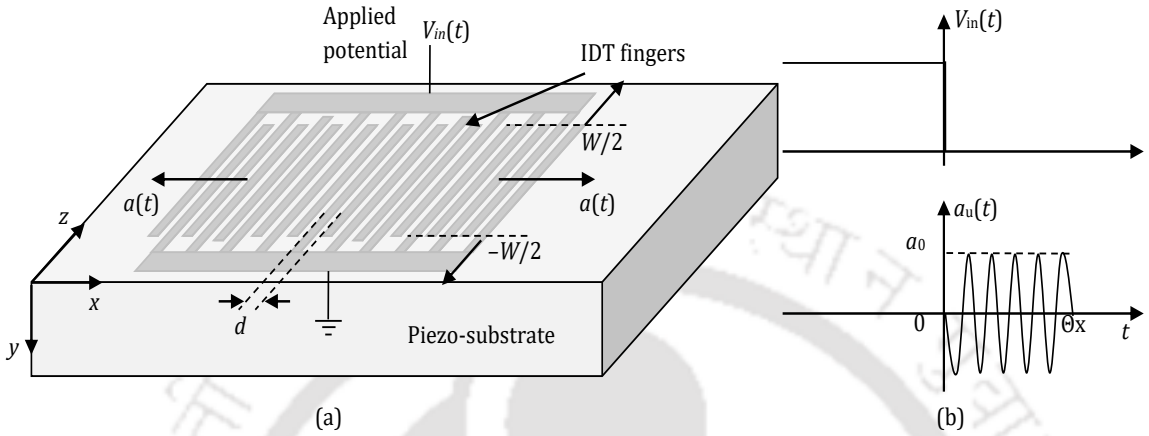

Figure 2. 2: (a) Schematic of IDT fabricated on piezo-substrate. (b) Response to the unit step voltage input.

$$P_R = \frac{\pi^2 N^2 a_0^2}{2}|U|^2 = \frac{\pi^2}{4} N^2 K_R f_0 C_1 |U|^2 \tag{2.5}$$

Where, $|U|$ is the amplitude of applied input signal. The detailed description about impulse response method is given in [51].

2.1.3 Coupling of Mode (COM) model

COM model is extensively used in designing of SAW devices [51], [25], [52]. This method is based on local analysis of way of two coupled waves evolve when propagating in both directions opposite to each other. This section gives a brief description about COM model. The COM model is discussed well by [25] and [53]. The COM model comprises of differential equations governing SAW mode amplitudes R(x, ω), S(x, ω) on either side of IDT and the current due to the flow of charges I(x, ω)(see Figure 2. 3)

$$\begin{aligned}
\frac{dR(x)}{dx} &= -jk_E R(x) + j\kappa_R e^{-j2k_0 x} S(x) + j\alpha_R V e^{-jk_0 x} \\
\frac{dS(x)}{dx} &= -jk_E S(x) + j\kappa_s e^{+j2k_0 x} R(x) - j\alpha_S V e^{+jk_0 x} \\
\frac{dI(x)}{dx} &= +j2\alpha_S R(x) e^{+j2k_0 x} + j2\alpha_R S(x) e^{-jk_0 x} - j\left(\frac{3\omega C_F / \lambda}{3 + j\omega R_F C_F}\right)_S V
\end{aligned} \tag{2.6}$$

where V is the voltage across the IDT electrodes, k0=2π/λ is transducer synchronous wave number, and

$$\kappa_E = +\frac{\omega}{v} - \left(\frac{2\alpha_R^2 \omega R_f^2 C_f^{\,2} \lambda}{9+(\omega R_f C_f)^2} \right) - j\left[\gamma + \left(\frac{6\alpha^2 R_f \lambda}{9+(\omega R_f C_f)^2} \right) \right]$$

$$\alpha_R = \frac{3\alpha e^{+j\phi_T}}{3+j\omega C_f R_f}$$

$$\alpha_S = \frac{3\alpha e^{-j\phi_T}}{3+j\omega C_f R_f} \qquad (2.7)$$

$$\kappa_R = +\kappa_i e^{+j\phi_B} + \frac{2j\alpha^2 R_f \lambda e^{-2j\phi_T}}{3+j\omega C_f R_f}$$

$$\kappa_S = +\kappa_i e^{-j\phi_B} + \frac{2j\alpha^2 R_f \lambda e^{+2j\phi_T}}{3+j\omega C_f R_f}$$

In the above equations ϕT = π and ϕB = π/2 are phase offsets of the grating and the potential respectively, and ω =2πf is the angular frequency.

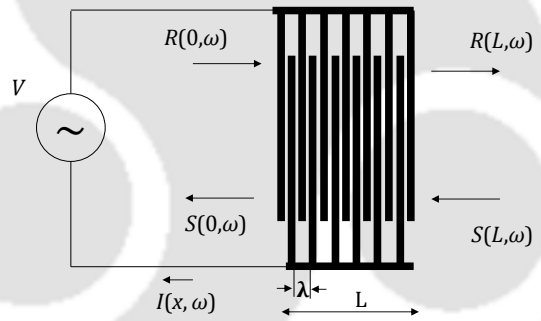

Figure 2. 3: Coordinates of an IDT [53].

The COM parameters are as follows. v phase velocity of SAW, α transduction coefficient, Rf thin film resistance in one transduction unit, Cf interdigital capacitance in one transduction period, κ the reflection parameter, γ propagation loss per unit length. The suffix R and S represent the values for the corresponding direction of wave propagation shown in Figure 2. 3. These parameters can be computed through computer simulation such as FEM or using experimental analysis of a test structure. The COM equations can be represented in P matrix form. The acoustic ports are treated as scattering port and electric port as admittance port and

$$\begin{bmatrix} S(0) \\ R(L) \\ I \end{bmatrix} = \begin{bmatrix} P_{11} & P_{12} & P_{13} \\ P_{21} & P_{22} & P_{23} \\ P_{31} & P_{32} & P_{33} \end{bmatrix} \begin{bmatrix} R(0) \\ S(L) \\ V \end{bmatrix} \tag{2.8}$$

where,

$$P_{11} = \frac{+jK_S \sin(DL)}{D\cos(DL) + j\Delta\sin(DL)}$$

$$P_{12} = \frac{D}{D\cos(DL) + j\Delta\sin(DL)} e^{-jK_0 L}$$

$$P_{13} = P_{31} + jL\frac{\sin(DL/2)}{DL/2} \times \frac{\alpha_s D\cos(DL/2) + j(K_S\alpha_R + \Delta\alpha_s)\sin(DL/2)}{D\cos(DL) + j\Delta\sin(DL)}$$

$$P_{22} = \frac{+jK_R \sin(DL)}{D\cos(DL) + j\Delta\sin(DL)} e^{-j2K_0 L}$$

$$P_{23} = P_{32} + jL\frac{\sin(DL/2)}{DL/2} \times \frac{\alpha_R D\cos(DL/2) + j(K_R\alpha_S + \Delta\alpha_R)\sin(DL/2)}{D\cos(DL) + j\Delta\sin(DL)}$$

$$P_{33} = +j2\left(\frac{K_S\alpha_R^2 + K_R\alpha_S^2 + 2\Delta\alpha_R\alpha_S}{D^3}\right) \times DL - \frac{D\sin(DL) + j\Delta(1-\cos(DL))}{D\cos(DL) + j\Delta\sin(DL)}$$

$$-2\left(\frac{K_S\alpha_R^2 + K_R\alpha_S^2 + 2\Delta\alpha_R\alpha_S}{D^3}\right) \times \left(\frac{1-\cos(DL)}{D\cos(DL) + j\Delta\sin(DL)}\right) \times j\left(\frac{3\omega C_f L/\lambda}{3 + j\omega R_f C_f}\right)$$

$$\Delta = K_E - K_0$$

$$D = \sqrt{\Delta^2 - K_R K_S}$$

P11 and P22 are the reflection coefficients, and P12 and P21 are the transmission coefficients. The remaining terms P13 and P23 correspond to the excitation coefficients of the IDT, and the term P33 represents the admittance of the structure relating the current flowing in the electrode (i) and the drive voltage (V). P31 and P32 terms represent the current generated by the waves arriving at the acoustic ports. Admittance or P33 can be calculated from simulations, and it is the most useful parameter in the device design.

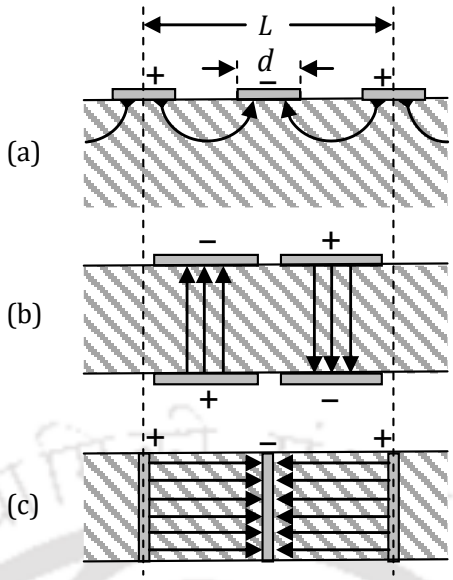

Figure 2. 4: (a) Electric field lines in a conventional SAW device. (b) Cross-field approximation. (c) In-line-field approximation.

2.1.4 Equivalent circuit model

The Mason equivalent circuit for SAW transducers is well explained by Smith et al. [54]. An equivalent electromechanical circuit can represent a periodic section of IDT. Two field models described in this method are shown in Figure 2. 4 (b) and (c). The cross-field model is constituted when SAW propagates in the direction normal to the excitation field. In the in-line-field model, the wave is generated in the direction parallel to the excitation field [51], [34]. Figure 2. 4(a) shows electric field lines in a conventional SAW device. The equivalent circuit model method of representation is based on the assumption that one of the two electric fields associated with the SAW device plays a dominant role.

The equivalent circuit model of one period of IDT is shown in Figure 2. 5. It consists of three ports, viz. two acoustic ports and one electric port. The electrical equivalent of the two acoustic ports is represented as SAW transmission line and the third port is represented as the electric port where the electric potential is applied and sensed. In this model, θ is expressed as $2\pi f/f_0$, where f is the frequency of the applied input potential and f_0 is the resonance frequency and θ is the periodic section transit angle. R_0 is the electrical equivalent to Z_0 or mechanical impedance given by

$$R_0 = \frac{Z_0}{\phi^2} \tag{2.9}$$

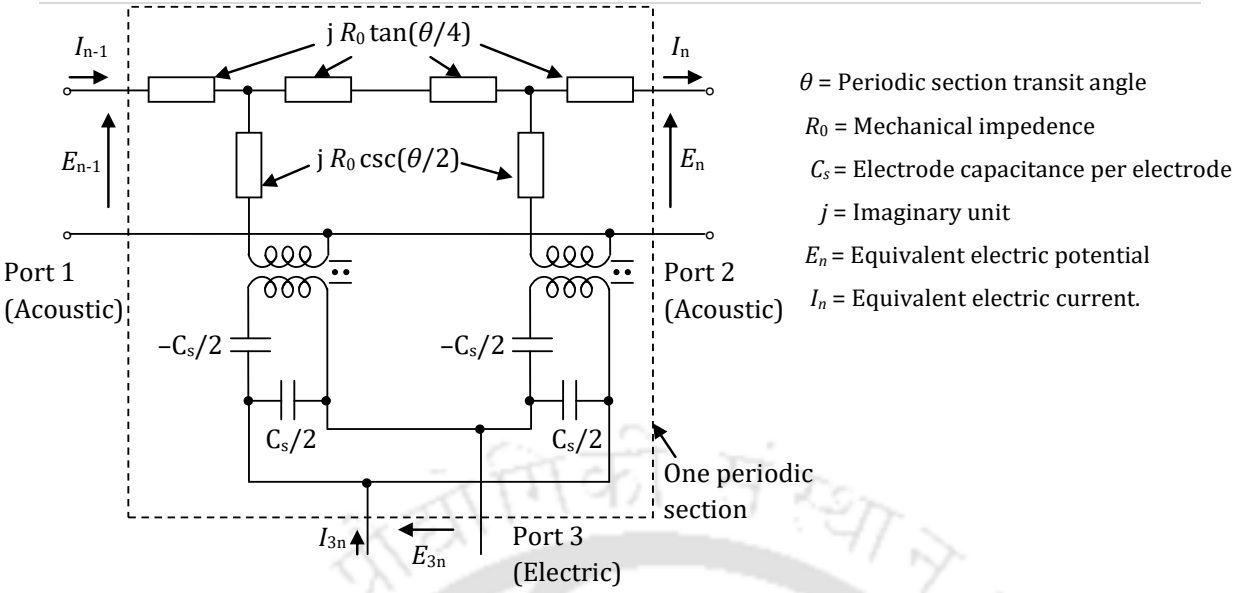

Figure 2. 5: Mason equivalent circuit of one period of IDT analysed by Smith *et al.* [54]

where $\phi = \varsigma C_s / 2$ is the turns ratio of an acoustic-to-electric circuit transformer, C_s is the static electrode capacitance of one periodic section and ς is a piezoelectric constant. In this model, the acoustic forces are converted into electric potentials as $E_n = F_n/\phi$ and SAW velocities are converted into equivalent electric currents $I_n = v_n' \phi$. These transformations allow the characteristic mechanical admittance (similar to the transmission line characteristic impedance expressed in ohms) to be expressed as an equivalent transmission line characteristic admittance as,

$$G_0 = \frac{1}{R_0} = \frac{\omega C_s K^2}{2\pi} \tag{2.10}$$

where K^2, represents electromechanical coupling coefficient and its values can be approximated by $-2\Delta v/v$, where, Δv is the change in SAW velocity when a thin metal film electrically shorts the piezoelectric surface. The values of K^2 for common substrates are given in Appendix A. The entire IDT can be realised by connecting acoustic ports in cascade and electrical ports in parallel as shown in Figure 2.5.

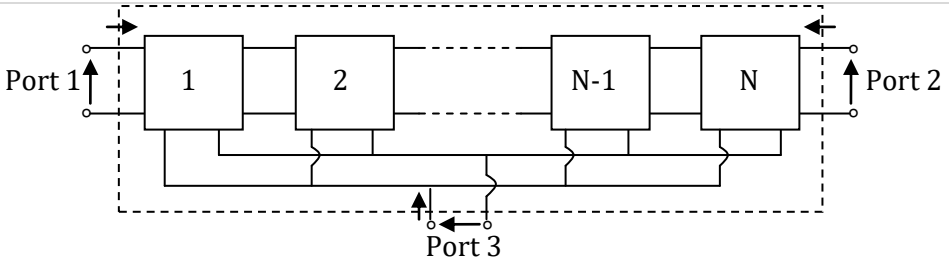

Figure 2. 6: Equivalent circuit for entire IDT, made up of *N* pairs of IDT finger with acoustic ports in cascade and electrical ports in parallel.

If the generator IDT and receiver IDT of the SAW device are completely matched, the Y parameters of the 3-port network using the equivalent circuit of a period of an IDT can be expressed as

$$\begin{bmatrix} I_1 \\ I_2 \\ I_3 \end{bmatrix} = \begin{bmatrix} -jG_0 \cot N\theta & jG_0 \csc N\theta & -jG_0 \tan(\theta/4) \\ jG_0 \csc N\theta & -jG_0 \cot N\theta & jG_0 \tan(\theta/4) \\ -jG_0 \tan(\theta/4) & jG_0 \tan(\theta/4) & j\omega C_T + 4jNG_0 \tan(\theta/4) \end{bmatrix} \begin{bmatrix} E_1 \\ E_2 \\ E_3 \end{bmatrix} \tag{2.11}$$

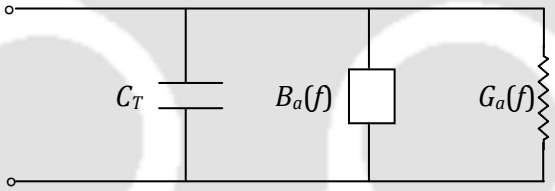

Figure 2. 7: Overall equivalent circuit of an IDT (Hartman, [5]).

where, $C_T = NC_s$ (total capacitance of IDT) [24].

The overall equivalent circuit of an IDT is shown in Figure 2.6 [4], [25]. The input admittance can be expressed as

$$Y(f) = G_a(f) + B_a(f) + j\omega C_T \tag{2.12}$$

where $G_a(f)$ is the radiation conductance, and $B_a(f)$ is the susceptance given as

$$G_a(f) \approx 8N^2 G_0 \left| \frac{\sin X}{X} \right|^2 \tag{2.13}$$

$$B_a(f) = 8N^2 G_0 \left| \frac{\sin(2X) - 2X}{2X^2} \right|^2 \quad (2.14)$$

where, $X = N\pi(f - f_0)/f_0$. The radiation susceptance is a reactive parameter that goes to zero at the resonance frequency. This term is often omitted in calculations near the resonance frequency because it is negligible compared to the entire IDT capacitance term.

2.2 Solution of SAW

The basics of piezoelectricity, governing equations for SAW propagation, boundary conditions and solutions to the differential equations are discussed in this section. In chapter 1, propagation of different types of acoustic waves in an elastic medium is described. SAW motor works on the influence of propagation of Rayleigh waves which is mainly focused in this thesis. So the study of the nature of the acoustic waves and piezoelectric theory to understand the SAW devices is mandatory. In this thesis, the term 'SAW' without further qualification is taken to mean Rayleigh waves.

2.2.1 Piezoelectricity

Different types of piezoelectric materials are used for designing of SAW devices. Single-crystal materials such as quartz, Lithium Niobate ($LiNbO_3$) and Lithium Tantalate ($LiTaO_3$) are widely used piezoelectric materials. These materials available in different orientations, to generate various types of waves on its surface. The used piezoelectric material to develop the SAW motor is 128° rotated, Y-cut X- propagated Lithium Niobate, which is having high electromechanical coupling effect.

The electromechanical coupling factor K^2 is constant to measure the ability to convert electrical energy to mechanical energy and vice versa, a measure of 'the smallness of the ineffective fraction of energy'.

$$K^2 = 2\left(\frac{\nabla v}{v}\right) \quad (2.15)$$

$$\frac{\nabla v}{v} = \frac{(v_f - v_m)}{V_f} \quad (2.16)$$

v_f= Velocity of the piezo material at no metallization (Isolation)

v_m= Velocity of the piezo material at full metallization (Short-circuit)

Table 2. 1: Surface –wave materials

Material	v_f (m/s)	K^2 (%)	Advantage	Disadvantage	Suitability
$LiNbO_3$ 128° Y-X	3979	5.5	Low bulk wave, Strong coupling	Large TCD	Wideband filters
$LiTaO_3$ 36° Y-X	4212	4.8	Strong coupling, moderate TCD	-	Low- loss filters, RF filters
ST-X quartz	3159	0.12	Small TCD	Weak Coupling	Narrow band filters, resonators, pulse compression

Temperature stability defined through temperature coefficient of delay (TCD). The electromechanical coupling constant can be derived, when the vibration mode of a transducer is taken along one of its axes from the equation (2.15). However, for an IDT K^2 is usually determined from experiments as it is quite difficult to determine theoretically because the fields are not uniform in nature. A piezoelectric material with large coupling factor is preferred during the making of a SAW motor.

Elasticity in a solid is concerned with the internal forces within it and displacement of solid from its equilibrium position [28]. The forces are expressed by stress T, while the displacements are expressed by strain S. The particle is an elementary region of a material much larger than the inter-atomic distance and much smaller than any characteristic elastic dimensions such as wavelength. Let us assume that in equilibrium state of solid, a particle is located at point $\mathbf{x} = (x_1, x_2, x_3)$ and displaced by an amount $\mathbf{u} = (u_1, u_2, u_3)$, where, the components u_1, u_2 and u_3 are the general components of coordinates x_1, x_2 and x_3, respectively. Thus the particle has been displaced to a new position $\mathbf{x} + \mathbf{u}$ as shown in Figure 2.8.

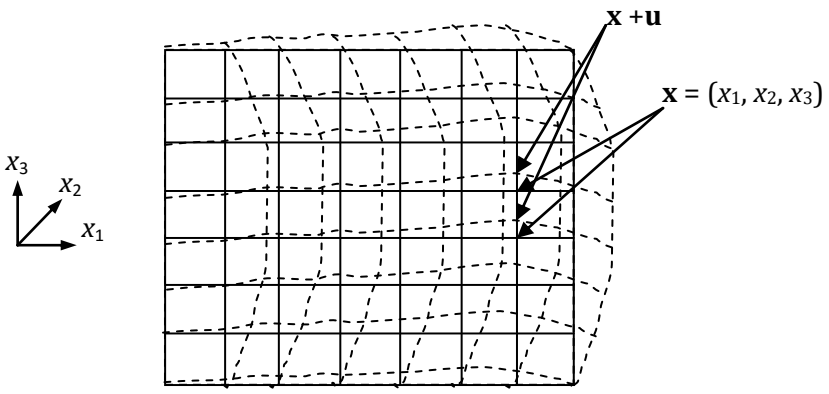

Figure 2. 8: Particles position in equilibrium and deformed states of the solid body. Note: The deformation of the solid is shown in broken lines [30].

If **u** is independent of **x,** there will be no internal force since this simply shows a displacement of a material as a whole, and also there will be no force if the material is rotated. The strain at each point can thus be defined as

$$S_{ij}(x_1, x_2, x_3) = \frac{1}{2}\left(\frac{\partial u_i}{\partial x_j} + \frac{\partial u_j}{\partial x_i}\right), \qquad i, j = 1,2,3. \tag{2.17}$$

Thus the strain is related to the internal forces. The strain is a second rank tensor and symmetrical $S_{ij} = S_{ji}$.

The stress T is defined as internal stress in the material *i.e.* force per unit area. The second-rank stress tensor is defined as $T_{ij}(x_1, x_2, x_3)$ and it is symmetric, $T_{ij} = T_{ji}$. According to Hooke's law, each component of stress is given by the linear combination of the strain components, and it is expressed as

$$T_{ij(mech)} = \sum_k \sum_l c_{ijkl} S_{kl}, \qquad i, j, k, l = 1, 2, 3. \tag{2.18}$$

Where, c_{ijkl} is the fourth-rank stiffness tensor. These elements are the physical properties of the materials under consideration [28].

2.2.2 Piezoelectricity and constitutive equations

Pierre and Jacques Curie has discovered Piezoelectric effect in 1880 [55]. The name piezoelectricity is derived from the Greek word which means 'electricity by pressure.' The external force exerted on piezoelectric material results in the generation of the electric field at the surface of the material which is proposed by Hankel. A simple

molecular model of piezoelectric material is given in Figure 2. 9 (a) and (b) [55]. Before an external force to the piezoelectric material, the gravity centres of positive and negative charges of each molecule of the piezoelectric material coincide. Thus the external effects of charges reciprocally cancel, and electrically neutral molecules appear. By applying an external force to the material, the internal reticular structures of the molecules deform that results in the separation of gravity centres of positive and negative charges of the molecules and generate the electric dipoles. The facing dipoles are mutually cancelled, and a distribution of linked charges appears at the surface of the piezoelectric materials. Figure 2. 9 (c) shows the linked charges inside the piezoelectric materials after subjecting an external force *F*. The polarisation generates an electric field which causes the flow of the free charges existing in the conductor in contact. The free charges will move towards the end where the polarisation is of opposite sign and will remain until the free charges neutralise the polarisation effects. When an external force is removed, the polarisation will disappear, and material gets equilibrium position. This process can be demonstrated using galvanometer. The demonstration consisting of a piezoelectric material with metal plate deposited at both ends and connected to the galvanometer as shown in Figure 2. 9 (d) and (e) [55].

This phenomenon known as the direct piezoelectric effect is defined as the linear coupling between the elastic stresses and strains to electrical and mechanical domains occurring in anisotropic materials. Likewise, by the converse piezoelectric effect, a strain is induced as a result of an applied electric field. Thus, they proved that certain types of crystals develop an electrical charge when exposed to mechanical stress. The stress, $T_{ij(elec)}$ produced by the piezoelectric effect is given by

$$T_{ij(elec)} = \sum_k e_{kij} E_k, \qquad i, j, k, l = 1, 2, 3. \tag{2.19}$$

Where electric field $E_k = -\frac{\partial V}{\partial x_k}$. Total stress T_{ij} is the sum of stresses due to the electric field E_k and mechanical strain and can be expressed as [28], [31]

$$\begin{aligned} T_{ij} &= \sum_k \sum_l c^E_{ijkl} S_{kl} - \sum_k e_{kij} E_k \\ &= \sum_k \sum_l c^E_{ijkl} S_{kl} + \sum_k e_{kij} \frac{\partial V}{\partial x_k} \end{aligned} \tag{2.20}$$

From (2.18) and (2.20)

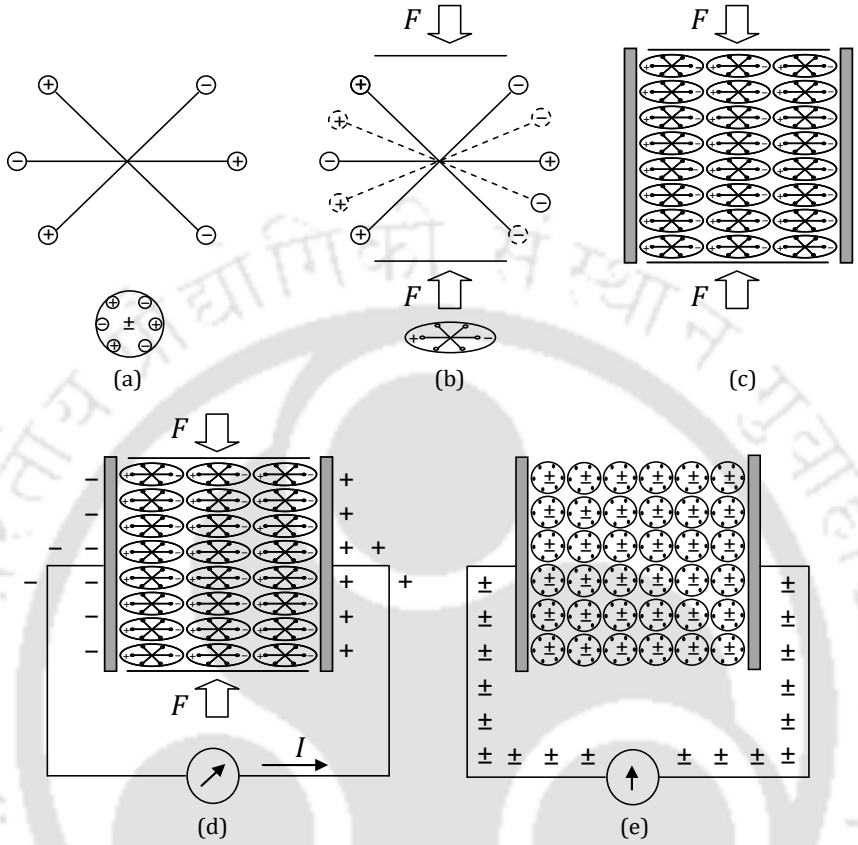

Figure 2. 9: Piezoelectricity in piezoelectric materials, (a) An unperturbed single molecule, (b) Molecule subjected to an external force *F*, (c) Polarisation effects in the piezoelectric material. (d) Neutralising the current flowing through the outer conductor after application of external force *F*. (e) Absence of current in the unperturbed material [55].

$$T_{ij} = \sum_k \sum_l c^E_{ijkl} \frac{\partial^2 u_k}{\partial x_k} + \sum_k e_{kij} \frac{\partial V}{\partial x_k} \qquad (2.21)$$

When an electric field is applied to the dielectric medium, the electric displacement can be expressed by electric field and permittivity tensor ε_{ij} of the dielectric medium. In the case of piezoelectric material, the additional electric field displacement caused by the strain is developed due to the piezoelectric effect. The total electric displacement D_i can then be given as

$$D_i = \sum_j \varepsilon_{ij}^s E_j + \sum_j \sum_k e_{ijk} S_{jk} \tag{2.22}$$

where, c_{ijkl}^E is the stiffness tensor for constant electric field (N/m²), S_{jk} is the strain components, e_{ijk} is the piezoelectric tensor relating elastic to electric fields (C/m²), ε_{ij}^s is the permittivity tensor for constant stress (F/m), and E_j is the electric field vector (V/m) [28].

2.2.3 Equation of motion

In the above equations if the stress and strain are functions of time and position then using Newton's laws of the equation of motion can be expressed [28]. The electric field distribution can be found by solving the equations of Newton and Maxwell simultaneously. For an elementary cube centred at $\mathrm{x}' = (x_1', x_2', x_3')$ with edge length of δ, density ρ, and the mass $\rho\delta^3$, the total force in terms of stress along x_i direction is given by

$$\delta^3 \left[\sum_j \frac{\partial T_{ij}}{\partial x_j} \right]_{\mathrm{x}'} \tag{2.23}$$

$$\rho \frac{\partial^2 u_i}{\partial t^2} = \sum_j \frac{\partial T_{ij}}{\partial x_j}, \qquad i, j = 1,2,3. \tag{2.24}$$

In the case of the piezoelectric medium, the travel speed of elastic waves is much slower than the electromagnetic waves. So the electric field can be expressed using quasi-static approximation by neglecting magnetic field. Thus Maxwell equation can be approximated as

$$\mathrm{curl}\, E = -\frac{\partial \mathbf{B}}{\partial t} = 0, \quad \mathbf{E} = -\mathrm{grad}\, V \tag{2.25}$$

where**B** is the magnetic field, **E** is the electric field derived from the scalar electric potential V [28].

$$E_i = -\frac{\partial V}{\partial x_i} \tag{2.26}$$

From equations (2.18), (2.20) and (2.26) the equation of motion for piezoelectric material can be expressed as [28]

$$\rho \frac{\partial^2 u_i}{\partial t^2} = \sum_j \sum_k \left\{ e_{kij} \frac{\partial^2 V}{\partial x_j \partial x_k} + \sum_l c^E_{ijkl} \frac{\partial^2 u_k}{\partial x_j \partial x_l} \right\} \tag{2.27}$$

In addition, the material is taken to be an insulator there are no free charges. Thus div D = 0. From equation[56]

$$\sum_i \sum_j \left\{ \varepsilon^S_{ij} \frac{\partial^2 V}{\partial x_i \partial x_j} - \sum_k e_{ijk} \frac{\partial^2 u_j}{\partial x_i \partial x_k} \right\} = 0 \tag{2.28}$$

The degrees of freedom are the global displacements u_1, u_2, and u_3 in the global x_1, x_2, and x_3 directions, respectively, and the electric potential V can be obtained by solving the equations (2.27) and (2.28) using appropriate boundary conditions [28].

2.2.4 Solution of surface wave in piezoelectric media

The solution of surface waves in isotropic and anisotropic materials is well explained with details and findings in [28] and [31]. This section contains the brief elaboration of boundary conditions and solutions for surface waves on a piezoelectric medium. In the case of a piezoelectric crystal, the orientation of the material plays a vital role in the propagation of the wave. For crystalline material, the uppercase X, Y, and Z with directions are defined by convention about the crystal lattice. For example, in the case of Y-cut, X propagating lithium niobate (Y–X cut $LiNbO_3$) material x_3 is parallel to crystal Y axis and x_1 is parallel to crystal X axis. The orientation of x_3 is also referred to as cut, so that for Y–X cut $LiNbO_3$ the crystal is Y-cut. The material tensors stiffness, permittivity and piezoelectric tensors are specified about the X, Y, and Z axes. The literature normally provides X-Y material tensors. For analysis, they must first to be rotated into the frame defined by x_1, x_2 and x_3 using tensor transformations. The algorithms for these transformations are well documented in [32] and also given in Appendix B of this thesis.

To determine the phase velocity and amplitude of the wave, the appropriate boundary conditions should be applied [28]. Normally, two cases are considered. The first instance is called as a free surface case where the space above the surface of the piezoelectric material is a vacuum, and no conductor is present so that there are no free charges. The second case is called as metallised case where the surface of the

piezoelectric material is covered with a thin metal layer with infinite conductivity and short outs the horizontal components of the electric field **E** [28]. These two cases give different surface wave velocity and measure the coupling between wave and electrical perturbation at the surface. For free surface case, if the wave number of the surface wave is β then the potential in vacuum $(x_3 \geq 0)$ (see Figure 2. 10) using Laplace's equation can be expressed as

$$V = V_0 e^{(-|\beta| x_3)} e^{j(\omega t - \beta x_1)} \tag{2.29}$$

Where, V_0 is a constant. For metallised surface case the potential at x_3 = 0 is zero. Also, the mechanical stress for either case at x_3 = 0 is given as

$$T_{13} = T_{23} = T_{33} = 0 \tag{2.30}$$

For surface wave solutions in piezoelectric medium, let us consider the partial waves in which the displacements and potential is denoted by $\mathbf{u}'$ and V', take the form

$$\mathbf{u}' = \mathbf{u}'_0 e^{(j\gamma x_3)} e^{j(\omega t - \beta x_1)} \tag{2.31}$$

$$V' = V'_0 e^{(j\gamma x_3)} e^{j(\omega t - \beta x_1)} \tag{2.32}$$

Where, β is the wave number of the surface wave, assumed to be real. These expressions are to satisfy the equations (2.27) and (2.28). By substituting equations (2.31) and (2.32) in equations (2.27) and (2.28) and these equations are then solved for γ numerically, and it gives eight solutions for γ. Consequently, for every solution of γ the relative solutions of $\mathbf{u}'$ and V' are obtained. The partial waves expression for normally considered values of γ are, therefore,

$$\mathbf{u}'_m = \mathbf{u}'_{0m} e^{(j\gamma_m x_3)} e^{j(\omega t - \beta x_1)}, \qquad m = 1,2,3,4. \tag{2.33}$$

$$V'_m = V'_{0m} e^{(j\gamma_m x_3)} e^{j(\omega t - \beta x_1)}, \qquad m = 1,2,3,4 \tag{2.34}$$

where $\mathbf{u}'_{0m}$ is the displacement and V'_{0m} is the potential corresponding to γ_m.

For half-space, a linear sum of these partial waves is assumed as

$$\mathbf{u} = \sum_{m=1}^{4} A_m \mathbf{u}'_m \tag{2.35}$$

$$V = \sum_{m=1}^{4} A_m V'_m \tag{2.36}$$

Where A_m is the coefficients such that the solution satisfies the electrical and mechanical boundary conditions for the free surface case and metallised surface case. The surface velocity can be determined by ω/β, and displacement and potential are **u** and V given by equations (3.35) and (3.36) [28].

2.3 Finite Element Method (FEM)

The finite element method (FEM) is a numerical technique that provides approximate

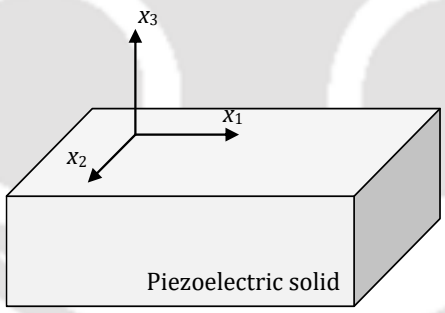

Figure 2. 10: Axes for surface wave solution.

solutions to the governing differential or integral equations of a complicated system through a discretization process [57] and [58]. FEM is used to solve the problems of engineering disciplines such as the areas of stress/strain analysis of solid structures, heat conduction analysis and fluid dynamics. The domain of the system (physical / mathematical) can be defined or subject to frequent changes (moving boundary problems such as transient-free surface water flow, large deformation problems, *etc*.)[58]. The boundary conditions can be well defined regarding prescribed loads and displacements, or sometimes less well defined as in fluid–structure interactions or

contact problems. The propagation of SAW governed by differential equations given in equations (2.27) and (2.28) must be solved along with complexities in the geometry of the device, materials used in the device, and proper boundary conditions [59]. This section gives some basic procedures and techniques used in finite element method formulations.

2.3.1 Input and output information in FEM

The following information needs to be input about the structure for which analysis in FEM to be carried out.

1. Coordinate systems according to the geometry is an important parameter to be input either in 3D or 2D.
2. The desired geometry of the proposed device to be solved. Assigning contact pair between slider and stator in the case of the SAW motor. Assigning master for stator and slave for the stator in contact pair between two solid bodies.
3. Material properties of the model: for example, in SAW devices material properties of the piezoelectric substrate such as elasticity matrix, piezoelectric constant, permittivity constant, and density are to be furnished and for IDT electrodes anisotropic material properties such as Young's modulus, density, Poisson ratio, etc. are to be provided.

For SAW motor the material properties of the slider, such as the type of material and consequence properties.

4. Boundary conditions at the boundaries of the structure are to be provided. For example in the case of stress/strain analysis for piezoelectric material, the boundary conditions can be displacement constraints and electrical boundary conditions such as electric potential, electric displacement, charge, etc.

For SAW motors the flexibility of motion of the slider, freedom in which direction of displacement of the slider. Boundary load to the slider along with body load. Defining the contact friction between slider and stator, and assigning coefficient of friction either static or dynamic to the contact body.

Further, the geometry domains are to be divided into smaller domains called elements which are connected at specific points called nodes as shown in Figure 2.11. The elements created in the geometry can be in the shape of triangular, quadrilateral, tetrahedral, or brick depending on the dimensionality. The output information in case of stress/strain analysis in piezoelectric material involves nodal and elemental

information, the solution to the primary unknown quantities, the displacements in all directions, and voltage are determined at nodes. These unknowns are called as

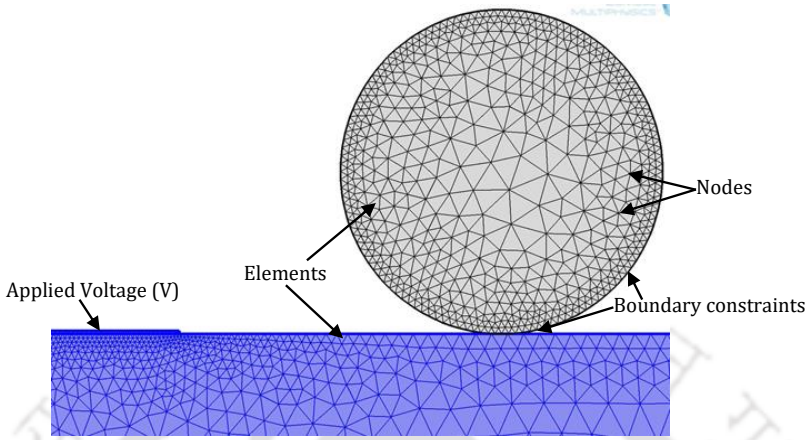

Figure 2. 11: Illustration showing a solid body discretized into a finite number of elements.

degrees of freedom (DOF).

In this thesis, the simulations and analysis of SAW motors are carried out by FEM using piezoelectric module of COMSOL Multiphysics software. The software has well-developed solvers, graphical user interface (GUI) and post-processing capabilities. More details of the software can be found in the user guide of the software [60].

2.3.2 Finite element simulation of SAW devices

FEM was a common practice to simulate the conventional SAW devices and have been reported by many researchers. Lerch *et al*.[61] presented a FEM scheme to calculate Eigenmodes and dynamic response to mechanical and electrical excitations of 2D and 3D piezoelectric transducer for any geometry. Rahman *et al*. [62] performed FEM simulation to study SAW based quantum devices. Atashbar *et al.* [63] simulated the mass loading effect of palladium sensing film in the presence of hydrogen gas. Ippolito *et al*. [64] performed the FEM based analysis of acoustic waves propagating on layered SAW devices. Wang *et al*. [65] used FEM carry out a study on the effects of change in film properties on the mass sensitivity of SAW sensors. Tikka *et al.*[66] reported the finite element modelling of SAW correlator. Subramanian *et al*. In most of the earlier works, the number of DOF to solve is significant due to the large size of the SAW structures considered in the model. To solve DOF for an entire SAW device, it requires

high computing facility and extensive computation time. Thus a valid approximation and simplified model have an obligation to perform FE simulation of SAW devices. In this chapter, the conventional SAW devices such as one-port SAW resonators and SAW delay line devices are simulated with metallic IDT on the piezo substrate structure using COMSOL Multiphysics.

2.3.3 The mathematical model for a SAW delay line

The IDT converts electrical energy to mechanical energy and vice versa as explained in IDT modelling. The mathematical model of a SAW delay line given by Feng *et al*. [67] is adopted in formulating the simplified simulation methodology. The transmitting IDT can be considered as a force generator that converts the electrical voltage to mechanical forces. These forces travel as SAW on the piezoelectric substrate. Consider a transmitting IDT as shown in Figure 2. 12, and with the number of force generators (fingers) of N_M equal to 5. If the force generated at each finger of transmitter IDT is proportional to the applied voltage, the force at n^{th} finger pair can be written as $F_n(t) = K_1 V_{in}(t)$

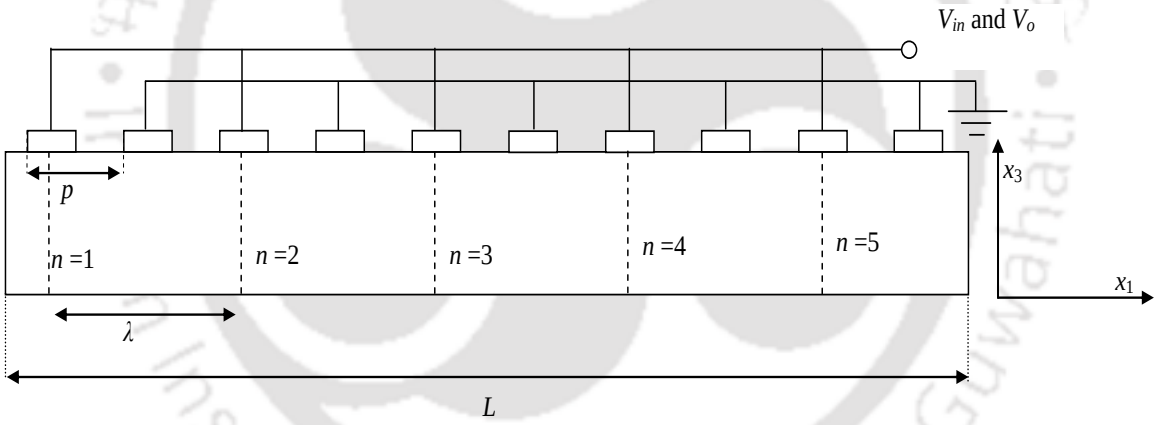

Figure 2. 12: A Typical IDT with five pairs of electrodes.

Where K_1 is proportionality constant of the transducer. V_{in} is the input voltage. The displacement of the wave **u** at the edge of IDT of N_M finger pair can be written as

$$\mathbf{u}(t) = \frac{1}{2v}\sum_{n=1}^{N_M} F_n\left(t - \frac{n\lambda}{v}\right) \tag{2.37}$$

The displacement of the wave at receiver IDT of the SAW delay line device with delay line of length L can be written as

$$\mathbf{u}(t)=\frac{1}{2v}\sum_{n=1}^{N_M}F_n\left(t-\frac{n\lambda+N_R\lambda+L}{v}\right) \tag{2.38}$$

Where N_R is the number of finger pair at the receiver IDT. Let q_{out} denote the electric charge produced when the electrodes are subjected to local strain. Assuming that the charge is the sum of the charges produced at each finger and the charge from each finger is proportional to displacement,

$$q_{out}(t)=K_2\sum_{l=1}^{N_R}u_l(t) \tag{2.39}$$

Accordingly assuming the output voltage is proportional to charge,

$$v_{out}(t)=K_3\,q_{out}(t) \tag{2.40}$$

K_2 and K_3 are proportionality constants. Thus combining the above equations, the output voltage can be expressed as

$$v_{out}(t)=\frac{K_1K_2K_3}{2v}\sum_{l=1}^{N_R}\sum_{n=1}^{N_T}v_{in}\left(t-\frac{n\lambda+l\lambda+L}{v}\right) \tag{2.41}$$

If an IDT of 100 finger pair and displacement at edge of point fifth pair from equation (34) can be rewritten as

$$\mathbf{u}(t)=\frac{1}{2v}\sum_{n=1}^{n=100}F_n\left(t-\frac{n\lambda}{v}\right)-\frac{1}{2v}\sum_{n=6}^{n=100}F_n\left(t-\frac{n\lambda}{v}\right) \tag{2.42}$$

$$\mathbf{u}(t)=\mathbf{u}_a(t)-\mathbf{u}_b(t) \tag{2.43}$$

The above equation can be further realised regarding time t as below

$$\mathbf{u}_a(t)=\frac{1}{2v}\sum_{n=1}^{n=100}F_n\left(t-\frac{n\lambda}{v}\right)\ \text{for all t} \tag{2.44}$$

$$\mathbf{u}_b(t)=\frac{1}{2v}\sum_{n=1}^{n=94}F_n\left(t-\frac{n\lambda}{v}\right)\ \text{for t >= n}\lambda/\text{v} \tag{2.45}$$

In general, equation (40) can be realised as a one-port SAW resonator consisting of single IDT with 100 finger pairs. As explained in the simulation of one-port SAW resonator it is convenient to model equation (40) and (41) by applying infinite periodic boundary conditions to a section of SAW resonator of length $n\lambda$ consisting of single or a pair of IDT.

The simulation procedure adopted in COMSOL Multiphysics to solve the SAW delay line model is explained in the following section.

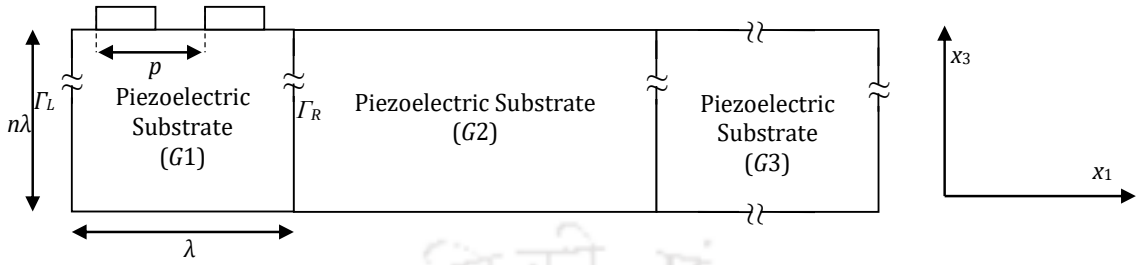

Figure 2. 13: SAW delay line structure considered for simulation.

2.4 Simulation of Conventional One Port SAW Resonator based on FEM in 2D

As explained in Chapter 1, one-port SAW resonator could be designed by a large number of IDT finger-pairs where multiple reflections occur between the fingers or by using reflectors either side of a short IDT having less number of fingers [6], [22]. The simulations of conventional SAW resonators by FEM are presented by many researchers [41], [44], [45]. However, we simulate it to compare the results of conventional SAW resonator with the results of the proposed SAW resonator.

2.4.1 Simulation methodology

An infinite number of IDT fingers on a 128° rotated Y-cut X- propagated Lithium niobate is used as the piezoelectric substrate, while a conventional one-port SAW resonator is considered for the simulation. Owing to the antiperiodic nature of IDT structure, the single electrode of a pair of IDT fingers is used, and appropriate boundary conditions are applied. The 2D geometry of a periodic segment of the resonator considered for the simulation is shown in Figure 2. 14. The dimensions used for simulations are as follows: electrode width (d) 100 µm, electrode pitch (p) 9 mm, depth of the piezo substrate 2000 µm (5 λ), and thickness of IDT fingers 0.2 µm. The values of elastic constants, permittivity constants, stress constants, and density are given in Appendix C. The bottom surface of the piezo substrate is kept fix, and all other boundaries are stress-free. The degrees of freedom of the right periodic boundary (Γ_R)

are set to be equal to those from the left periodic boundary (ΓL) (see Figure 2. 14). In general, the expressions for the periodic boundary conditions are given in equation (2.46). An alternative driven voltage of 1 V is applied to the IDT fingers. An extremely fine mesh with minimum element quality of 0.7 with 32 mesh elements of per wavelength is adopted for the 2D simulation. The number of degree of freedom solved is in the order of around 2×10^5. The harmonic analysis is performed to find the

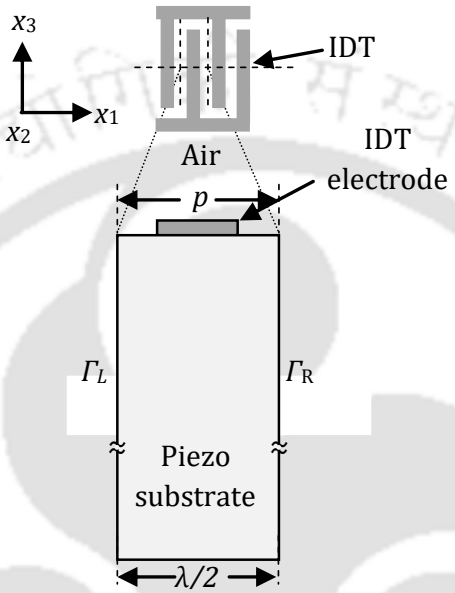

Figure 2. 14: 2D Geometry of the periodic section used for the simulation.

characteristics and parameters of the resonator.

The expressions for the periodic boundary conditions are given below.

$$U_{left} = (-1)^n U_{right}$$
$$V_{left} = (-1)^n V_{right} \quad (2.46)$$

2.5 Results and Discussions

The results of simulation of conventional SAW resonator are shown in Figure 2. 15 and Figure 2. 16. The total displacement profile, *x*-displacement profile and *y*-displacement profile of the resonator at the resonance frequency f_r of 8.37 MHz are shown for substrate depth of about 3.75 λ in Figures 2.15 (a), (b), (c) and (d), respectively. The substrate depth of 3.75 λ is shown for simplicity. It is shown in Figure 2.15 that the displacement is approaching zero after 1 λ depth of the substrate, which depicts the

nature of Rayleigh wave SAW. The resonance frequency of the resonator is identified as the frequency for which the susceptance crosses zero value. The plot of total displacement as a function of normalised frequency given in Figure 2.16(a) shows a peak at the resonance frequency. The normalised frequency is expressed as $\eta = 2pf/v_0$, where, v_0 = 3990 m/s is the free surface velocity of the substrate. The curves of harmonic admittance per period as a function of normalised frequency for conventional SAW resonator are shown in Figure 2. 16 (b).

Figure 2. 16 (b) shows the closer view of the curve of harmonic admittance per period as a function of normalised frequency near the resonance frequency. In the case of the real device, it would be lower due to the finite aperture, attenuation and damping. This simulation does not consider the attenuation or damping and assumes the infinite width of the aperture of IDT fingers in x_2 direction.

The free surface resonance frequency f_0 calculated from the Eigen mode analysis of the piezo substrate is 8.37 MHz. The resonance frequency is affected by the mechanical and electrical properties as mass loading, and conductivity of the metallic IDT fabricated on the piezo substrate effects SAW phase velocity and it requires

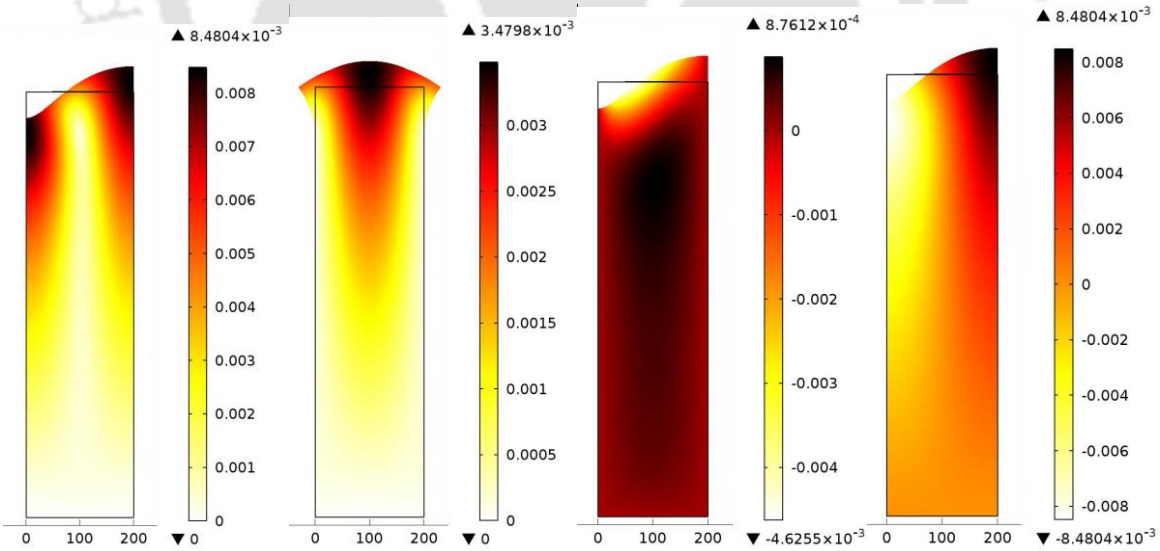

Figure 2. 15: Displacement profile in a SAW resonator at resonance frequency 8.37 MHz with deformed shape, (a) Total displacement profile at resonance, (b) Total displacement profile at antiresonance, (c) *x* displacement profile, (d) *y* displacement profile. Note: For simplicity, the substrate depth shown in the Figure is about 400 λ.

consideration to these factors while designing [32],[68].

The quality factor Q_r at the resonance frequency of the convention SAW resonators is calculated from Figure 2.16(b). The expression for quality factor is given as [34], [69]

$$Q_r = \frac{f_r}{\Delta f} \tag{2.47}$$

where, Δf is the bandwidth at half of the peakconductance[34], [69] (see Figure 2.16(b)).

The capacitance ratio which is a measure of the resonator performance is calculated from Figure 2.16(c). The capacitance ratio γ is expressed as [34]

$$\gamma = \frac{f_r^2}{f_a^2 - f_r^2} \tag{2.48}$$

Where, f_a is anti-resonance frequency (see Figure 2.16(c)). The capacitance ratio for the conventional SAW resonator computed from the simulation is 28.

2.5.1 Simulation of conventional one-port SAW resonator based on FEM in 3D

The results in the previous section are obtained with 2D FEM by considering infinite aperture of IDT fingers. In this section, a conventional SAW resonator with a finite aperture having an infinite number of IDT fingers with a simplified model is simulated. For 3D simulation, a piezo solid application mode of COMSOL Multiphysics is used. The simulation is carried out taking a half wavelength consisting of a single electrode of antiperiodic IDT fingers is used. The dimensions used for 3D simulation are the same as 2D simulation except for the depth of piezo-substrate h_s and aperture W. The depth of piezo-substrate is truncated to 5 λ since SAW energy concentrates near the substrate depth of one wavelength. The simplified model is used to reduce the number of nodes and reduce computation cost. The material constants used for the simulation are given in Appendix C. The bottom surface of the substrate is fixed and all other boundaries are stress-free. It is possible by modelling a thin strip of athickness of W in x_2 direction and applying zero displacement constraint in the x_2 direction on the both side boundaries normal to the direction of wave propagation. Rayleigh SAW has no variation and no component of displacement vectors in the x_2 direction [41]. The antiperiodic boundary condition is applied to left (Γ_L) and right (Γ_R) sides of the

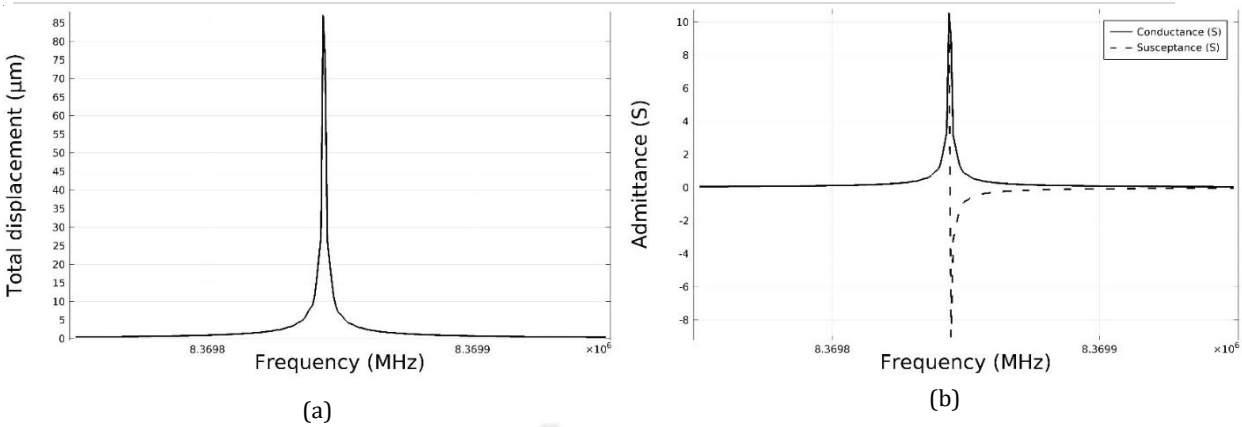

Figure 2. 16: Results of simulation of a SAW resonator, (a) Plot of total displacement as a function of normalised frequency, (b) Plot of harmonic admittance as a function of normalised frequency

periodic section as given in section 2.9.1. The Eigen mode analysis is performed to compute the resonance frequency of the SAW resonator.

The resonance frequency is identified from the list of Eigen mode frequencies and their displacement amplitude, the mode of vibration and the charge distribution on the IDT fingers are studied. At resonance frequency, the displacement is maximum between the fingers of the resonator while at anti-resonance frequency the displacement is maximum in the middle of the finger as given in section 2.9.1. The charge distribution is symmetry and antisymmetric at resonance and antiresonance frequencies.

2.6 Simulation of a Conventional SAW Delay Line

The conventional SAW delay line device has been simulated using FEM by many researchers [63], [70], [71]. In this section, a conventional SAW delay line device is simulated to compare the simulation results with the proposed SAW delay line device configuration described in the next chapter.

2.6.1 Simulation methodology

A SAW delay line device with a delay of 3 λ (λ = 1200 µm) is simulated by FEM using COMSOL Multiphysics. In this simulation, three pairs of IDT fingers for transmitter IDT and receiver IDT fabricated at the two ends of the piezo substrate are considered. The dimensions used for simulations are as follows: electrode width (d) 100 µm, electrode pitch (p) 200 µm, depth of the piezo substrate 400 µm (1 λ), and thickness of IDT fingers 0.2 µm [72].YX $LiNbO_3$ piezoelectric material is used as a piezo substrate and

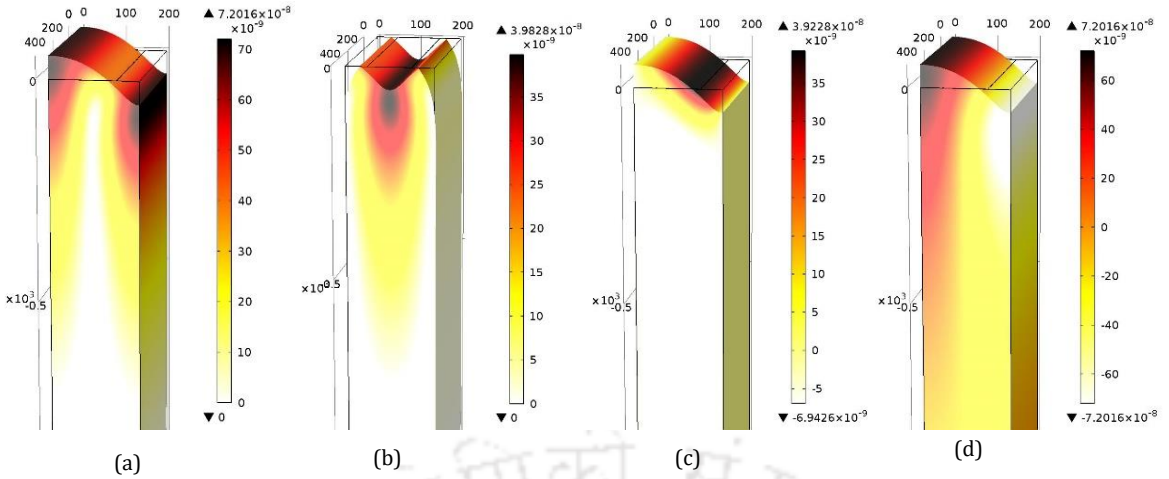

Figure 2. 17: Displacement profiles at resonance frequency 8.282835 MHz, (a) Total displacement profile, (b) *x* displacement profile with deformed shape, (c) *y* displacement profile with the deformed shape. Note: For simplicity, the substrate length shown in the

aluminium metal is used as IDT electrodes. The values of elastic constants, permittivity constants, stress constants, and density are given in Appendix C. 3D geometry of SAW delay line device used for simulation is shown in

Figure 2. **17**. The following boundary conditions are applied to the model. The top surface of the substrate is assumed stress-free and the bottom surface is fixed in its position. The critical damping is assumed at the edge of the transmitter B_L, receiver B_R, and bottom of the substrate B_B to avoid reflections of the acoustic waves as shown in Figure 2. 18.

The equations relating to critical damping are provided in Appendix D. The alternate fingers are shorted and 1 V sinusoidal driven voltage of its resonance frequency is applied. The resonance frequency is about 8.37 MHz. An optimised mesh density is used for the simulation. To analyse the propagation of SAW over the delay line, transient analysis is performed using direct solver SPOOLES available in COMSOL

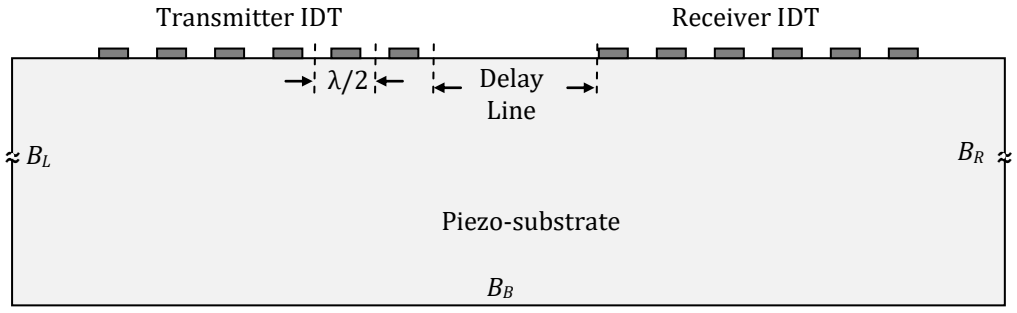

Figure 2. 18: 2D schematic of the SAW delay line device used in simulation.

Multiphysics [60] with the time interval of 10 ns for aduration up to 1 µs. The displacements and potential at the receiver electrode are recorded at every instant.

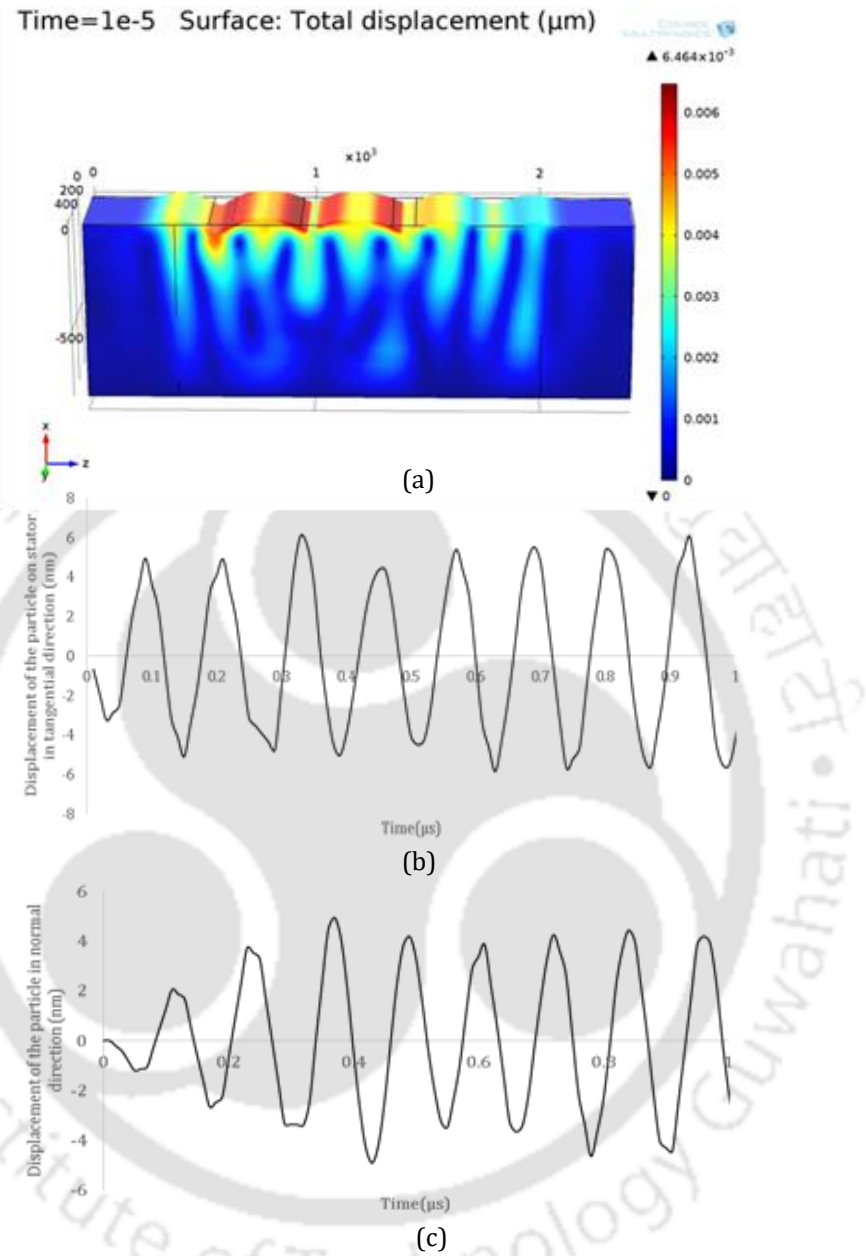

Figure 2. 19: Results of simulation of a conventional SAW delay line device, (a) Total displacement profile at time 10 ns, and, (b) Displacement of the particle in tangential direction, (c) Displacement of the particle in the normal direction.

2.6.2 Results and discussions

The transient analysis of SAW delay line device is performed for the time duration of 1 µs. Figure 2. 19 (a) shows the total displacement profile of SAW delay line device at time 1 µs. The output electrical potential, *x* displacement and *y* displacement are measured at the receiver IDT electrodes. The plots of output potential, *x* displacement and *y* displacement as a function of time are shown in Figure 2. 19 (b), and (c).

The output electric potential of 0.3 V is obtained at the receiver IDT electrodes. In SAW delay line device, delay time is one of the important parameters. The delay time calculated from the free surface velocity of 3478 m/s is 1 μs. x displacement and y displacement of about 6 nm and 6 nm are obtained at time 1 μs. An identical SAW delay line device with proposed configuration is simulated in chapter 3 and the results are compared.

2.7 Summary

In this chapter, a brief introduction to various modelling techniques such as delta function method, impulse response method, equivalent circuit method, COM model, and numerical simulation methods like FEM was discussed. Additionally, this chapter presents piezoelectricity, the equation of motion, and solution to surface waves in piezoelectric media.

Simulations based on FEM using COMSOL Multiphysics to determine the free surface SAW phase velocity and adequate mesh density for the simulation are performed. Simulation of one-port SAW resonator is done so that the results will be used to compare the proposed SAW device configuration. From the FEM simulation, it is presented that a small aperture length is sufficient to model a SAW resonator to study the resonance frequency, admittance and other parameters of the resonator.

In order to find out the delay time and attenuation in the output electric potential, the Simulation of SAW delay line is performed. The device parameters such as velocity dispersion, reflection coefficient, and effective permittivity as a function of metallization ratio are presented. There were frequent discrepancies in actual function of devices. The basic design of SAW transducers has to be optimised with the help of modelling techniques. Simulations of SAW devices help in estimating and visualising the SAW device response before fabricating these devices.

3

Modelling and Simulation of Conventional SAW Motors

A brief introduction to ultrasonic motors (USM) and the literature survey of surface acoustic wave (SAW) motors are presented in chapter 1. Chapter 2 covers the modelling of interdigital transducers (IDTs) and finite element (FE) simulation of conventional SAW resonators and delay line devices. This chapter deals with the modelling of the interaction of SAW with slider and simulation of conventional SAW linear motors.

A conventional SAW linear motor consists of a slider placed in contact with a piezoelectric stator [36]. The operation of a SAW linear motor is based on the frictional drive generating high tangential force on the slider at the contact points with the stator as the Rayleigh wave travels on the surface of the stator [37]. The following section describes modelling of a single point contact in SAW motors having a spherical slider.

3.1 Modelling of SAW Motor with Single Point Contact

The schematic diagram of a spherical slider placed in contact with a stator of SAW motor is shown in Figure 3. 1. The SAW motor consists of a stator made of 128° rotated Y-cut X-propagated lithium niobate ($LiNbO_3$ or LN) piezoelectric substrate. With the application of power supply to the substrate, mechanical deformation occurs due to Rayleigh wave is propagation on the surface of the stator and the spherical ball starts moving due to frictional force [36].

3.1.1 Wave motion

Assume that the Rayleigh wave is propagating in X direction and the displacement components of the stator surface in normal and tangential direction are,

$$z_{st} = \hat{z}_{st} \cos(\omega t + kx) \tag{3.1}$$

$$x_{st} = \hat{x}_{st} \sin(\omega t + kx) \tag{3.2}$$

Where $\hat{z}_{st}$ and $\hat{x}_{st}$ are the amplitudes of the wave in normal and translational directions respectively, ω is the angular frequency and given by $\omega = 2\pi f$, and k is the wave number given by $k = 2\pi/\lambda$. Where f is the frequency of the wave while λ is the wavelength.

3.1.2 Modelling of contact mechanics between slider and stator

The Figure 3. 1 illustrates that, when a spherical slider is placed on a piezoelectric stator, there exists a contact between stator and slider due to load F_l provided from the top of the slider [73]. R is the radius of the slider; F_n is the force generated in the normal direction, a tangential force F_t is acting on the slider [44].

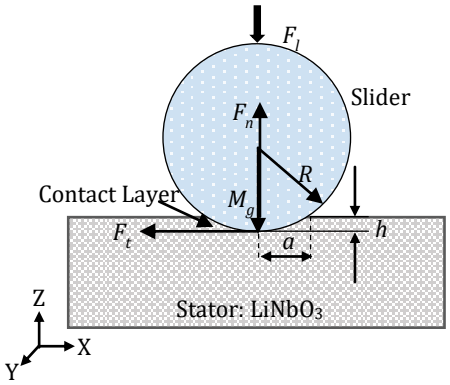

Figure 3. 1: Schematic diagram of a spherical slider placed in contact with a stator.

If $z_{st} \leq z_{sl}$, the slider is not in contact with the stator and the tangential force on the slider is zero [74]. If $z_{st} > z_{sl}$, the slider makes contact with the stator with a contact length of a as shown in Figure 3. 1. Whenever the slider is in contact with stator, the contact is normally described with two conditions, i.e. stick and slip. If $| F_t | \leq \mu F_n$, the slider sticks on the stator substrate surface so that no slip is generated. On the other hand, if $| F_t | > \mu F_n$, then a slip occurs between the slider and the stator substrate surface [75]. The slip zone is responsible for the frictional loss and resulting wear [76].

The spherical shape of the slider is a perfect shape for SAW motor arrangement. Initially, the slider makes a single point contact with the stator and later deforms its shape into circular point contact with the application of preload [73], [77]. The required preload depends on contact models. The purpose of the modelling is to obtain the design parameters and behaviour of the device. The modelling of the device carried out using Hertz's contact model [73] assuming that the spherical slider is placed upon a flat rigid plane type stator. The spherical slider is mounted with a single point of contact on the Rayleigh wave is taken into consideration for the analysis [78]. The tangential components of the surface wave are responsible for the generation of friction force on the slider at the contact point along the horizontal direction. The modelling of the ultrasonic motors is reported by Feenstra [74] and Zhu [79].

The force in normal direction is given by [73],

$$F_n = \frac{4}{3} E R^{1/2} h^{3/2} \tag{3.3}$$

Where $h = z_{sl} - z_{st}$, which decides whether the slider is making contact with wave or sliding. z_{sl} is the vertical position of the slider.

where, $$k_n = 4/3\, E R^{1/2} \tag{3.4}$$

E is the composite Young's modulus can be calculated from the Hertz's contact theory [73], [80],

$$E = \left(\frac{E_{sl} E_{st}}{E_{sl}\left(1-\nu_{st}^2\right) + E_{st}\left(1-\nu_{sl}^2\right)} \right) \tag{3.5}$$

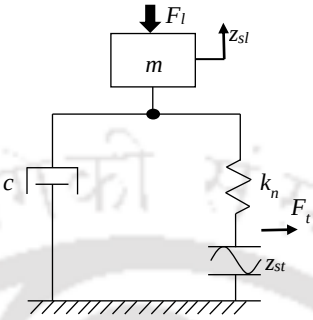

Figure 3. 2: An Iconic model for stator and slider arrangement [5].

The coefficient of elasticity *i.e.* E_{sl}, E_{st} are Young's modulus of the slider and stator while ν_{sl}, ν_{st} are the Poisson's ratio of the slider and stator respectively. The radius of slider and stator are given as R_{sl}, R_{st} respectively and the composite radius R of both of them can be represented as [73],

$$\frac{1}{R} = \frac{1}{R_{st}} + \frac{1}{R_{sl}} \tag{3.6}$$

As the stator is a flat plane elastic surface, the radius of the stator is considered as infinite. Hence the radius of the slider becomes the composite radius.

$$R = R_{sl} \tag{3.7}$$

When preload is applied to the slider the point contact transforms to area contact due to deformation of the stator, so the radius of the contact area of slider is given by [73],

$$a = \left(\frac{3}{4} \frac{F_n R}{E} \right)^{1/3} \tag{3.8}$$

Maximum contact pressure P_{max} generated at the junction of slider and stator can be given by,

$$P_{\max} = \frac{3}{2} \frac{F_n}{\pi a^2} \tag{3.9}$$

The acceleration of the slider in normal direction can be calculated from Newton' motion law. From the Figure 3. 2 the equation for the motion of the slider having mass '*m*' can be calculated from mass- spring- damping relation as,

$$m\ddot{z}_{sl} = F_n - F_l - c\dot{z}_{sl} \tag{310}$$

The displacement of the slider in normal direction during the slider in contact with Rayleigh wave is represented as [74]:

$$\dot{z}_{sl} = \frac{1}{m}\int (F_n - F_l - c\dot{z}_{sl})dt \tag{3.11}$$

Due to sliding of the slider over stator, some variation in space between stator and slider "*h*" occurs and is given by,

$$h = \hat{z}_{st}\cos(\omega t) - z_{sl} \tag{3.12}$$

The displacement of the slider in normal direction during the sliding position with Rayleigh wave is represented in mathematically as:

$$\dot{z}_{sl} = \frac{1}{m}\int (-F_l - c\dot{z}_{sl})dt \tag{3.13}$$

During contact between the slider and stator, there is no space between them, *h* is given by,

$$h = 0 \tag{3.14}$$

Below table shows the parameters taken for simulation of the motion of the slider.

Table 3. 1: Parameters used for simulation

No.	Description	Symbols	Values	Units
1	Amplitude of the wave	$\hat{z}_{st}$	12	nm
2	Applied frequency	f	8.28	MHz
3	Young's modulus of slider	E_1	215	GPa
4	Young's modulus of stator	E_2	173	GPa
5	Poisson's ratio of slider	ν_1	0.29	
6	Poisson's ratio of stator	ν_2	0.345	
7	Combined radius	R	1	mm
8	Mass of the slider	m	4	mg
9	Applied Preload	F_l	5	mN
10	Coefficient of friction	μ_d	0.18	

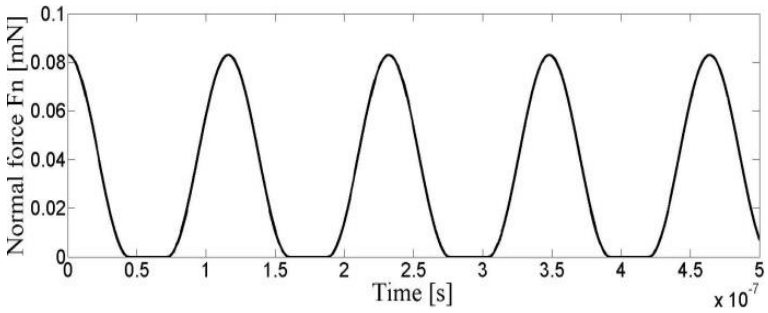

Figure 3. 3: Normal force is acting on the slider from the stator.

Preload force applied to the slider can be represented by,

$$F_l = \bar{F}_n \tag{3.15}$$

$$F_l = \frac{16}{3\sqrt{2}} \frac{\hat{z}_{st}^{3/2} k_n}{\pi} \tag{3.16}$$

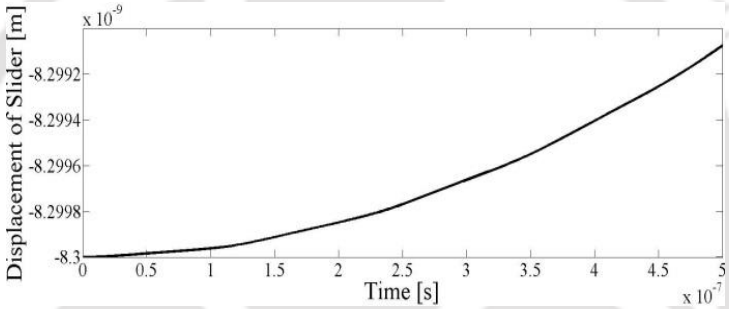

Figure 3. 4: Displacement of the slider in the normal direction.

The Figure 3. 4 shows the normal displacement of the slider for 0.5 μs. Displacement of the slider in the normal direction is seen in the Figure 3. 5 i.e. the vibration of the slider upon the stator reaches to steady state after passing through some propagating waves due to dissipation by air damping R_z. The steady condition of the normal slider displacement is observed with the increase in time. The rise time for the normal displacement of the wave is 0.02 ms, and it is observed that there exists a continuous contact between the slider and the stator for small amplitudes.

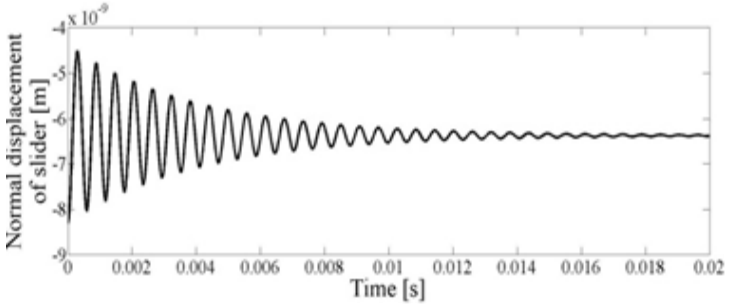

Figure 3. 5: Steady state displacement of the slider in the normal direction.

The contact between the slider and the wave will be irregular and will not be in any regular contact if the amplitude of the wave is uneven. The slider makes tangential contact position at the crest of the wave where the tangential velocity component is maximum. When velocity of the wave is greater than the velocity of the slider, $\dot{x}_{st} > \dot{x}_{sl}$, the motion of the slider will be in reverse direction of the propagation of the wave [81]. When the velocity of the slider is greater than the velocity of the wave $\dot{x}_{st} < \dot{x}_{sl}$, frictional force is negative and the speed of the slider will decrease [36]. The displacement of the slider in tangential direction can be represented by,

$$\dot{x}_{sl} = \frac{1}{m}\int F_t dt \tag{3.17}$$

The tangential frictional force F_t depends on the sliding velocity, the dynamic coefficient of friction μ_d and the normal force F_n. The sliding velocity is zero if $|F_t| < \mu_d F_n$. The tangential friction can be given by. Force in tangential direction is provided by,

$$F_t = \mu_d F_n sign(\dot{x}_{st} - \dot{x}_{sl}) \tag{3.18}$$

The $sign(\dot{x}_{st} - \dot{x}_{sl})$ indicates the direction of the movement of the slider while the velocity of the wave in tangential direction can be given by,

$$\dot{x}_{st} = \hat{x}_{st}\omega\cos(\omega t) \tag{3.19}$$

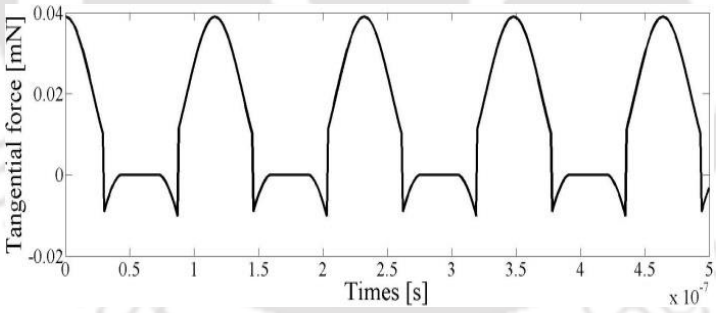

Figure 3. 6: Tangential forces are acting on the slider from the stator.

The Figure 3. 6 shows tangential force F_t acting on the slider for the provided burst of signals, while the Figure 3. 7 shows the step response and tangential velocity of the slider to the respectively applied burst of wave signal to the slider. The average tangential force per period F_t is greater than zero; the slider will accelerate. The tangential velocity of the slider gets its saturation and start breaking when it reaches to 0.085 m on time is 0.08 s. This happens due the wave amplitude becomes zero.

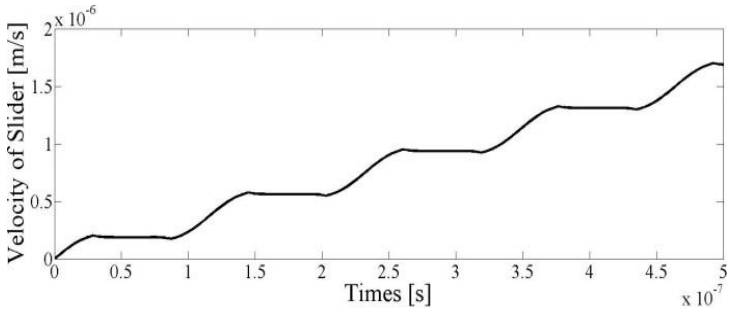

Figure 3. 7: Velocity of the slider in a translational direction.

A different coefficient of friction is applied to the slider and observed the velocity of the slider on a predefined preload as shown in Figure 3. 8, and it is concluded that when the coefficient of friction applied to the slider is 0.45, it can obtain the highest and stable velocity of 0.3 m/s is achieved.

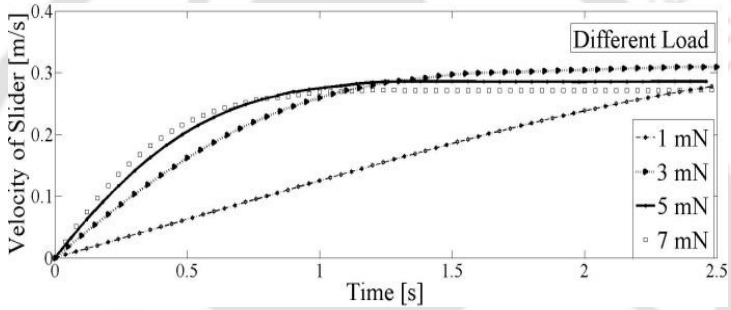

Figure 3. 8: Different velocities of the slider for differently applied preload.

Different preload is applied to the slider and observed the velocity of the slider on a pre-defined coefficient of friction as shown in Figure 3. 9. Moreover, concluded that with the 5 mN preload the velocity is stable and achieves the highest peak of 0.3 m/s. To achieve both preload and coefficient of friction various samples were tried to get a stable and highest velocity of the slider.

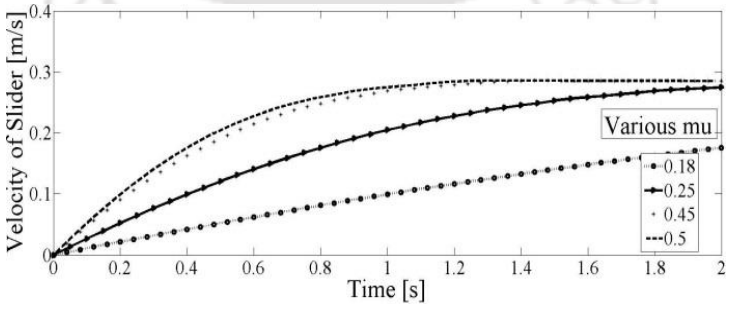

Figure 3. 9: Different velocities of the slider for the different coefficient of friction applied.

3.2 Analysis of Multiple Point of Contact of the SAW Motor

In the previous section, the modelling for the single point contact of the SAW motor is carried out. When multiple numbers of spherical balls are kept upon the stator, then a multiple points of contacts will occur at the junction of the stator and slider. So to analyse the multiple point contact more than one slider is taken into consideration. With some assumptions such as the surface of the stator is flat, identical projections, independent deformation of contact points from other contact points and uniformly distributed preload force, the multiple contact points can behave as single point contact.

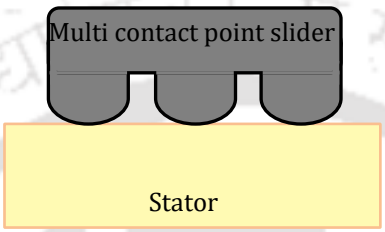

Figure 3. 10: Multiple sliders make point contact with the substrate.

For modelling, the structure is made of single slider mass m with air damping c driven by the normal vibration velocities by three compliant contacts k_n. The interaction is via a compliant contact k_t, a little mass d_m and a friction sub-model R_c. As the contact points are situated with some space gap among themselves, so the phase lag between the wave motions is $2\pi/3$ which is calculated according to some the slider are there to make contact.

3.2.1 Normal motion

As the wave period is small compared to the normal rise time, the average normal force,

$$\dot{z}_{sl} = \frac{1}{m}\int\left(\bar{F}_{n,sum} - F_l - c\dot{z}_{sl}\right) \tag{3.20}$$

$$\dot{z}_{sl} = \frac{1}{m}\int\left(p\bar{F}_{n,sum} - F_l - c\dot{z}_{sl}\right) \tag{3.21}$$

3.2.2 Tangential motion

The tangential force, which acts on the slider mass is

$$F_{t,sum} = \sum_{i=1}^{p} F_{t,i} \tag{3.22}$$

Where p is the number of projections and $F_{t,i}$ the tangential force of projection i. The wave period is very small relative to the tangential rise time. So the average force $F_{t,sum} = pF_t$. The

Figure 3. 11 shows the normal displacement, normal force, tangential velocity and tangential force of the multiple point contact slider.

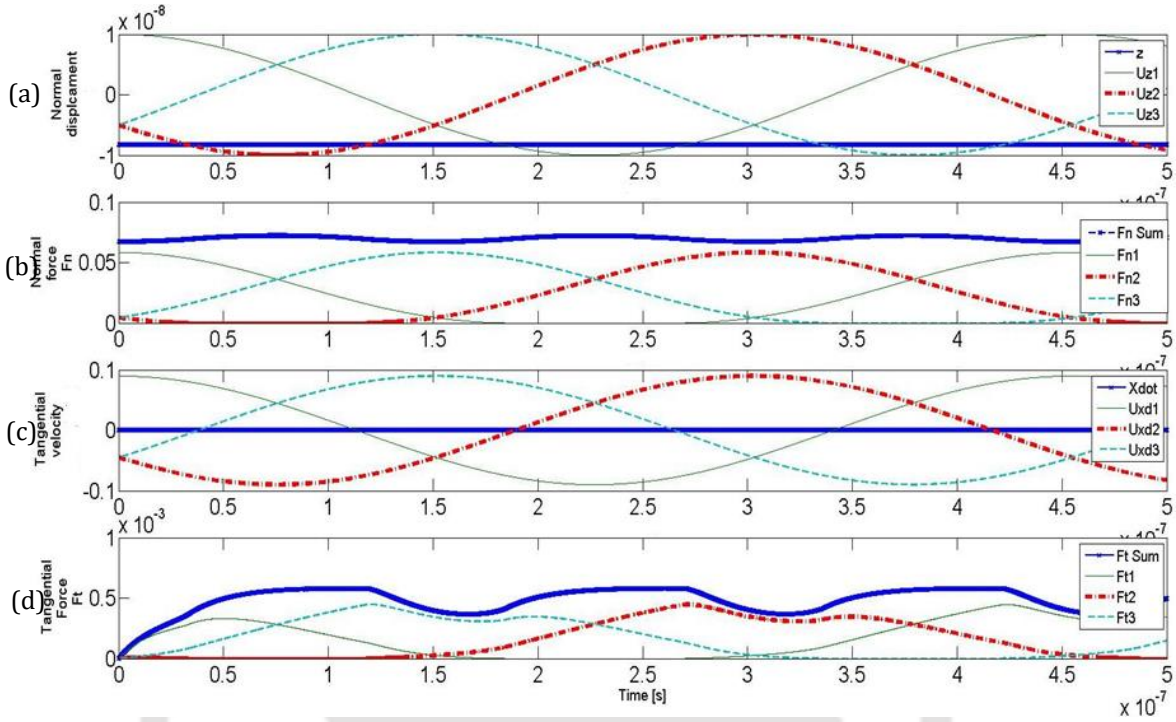

Figure 3. 11: (a) Normal slider displacement z_{sl} on multiple waves z_{st}, (b) Individual and average normal force F_n (c) Tangential slider velocity $\dot{x}_{sl}$ correspond to multiple wave velocity $\dot{x}_{st}$, and (d) Individual and average tangential force F_t .

3.3 Finite Element Simulation of the Device

As described in chapter 2, the finite element (FE) simulation method is a numerical technique to provide feasible solutions to the principal equations of a composite structure through a discretization procedure [58]. It is assumed that a spherical ball is placed upon a flat rigid plane type stator and modelling the device is done with Hertz's contact model.

3.3.1 Finite element modelling and simulation of SAW motor using ball as slider

The analysis of a single point of contact between a spherical slider and the Rayleigh wave is carried out in the following SAW motor model. Initially the slider oscillates in the vertical direction due to the generation of vertical force resulting from propagation of the wave. The slider goes through stick and slip states due to the contact friction [82].

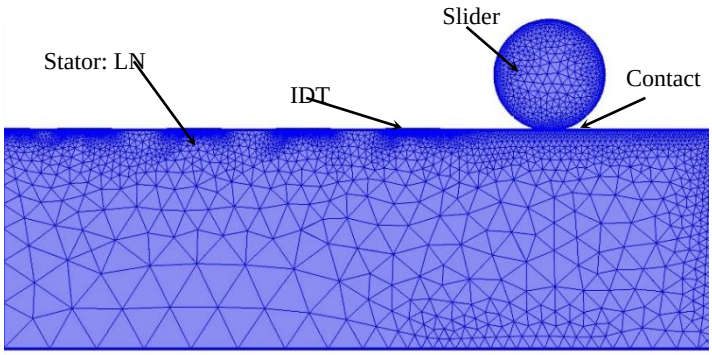

Figure 3. 12: Schematic of SAW motor designed in COMSOL Multiphysics.

The contact between stator and slider can be represented as per Figure 3. 12. The COMSOL Multiphysics is used for the FE simulation of the SAW motor model where it uses the coupling of piezoelectric and solid mechanics physics. The FE simulation was done and analysed in 3D plane geometry.

3.3.1.1 Generating the model of the SAW motor

The 3D plane geometry of a delay line made on a LN substrate of width 400 μm (1 λ), length 2000 μm (5 λ) and height 800 μm (2 λ) [72]. An array of IDT electrodes of aperture 400 μm (1 λ), width 100 μm (λ/4) and thickness 0.2 μm is made on stator. The device is terminated with the perfect matching layer to avoid reflections at the edges. The dimensions of the IDT and substrate are decided by Hartmann [68].

The slider is placed in the active region of the delay line with distance from the IDTs [40] for providing sufficient space for the motion of the slider with the size of the diameter of 200 μm. The stator was set up with LN material. The properties of the LN such as elastic coefficients, density for being declared [83], [84]. The comb-shaped electrodes were assigned with aluminium (Al) material as it is light in weight as well as of good conductance. Due to Al material, the mass loading effect will be minimised. The slider is assigned with silicon (Si) material, as fabrication of the projection of different shape is tried through fabrication facility.

3.3.1.2 Domain settings

In sub-domain settings, the stator is assigned as a piezoelectric element, for which the FE will treat and solve the governing equations for piezoelectric material [60]. The comb-shaped electrodes are declared as a linear element along with electric elements. This makes the Multiphysics software to solve the principal equations related to electrical for the electrode. The slider is made of linear materials.

3.3.1.3 Boundary settings

Boundary settings of the Multiphysics software play a vital role in simulating the proposed device. The slider is made as contact pair with the surface of the stator. The movement of the side boundary of the slider is kept free to move in prescribed displacement. To solve the model, triangular meshing was done for all the domains. The contacting surfaces were meshed declaring the master and slave. While the stator is treated as master and slave is declared to the slider. There should be a ratio of 1:2 between master and slave meshing. In this meshing a 2D device can be analysed properly [85].

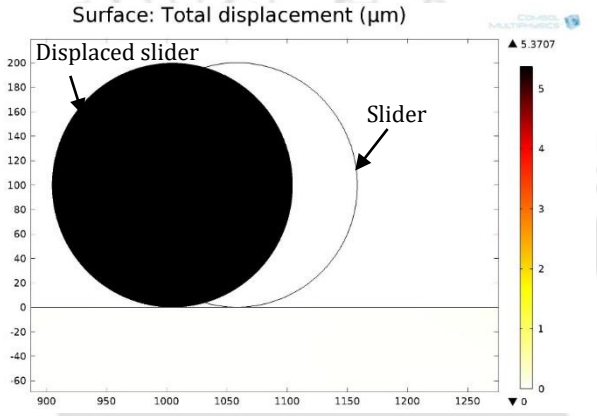

Figure 3. 13: Schematic diagram of FE simulated SAW motor with a ball as a slider.

Each surface point in the piezoelectric medium moves along an elliptical locus, as the Rayleigh SAW is nothing but a coupled wave of the longitudinal wave and the shear wave. The wave motion is attenuated in the thickness direction, so permitting rigid mounting at the bottom of the substrate [86]. The amplitude of normal displacement of the stator is 15 nm whereas the horizontal component is 10 nm. The amplitude of the motion of the point on the stator helps the slider to make a motion, due to friction generated due to trough and crest of the Rayleigh wave.

3.3.1.4 Solution of the structure

The 2D FE simulation of the SAW motor with a ball as the slider is shown in Figure 3. 13. The ball makes a translational motion on the surface of the stator. The FE simulation was observed with an excitation of voltage 100 V for 150 μs. The motion of the slider achieved a distance of 4.5 μm. During this motion, the average force acting on the slider is of 350 mN. The force about 350 mN is applied through the motion of the Rayleigh wave propagation to the slider as shown in Figure 3. 14. The motion of the ball moves in step size at the initial phase of time of the application of the excitation but it later stage the motor moves smooth once it moves with the inertia of the ball as shown in the Figure 3. 15.

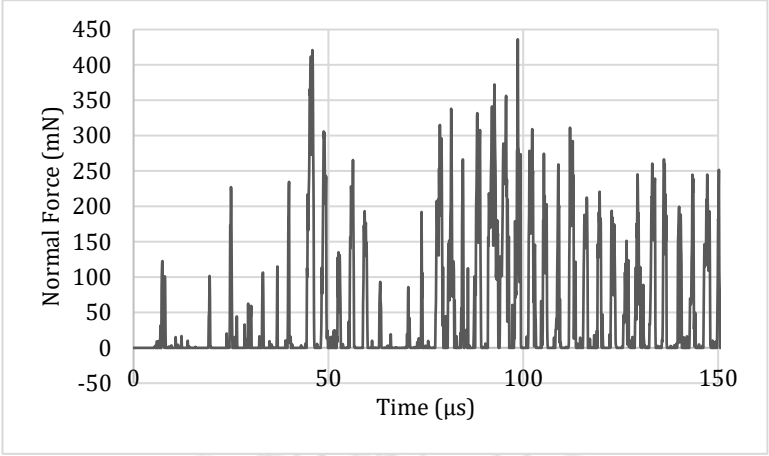

Figure 3. 14: Normal force is acting on the ball.

The motion of the ball achieves the translational velocity of 30 mm/s for the FE simulation of 150 µs as shown in Figure 3. 16. If the supplied excitation will be disconnected, then the velocity drops suddenly and stabilises within a fraction of µs. Motion happens to be in step size at the initial time of the application of the excitation, but it seems to be smooth once it moves with the inertia of the ball.

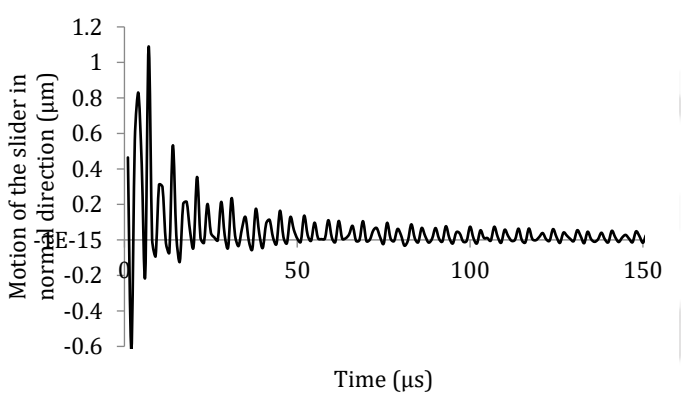

Figure 3. 15: Motion of the SAW motor in the normal direction.

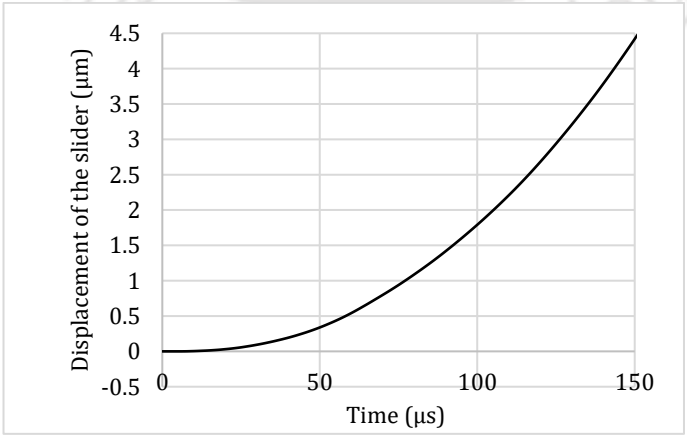

Figure 3. 16: Displacement of the slider in a translational direction.

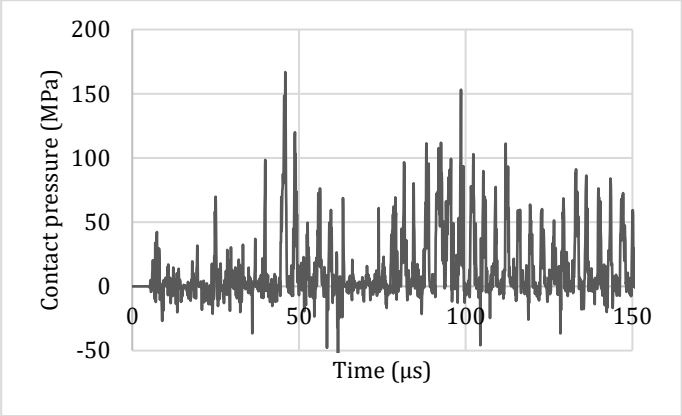

Figure 3. 17: Contact pressure on the stator due to the motion of the ball.

The contact pressure between stator and slider reaches 100 MPa with the present physical conditions. The Figure 3. 17 shows the contact pressure occurring at the surface of the stator due to the motion of the slider.

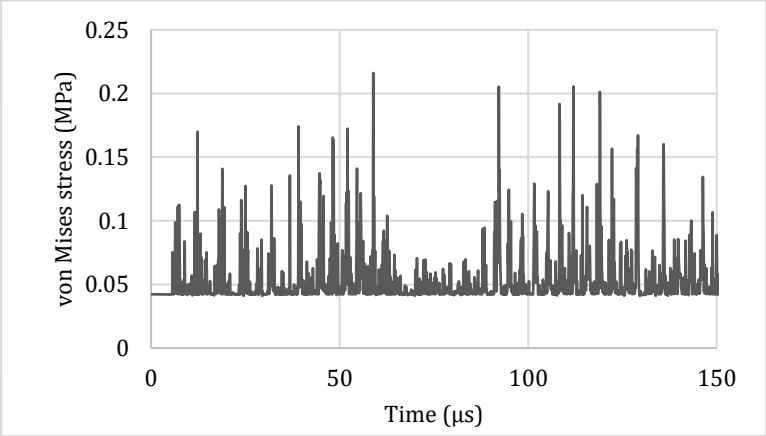

Figure 3. 18: von Mises stress on the stator due to the motion of the ball.

The Figure 3. 18 shows von Mises stress in the stator at a point beneath the contact point of slider and stator. From the figure it is found that the maximum von Mises stress is about 0.25 MPa which is well below 37 MPa, the yield stress of lihium niobate [83].

3.3.2 Finite element modelling and simulation of SAW motor using flat plane cuboid slider

The linear SAW motor is configured as shown in the Figure 3. 19, Where an LN substrate is used as the stator. A comb structured IDT was fabricated upon the stator. When RF power is applied the IDTs generate Rayleigh wave. As per delay line and the Rayleigh wave propagation, it is observed that the wave is propagating in right (x) direction and the surface points are making anticlockwise elliptical motion. This elliptical motion of the points puts stress on the contact points of the slider, which forces to move in the opposite

direction of the propagation of the wave. FE simulation of the SAW motor is carried out in COMSOL Multiphysics using coupling of piezoelectric and solid mechanics modules.

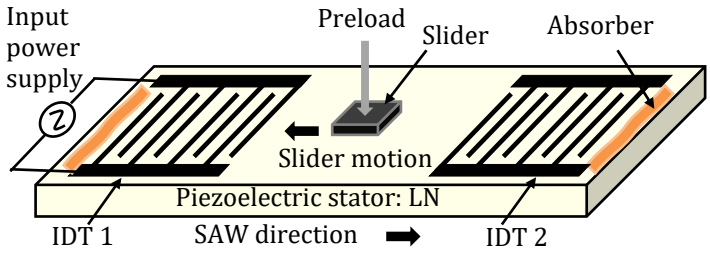

Figure 3. 19: Schematic of SAW motor consists of stator and slider without projections.

The FE simulation of SAW motor using a flat plane slider (having no projections at its surface) is represented [50]. The parameters [87] involved in simulating the proposed SAW motor is given in Table 3. 2. This table contains the material properties of the used stator and slider such as Young's modulus, Poisson's ratio and density. It also contains the applied preload which is calculated from the amplitude of propagation of SAW. The voltage applied for this simulation is 100 V.

3.3.2.1 Creating the geometry of SAW motor

The 3D plane geometry of a delay line made by placing 4 number of IDT electrodes of aperture 400 µm (1 λ), width 100 µm (¼ λ) and thickness 0.2 µm on a LN substrate of width 400 µm (1 λ), length 2200 µm (5 λ) and height 800 µm (2 λ). The device is terminated with the perfect matching layer to avoid reflections at the edges. A silicon (Si) slider of size 400 µm x 400 µm x 100 µm is placed in the active region. The properties of LN such as elastic coefficients, coupling coefficients, relative permittivity and material density are adapted from [84].

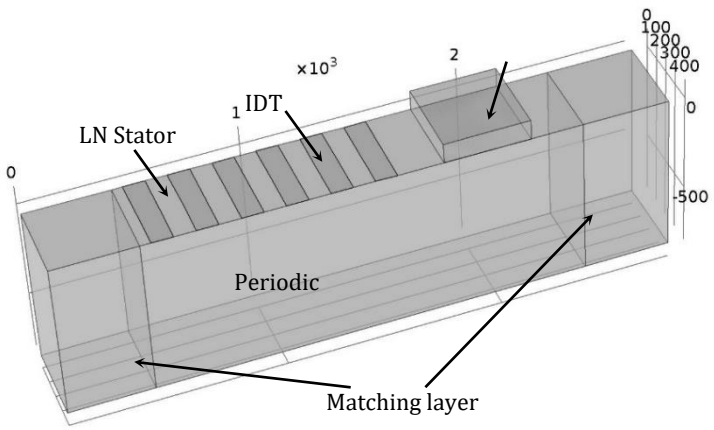

Figure 3. 20: Schematic structure of SAW motor having slider without projections.

Al is used for IDTs areas it is lightweight and highly conductive. The material used for the slider and projections is Si.

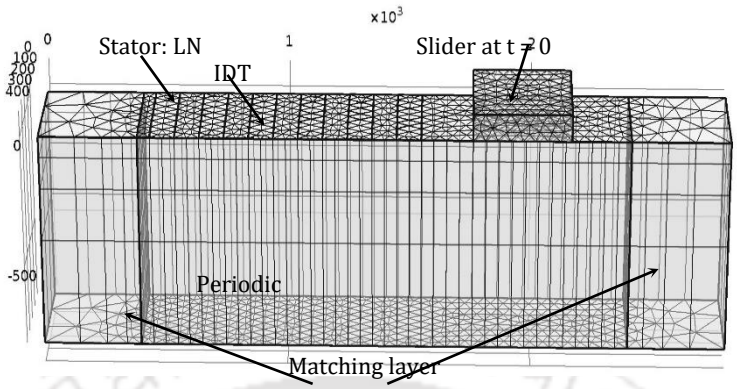

Figure 3. 21: Schematic structure of SAW motor having slider without projections after meshing.

3.3.2.2 Multiphysics settings

The boundary settings in FE simulation are as follows. The bottom of the stator is fixed while the ends are terminated with perfect matching layers to avoid reflections. The Periodic boundary condition is applied to the aperture. The slider and stator are defined as contact pair. The boundaries of the slider are set free. Swept meshing was applied for all the domains [88].

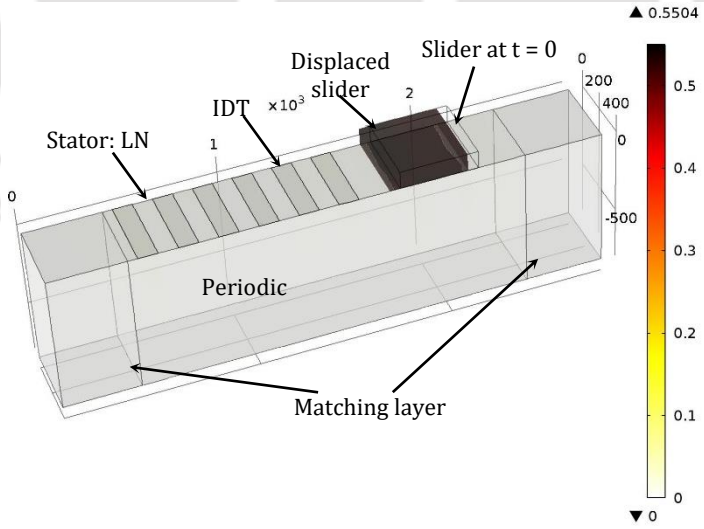

Figure 3. 22: Schematic structure of SAW motor having slider without projections.

When a calculated preload is supplied from the top of the slider, then slider makes a tight contact with the stator. Once the generated Rayleigh SAW wave passes under the slider it

makes a frictional contact with the bottom surface of the slider. This frictional force between stator and slider due to pressure from the top side of the slider makes it move in the reverse direction of propagation of Rayleigh wave. Whenever the slider is in contact with the stator, the slider-stator interaction goes through stick and slip states and the tangential force moves the slider as shown in Figure 3. 22.

3.3.2.3 Simulation of SAW motor

The preload is applied on the slider to increase friction at the contact surface with the stator. As the generated Rayleigh SAW wave passes under the slider, it makes a frictional contact with the bottom surface of the slider. This frictional force on the slider drives the slider in the direction opposite to the direction of propagation of SAW as shown in Figure 3. 24.

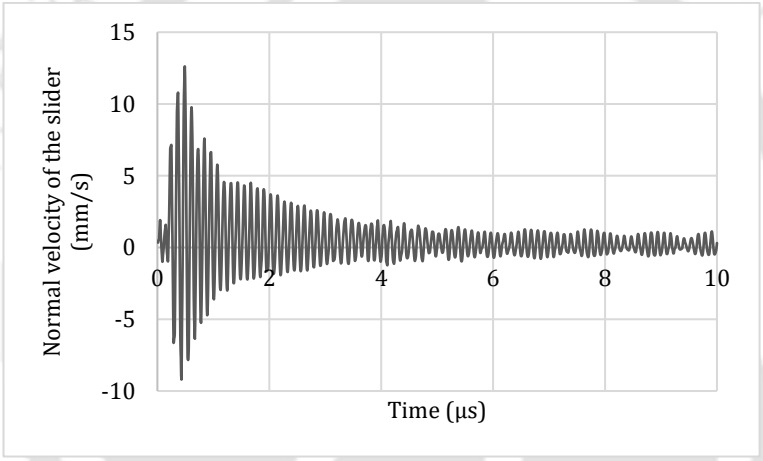

Figure 3. 23: Normal velocity of the sliderattains steady state at 10 μs.

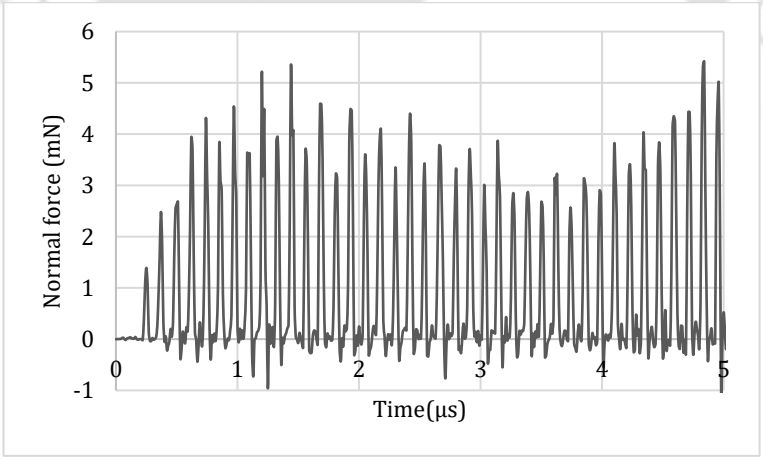

Figure 3. 24: Normal force on the slider due to the motion of the slider.

The normal component of the displacement of a point on the surface of the stator for the excitation shows the amplitude of the wave in the normal direction as 6 nm for 100 V. The

translational displacement of the particle motion on the surface of the stator for the excitation shows the amplitude of the wave in the translational direction as 8 nm for 100 V. The normal displacement of the slider stabilises after a certain amount of wave passes under it as shown in Figure 3. 23.

The force generated on the slider through the stator is shown in Figure 3. 24. The force generated on the slider through the stator makes the slider to move in the translational direction as shown in Figure 3. 25. The plot shows slider having no projections moves a distance of 0.55 µm for a time of 10 µs for application of a continuous excitation of an amplitude of 100 V.

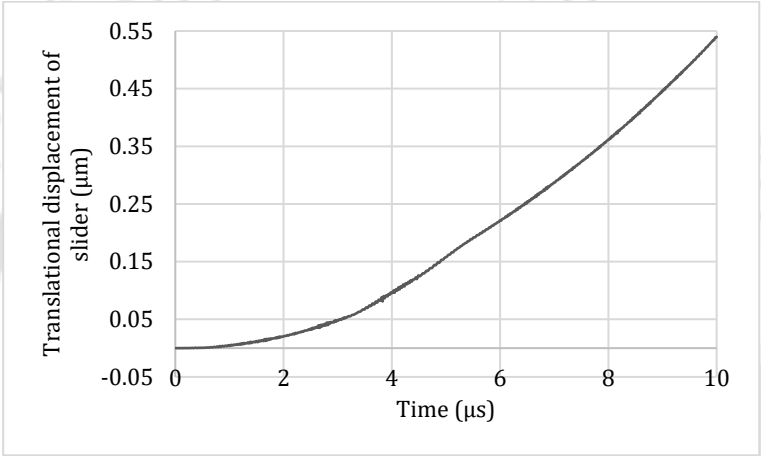

Figure 3. 25: Translational displacement of slider 0.55 µm at the end of 10 µs.

The slider to move in a translational direction with a velocity of 55 mm/s for the time of 10 µs for application of a continuous excitation of an amplitude of 100 V.

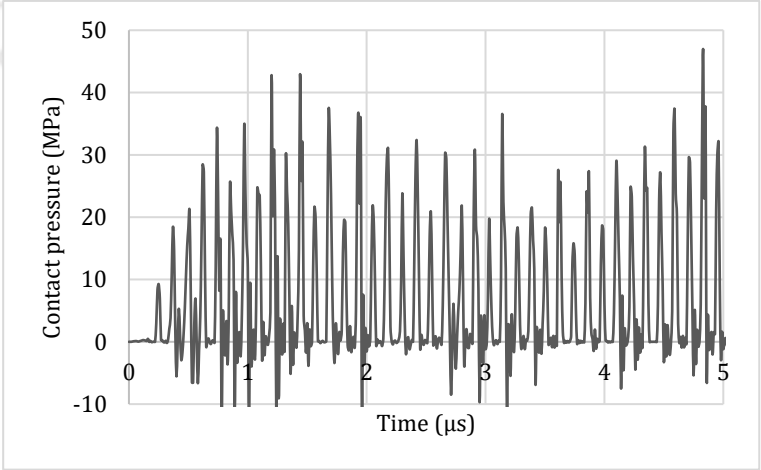

Figure 3. 26: Contact pressure generating on the stator due to the motion of the slider.

The application of excitation of 100 V, where it generates a pressure of about 15 MPa as shown in Figure 3. 26. The high amplitude results in a high-pressure generation at the contacting point of the slider and stator. This shows that the high pressure is generated due to high contact, and the high contact means a high amount of force will be applied to the contacting projections, which makes high-speed motion as compared to the low excitation.

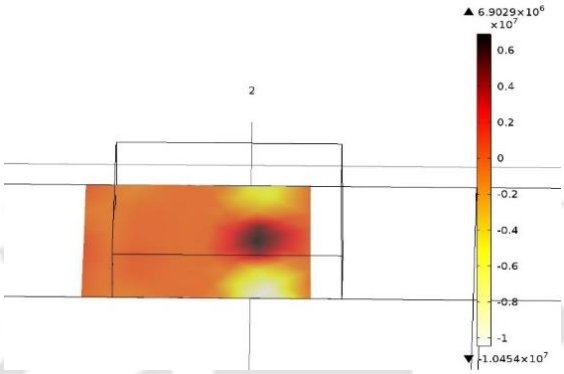

Figure 3. 27: Schematic of SAW motor with plain slider generating pressure on the stator.

Figure 3. 27 shows a structural form of generation of contact pressure on the stator through the slider.

3.3.3 Finite element simulation of SAW motor using cuboid slider having projections

The linear SAW motor is configured as shown in the Figure 3. 19 represents a SAW motor using a flat plane, as to reduce the sticking problem of the slider with stator [89], a new configuration of the slider is presented as shown in Figure 3. 28.

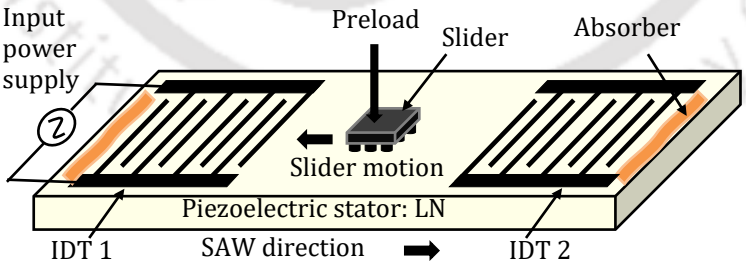

Figure 3. 28: Schematic diagram of SAW motor consists of stator and slider with projections.

The FE simulation of the SAW motor is carried out in COMSOL Multiphysics using coupling of piezoelectric and solid mechanics modules. To configure the linear motor device with materials, the block which is to be treated as the stator is configured with LN material. The elastic coefficients for LN are declared [84]. The parameters applied for the FE simulation.

Table 3. 2: Parameters applied for the simulation

No.	Parameters	Symbols	Value	Units
1	Young's modulus of slider	*E1*	169	GPa
2	Young's modulus of stator	*E2*	173	GPa
3	Poisson's ratio of slider	ν_1	0.3	-
4	Poisson's ratio of slider	ν_2	0.345	-
5	Frequency	*F*	8.36985	MHz
6	Load	F_L	1.66	mN
7	Static coefficient of friction	μ_s	0.45	-
8	Dynamic coefficient of friction	μ_d	0.15	-
9	Radius of the slider	*R*	20	µm
10	Mass of the slider	*m*	0.4	mg

3.3.3.1 Generating geometry of the SAW motor

The 3D plane geometry of a delay line made by placing IDT electrodes of aperture 400 µm (1 λ), width 100 µm (λ/4) and thickness 0.2 µm on an LN substrate of width 400 µm (1 λ), length 2000 µm (5 λ) and height 500 µm. The device is terminated with the perfect matching layer to avoid reflections at the edges. A silicon (Si) slider of size 400 µm x 400 µm x 100 µm is placed in the active region. To avoid the problem of sticky surfaces, cylindrical projections of diameter 20 µm and centre to centre space of 40 µm are made on the surface of the slider in contact with the stator as shown in Figure 3. 29.

The properties of LN such as elastic coefficients, coupling coefficients, relative permittivity and density are adapted from [84] and used for carrying out the simulation. Al is used for IDTs as it is lightweight and highly conductive. The material used for the slider and projections is Si. Table 1 presents the list of parameters of slider and stator used for simulating the device.

3.3.3.2 Multiphysics settings

The boundary settings in FE simulation are as follows. The bottom of the stator is fixed while the ends are terminated with perfect matching layers to avoid SAW reflections. The slider and stator are defined as contact pair. In contact pair, the LN stator is treated as a master while the slider is a slave. With deformation of the stator due to the application of RF power, the slider can be functioned. The boundaries of the slider are set free in all the direction. The SAW motor is divided into a finite number of elements and meshed with triangular meshing on the boundaries of all the domain. Swept meshing was applied for all the domains to analyse the characteristic of every element [58].

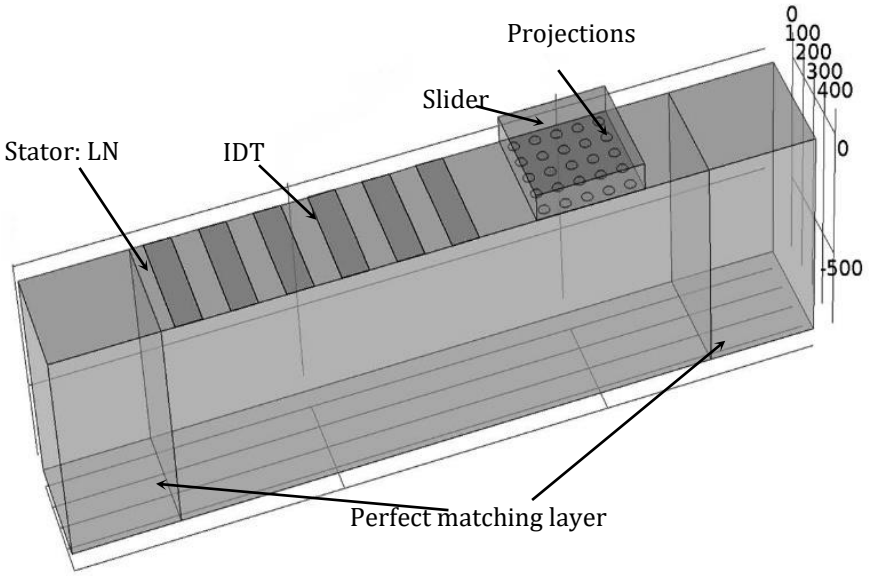

Figure 3. 29: Schematic of SAW motor designed in COMSOL Multiphysics showing various domains.

The surface acoustic wave (SAW) motor which makes a linear motion is shown in figure 2.1. An LN substrate is used as the stator, where interdigital transducers (IDT) in comb shape were fabricated upon the stator. When a predetermined range of radio frequency (RF) power is applied, the IDTs generate Rayleigh wave which makes mechanical deformation on the surface of the stator. It is observed that the SAW is propagating in right (x) direction and the surface points are making anticlockwise elliptical motion in reverse of it i.e. in –x direction. The elliptical motion of the points generates stress on the contact points of the slider, which forces the slider to move in the reverse of the propagation direction of wave [3].

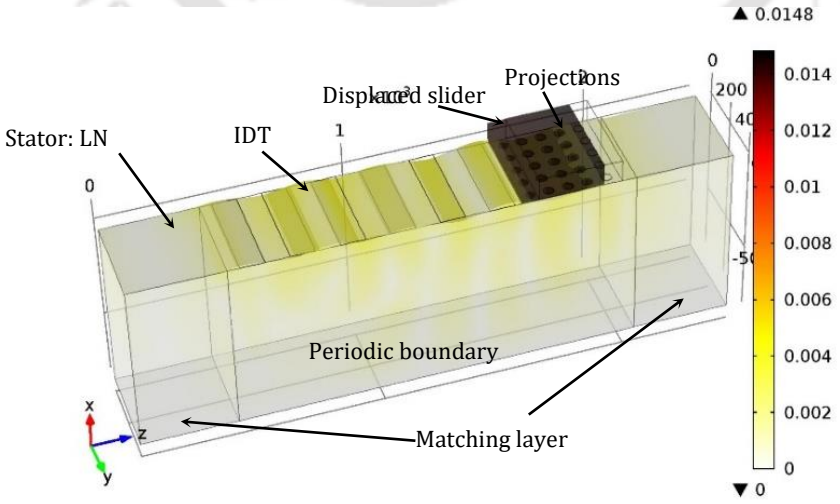

Figure 3. 30: Schematic of SAW motor showing the displacement profile simulated in COMSOL Multiphysics.

When a calculated preload is supplied from the top of the slider as per equation (9), then slider makes a tight contact with the stator. Once the generated Rayleigh SAW wave passes under the slider it makes a frictional contact with the bottom surface of the slider. This frictional force between stator and slider due to pressure from the top side of the slider makes it move in the reverse direction of propagation of Rayleigh wave.

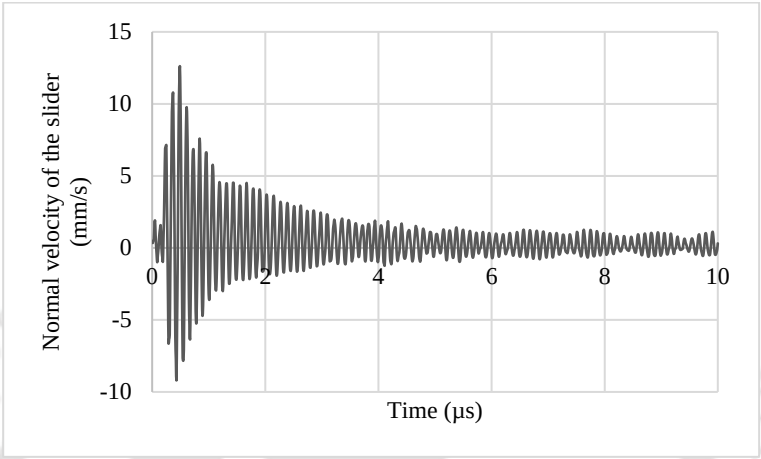

Figure 3. 31: Normal velocity of the slider attains steady state at 10µs.

Whenever the slider is in contact with the stator, the slider-stator interaction goes through stick and slip states and the tangential force moves the slider as shown in Figure 3. 33. The slider makes two types of motion as per the mathematical presentation above. The oscillation of slider in normal direction minimises with the passage of the wave under the slider after a certain time as shown in Figure 3. 31.

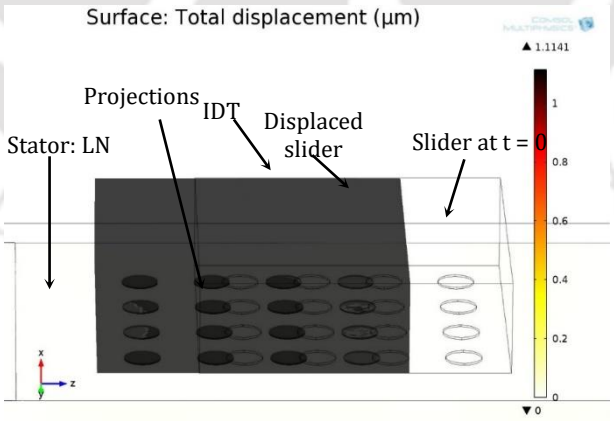

Figure 3. 32: Schematic of FE simulated SAW motor showing the displacement of the slider.

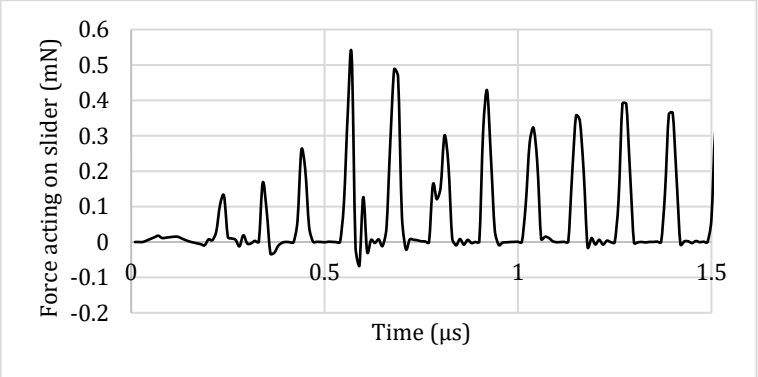

Figure 3. 33: Tangential force acting on the slider.

The motion of the slider in normal direction gets stabilised after some high peaks with a couple of waves passed. Initially, the slider oscillates with high amplitude in the normal direction, but the oscillations decrease after a time of about 2 ms.

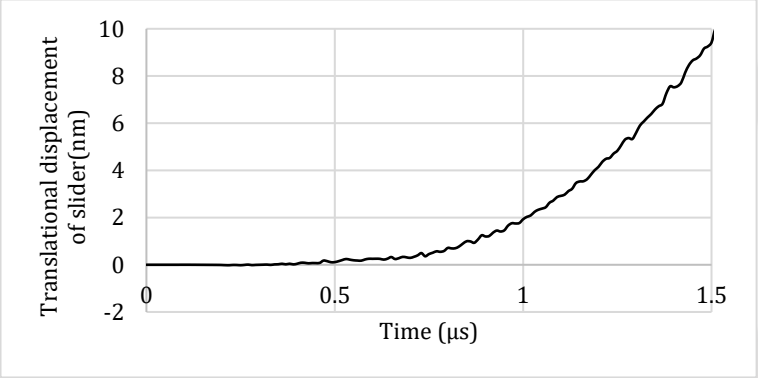

Figure 3. 34: Thetranslational motion of the slider.

The translational motion of the slider achieved which is shown in the Figure 3. 34, where the slider moves in a step size motion. The slider moves in the reverse direction of propagation of Rayleigh wave. It achieves a displacement of 10 nm in 1.5 µs.

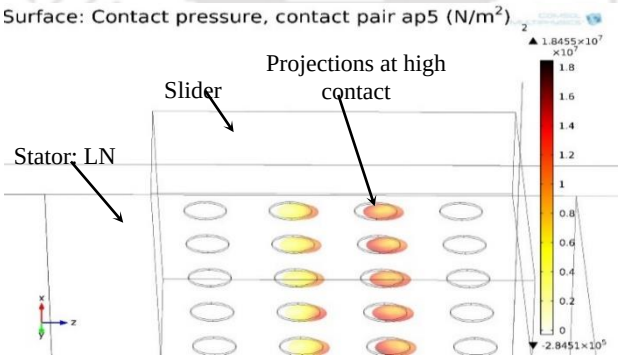

Figure 3. 35: Pressure profile in the slider during simulation of SAW motor.

At the contact position, the wave puts pressure on the slider to move in the direction of the motion of the point on the surface of the stator. Figure 3. 35 shows pressure profile in the stator; middle two rows of projections are in contact with the wave while other two rows are not in contact.

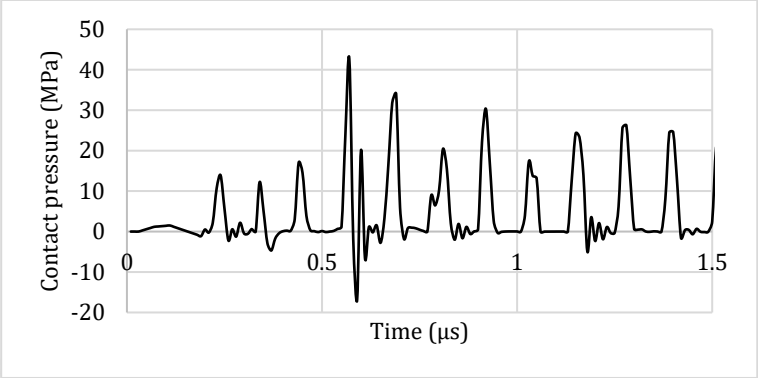

Figure 3. 36: Contact pressure on the stator due to themotion of the slider.

The tangential force acting on the slider at a point on the projection is shown in Figure 3. 36.

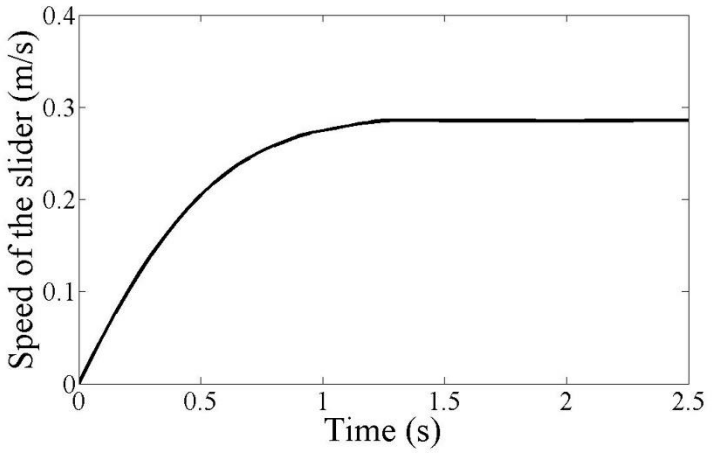

Figure 3. 37: Graph showing the velocity of the slider showing steady-state velocity at the end of 2.5 s.

It shows that due to contact frictional motion the slider generates an average of 30 MPa stress on the stator. The force generated on the slider through the stator is shown in Figure 3. 36. The plot shows slider having cylindrical projections gets a force of 0.3 mN through the propagation of the SAW.

The high amplitude results in a high-pressure generation at the contacting point of the slider and stator. This shows that the high pressure is generated due to high contact, and the high contact means a high amount of force will be applied to the contacting projections, which makes high-speed motion as compared to the low excitation. The translational

velocity of the slider achieved, where the slider achieves a speed of 0.3 m/s. Initially, it acts in step size but later stages it achieves a velocity and moves smoothly as shown in the Figure 3. 37, which is attained when a continuous sinusoidal signal is applied to the slider.

3.3.4 Comparative motion of slider with different voltage supply

Application of different amplitude of excitations results in better displacement of the slider. In this section study for simulation of the slider for two voltage supplies done. One with 100 V and other with 150 V excitation is applied to the IDTs of the stator [87].

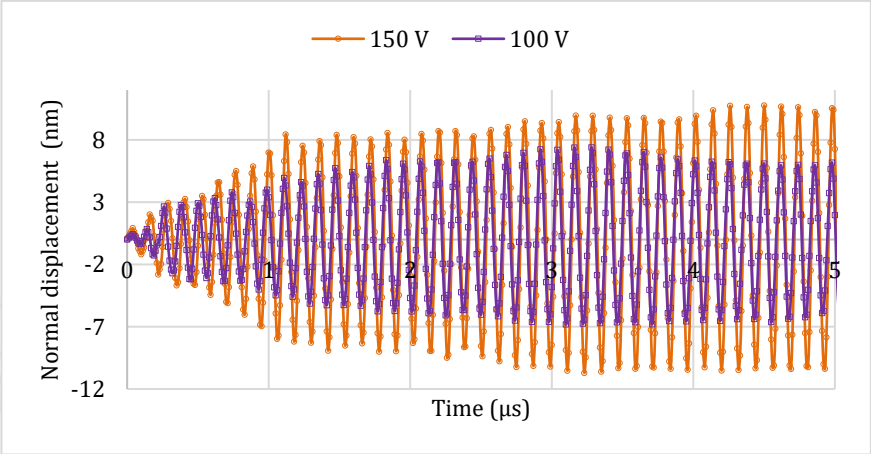

Figure 3. 38: Displacement of the vertical component on the surface of the stator.

The parameters used for the work is given in Table 3. 2, wherein voltage supply two different voltages taken for the work is mentioned. The difference in the normal displacement of the particle motion on the surface of the stator for two different excitations is represented by Figure 3. 38. It shows the amplitude of the wave in the normal direction as 11 nm for 150 V and 7 nm for 100 V.

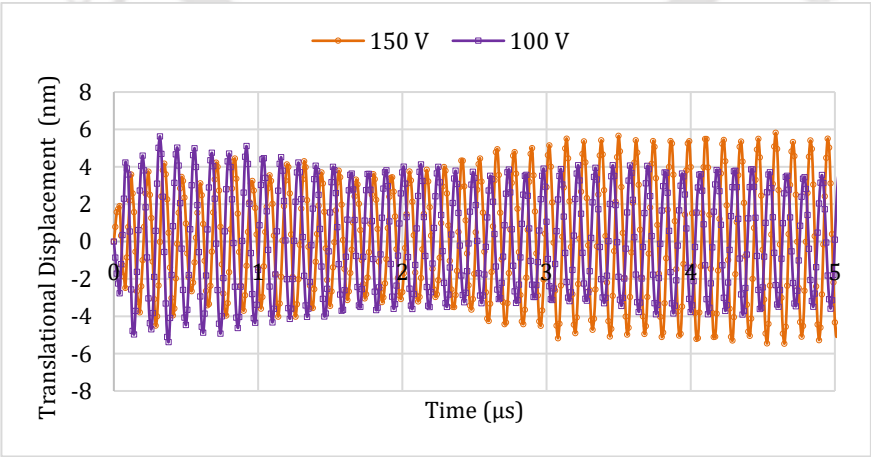

Figure 3. 39: Displacement of the horizontal component on the surface of the stator.

The difference in the normal displacement of the particle motion on the surface of the stator for two different excitations is represented by Figure 3. 39. It shows the amplitude of the wave in the translational direction as 6 nm for 150 V and 5 nm for 100 V.

The translational displacement of the slider observed about 15 nm and 10 nm for the excitation of 150 V and 100 V respectively for the motion for 1.5 μs as shown in Figure 3. 40.

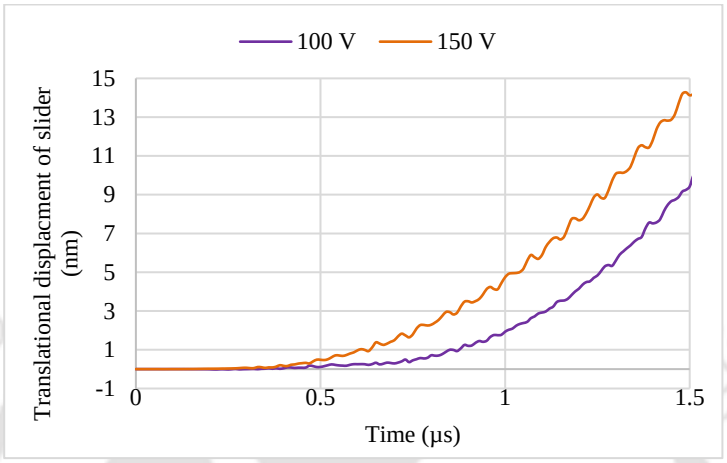

Figure 3. 40: The translational motion of the slider for different voltage supply.

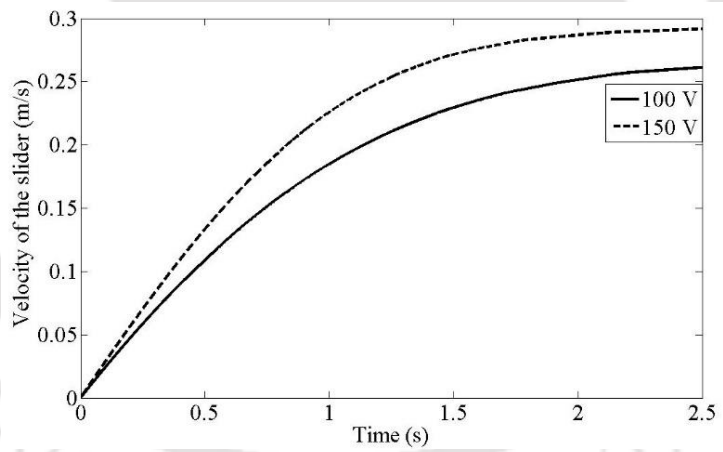

Figure 3. 41: Velocity of the slider at the end of 2.5 s.

Upto 2 μs, the slider used to move at the almost same scale of displacement but as the time progresses the difference in the displacement of the slider for both the amplitude of the excitation changes. In both cases, the slider moves proportionally to the cycle of the Rayleigh wave.

The slider moves on the surface of the stator with the passage of each cycle and each cycle of the Rayleigh SAW contributes to moving the slider. As the slider is having cylindrical projections on the both sides of its contacting surfaces. Due to the friction of contact the slider used to get the force at the top and bottom stators to move with the wave. Each cycle

of the SAW makes a contribution to move the slider in steps. The Figure 3. 41 gives the velocities of the slider for application of two different voltage excitations.

3.3.5 Comparative study of SAW motors using cuboid slider with flat plane and with projections at its surface

The comparison between normal motions of 2 types of the slider with and without projections is represented in Figure 3. 42 of the SAW motor. From the plot for normal displacement of the slider, it shows all are achieving their stabilisation condition after the slider is run for some time.

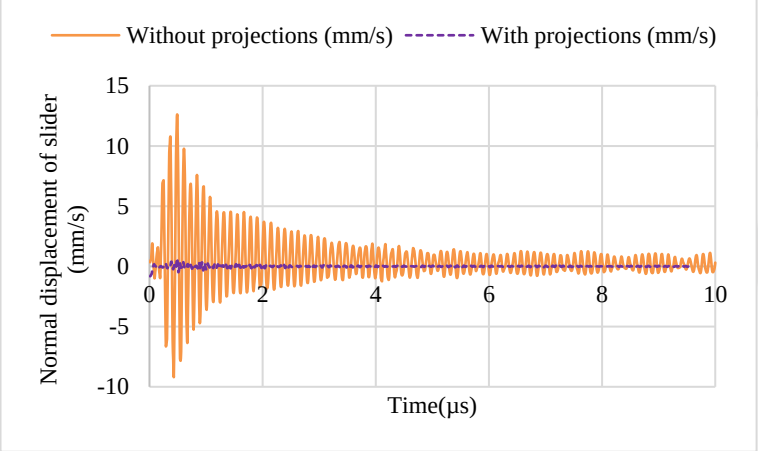

Figure 3. 42: Steady state displacement of the slider in the normal direction.

The force generated on the various types of the slider through the stator is shown in Figure 3. 43. The plot shows that the slider having no projections gets the high force of about 1.5 mN to be driven by the wave. The slider having cylindrical projections gets a force of 0.05 mN, which very less as compare to another type of the slider.

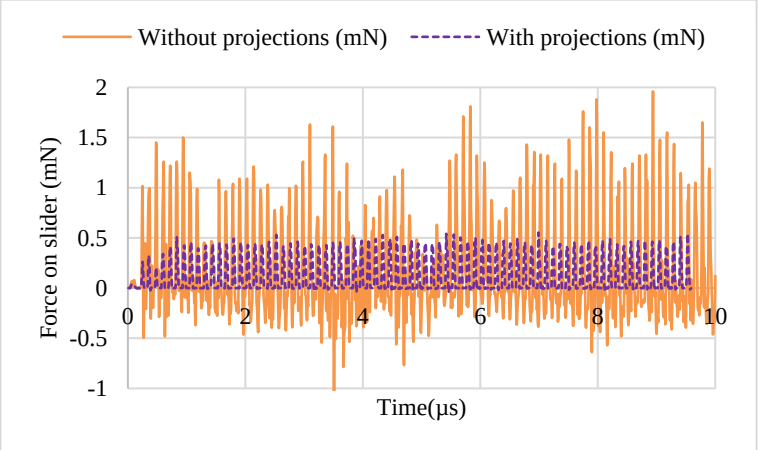

Figure 3. 43: Comparative study of the force acting on the slider with and with projections.

The translational displacement of the slider observed about 1.1 µm and 0.5 µm for with and without projections respectively for the excitation of 100 V in 10 µs as shown in Figure 3. 44. The initial phase of transition the slider having cylindrical and no projections started making a motion. In all the cases the slider moves proportionally to the cycle of the Rayleigh wave.

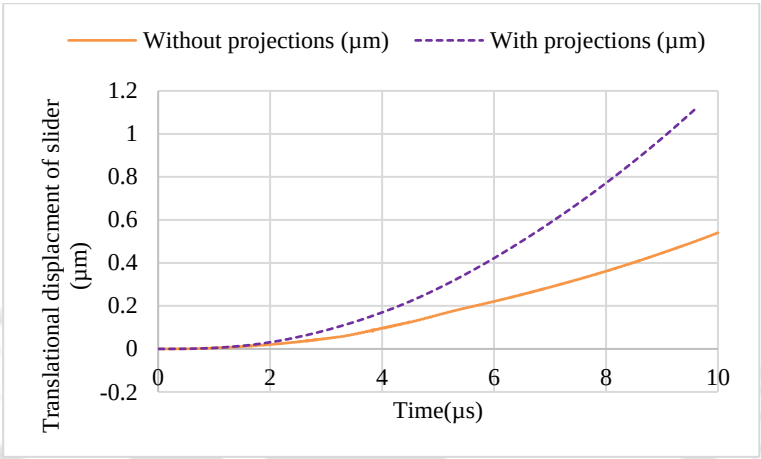

Figure 3. 44: The comparative result of the translational displacement of the slider with different sliders at equal applied voltage of 100 V.

The translational velocity of the slider observed about 110 mm/s and 50 mm/s for with and without projections respectively for the excitation of 100 V in 10 µs. The initial phase of transition the slider having cylindrical and no projections started making a motion. In all the cases the slider moves proportionally to the cycle of the Rayleigh wave.

Comparison plot for contact pressure is showing that the slider without projections generates less pressure as compared to the slider with projections as shown in Figure 3. 45. Compare to the application of excitation is very clear, where it generates a pressure of about 12 MPa in cylindrical whereas 3 MPa in the case of the slider having no projections. The high amplitude results in a high-pressure generation at the contacting point of the slider and stator. This shows that the high pressure is generated due to high contact, and the high contact means a high amount of force will be applied to the contacting projections, which makes high-speed motion as compared to the low excitation.

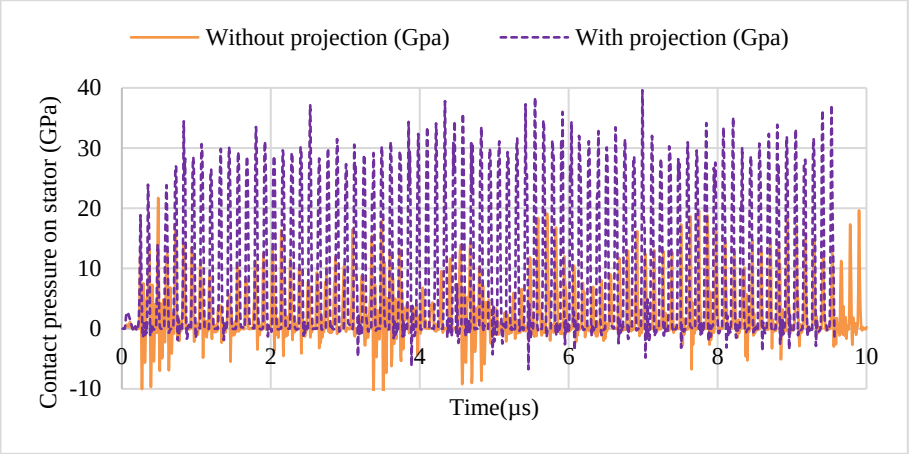

Figure 3. 45: Comparative result of the contact pressure on the stator with different sliders at equal applied voltage of 100 V.

3.4 Summary

This chapter presents the mathematical modelling and FE simulation using COMSOL of conventional SAW motors. Initially, mathematical modelling of the conventional SAW motors was done. The mathematical modelling was verified by using MATLAB and able to achieve the results, which were earlier produced by researchers. Then the FE simulation of SAW motors are carried out using the ball as a slider, analysed the results obtained from simulation. Then the SAW motor with cuboid having cylindrical projections at the contacting side with stator is simulated. Later the slider without the projections is simulated. The comparative study of the SAW motor is carried out with various voltage supplies and with various type of projections. In the next chapter, the design and working principle of proposed SAW motor depending on Rayleigh wave is explained.

4

Dual Friction-drive SAW Motor using Cuboid Slider

In chapter 3, the conventional SAW motor with a slider in the shape of sphere and cube, with and without projections, are discussed and verified along with their results through mathematical modelling and FE simulations. Some comparative studies related to voltage and shape of the slider are presented. In this chapter, the proposed dual friction-drive SAW motor structure is discussed. The chapter progresses with the introduction to the proposed SAW motor, assembly, working principle, followed by mathematical modelling and FE simulation of dual friction drive motor. Various comparisons are carried out to optimise and check the performance of the SAW motor.

Conventionally, a SAW linear motor consists of a slider held tightly in contact with the surface of a piezoelectric stator and the required preload is applied through a lubricated guide rail to reduce friction at the top side of the slider while increasing friction between the stator and the bottom surface of the slider [42], [26]. To achieve the conflicting friction-related requirements at the two sides of the slider and to guide the slider to move in a predefined path, normally heavy and bulky lubricated guide rails are used. The detail configuration and operating mechanism of conventional SAW motors are discussed in chapter 1, and modelling and FE simulation of different configurations are presented in chapter 3.

The proposed dual drive SAW linear motor can overcome the limitations mentioned above for the conventional SAW linear motor. In the proposed SAW linear motor an additional stator replaces the bulky guide rail to drive the slider from two sides and greatly simplifies the operating mechanism. The slider with a uniform array of projections on both contact surfaces is sandwiched between two identical stators aligned to generate SAWs that drive the slider from top and bottom sides as shown in Figure 4. 1. The glass substrates provide support to the piezoelectric stators and supply preload. In each stator, SAW propagating on the surface of the stator interacts with the slider at the contact points and the frictional

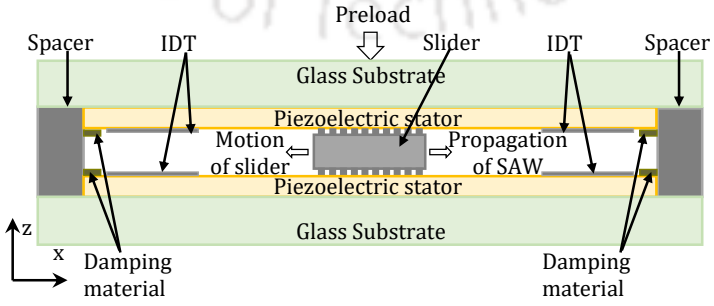

Figure 4. 1: Schematic diagram of Sandwich structured SAW motor with a slider having a uniform array of projections.

force acts on the slider in the direction opposite to the propagation of SAW, as described in chapter 1 for the conventional SAW motor.

4.1 Dual Friction-Drive SAW Motor having Slider with Projections

The distinct feature of the proposed design is a slider with a uniform array of projections on both contact surfaces sandwiched between two identical piezoelectric stators providing friction drive at both contact surfaces. Each stator has an interdigital transducer (IDT) fabricated on the piezoelectric substrate on either side of the slider as shown in Figure 4. 1. SAW generated on the stator surface interacts with the slider at the line of contact and the frictional force acts on the slider in the direction opposite to the SAW propagation.

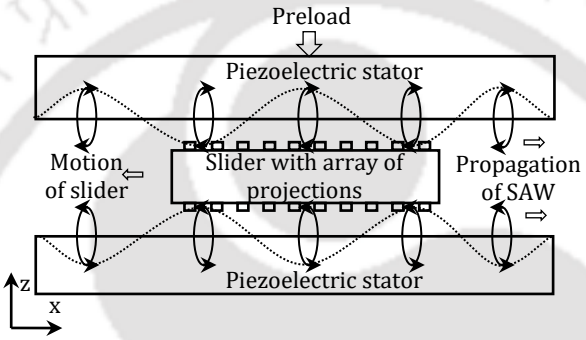

Figure 4. 2: Schematic of a slider driven by two SAWs generated on the surface of the stators.

By applying synchronous excitation to two IDTs on one side of the motor, one each from the top and bottom stators, the Rayleigh waves start propagating on the stator surfaces and provide a frictional force on the slider at the contact points as represented in Figure 4. 2. Since the waves propagate in the same direction on the two stator surfaces facing each other, the elliptical motions of the surface points in the bottom and top stators are anticlockwise and clockwise respectively, generating frictional forces on the two contact surfaces of the slider and driving the slider towards the activated IDTs. The direction of motion of the slider is changed by switching the excitation to the IDT pair on the opposite side of the motor, thus forward or reverse translational motion is possible.

4.1.1 Modelling of contact mechanics between slider and stator

In the proposed dual drive SAW motor, the slider is held between two identical lithium niobate stators with adequate preload. Figure 4. 3 shows a section of a slider around a pair of projections and the forces acting on the slider by the interaction between the slider and the two stators as synchronised Rayleigh waves propagate on the stator surfaces in the presence of the applied preload,F_l.$F_{n,T}$and$F_{n,B}$arethe forces acting on the slider in a normal

direction from top and bottom, respectively. $F_{t,T}$ and $F_{t,B}$ are the forces acting on the slider in a tangential direction from top and bottom, respectively. R is the centre-to-centre distance between the slider and the stator. 'a' is the contact length is the radius of the cylindrical projections, and h is the parameter which decides stick and slip of slider on Rayleigh wave, at the contact layers between the stators and the slider.

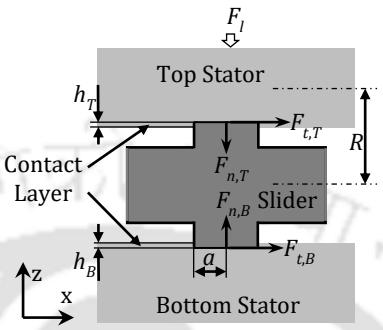

Figure 4. 3: Schematic of the slider with cylindrical projections placed between two stators with preload.

The main aim of the modelling is to obtain the design parameters and behaviour of the device. The modelling of the device starts with the help of Hertz's contact model [73]. For primary stage, it is assumed that a slider is placed upon a flat rigid plane stator. This model considers the analysis of a single point of contact between a slider and the Rayleigh wave generated on the stator. The stator surface has a roughness in nanometre and has a great impact on the contact mechanics between the stator and slider.

The friction drive mechanism at the interface of projections and stator undergoes stick, slip zones in every cycle as discussed in chapter 1, and the model for contact friction is different for the two states. The Rayleigh wave has both normal and tangential components. The normal component of the surface wave generates additional normal force on the slider and increases the contact friction while the tangential component drives the slider.

Morita *et al*., [36] in 1999 first presented mathematical modelling of a single contact point in a conventional SAW motor consisting of a spherical slider driven by a piezoelectric stator. The work is extended to multiple contact points of a slider by Feenstra [74] in 2005. The modelling of the cubical slider with cylindrical projections was reported by Asai et al. [75], and Shigematsu *et al*., [29]. The modelling of the proposed dual-friction drive SAW motor is presented below and the notations used are as follows.

The Rayleigh wave propagating on the surface of a stator has both normal and tangential displacement components. The Rayleigh wave motion in normal direction of the bottom and top stator is given by

$$z_{st} = \hat{z}_{st} \cos(\omega t + kx) \tag{4.1}$$

The Rayleigh wave motion in tangential direction of the bottom and top stator is given by

$$x_{st} = \hat{x}_{st} \sin(\omega t + kx) \tag{4.2}$$

Where the angular frequency $\omega = 2\pi f$, the resonance frequency is f.

The composite Young's modulus E can be calculated from the Hertz contact theory,[73],

$$E = \left(\frac{E_{sl} E_{st}}{E_{sl}\left(1-\nu_{st}^2\right) + E_{st}\left(1-\nu_{sl}^2\right)} \right) \tag{4.3}$$

The coefficient of elasticity i.e. Young's modulus are E_{sl}, E_{st} and the Poisson's ratio are ν_{sl}, ν_{st} of the slider and stator respectively. The normal force acting on the slider can be calculated as,

$$F_n = 4/3\, ER^{1/2} h^{3/2} \tag{4.4}$$

Where $h = z_{sl} - z_{st}$, which decides whether the slider is making contact with wave or sliding. z_{st} is the normal position of the slider.

$$k_n = 4/3\, ER^{1/2} \tag{4.5}$$

According to Hertz contact theory, the normal direction force generated due to the application of Rayleigh wave and the application of preload from outside of the stator:

Normal direction force generated from bottom side stator

$$F_{n,B} = k_{n,B} h_B^{3/2} \tag{4.6}$$

Normal direction force generated from top side stator

$$F_{n,T} = k_{n,T} h_T^{3/2} \tag{4.7}$$

v: Poisson's ratio of the slider and the stator,

The radius of the slider remains same for both top and bottom portion of the slider

$$R_B = R_T = R \tag{4.8}$$

Hence the spring force will be the same in ideal case:

$$k_{n,B} = k_{n,T} = k_n \tag{4.9}$$

The crucial point is the contact conditions between the slider and the stator because the squeezed air film (c: air damping) disturbs the friction drive [90]. In high frequency operation, the effect of the squeezed film is significant due to the small vibration amplitude of displacement. For a friction drive with high frequency vibrations in the order of nano meters, a high contact pressure of 100 MPa is required [91]. The application of a sufficiently large contact pressure, i.e., a preload, would diminish the air film effect on the friction drive [30].

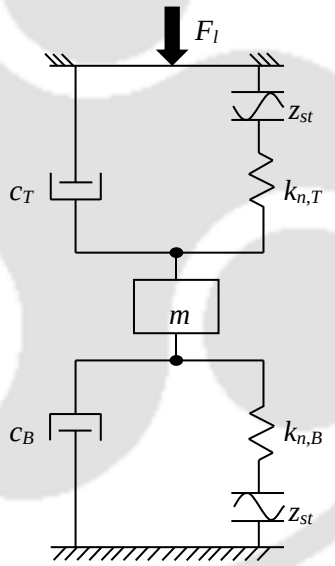

Figure 4. 4: Diagram for the normal force acting on a slider placed between two stators.

From Figure 4. 4 mass, spring and damping the velocity of the slider can be found out as,

$$m\ddot{z}_{sl} = \left(-F_l + F_{n,T} - F_{n,B} - c_T\,\dot{z}_{sl} - c_B\,\dot{z}_{sl}\right) \tag{4.10}$$

$$\ddot{z}_{sl} = \frac{1}{m}\left(-F_l + k_n h_T^{3/2} - k_n h_B^{3/2} - c_T\,\dot{z}_{sl} - c_B\,\dot{z}_{sl}\right) \tag{4.11}$$

The velocity of the slider can be given as [74], when in contact

$$\dot{z}_{sl} = \frac{1}{m}\int\left(-F_l + k_n\left(h_T^{3/2} - h_B^{3/2}\right) - \dot{z}_{sl}\left(c_T + c_B\right)\right)dt \tag{4.12}$$

The small displacement can be given as

$$h_B = \hat{z}_{st}\cos(\omega t) - z_{sl} \text{ and } h_T = \hat{z}_{st}\cos(\omega t) - z_{sl} \tag{4.13}$$

When not in contact

$$\dot{z}_{sl} = \frac{1}{m}\int\left(-F_l + c_T\,\dot{z}_{sl} - c_B\,\dot{z}_{sl}\right)dt \tag{4.14}$$

$$\dot{z}_{sl} = \frac{1}{m}\int\left(\dot{z}_{sl}\left(c_T - c_B\right) - F_l\right)dt \tag{4.15}$$

$$h_T = h_B = 0 \tag{4.16}$$

Preload F_L applied to the system from outside can be given by,

$$F_l = \bar{F}_n \tag{4.17}$$

$$F_l = \frac{1}{2\pi}\int_{-\pi}^{\pi} F_n\, d\omega t \tag{4.18}$$

$$F_l = \frac{1}{2\pi}\int_{-\pi}^{\pi}\left(F_{n,B} + F_{n,T}\right)d\omega t \tag{4.19}$$

$$F_l = \frac{k_n}{\pi}\int_0^{\theta}\left[\left(\hat{z}_{st}\cos(\omega t) - z_{sl}\right)^{3/2} + \left(\hat{z}_{st}\cos(\omega t) - z_{sl}\right)^{3/2}\right]d\omega t \tag{4.20}$$

$$F_l = \frac{2k_n}{\pi}\int_0^{\theta}\left[\left(\hat{z}_{st}\cos(\omega t) - z_{sl}\right)^{3/2}\right]d\omega t \tag{4.21}$$

The wave amplitude at the transition point of the release amplitude is $u_{zr.}$ The slider displacement at this transition point is z=-u_{zr}.

$$F_l = \frac{2k_n}{\pi}\int_0^{\pi}\left[\left(\hat{z}_{st,r}\cos(\omega\,\mathrm{t}) + \left(\hat{z}_{st,r}\right)^{3/2}\right)\right]d\omega t \tag{4.22}$$

$$\hat{z}_{st,r} = \left(\frac{3}{16}\frac{\pi F_l\sqrt{2}}{k_n}\right)^{2/3} \tag{4.23}$$

The minimum driving voltage or vibration amplitude for the slider in SAW motor seems to depend on the pre-load [92]. Some parameters need to be compromised such

as the high-speed and the large thrust for optimum pre-load condition [92]. At too high pre-load condition, a slider never moves anymore as it sticks with the stator [89]. In the case of the high pre-load, the stationary speed is low but the thrust is high but in the low pre-load condition, they are vice versa. Moderate pre-load condition should be investigated to pull out the performance in itself [92]. For motion in tangential direction

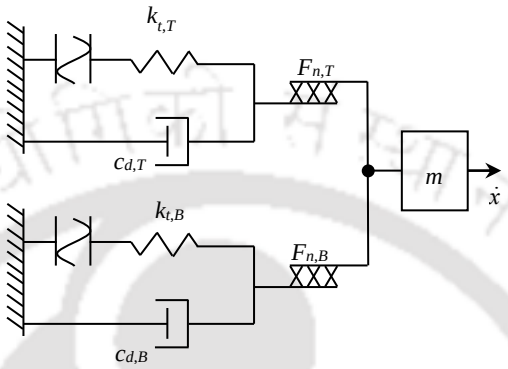

Figure 4. 5: Diagram for the tangential force acting on a slider placed between two stators.

$\dot{x}_{st}$ are the tangential wave vibration velocity from the bottom and top stator while $\dot{x}_{sl}$ is the velocity of the slider. The sliding velocity $v_{rb}$is $\dot{x}_{sb} - \dot{x}_{sl}$ and v_{rt} is $\dot{x}_{st} - \dot{x}_{sl}$.

Hence the tangential displacement of the slider can be given by,

$$\dot{x}_{sl} = \frac{1}{m}\int \left(F_{t,B} + F_{t,T}\right)dt \tag{4.24}$$

The tangential force applied from bottom stator is

$$F_{t,B} = \mu_d F_{n,B} sign(\dot{x}_{st} - \dot{x}_{sl}) \tag{4.25}$$

The tangential force applied from top stator is

$$F_{t,T} = \mu_d F_{n,T} sign(\dot{x}_{st} - \dot{x}_{sl}) \tag{4.26}$$

The tangential wave vibration velocity from top and bottom stator

$$\dot{x}_{st} = \hat{x}_{st}\omega\cos(\omega t) \tag{4.27}$$

4.1.2 Calculation of preload F_p for slider

The preload is calculated with an applied excitation of $A\sin(2\pi ft)$ and amplitude 'A' obtained for a$LiNbO_3$ surface particle with frequency 8.28 MHz.

Table 4. 1: Calculation of the preload depending on the amplitude of the propagating wave

No.	Volt.	X-Disp (nm)	Y-Disp(nm)	Total Disp (nm)	Fp (N) for 50 x 10^{-6}	Fp (N) for 100 x 10^{-6}	Fp (N) for 150 x 10^{-6}	Fp (N) for 200 x 10^{-6}	Fp (N) for 0.5 x 10^{-3}	Fp (N) for 1 x 10^{-3}
1	1	-0.03 to +0.03	-0.06 to +0.06	0.12	5.0205 x 10^{-7}	7.1001 x 10^{-7}	8.6958 x 10^{-7}	1.0041 x 10^{-6}	1.5876 x 10^{-6}	2.2452 x 10^{-6}
2	10	-0.3 to +0.3	-0.6 to +0.6	1.2	1.5876 x 10^{-5}	2.2452 x 10^{-5}	2.7499 x 10^{-5}	3.1753 x 10^{-5}	5.0205 x 10^{-5}	7.1001 x 10^{-5}
3	50	-5 to +5	-4.5 to +4.5	6	3.2609 x 10^{-4}	4.6116 x 10^{-4}	5.6481 x 10^{-4}	6.5219 x 10^{-4}	0.0010	0.0015
4	80	-6 to +6	-5.5 to +5.5	15	4.4062 x 10^{-4}	6.2313 x 10^{-4}	7.6318 x 10^{-4}	8.8124 x 10^{-4}	0.0014	0.0020
5	100	-6 to +6	-6 to +6	16	5.0205 x 10^{-4}	7.1001 x 10^{-4}	8.6958 x 10^{-4}	0.001	0.0016	0.0022
6	120	-7 to +7	-7 to +7	20	6.3266 x 10^{-4}	8.9471 x 10^{-4}	0.0011	0.0013	0.002	0.0028
7	150	-10 to +10	-12 to +12	24	0.0014	0.0020	0.0025	0.0028	0.0045	0.0064
8	180	-12 to +12	-15to +15	28	0.0020	0.0028	0.0034	0.0040	0.0063	0.0089
9	200	-15 to +15	-17 to +17	30	0.0024	0.0034	0.0041	0.0048	0.0076	0.0107

4.1.3 Design of the slider

The slider is normally made of silicon in cuboid shape [26] and has an array of projections on the contact surface. The contact condition is crucial as the squeezed air film at the stator-slider interface causes theproblem of sticky surfaces and disturbs the friction drive. Therefore an array of projections is usually fabricated on the slider surface [93]. In the proposed dual friction-drive, the slider is made of silicon with uniform array of projections on both the surfaces [94]. The projections on the two sides of the slider should have the identical pattern and the opposite projections should have a common axis. The cross-section of the projections can be circular, rectangular, etc. The density of the projections on a slider is such that it accommodates an integral number of projections per wavelength. Three-dimensional and cross-sectional views of a typical slider having projections on both surfaces are shown in Figure 4. 6. The projections form air flow channels at the contact surfaces and reduce damping due to air while the slider is in motion.

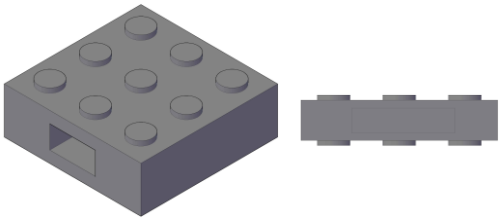

Figure 4. 6: Schematic of the slider having an array of projections on both contact surfaces.

4.2 Finite Element Simulation of the DFD SAW Motor

The finite element simulation of dual friction-drive SAW motor is carried out using COMSOL Multiphysics for different types of sliders. Initially, the 3D geometry of the device is created. The physics related to the structure is assigned and boundary conditions are provided.

4.2.1 Geometry of dual friction-drive SAW motor

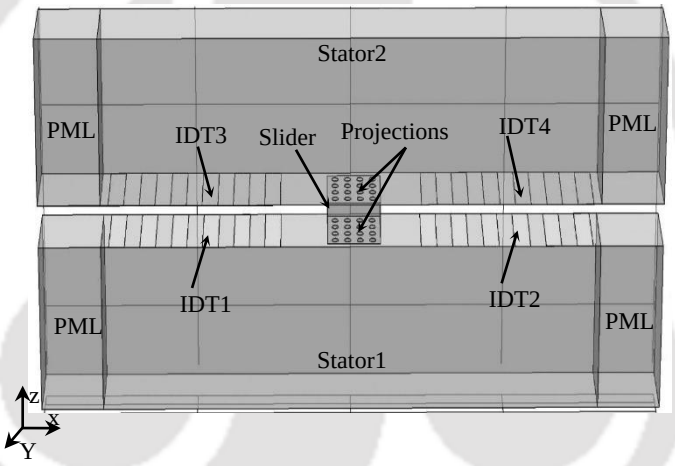

Figure 4. 7: Schematic of SAW motor structure created for simulation.

The geometry of the SAW motor consists of two identical stators facing each other and holding a cuboid slider as shown in Figure 4. 7. The IDTs of wavelength λ of 400 μm with 6 fingers each of width 100 μm (¼ λ) and thickness 0.2 μm and aperture 400 μm (1 λ) are placed on two sides of each stator. The stator of the SAW motor is made of IDTs on a substrate of width 400 μm (1 λ), length 4000 μm (10 λ) and thickness 800 μm (2 λ). The delay line having an active region of 3 λ is created to operate the slider. The device is terminated with perfect matching layers (PML) to avoid reflections at the edges. A cuboid slider of size 400 μm x 400 μm x 200 μm is placed in the active region. To avoid the problem of sticky surfaces, cylindrical projections of 40 μm diameter and 2 μm height with thecenter to centre distance of 80 μm are made on the surfaces of the slider in contact with the stators.

4.2.2 Assigning materials for the specified domains of the SAW motor model

A 128° Y-cut X-propagated lithium niobate, ($LiNbO_3$) is assigned as a piezoelectric material for the stator substrate. The properties of lithium niobate viz. elastic coefficients, coupling coefficients, relative permittivity, Young's modulus, Poisson's ratio and density are specified [6]. Aluminium (Al) is assigned to the IDTs due to its light weight and high conductivity. Silicon (Si) is assigned to the cuboid slider with projections as fabricating projections in Si is easy [7]. Table 4. 2 presents the list of parameters of the slider and stators used for simulating the device.

Table 4. 2: Parameters used in simulation

Parameters	Symbols	Value	Units
Young's modulus of slider	E_{sl}	215	GPa
Young's modulus of stator	E_{st}	173	GPa
Poisson's ratio of slider	v_{sl}	0.29	-
Poisson's ratio of stator	v_{st}	0.345	-
Preload	F_n	5	mN
Length of slider	ln	400	µm
Thickness of slider	wd	200	µm

4.2.3 Multiphysics settings

In subdomain settings, the stator is assigned as a piezoelectric element. The IDTs and slider are declared as linear elastic elements. The IDTs are assigned with electric elements to apply input power. The boundary settings in the FE simulation are as follows. The bottom part of the bottom stator is fixed while the sides of the top stator are fixed to facilitate application of preload from the top. The influence of wave reflections from boundaries can be reduced by assuming critical damping along the boundaries [64]. In order to avoid reflection of waves from the boundaries or edges of the SAW devices, the terminals are truncate as artificial absorbing boundaries known as perfect matching layers (PML). This can be achieved by employing suitable values for Rayleigh damping coefficients in the COMSOL Multiphysics software[88].The parameters are declared such as the mass proportional damping parameter (A_{dm} = 0), stiffness proportional damping parameter (B_{dk} = $1/\pi.f$) and damping ratio (ξ = 1).

In Rayleigh damping model, the Rayleigh damping matrix $\boldsymbol{Z}$ is a linear combination of mass matrix and stiffness matrix as given below

$$\xi = A_{dM} M + B_{dk} k \tag{4.28}$$

where the mass proportional damping parameter (A_{dM}) and stiffness proportional damping parameter (B_{dk}) are damping coefficients and they are related to damping ratio (ξ) as

$$\xi = \frac{A_{dM} + B_{dk}\omega^2}{2\omega} \tag{4.29}$$

The absorbing boundary can be achieved by assuming critical damping, ξ= 1 and A_{dm} = 0 then B_{dk} = $1/\pi.f$.

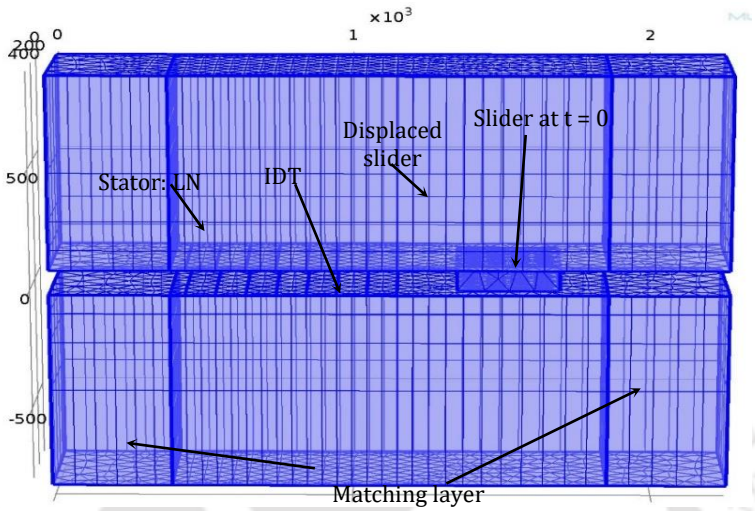

Figure 4. 8: Schematic of the meshed structure of the dual friction-drive SAW motor.

The slider and stator are defined as a contact pair with the stator as the master and the slider as the slave. Dynamic coefficient of friction is assigned at the contact surface between stator and slider. All boundaries of the slider are set free. The preload is applied on the top stator. The SAW motor structure consists of individual subsystems whose functions, in general, are known before the FE simulation. The basic units of the discretized subsystems are called finite elements which are properly distributed throughout the system [58]. To obtain the finite elements, an initially triangular meshing with a maximum element size of λ/8 and minimum element size of λ/32 [88], is adopted, followed by swept meshing for all the domains. The schematic of the SAW motor after meshing is represented in Figure 4. 8.

4.2.4 Results of simulation of dual friction-drive SAW motor

For excitation voltages below approximately 30 V, the SAW motor undergoes the dead zone where the slider does not move [95][49][92]. Hence the FE simulation is carried out with a sinusoidal voltage excitation of 100 V. The frequency of excitation is 8.37 MHz as found in Section 2.5. With the excitation applied to the IDTs on the same side of the two stators, Rayleigh SAW propagate in the forward horizontal direction in each stator. Since the stators are kept facing each other, the surface points of the bottom stator make anticlockwise elliptical motion whereas the surface points of the top stator make clockwise elliptical motion as represented in Figure 1.27 of Chapter 1 and verified by COMSOL simulation as

shown in Figure 4. 9. The displacement of the surface of the stator has components in both normal and tangential directions. The deflection of the stator in the normal direction given in Figure 4. 10 indicates the vibration amplitude of about 8 nm.

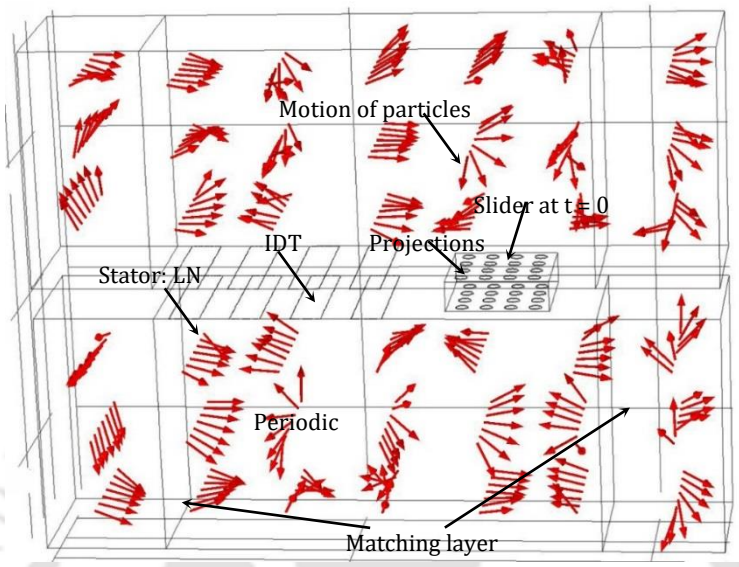

Figure 4. 9: COMSOL displacement arrow plot

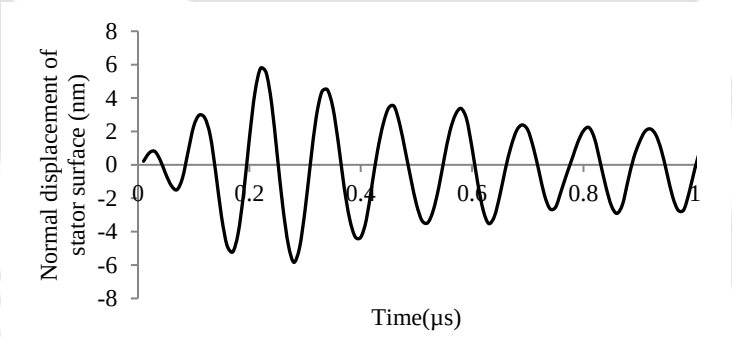

Figure 4. 10: Normal displacement of a particle on the stator.

An optimum pre-load of 2.8 mN is applied as discussed in Section 4.1.2 to generate adequate friction at the contact surfaces of the slider with the stators [96]. The operation of the SAW motor mainly depends on the condition of friction drive [81]. The friction drive condition at the projection of the slider and stator interface is subdivided into stick and slip zones [97], which change significantly as the rotor/slider speeds up [96]. According to the Hertz contact theory [73], the tangential force as shown in Figure 4. 13 (b) on the slider moves the slider in the direction opposite to the direction of wave propagation.

The maximum velocity the slider can achieve is equal to the maximum vibration velocity of the wave in the tangential direction i.e. at the crest of the wave [81]. When $\dot{X}_{st} > \dot{X}_{sl}$, the

frictional force and the slider velocity are in the same direction. Therefore, tangential force on the slider is positive, and the slider is accelerated to the *x* direction. Whereas if $\dot{x}_{st} < \dot{x}_{sl}$, the frictional force is negative for the slider because the frictional force direction is the reverse of the moving direction. Hence, the slider speed would be decreased. The rest of the time, the slider is not in contact with stator and no force acts on the slider.

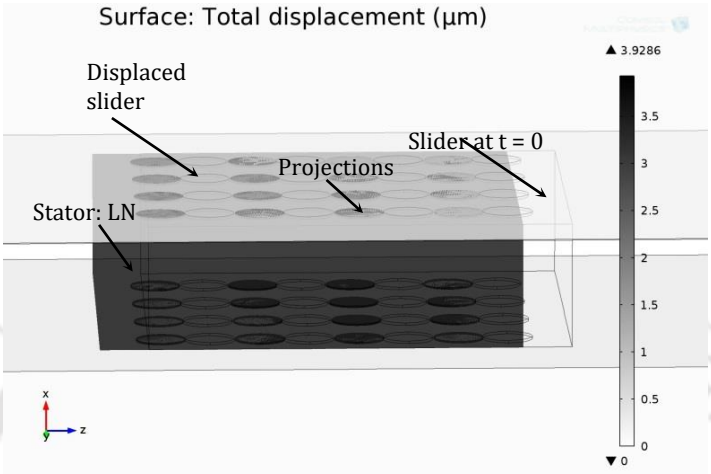

Figure 4. 11: Schematic of surface deformation profile of the dual friction-drive SAW motor showing the displacement of the slider between the stators.

The motion of the slider in normal direction due to the normal force generated from both the stators. Due to a sudden excitation of Rayleigh wave, initially the slider deforms and moves in a normal direction, but when a continuous excitation is provided then the motion changes to a smooth translational movement. The motion of the slider depends on the motion of the wave both in normal and tangential direction. Figure 4. 11 shows the surface profile of the SAW motor where the slider is displaced from its original position moved a distance of 5 nm at the end of 1 µs of applied excitation. At this point of time, the slider makes steady displacement in the normal direction. As the number of the wave passes under the slider in the normal direction the oscillation of the slider reduces and picks the inertia and converts all the energy to move in a translational direction. The displacement of the point of contact on the slider plotted in Figure 4. 12 shows the motion of the slider in steps each corresponding to a cycle of the Rayleigh wave. After the initial transients, the step size of about 4 nm is visible after 4 µs. The motion of the slider depends on the motion of the wave both in normal and tangential direction.

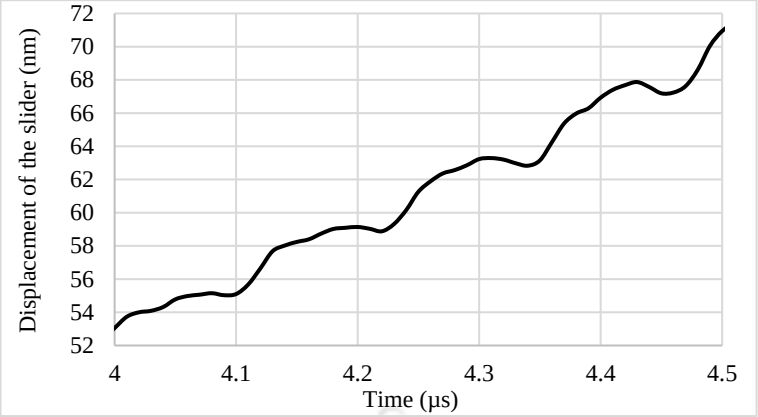

Figure 4. 12: Initial displacement of the slider in the horizontal direction of the SAW motor and the step motion of the slider produced per cycle of input is visible.

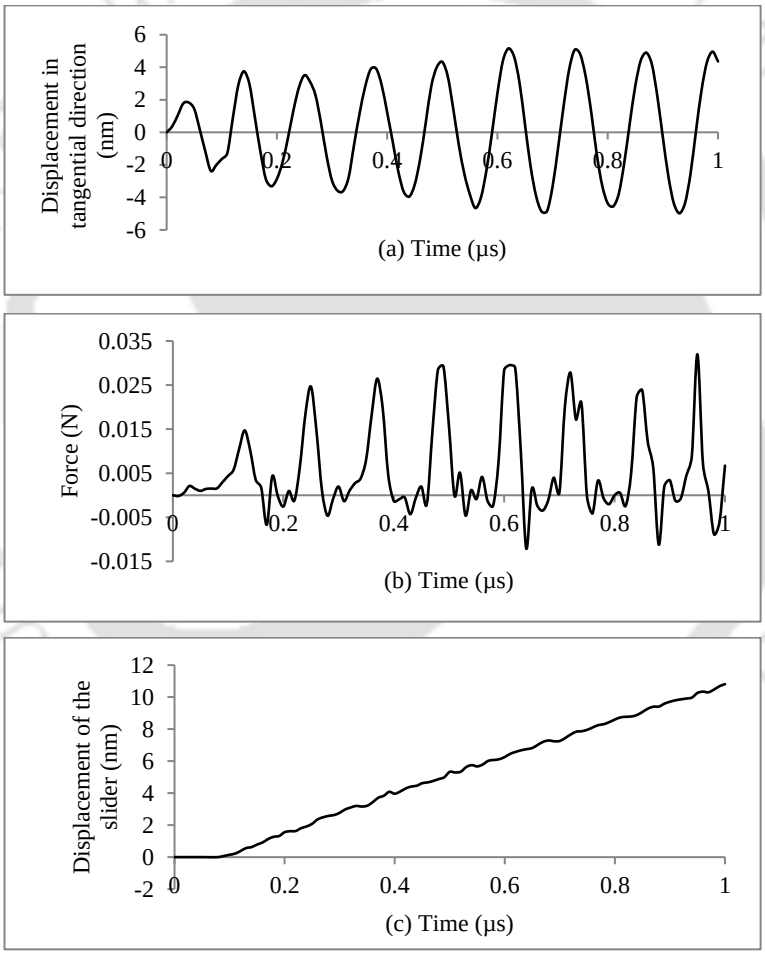

Figure 4. 13: (a) Tangential displacement of the stator surface, (b) Tangential force applied to the slider, (c) Tangential displacement of the slider.

When the slider moves on the surface of the stator, the pressure generated at the point of contact between slider and stator is given in Figure 4. 13. The figure shows an amount of 25 MPa of pressure generated which is validated through the mathematical modelling [95]. The

figure indicates that the low dense projection slider was working at higher contact pressure. The contact pressure depends on the number and size of the projections present on the surface of the slider [98].

The results of simulation for continuous sine wave excitation in Figure 4. 14 show the translational motion of the slider along the horizontal direction. Thus the slider is able to make a translational motion in both forward and reverse directions along the horizontal axis. When continues wave passes under the slider, the step motion of the slider picks to move at a constant speed of motion due to the inertia of motion. This movement of the slider is observed from the graph shown below.

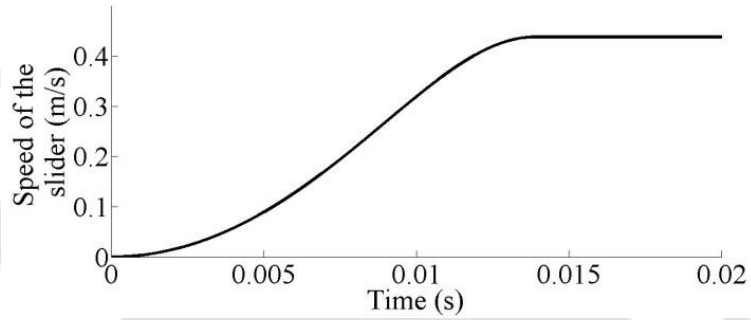

Figure 4. 14: Steady-state velocity of the slider at the end of 0.02 s.

In the case of the slider where it is tightly held with help of a guide rail reaches to the velocity of only 0.3 m/s but this sandwiched structure reaches to more than high velocity. The slider starts moving in a tangential direction with a velocity of 0.7 m/s in sandwich structured SAW motor. The velocity of the slider is achieved to 0.7 m/s with 100 μs.

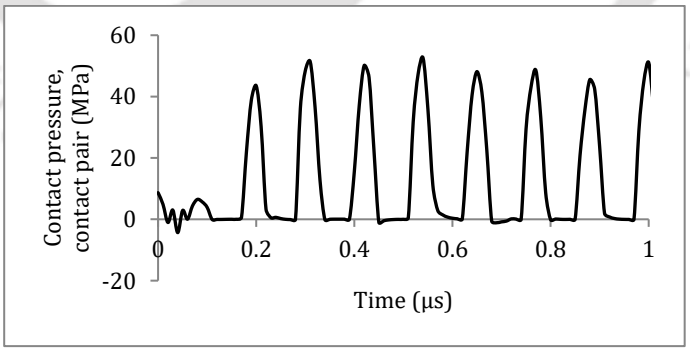

Figure 4. 15: Contact pressures generated due to the motion of the slider of the SAW motor.

The reaction moment in the tangential direction is achieved from the simulation and can be represented in the below figure. This tangential reaction helps the slider to move forward with small steps. The applied preload generates high frictional force on the slider at both the contact surfaces and the slider performs a translational motion in reverse of horizontal

direction. Similarly, if IDTs present on the other side is activated instead of present activated IDTs, the slider will perform a translational motion in the opposite direction i.e. in the +X direction. The contact pressure at the bottom side point of the slider in contact with stator is greater than the top side point of the slider to the stator. The Figure 4. 15 shows the simulated result of contact pressure of the top and bottom points of the slider in contact with the stator.

Due to the arrangement of sandwich SAW motor accomplish miniaturisation of these devices including weight and size reduction keeping the output efficiency unharmed through the combination of the linear motor package. It gets rid of the guide rail and lubrication by providing friction drive on both sides of the moving part. This invention has applications where a light weight and the efficient motor is required to move the elements such as lenses in the camera, mirrors in precision instruments.

The wavelength of the SAW motors is very short in nature, approximate to micrometres thence the driving frequency rises to MegaHertz range because of the miniaturisation of the stator. Because of which the frequency drive condition has to be tested at high frequency in MegaHertz range and the elastic vibration amplitude i.e. in nanometres. In this case, as the device goes to micro level in terms of size and operates with small amplitude i.e. around 12 nm and high frequency about 8.28 MHz, the effect of contact pressure due to air becomes significant. So it is expected that a high contact pressure between stator and slider is required for the friction drive. The motion of the slider upon the surface of the stator is both in the forward and backwards direction of the horizontal axis.

4.2.5 Comparison study of different voltage supply of excitation

Application of different amplitude of excitations results in better displacement of the slider. In this section study for simulation of the slider for two voltage supplies done. One with 100 V and other with 150 V excitation is applied to the IDTs of the stator. The parameters used for the work is given in

Table 4. 3, wherein voltage supply two different voltages are taken for the workis mentioned.

Table 4. 3: Parameters used for simulation

Parameter	Symbol	Value	Units
Frequency applied	f	8.282835	MHz
Preload	F_n	2.05	mN
Young's modulus slider	E_1	169	GPa
Young's modulus stator	E_2	172	GPa
Poisson's ratio slider	ν_1	0.3	

Poisson's ratio Stator	ν_2	0.345	
Radius of projection	R	20	µm
Voltage applied	V	100/125/150	V
Wavelength	λ	400	µm
Mass of the ball	m	0.4	µg
Static coefficient of friction	μ_s	0.45	
Dynamic coefficient of friction	μ_d	0.15	

The two different normal displacement of the particle motion on the surface of the stator for two different excitations is represented by Figure 4. 16. It shows the amplitude of the wave in the normal direction as 11 nm for 150 V and 7 nm for 100 V.

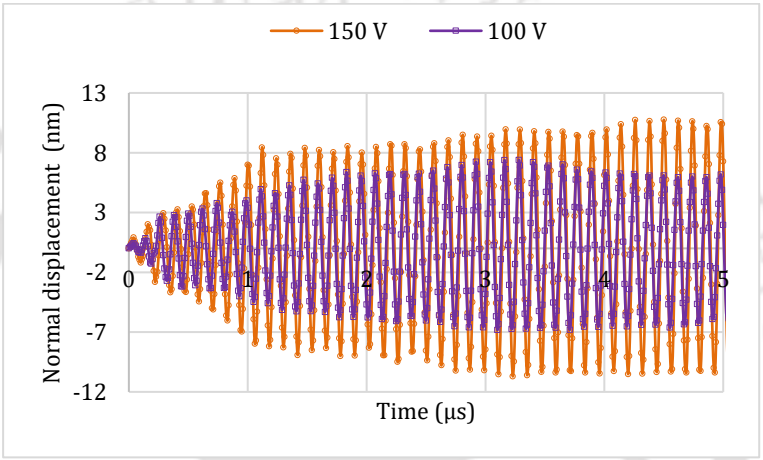

Figure 4. 16: Displacement of the particle present on the surface of the stator in the normal direction.

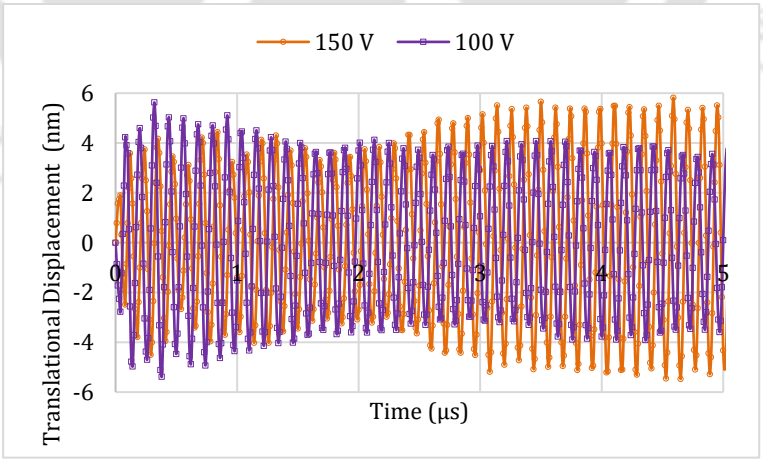

Figure 4. 17: Displacement of the particle present on the surface of the stator in the tangential direction.

The difference in the translational displacement of the particle motion on the surface of the stator for two different excitations is represented by Figure 3. 39. It shows the amplitude of

the wave in the translational direction as 6 nm for 150 V and 5 nm for 100 V. In Figure 4. 18, it shows the simulated result of displacement of the slider in the SAW motor after a time of 10 µs. Figure 4. 18 shows how the slider has moved a distance as compared to the position of the slider at time = 0. At this point of time, the displacement of the slider in normal direction gets stabilised. As the number of the wave passes under the slider in the normal direction the oscillation of the slider reduces and picks the inertia and converts all the energy to move in a translational direction. The normal direction displacement is shown in Figure 4. 19, where the slider moves upto 3 mm/s for 150 V and 2 mm/s for 100 V of the excitation at the initial phase.

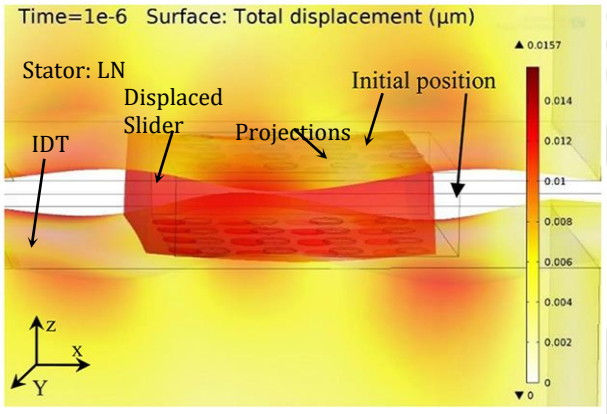

Figure 4. 18: Schematic of motion of the slider in SAW motor structure.

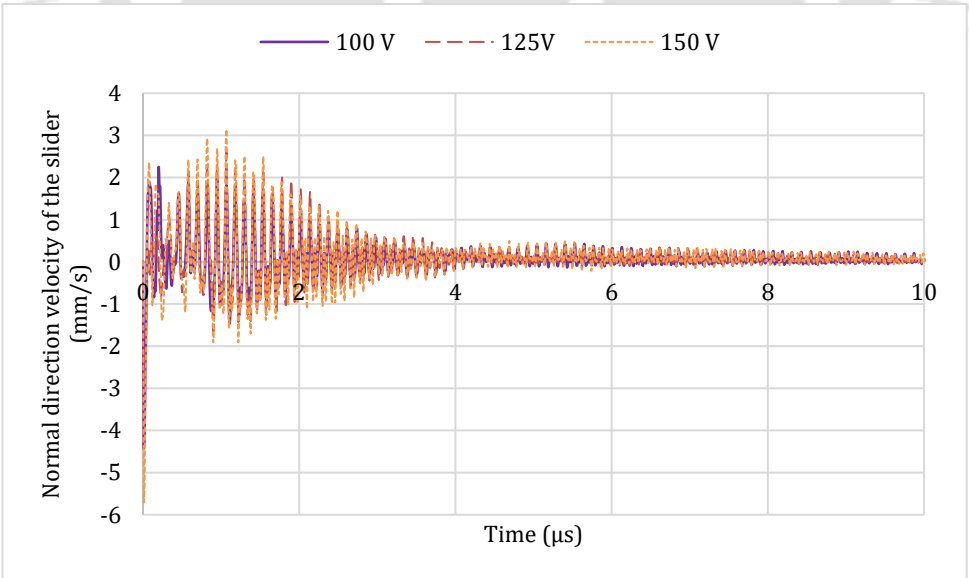

Figure 4. 19: Displacement of the slider of SAW motor in the normal direction.

The translational displacement of the slider observed about 350 nm and 150 nm for the excitation of 150 V and 100 V respectively for the motion for 10 µs as shown in Figure 4. 20. Upto 2 µs, the slider used to move at the almost same scale of displacement but as the time

progresses the difference in the displacement of the slider for both the amplitude of the excitation changes. In both cases, the slider moves proportionally to the cycle of the SAW.

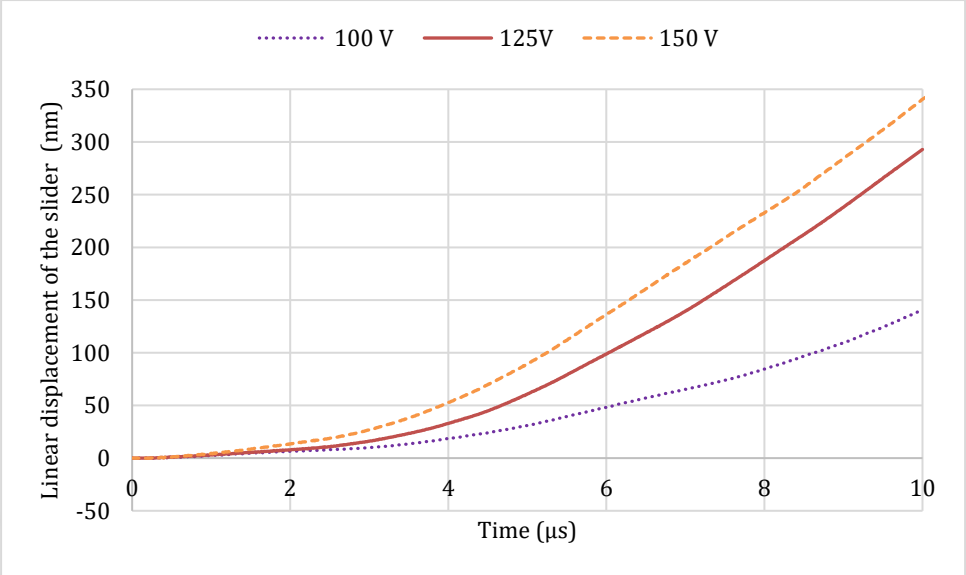

Figure 4. 20: Displacement of the slider of SAW motor in the tangential direction.

The velocity of the slider for a timed lap of 10 µs for both the excitations is carried out. It moves along with the passage of each cycle. So each cycle of the Rayleigh SAW contributes to moving the slider. As the slider is having cylindrical projections on the both sides of its contacting surfaces. Due to the friction of contact the slider used to get the force at the top and bottom stators to move with the wave. Each cycle of the SAW contributes to moving the slider in steps, Figure 4. 21 shows the enlarged plot for the motion of the slider. In the enlarged plot, it is clearly visible that the slider moves in steps.

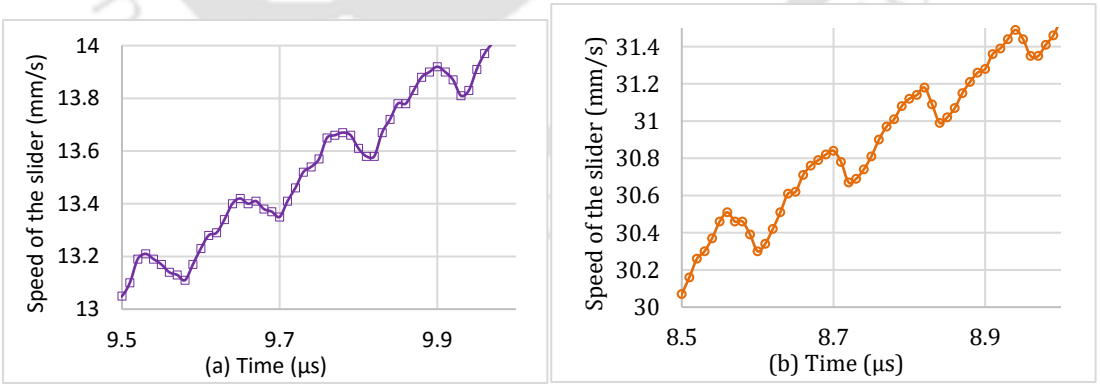

Figure 4. 21: Graph showing an enlarged version of motion of slider for (a) 100 V (b) 150 V.

Each step contributes an approximate of 0.2 mm/s to the slider to boost and move further in its path along with the propagation of the SAW. The plot gives an idea of motion of the body, as the wave passes under the slider, the particle puts pressure on it. The pressure on the slider is generated through the top point of the wave making anti-clockwise elliptical

motion and moves ahead. But when the wave is completely passed then due to the bottom point of the wave, it drags the slider back for which a small back step motion is occurring.

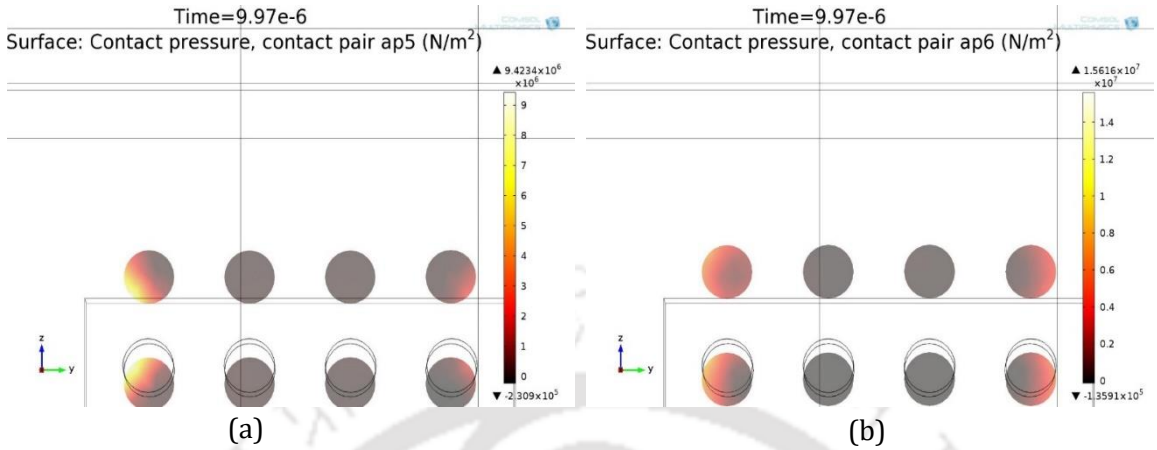

Figure 4. 22: Schematic showing contact pressure generated at (a) bottom and (b) top contacting point of the SAW motor.

Figure 4. 22 shows the simulated structure of the SAW motor for the contact pressure generated by the stator due to bottom and top projections of the slider.

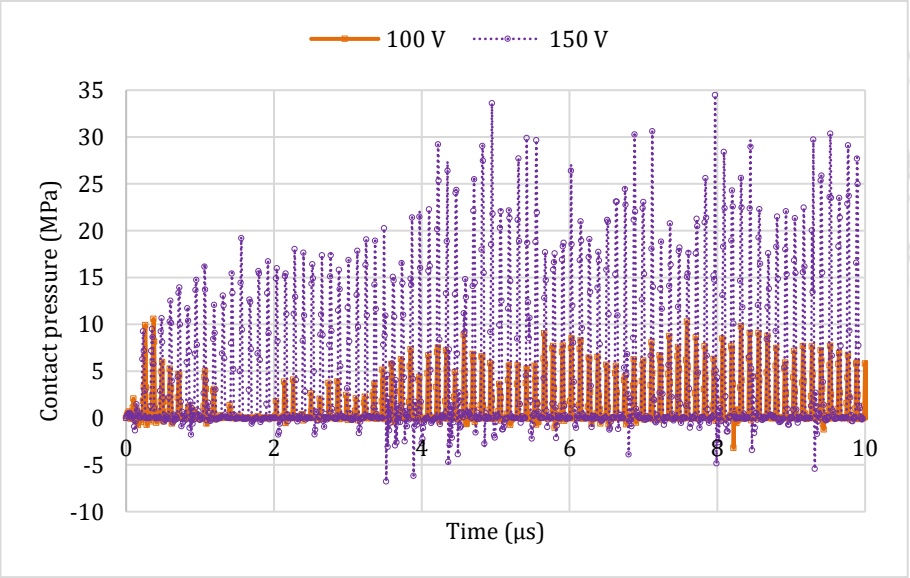

Figure 4. 23: Graph showing the contact pressure generated by contacting point of the SAW motor.

When slider moves on the surface of the stator due to provided excitations, the slider puts pressure on the stator. The figure shows that the points available at the ends sides carry much pressure as compared to the projections available inside. Contact pressure compares to the application of excitation is very clear, where with the application of 100 V, it generates a pressure of about 10 MPa as compared to 30 MPa in 150 V. The high amplitude

results in a high-pressure generation at the contacting point of the slider and stator. This shows that the high pressure is generated due to high contact, and the high contact means a high amount of force will be applied to the contacting projections, which makes high-speed motion as compared to the low excitation.

4.2.6 Comparison study of different shape of projections on the surface of the slider

This section deals with the comparison study of use of the different shape of projections on the surface of the slider. The FE simulation of the SAW motor in Figure 4. 24 (b) shows how the slider has moved a distance as compared to the position of the slider at time = 0 after a time of 1 µs. The translational displacement of the slider observed about 22 nm and 12 nm for square and cylindrical cross-sectional respectively for the excitation of 100 V in 1 µs as shown in Figure 4. 25.

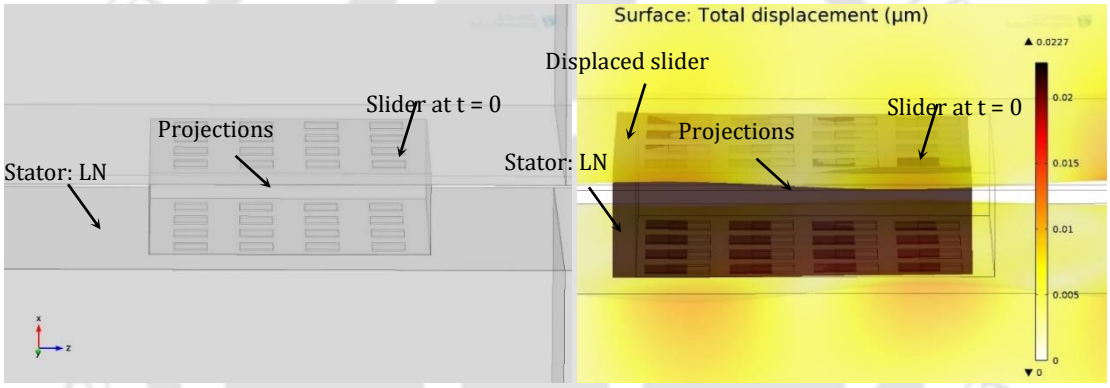

Figure 4. 24: Schematic of the slider (a) before FE simulation (b) after FE simulation of SAW motor.

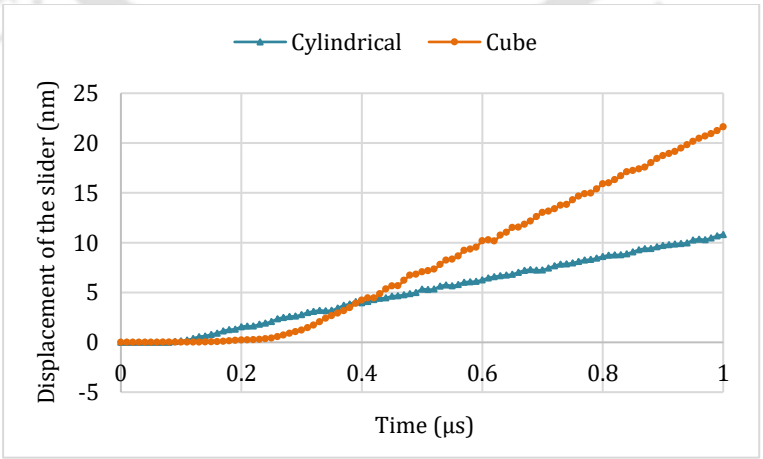

Figure 4. 25: Displacement of the slider of SAW motor in the tangential direction.

The initial phase of transition the slider having cylindrical projections, started making motion whereas the slider having square section projections starts with a less time but overtakes the other type of slider. The slider moves proportionally to the cycle of the Rayleigh wave.

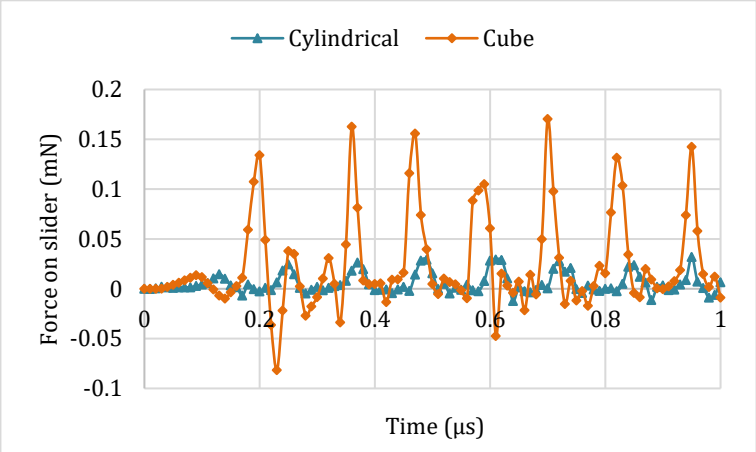

Figure 4. 26: Force generated on the slider of the SAW motor.

Figure 4. 26 shows Force generated on the slider with square sectional projection is higher than the slider with cylindrical section. In the case of the square the force generated on the slider from the wave is 0.16 mn whereas 0.04 for the cylindrical one.

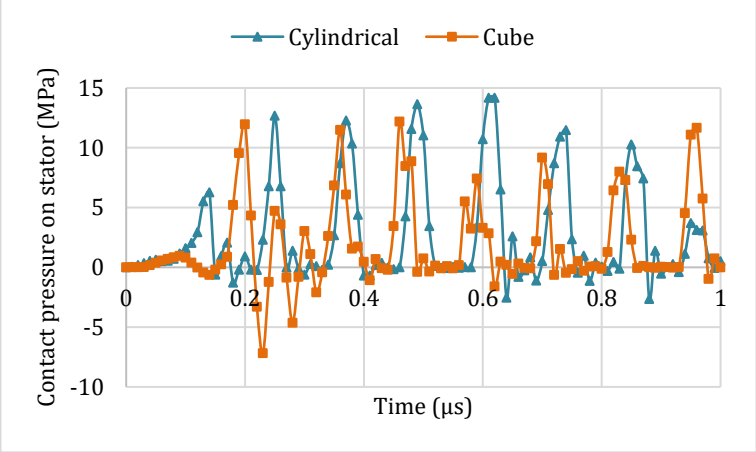

Figure 4. 27: Contact pressure generated at contacting point of the SAW motor.

Contact pressure compares to the different types of projections is not varying in terms of generated pressure of 14 MPa on the surface of the stator for a fixed amplitude of excitation of 100V. The amplitude of the excited wave results in a high-pressure generation at the contacting point of the slider and stator. This Figure 4. 28 shows that the high contact pressure is generated due to frictional contact in terms of geometrical representation.

Figure 4. 27 shows the plot for the generation of contact pressure, where the difference between the pressures is not high.

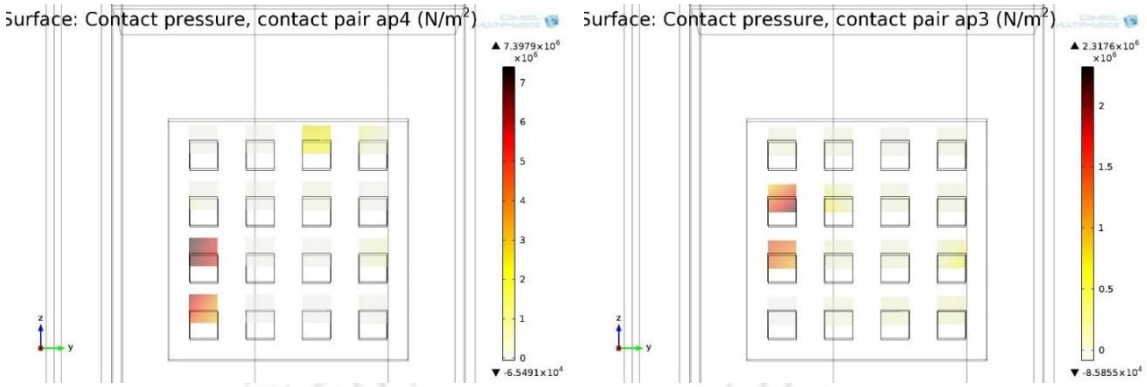

(a) (b)

Figure 4. 28: Schematic showing the contact pressure generated at (a) bottom and (b) top contacting point of the SAW motor.

4.2.7 Comparison based Projection excitation voltage of 100 V and no phase difference

A comparative study is carried out based on a number of projections while keeping the excitation amplitude fixed. The Figure 4. 29 shows the comparative study and represents the motion of the slider for a different number of the cylindrical projections.

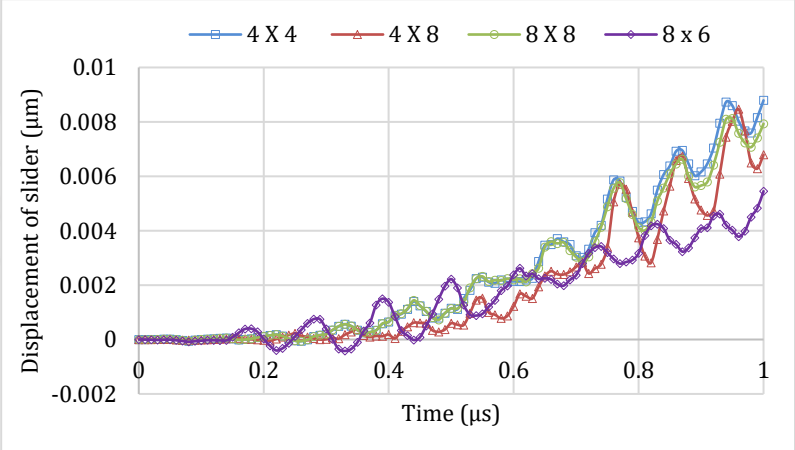

Figure 4. 29: Displacement of the slider at the point of contact.

The plot shows the motion of the slider for 4x4, 4x8, 8x8 and 8x6 number of projections. The efficient motion of the slider is achieved when the number of the projections is 4x4, *i.e.* the load provided for 4 projections and at cylindrical projections are fabricated at both sides contacting surfaces in 4x4 for length and breadth. Even upto the number of projections of 4x8 gives a matching result for the load applied for 4 projections. In the case of the 8x6 of projections, the motion of the slider is less in another way not efficient one when a load is applied for 8 projections.

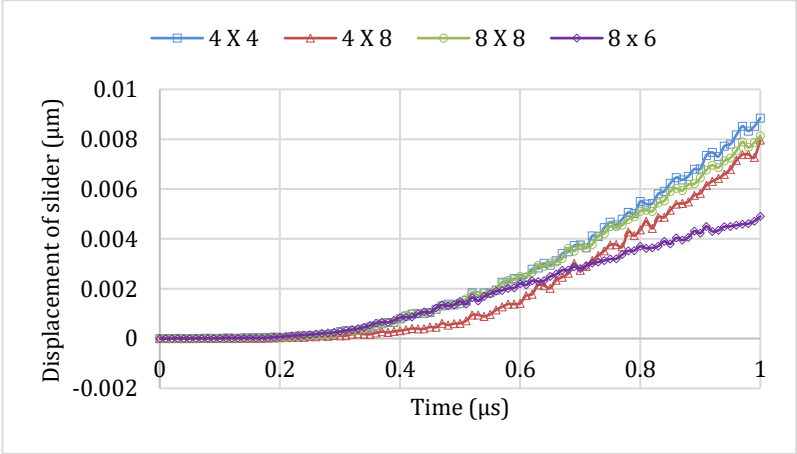

Figure 4. 30: Displacement of the slider at centre.

4.2.8 Comparison based on phase difference excitation voltage 100 V and 8 projections

A comparative study is carried out based on the application of excitation with the different phase difference while keeping the excitation amplitude fixed to 100 V and 8 projections. The Figure 4. 31 shows the comparative study and represents the motion of the slider for application of excitation with the phase difference.

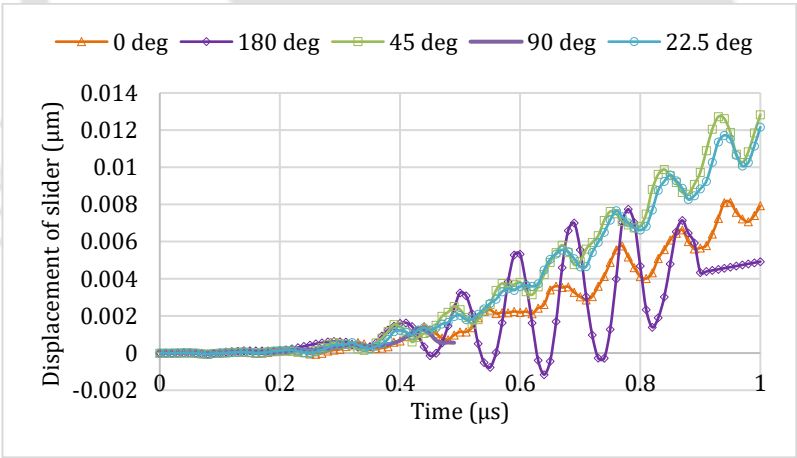

Figure 4. 31: Displacement of the slider at the point of contact.

The plot shows the motion of the slider for 0, 22.5, 45, 90, 180 degrees of phase difference. The efficient motion of the slider is achieved when the phase difference between topside and bottom side IDTs are in a 45-degree phase difference, while the number of the projections are 8, *i.e.* the load provided for 8 projections and at cylindrical projections are fabricated at both sides contacting surfaces in 8x8 for length and breadth. But when there is a phase difference of 180 degree between top and bottom IDTs, the motion of the slider is very less due to energy dissipation through high oscillation as shown in Figure 4. 31.

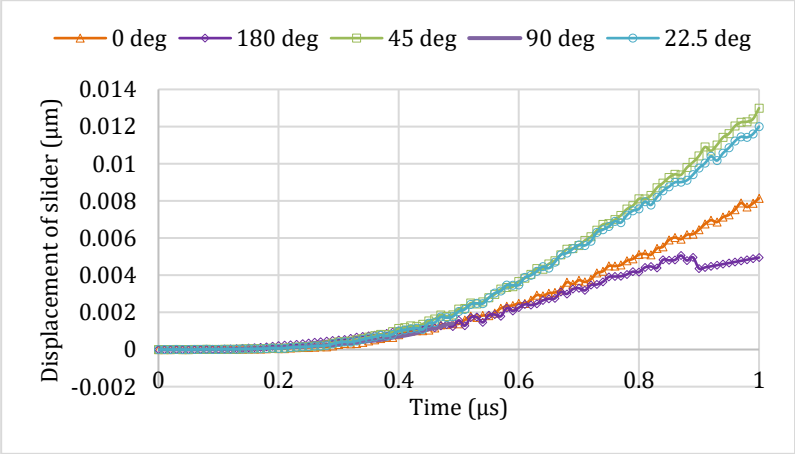

Figure 4. 32: Displacement of the slider at centre.

4.2.9 Comparison based on Voltage with 8 projections and no phase difference

A comparative study is carried out based on the application of excitation with different amplitudes while keeping the excitation phase fixed to with 8 projections. The Figure 4. 33 shows the comparative study and represents the motion of the slider for application of excitation with different amplitudes.

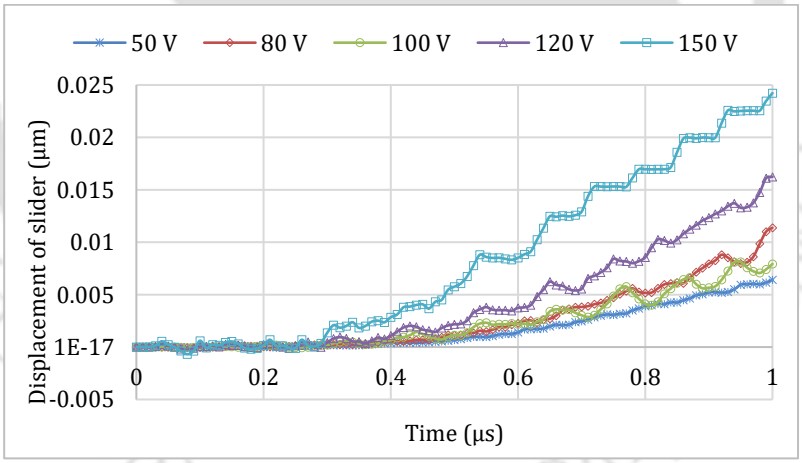

Figure 4. 33: Displacement of the slider at the point of contact.

The plot shows the motion of the slider for 50 V, 80 V, 100 V, 120 V, and 150 V of different amplitudes. At 150 V application, the slider moves faster as the height of the wave point is high which penetrates high amount of force on the slider, which helps to push the slider fast as compare to other amplitudes. The peak motion of the slider is achieved when the phase difference between topside and bottom side IDTs are fixed, while the no. of the projections are 8, *i.e.* the load provided for 8 number of cylindrical projections are fabricated at both side contacting surfaces in 8x8 for length and breadth as shown in Figure 4. 33.

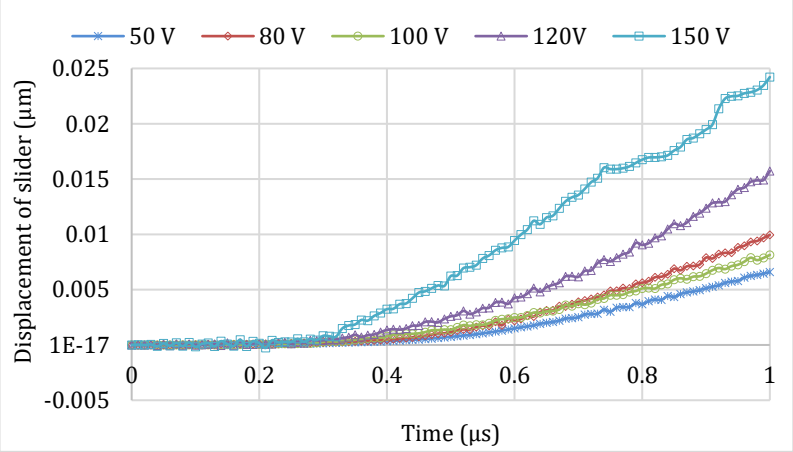

Figure 4. 34: Displacement of the slider at centre.

4.3 Different case studies done through simulation

1. IDTs on one side of the conventional motor, a cuboid slider is kept in straight at one end with absorption at IDT side to absorb the waves.
2. IDTs on one side of the DFD motor, a cuboid slider is kept in straight at one end side and absorption material kept at end of IDT side.
3. IDTs on one side of the conventional motor, a cuboid slider kept in inclined at one end with absorption at IDT side to absorb the waves.
4. IDTs on one side of the DFD motor, a cuboid slider kept in inclined at one end side and absorption material kept at end of IDT side.
5. IDTs on one side of the conventional motor, a cuboid slider with cylindrical projections in one side surface kept in straight at one end with absorption at IDT side to absorb the waves.
6. IDTs on one side of the DFD motor, a cuboid slider with cylindrical projections in two side surfaces slider kept in straight at one end side and absorption material kept at end of IDT side.
7. IDTs on one side of the conventional motor, a cuboid slider with cylindrical projections in one side surface slider kept in inclined at one end with absorption at IDT side to absorb the waves.
8. IDTs on one side of the DFD motor, a cuboid slider with cylindrical projections in two side surface slider kept in inclined at one end side and absorption material kept at end of IDT side.

4.3.1 Without any phase difference

1. IDTs on both side of the conventional motor, a cuboid slider kept in straight at middle without absorption at IDT side but a space of λ /8.

2. IDTs on both side of the DFD motor, a cuboid slider kept in straight at middle without absorption material kept at end of IDT side but a gap of λ /8 both side end.
3. IDTs on both side of the conventional motor, a cuboid slider kept in inclined at middle without absorption at IDTs but a space of Lamb/8 is left at the both side end of substrate.
4. IDTs on both side of the DFD motor, a cuboid slider kept in inclined at middle without absorption material kept at end of IDT side but a space of λ /8 is left at both side ends.
5. IDTs on both side of the conventional motor, a cuboid slider with cylindrical projections in one side surface kept in straight at middle of substrate without absorption at IDT side but a space of λ /8 is left at the end sides.
6. IDTs on both side of the DFD motor, a cuboid slider with cylindrical projections in two side surfaces slider kept in straight at middle without absorption material kept but a space of λ /8 is left at both side end.
7. IDTs on both side of the conventional motor, a cuboid slider with cylindrical projections in one side surface slider kept in inclined at middle without absorption at IDT side but a space of λ /8.
8. IDTs on both side of the DFD motor, a cuboid slider with cylindrical projections in two side surface slider kept in inclined at middle without absorption material kept at end of IDT side but a gap of λ /8 is provided.

4.3.2 With phase difference

1. IDTs on both side of the conventional motor, a cuboid slider kept in straight at middle without absorption at IDT side but a space of λ /8.
2. IDTs on both side of the DFD motor, a cuboid slider kept in straight at middle without absorption material kept at end of IDT side but a gap of λ /8 both side end.
3. IDTs on both side of the conventional motor, a cuboid slider kept in inclined at middle without absorption at IDT but a space of λ /8 is left at the both side end of substrate.
4. IDTs on both side of the DFD motor, a cuboid slider kept in inclined at middle without absorption material kept at end of IDT side but a space of λ /8 is left at both side end.
5. IDTs on both side of the conventional motor, a cuboid slider with cylindrical projections in one side surface kept in straight at middle of substrate without absorption at IDT side but a space of λ /8 is left at the end sides.
6. IDTs on both side of the DFD motor, a cuboid slider with cylindrical projections in two side surfaces slider kept in straight at middle without absorption material kept but a space of λ /8 is left at both side end.

7. IDTs on both side of the conventional motor, a cuboid slider with cylindrical projections in one side surface slider kept in inclined at middle without absorption at IDT side but a space of λ /8.
8. IDTs on both side of the DFD motor, a cuboid slider with cylindrical projections in two side surface slider kept in inclined at middle without absorption material kept at end of IDT side but a gap of λ /8 is provided.

4.3.3 Load given to one end with variations to the slider

1. IDTs on both side of the conventional motor, a cuboid slider kept in straight at middle without absorption at IDT side but a space of λ /8.
2. IDTs on both side of the DFD motor, a cuboid slider kept in straight at middle without absorption material kept at end of IDT side but a gap of λ /8 both side end.
3. IDTs on both side of the conventional motor, a cuboid slider kept in inclined at middle without absorption at IDTs but a space of λ /8 is left at the both side end of substrate.
4. IDTs on both side of the DFD motor, a cuboid slider kept in inclined at middle without absorption material kept at end of IDT side but a space of λ /8 is left at both side ends.
5. IDTs on both side of the conventional motor, a cuboid slider with cylindrical projections in one side surface kept in straight at middle of substrate without absorption at IDT side but a space of λ /8 is left at the end sides.
6. IDTs on both side of the DFD motor, a cuboid slider with cylindrical projections in two side surfaces slider kept in straight at middle without absorption material kept but a space of λ /8 is left at both side end.
7. IDTs on both side of the conventional motor, a cuboid slider with cylindrical projections in one side surface slider kept in inclined at middle without absorption at IDT side but a space of λ /8.
8. IDTs on both side of the DFD motor, a cuboid slider with cylindrical projections in two side surface slider kept in inclined at middle without absorption material kept at end of IDT side but a gap of λ /8 is provided.

Table 4. 4: Summary of case studies mentioned above

No.	Type of Case	Driving load	Distance covered	Velocity as per initial motion	Total displacement	Contact pressure
1	IDTs on one side of the conventional motor, a cuboid slider kept in straight at one end with adsorption at IDT	1 N	2.2 µm/50 µs (Slant)	0.14 m/s in 50 µs (Slant)	2.2 µm/50 µs (Slant)	1.5 (MPa) /40 µs (Slant)

	side.					
2	IDTs on one side of the DFD motor, a cuboid slider kept in straight at one end side and absorption material kept at end of IDT side. (No load)	1 N	Slider starts slanting, so two different point motion observed 0.55 µm/ 2.1 µs and 0.44 µm/ 2.1 µs	0.7 m/s in 2.1 µs	0.55 µm/ 2.1 µs and 0.44 µm/ 2.1 µs	18 (Mpa) /2 µs
2.1	IDTs on one side of the DFD motor, a cuboid slider kept in straight at one end side and absorption material kept at end of IDT side.	1 N	slanting 1.1 µm/2.5 µs and 0.9 µm/2.5 µs	1.1 m/s in 2.5 µs and 0.9 m/s in 2.5 µs	1.1 µm/ 2.5 µs and 0.9 µm/ 2.5 µs	3.6 (MPa) in 2.5 µs
2.2	IDTs on one side of the DFD motor, a cuboid slider kept in straight at one end side and absorption material kept at end of IDT side.	1 N	slanting 3.4 µm/ 3.5 µs and 3.2 µm/ 3.5 µs	1.8 m/s in 3.5 µs and 1.7 m/s in 3.5 µs	3.4 µm/ 3.5 µs and 3.2 µm/ 3.5 µs	1.5 (Pa) in 18 µs
3	IDTs on one side of the DFD motor, a cuboid slider kept in inclined at one end side and absorption material kept at end of IDT side.	1 N	No further slanting 1.9 µm/ 4.5 µs	1.2 m/s in 4.5 µs	1.9 µm / 4.5 µs	7.5 (MPa) in 4.2 µs
4	IDTs on both side of the conventional motor, a cuboid slider kept in straight at middle without absorption at IDT side but a space of λ/8. (Without Phase difference)	1 N	Slider is not moving in a particular direction rather it fluctuate to left and right of X-axis. 0.06 µm/ 5 µs to -0.12 µm/ 12.5 µs	0.25 m/s in 5 µs to -0.045 m/s in 12.5 µs	0.13 µm/ 12.5 µs	
5	IDTs on both side of the DFD motor, a cuboid slider kept in inclined at middle without absorption material kept at end of IDT side but a space of λ/8 is left at both side end. (Without phase difference)	1 N	5.5 µm/ 50 µs	0.14 m/s	5.5 µm/ 50 µs	2.6 (MPa) at 4 µs
6	IDTs on both side of the DFD motor, a cuboid slider with cylindrical projections in two side surfaces slider kept in	2 N	0.03 µm/ 3.7 µs	0.25 m/s at 2.0 µs	0.03 µm/ 3.7 µs	24 (MPa) at 3.4 µs

	straight at middle without absorption material kept but a space of λ/8 is left at both side end.(With K phase difference)					
7	Cuboid slider with load is kept in between sandwich structure of stator which having λ/8 gap at both side end	1 N	14 µm / 26 µs	1 m/s at 12 µs	14 µm / 26 µs	10 (MPa) at 26 µs
7.1	Cuboid slider with load is kept in between sandwich structure of stators which having λ/8 gap at both side end.	2 N	15 µm/ 28.2 µs	1 m/s at 12 µs	15 µm/ 28.2 µs	30 (MPa) at 28 µs

4.4 Comparison between conventional and DFD SAW motor

A comparative study is carried out between the conventional SAW motor and the DFD SAW motor with an application same excitation voltage while keeping the excitation phase fixed to with 8 projections.

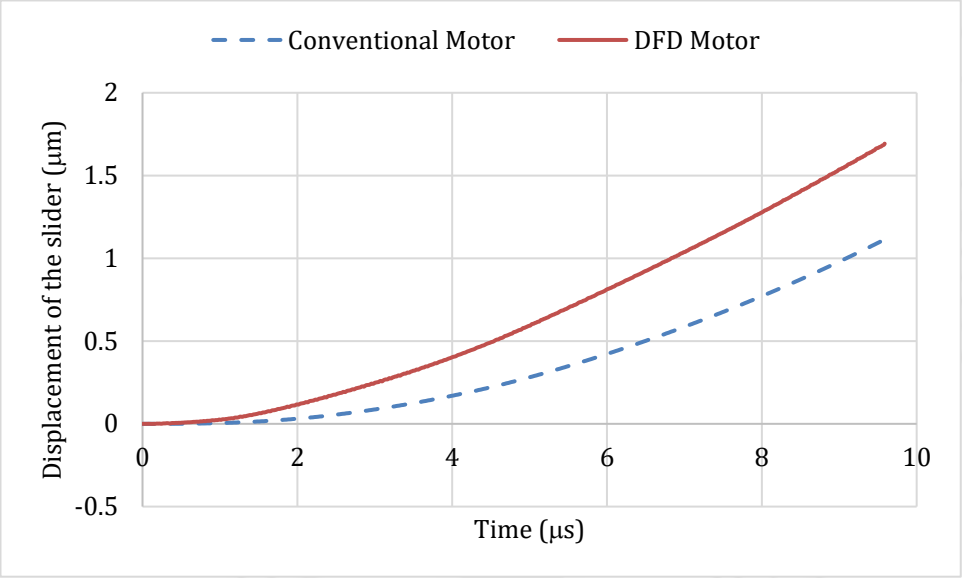

Figure 4. 35: Comparison of motion of the slider between conventional and DWD SAW motor.

The Figure 4. 35 shows the comparative study and represents the motion of the slider for application of excitation. It gives a clear picture that the DFD motor makes a quicker motion of 1.69 µm at the end of 9.58µs as compared to the conventional SAW motor which makes 1.11 µm at the end of 9.58 µs. The DFD motor moves an additional 0.58 µm distance as compared to the conventional motor with equal excitation voltage and same time duration.

4.5 Dual Friction-drive SAW Motor with Flat Plane Slider

A sandwich structure SAW motor can be made using a flat plane slider[99] as shown in Figure 4. 36. The arrangement of the DFD SAW motor is done as like previous section motor. In this type of motor, the material of stator changes from Single crystal lithium niobate $LiNbO_3$ to chemically reduced $LiNbO_3$. Due to thelarge piezoelectric coefficient, the single crystal lithium niobate is used widely for developing surface acoustic wave (SAW) devices. Low electric conductivity, which is on the order of 10−15 $(\Omega.cm)^{-1}$[100], coupled with the intrinsic pyroelectricity of lithium niobate generates pyroelectric surface charges with temperature changes. The surface charging effect causes contact electrification when lithium niobate is used as a contacting material. The surface charging and due to this sparking occurs which may damage electrodes and crack the crystals during device production processes [101].

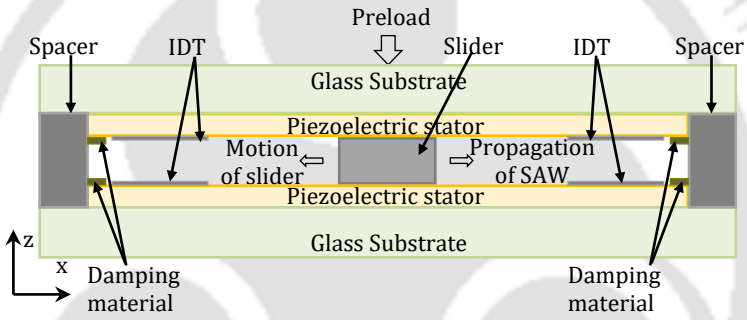

Figure 4. 36: Schematic of DFD SAW motor with the flat plane slider.

Table 4. 5: Parameters taken for simulation of the device

Parameter	symbol	value	Units
Frequency applied	f	8.28e6	[Hz]
Preload	F_n	2.63e-3	[N]
Young's modulus slider	E_1	1.69e11	[Pa]
Young's modulus stator	E_2	1.72e11	[Pa]
Poisson's ratio slider	ν_1	0.3	
Poisson's ratio Stator	ν_2	0.345	
Voltage applied	V	150	[V]
Wave length	λ	400e-6	[m]
length	ln	340e-6	[m]
width	wd	20e-6	[m]
Mass of the slider	m	0.4e-6	[kg]
Static coefficient of friction	μ_s	0.45	
Dynamic coefficient of friction	μ_d	0.15	

The surface charging is predicted to increase water adsorption on the surface in an atmospheric environment due to the diffuse electric double layer effect [16]; the film

thickness of water on lithium niobate increases with relative humidity up to more than 15 nm [17]. The wetting water produces capillary condensation around surface sites such as cracks and pores or asperity contact sites when contacting rough surfaces [102]. The adhesion force between slider and stator at contacting surfaces increases the relative static coefficient of friction [103].The surface charging effect can be reduced by increasing of electric conductivity while keeping SAW propagation characteristics unchanged [14]. Hence, the post-growth chemical reduction method for lithium niobate is studied [14], [20], because the electric conductivity of dielectric crystals increases when they are reduced [20]. Contact electrification is considered to be the cause of sticking phenomenon in the SAW motor in the present study [21], [22]. The use of chemically reduced lithium niobate, hence, would eliminate the undesirable sticking phenomenon through reduced surface charging and enhance the stability of the SAW motor.

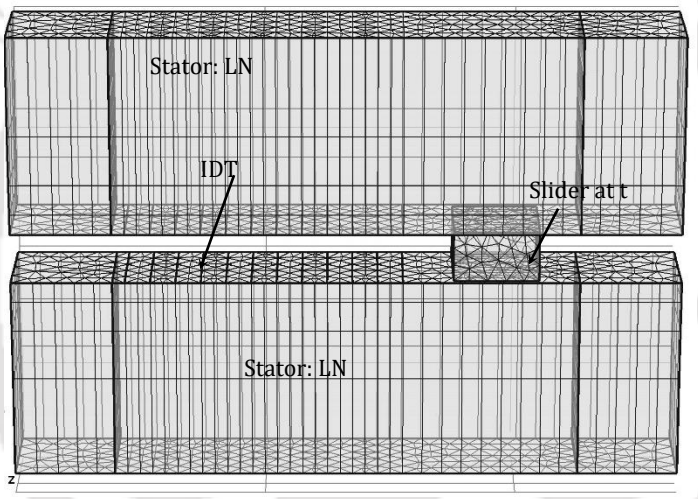

Figure 4. 37: Schematic model of the of DFD SAW motor in COMSOL Multiphysics after meshed.

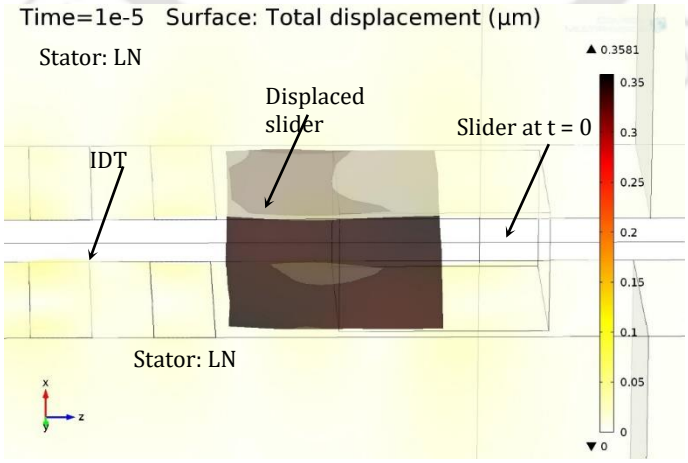

Figure 4. 38: Simulated surface profile of the DFD SAW linear motor showing the motion of the flat plane cuboid slider.

The SAW motor needs threshold voltage; that is, it expands its dead zone, in a humid environment, which is probably due to the increase of meniscus force and the resulting static frictional force. Because the adsorbed water film thickness increases with the surface charge [16], reducing the surface charge would diminish the film thickness and the meniscus force.

Thus, it could be expected that the use of chemically reduced lithium niobate would reduce the expansion of the dead zone and make the SAW motor less sensitive to humidity. The Figure 4. 37 shows the Schematic model of the of DFD SAW motor in COMSOL Multiphysics after meshing is carried out for the simulation. The surface profile of the displaced slider is shown in Figure 4. 38. The displacement amplitude of the point on stator is7 nm in the normal direction and 7 nm in translational directions.

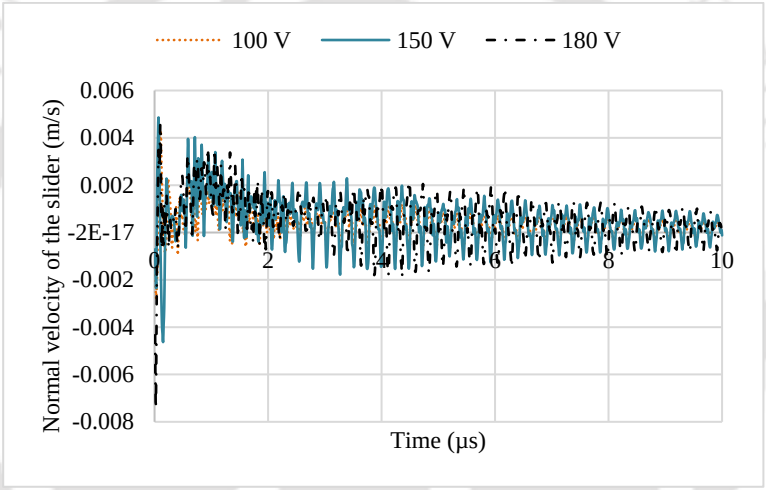

Figure 4. 39: Normal displacements of the slider of simulated SAW motor.

Figure 4. 39 shows normal displacement of slider indicating the highest oscillation at the initial phase of excitation.

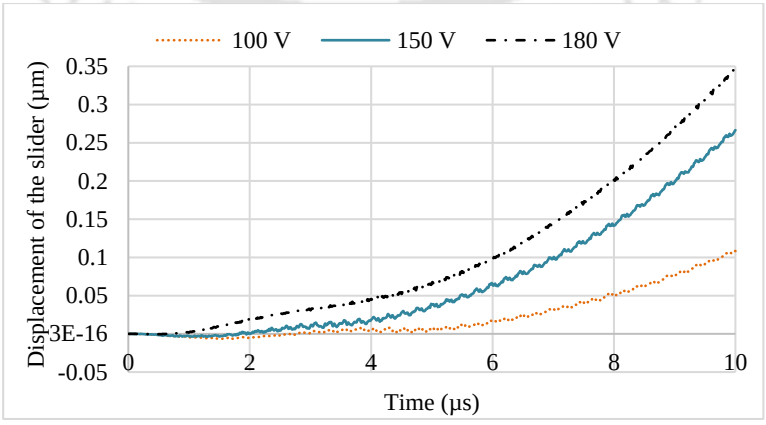

Figure 4. 40: Translational displacement of slider of simulated SAW motor.

The motion of the slider is stabilised in the normal direction and moves in the translational direction. The translational displacement of the slider in the SAW motor is simulated for three different voltage signals as shown in Figure 4. 40. It is found that the slider achieves a distance of 0.105 µm with the application of 100 V at the end of 10 µs. While 0.267 µm and 0.35 µm are achieved at the end of 10 µs for the same slider with the application of 150 V and 180 V respectively.

The contact pressure on the surface of the stator in the SAW motor is simulated for three different voltage signals as shown in Figure 4. 41. It is found that the contact pressure of 10 MPa, 20 MPa, and 25 Mpaon the surface of the stator is measured with the application of 100 V, 150 V, and 180 V respectively.

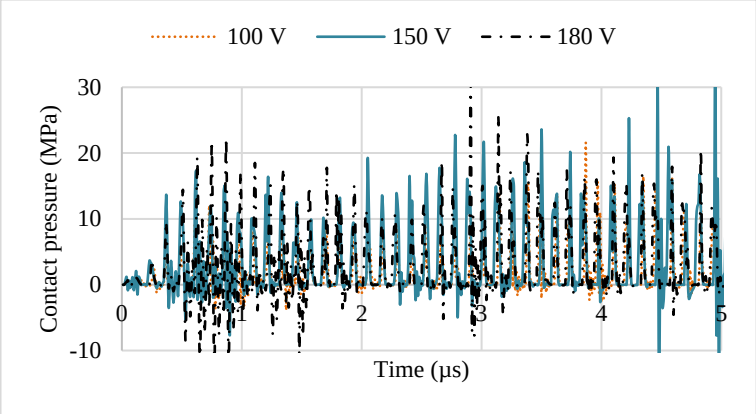

Figure 4. 41: Contact pressure of simulated SAW motor.

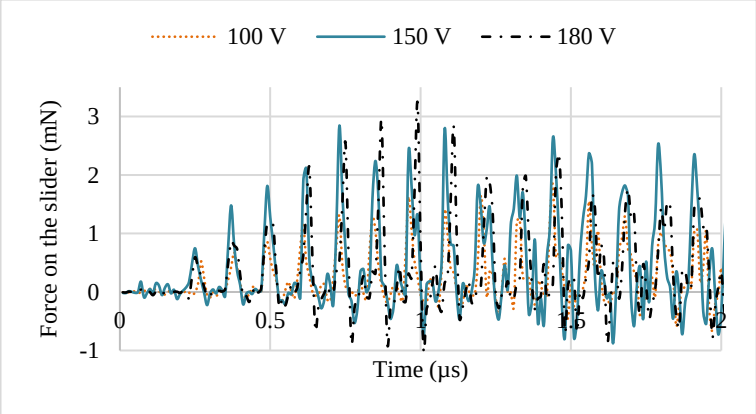

Figure 4. 42: Force applied on the slider of simulated SAW motor.

The force on the contacting surface of the slider is simulated for the SAW motor for three different voltage signals as shown in Figure 4. 42. This simulation is carried out without any phase difference of the applied excitation to the top and bottom stator with a Voltage supply of 100 V, 150 V, and 180 V.

4.5.1 Comparative study of different shape of sliders

The comparison among normal motions of 3 types of the slider is represented in Figure 4. 43 of the SAW motor made. From the plot for normal displacement of the slider, it shows all are achieving their stabilisation condition after the slider is run for some time.

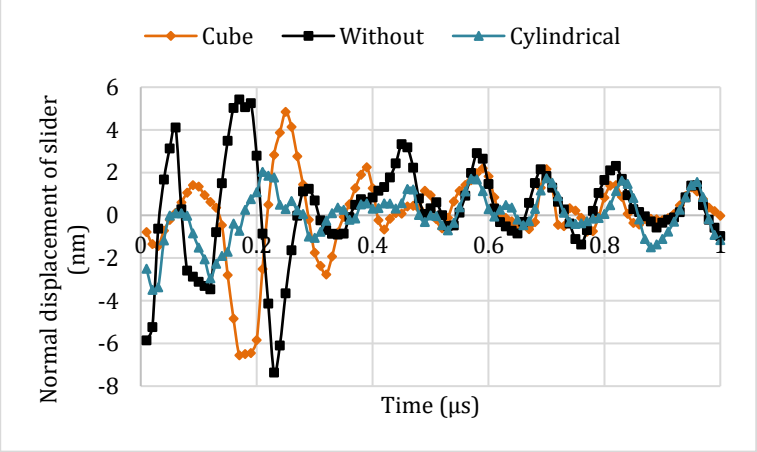

Figure 4. 43: Normal direction displacement of the slider.

The force generated on the various types of the slider through the stator is shown in Figure 4. 44. The plot shows that the slider having no projections gets the high force of about 0.25 mN to be driven by the wave. The slider having cylindrical projections gets a force of 0.05 mN, which very less as compare to other two types of the slider.

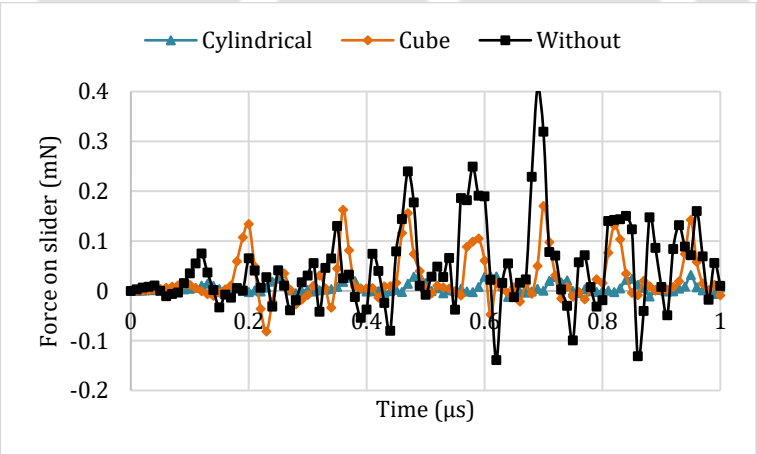

Figure 4. 44: Force acting on the slider due to Rayleigh wave propagation on the surface of the stator.

The translational displacement of the slider observed about 25 nm, 22 nm and 11 nm for projection, square and cylindrical cross-sectional projections respectively for the excitation of 100 V in 1 μs as shown in Figure 4. 45. The initial phase of transition the slider having cylindrical and no projections started making motion whereas the slider having square

section projections starts with a less time but overtakes the cylindrical type projection of slider. In all the cases the slider moves proportionally to the cycle of the Rayleigh wave.

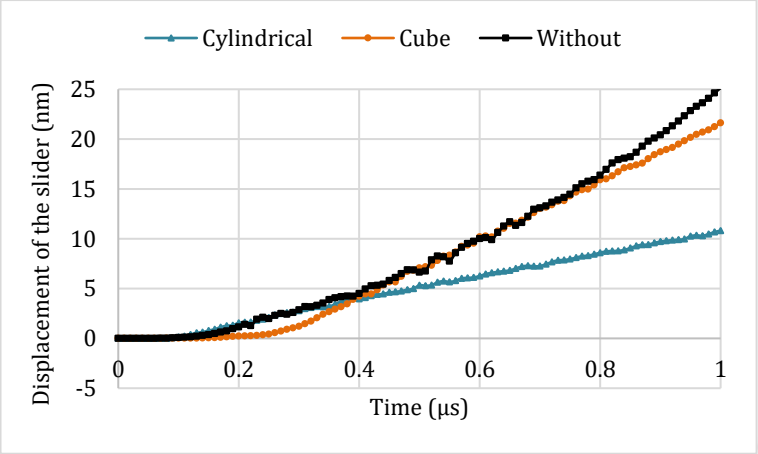

Figure 4. 45: The translational motion of slider.

Comparison plot for contact pressure is showing that the slider having no projections generate less pressure as compare to other two as shown in Figure 4. 46. The slider with cylindrical and square projections generate almost equivalent contact pressure on the stator.

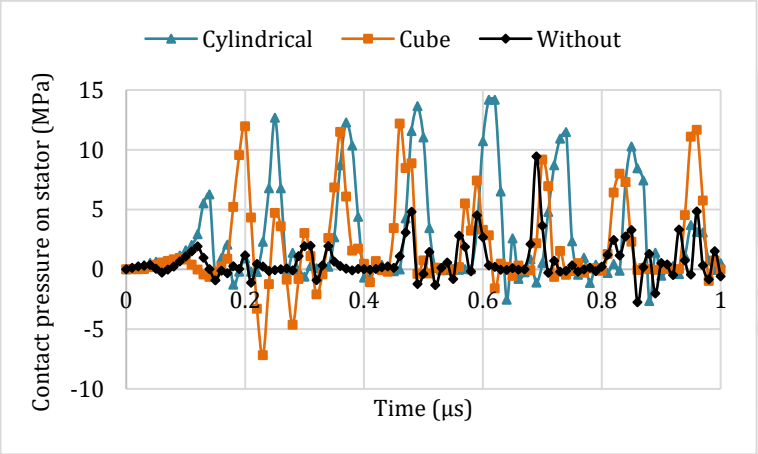

Figure 4. 46: Contact pressure between slider and stator at contacting interface.

Compare to the application of excitation is very clear, where it generates a pressure of about 12 MPa in both cylindrical and square whereas 5 MPa in the case of the slider having no projections. The high amplitude results in a high-pressure generation at the contacting point of the slider and stator. This shows that the high pressure is generated due to high contact, and the high contact means a high amount of force will be applied to the contacting projections, which makes high-speed motion as compared to the low excitation.

4.6 Control of SAW motor

The Figure 4. 47 shows the schematic circuit diagram to activate the IDTs for achieving motion of the slider of the SAW motor.

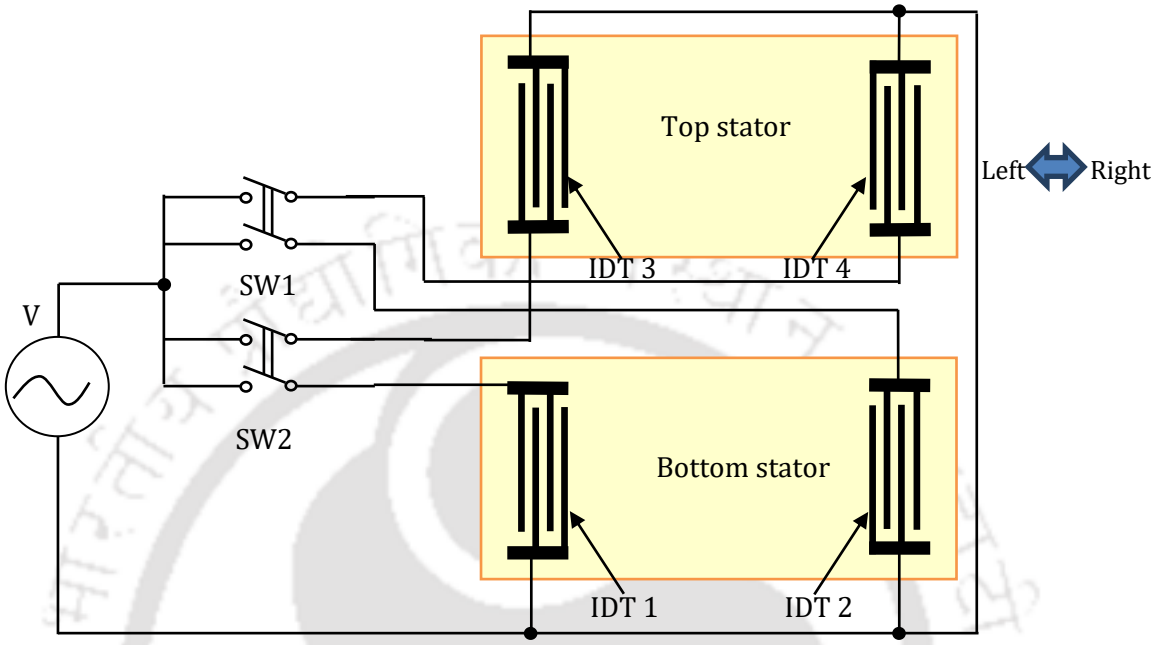

Figure 4. 47: Control circuit for DFD SAW motor in a single axis.

The SW1 is the combination of activation of IDT 2 and IDT 4, which results in the translational motion of shaft towards right side direction or towards these two IDTs. The SW2 is the combination of activation of IDT 1 and IDT 3, which results in the translational motion of shaft towards left side direction or towards these two IDTs.

The Figure 4. 48 shows the schematic circuit diagram to activate respective IDTs for achieving different types of motion of the slider of the SAW motor. The SW1 is the combination of activation of IDT 1 and IDT 5, which results in the translational motion of shaft towards left direction or towards these two IDTs. The SW2 is the combination of activation of IDT 2 and IDT 6, which results in the translational motion of shaft towards right direction or towards these two IDTs. The SW3 is the combination of activation of IDT 4 and IDT 7, which results in the translational motion of shaft towards back direction or towards these two IDTs. The SW4 is the combination of activation of IDT 3 and IDT 8, which results in the translational motion of shaft towards front direction or towards these two IDTs.

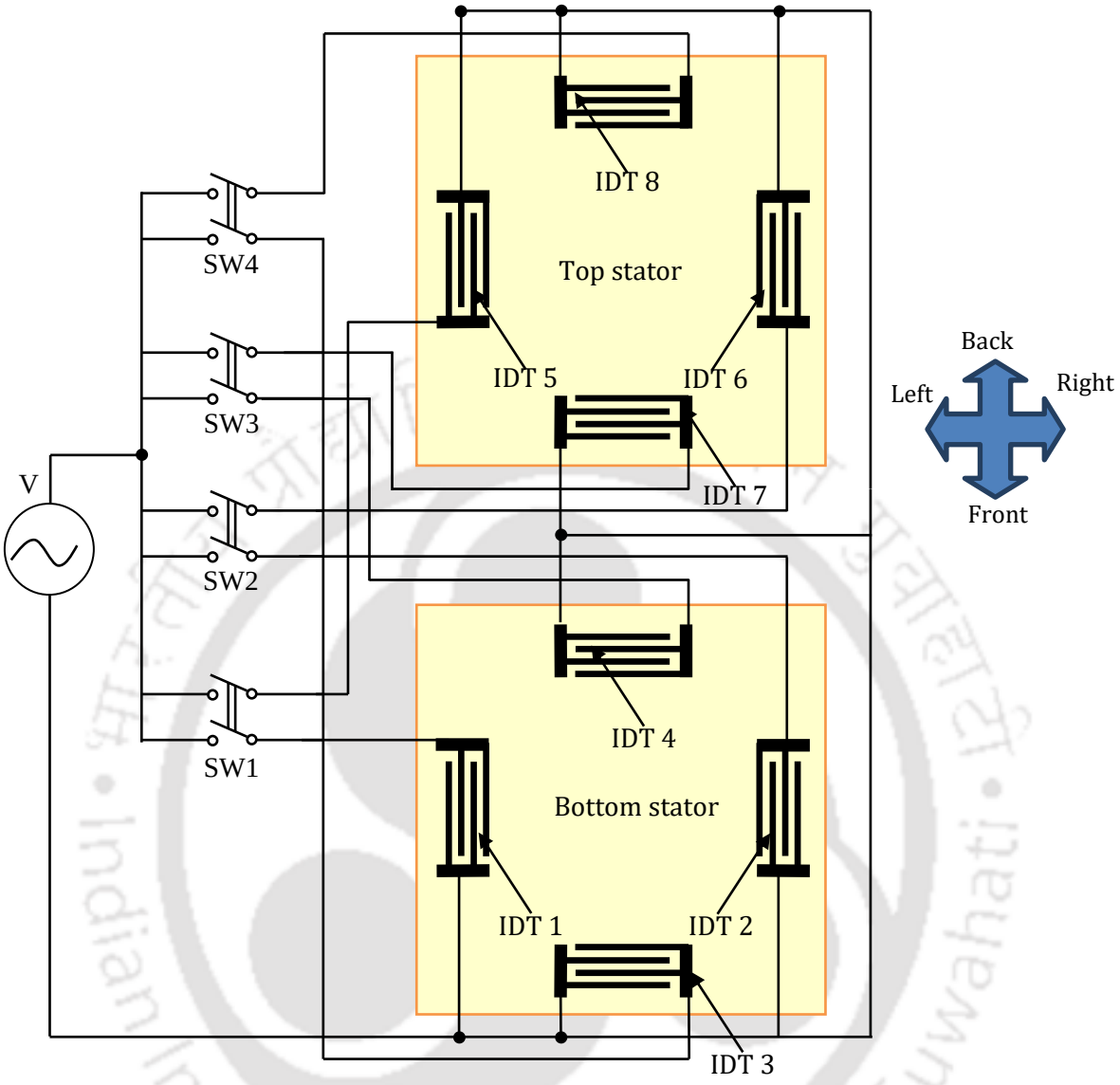

Figure 4. 48: Control circuit for DFD SAW motor in dual axis freedom.

4.6.1 Simultaneous translational motion in X and Z directions

In the saw motor device, by applying alternate excitations in a time-multiplexing way repeatedly, simultaneous motion in X and Z directions is achieved.

4.7 Summary

This chapter dealt with a dual friction-drive SAW motor using a cuboid slider. The modelling of the contact mechanics between a flat plane stator and a cuboid slider is carried out to get the parameters such as contact pressure, required preload and motion of the shaft. The proposed DFD SAW motor is analysed with the help of finite element simulation using COMSOL Multiphysics for the translational motion. For the FE simulation, the

coefficient of friction for the motor is taken as 0.45 from literature with experimental results. Simultaneously the preload plays a distinguished role to decide the friction force between stator and slider and taking different preload weights, it is found to be 5 mN. In FE simulation, various aspects are discussed like domain settings, boundary settings, material constants and finally the time domain analysis. The DFD SAW motor with the cuboid slider can make a translational motion at a low amplitude of 12 nm and high frequency of 8.28 MHz Rayleigh wave. It is concluded that a balanced condition of both frictional force and preload is necessary with respect to the deformation of the wave for the smooth motion of the motor. Then the various shape of sliders and the projections are taken into consideration for the analysis of the motion of the motor through FE simulation. In the SAW motor, sliders with cylindrical projections, square projections and flat plane are taken for the comparative study of the motion. Subsequently a various range of voltages are applied to the IDTs of the stators and achieved the comparative results from the FE simulation. With all the configurations mentioned above the conventional SAW motors have only one degree of freedom. The slider with a uniform array of projections on its contact surfaces is made of at least one material selected from semiconductor, ceramic, metal and polymer, and the projections on the two sides of the slider have a common axis with a cross-section of circular, square, rectangular, or any other suitable shape. Finally, the control circuit is introduced to activate the required IDTs for the desired motion of the shaft, for either translational or rotational motion. So that the activation of IDTs makes the slider to move in a particular direction as forward or reverse direction along the propagation of Rayleigh wave. By applying alternate excitations in time multiplexing repeatedly, simultaneous motion in X and Z directions is achieved with the help of control switches.

5

Dual Friction-drive SAW Motor using Cylindrical Shaft

In Chapter 4, the proposed dual friction-drive (DFD) SAW motor structure is discussed and the respective results are verified by the mathematical modelling and FE simulations. This chapter presents the modelling and simulation of DFD SAW motor with a cylinder shaft as a slider. The chapter progresses with the introduction to the proposed DFD SAW motor, the assembly, the working principle and the mathematical modelling along with FE simulation. Various comparisons are carried out to check and optimise the performance of the SAW motor. This Chapter comprises of the construction of the saw motor, stating the placement of cylinder over the stator, generation of SAW occurs due to the application of RF power supply. Then the modelling and simulation of the device.

The work leads to the development of a translational and rotational surface acoustic wave motor. The concept consists of a $LiNbO_3$ stator equipped with IDTs in order to generate SAW at the side ends of this stator. A cuboid slider is pressed with an appropriate force against each side of the slider surface such that the waves will have sufficient grip on the slider and subsequently causes it to move in a prescribed direction. FE simulations and experiments are performed to create insight to optimise the motor as reported in chapter 4. During the simulations and experiments, a change in the configuration of the motor by replacing the slider by a cylindrically shaped object is done. This configuration is shown in Figure 5. 1. In this case, the motion of the motor will no longer be along the stator surface (linear) only but also will have a rotating character.

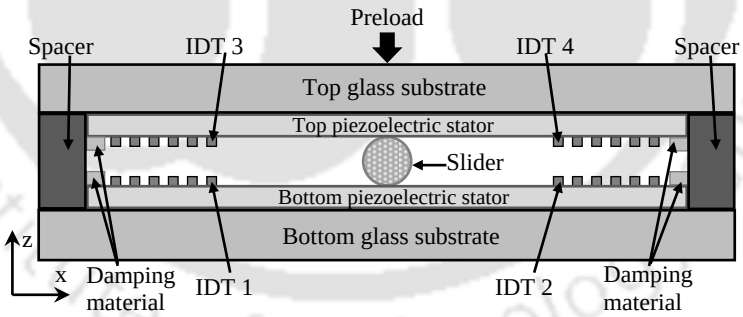

Figure 5. 1: DFD SAW motor where a cylindrical shaft is placed between identical piezoelectric stators.

5.1 Dual Friction-drive SAW Motor using Cylindrical Shaft

The proposed SAW motor with a cylindrical shaft placed between two identical piezoelectric stators, capable of making both translational motions in forward and reverse directions while rotational motion in clockwise and anti-clockwise directions [36]. When an RF voltage is applied to the IDTs of the top and bottom piezoelectric stators in a

synchronised manner, SAW is generated and propagated in the same direction on the surface of the stators as shown in Figure 5. 1. Initially, the generated waves will propagate with a straight wave front (Fresnel zone). The length of this zone (Fresnel) depends on the width of the IDT (w) and the wavelength (λ) of the Rayleighwaves. When the waves have travelled a greater distance than the length of the Fresnel zone, the wave fronts will become curved. This zone is called the Fraunhoffer zone. The Fresnel zone is the most effective area for the cylinder. The generation of SAW on the stator surface interacts with the shaft at the line of contact and the frictional force acts on the shaft in the direction opposite to the SAW propagation, when a cylinder is placed over a stator and SAW propagates on its surface. The two identical piezoelectric stators provide friction drive at the contact surfaces of the shaft.

The SAW travels in X- direction, whereas the particles present on the surface of the stator travels in the reverse direction of the propagation wave, i.e. in -X - direction on the surface of the stator. Hence the particles present at the surface of both the substrate will make a motion towards one direction. Figure 5. 2 illustrates if the same wave is propagated simultaneously on both the surfaces and the shaft is held tightly between them then the shaft experiences a high contact pressure from top and bottom sides of the stators.

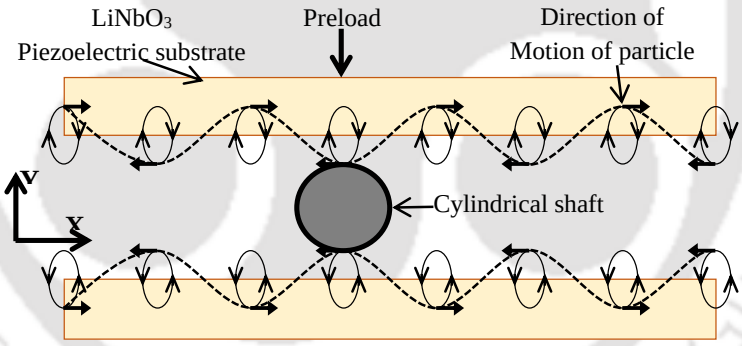

Figure 5. 2: Schematic diagram of DFD SAW motor with cylindrical shaft loaded on SAW making a translational motion.

The elliptical motion of the particles generates a frictional force on shaft due to tight contact between the shaft and stators so the shaft will be displaced in the direction of motion of the particles due to the transfer of the velocity of the particle to the shaft. So the shaft will be pushed to one direction only, which will make it move in one side axis only i.e. -X axis. So the shaft will be moving towards left.

5.1.1 Design of the cylinder

At the initial phase, the material and the optimal size of the cylindrical shaft was not clear. A cylinder in alarge size can become heavy resulting in large inertia and the preload. This

makes it more difficult to rotate the cylinder. Otherwise, if it is made small it can become so light that an additional preload needs to be used to cause sufficient grip onto the stator. However, worse, it will have a very small contact area and therefore the maximum torque will be bounded. It is very important that the cylinder to be made of a material that has enough friction with respect to the stator surface so that the waves have sufficient grip to make it rotate. The contact between the cylinder and stator will partly determine which parameter values of the cylinder will be optimal. Therefore, it is important to look more closely to this contact.

5.1.2 Modelling of contact mechanics between shaft and stator

In the proposed dual drive SAW motor, the shaft is held between two identical LN stators with adequate preload.

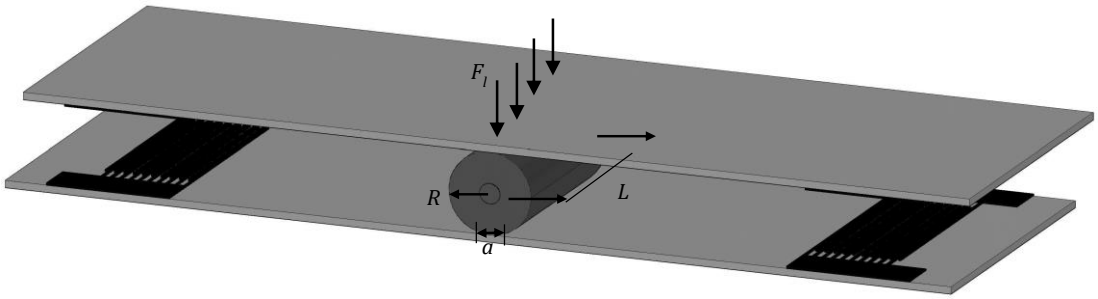

Figure 5. 3: A cylindrical shaft is sandwiched between two identical LN stators.

The Figure 5. 2 represents the operation of the SAW motor based on the surface vibration and frictional force due to high contact between the shaft and stator. The vibration and frictional force between the stator and shaft outcomes high force, high stiffness and a high degree of precision. The main aim of the modelling part is to obtain the design parameters and behaviour of the device. The modelling the device starts with the help of Hertz's contact model [73]. For primary stage, it is assumed that a shaft is placed upon a flat rigid plane type stator. This model considers the analysis of a single point of contact between a shaft and the Rayleigh wave generated on the stator. The stator surface has a roughness in nanometre and has a great impact when calculating the contact mechanics between the stator and shaft. Whenever the wave is in contact with the shaft, the contact friction goes through stick and slip states.

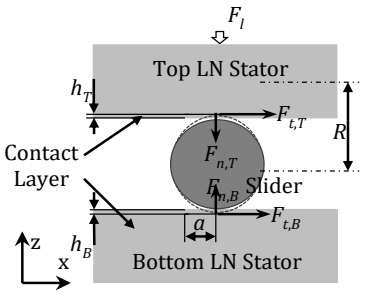

Figure 5. 4: Schematic of cylindrical shaft placed between two stators with preload.

Figure 5. 4 shows a section of a DFD SAW motor and the forces acting on the shaft as a result of interaction between the shaft and the two stators due to the propagation of synchronised Rayleigh waves on the stator surfaces in the presence of F_l as the applied preload. While$F_{n,T}$and$F_{n,B}$arethe forces acting on the shaft in a normal direction from top and bottom, respectively. $F_{t,T}$and$F_{t,B}$arethe forces acting on the shaft in a tangential direction from top and bottom, respectively. According to the mathematical modelling of the USMs, [15], [74] as the Rayleigh wave is propagating on the surface of the stators so the normal and tangential displacement of surface components can be found from following equations.

The Rayleigh wave motion in normal direction of the top and bottom stator is given by,

$$z_{st} = \hat{z}_{st}\cos(\omega t + kx) \tag{5.1}$$

The Rayleigh wave motion in translational direction of the top and bottom stator is given by,

$$x_{st} = \hat{x}_{st}\sin(\omega t + kx) \tag{5.2}$$

Where $\left(\omega = 2\pi f, k = \frac{2\pi}{\lambda}\right)$

Where z_{st} and x_{st} are the vibration amplitude in vertical and horizontal direction, ω is the angular frequency, k is the wave number, and x is the position.

The radius of both shaft and stator are R_{sl}, R_{st} of respectively. The composite radius R of both of shaft and stator is

$$R = \left(\frac{R_{sl}R_{st}}{R_{sl} + R_{st}}\right) \tag{5.3}$$

The composite Young's modulus E can be calculated from the Hertz contact theory,[73],

$$E = \left(\frac{E_{sl} E_{st}}{E_{sl}\left(1-\nu_{st}^2\right) + E_{st}\left(1-\nu_{sl}^2\right)} \right) \tag{5.4}$$

The coefficient of elasticity i.e. Young's modulus are E_{sl}, E_{st} and the Poisson's ratio are ν_{sl}, ν_{st} of the shaft and stator respectively.

5.1.3 Cylindrical shaft placed on the surface of the stator

When a cylindrical shaft is placed on the surface of the stator. F_l the Preload, "a" the width of the contact between shaft and the stator, L the length of the shaft, h the height of the variation when the wave propagates, and R the Radius of the shaft. As stator, if flat surface, Radius of the stator is infinite,Preload

$$F_l = \frac{\pi a^2}{4R} E \tag{5.5}$$

Contact width

$$a = \sqrt{\frac{4F_l R}{\pi EL}} \tag{5.6}$$

Maximum contact pressure P_{max} generated at the junction of shaft and stator can be given by,

$$P_{\max} = \frac{2F}{\pi aL} \tag{5.7}$$

By putting the value of 'a of eq 5.6 in eq 5.7

$$P_{\max} = \sqrt{\frac{FE}{\pi RL}} \tag{5.8}$$

So the normal force generated to counter the load given from top side

$$F_n = \frac{\pi}{4} ELh \tag{5.9}$$

Stiffness is given by,

$$k_n = \frac{\pi}{4} EL \tag{5.10}$$

The height difference due to motion of the Rayleigh SAW between shaft and the stator is given by,

$$h = \frac{F}{\pi LE}\left[1 + \ln\left(\frac{\pi L^3 E}{FR}\right)\right] \tag{5.11}$$

From mass, spring and damping the velocity of the shaft and newton's motion law,

$$F = m\ddot{z}_{sl} \tag{5.12}$$

$$\ddot{z}_{sl} = F / m \tag{5.13}$$

$$m\ddot{z}_{sl} = \left(-F_l + F_{n,T} - F_{n,B} + c_T \dot{z}_{sl} - c_B \dot{z}_{sl}\right) \tag{5.14}$$

c: Air Damping, k_n: Spring constant, z: Motion of the shaft in the normal direction, $\dot{z}$: Velocity of the shaft, $\ddot{z}$: Acceleration, m: Mass of the shaft, w: Angular frequency, f: frequency, μ: Coefficient of friction. During contact of shaft with wave, The velocity of the shaft can be given as [74], when in contact

$$\dot{z}_{sl} = \frac{1}{m}\int\left(-F_l + k_n\left(h_T^{3/2} - h_B^{3/2}\right) + \dot{z}_{sl}\left(c_T - c_B\right)\right)dt \tag{5.15}$$

The small displacement can be given as

$$h_B = \hat{z}_{st}\cos(\omega t) - z_{sl} \text{ and } h_T = \hat{z}_{st}\cos(\omega t) - z_{sl} \tag{5.16}$$

Non-contact

$$\dot{z}_{sl} = \frac{1}{m}\int\left(-F_l + c_T \dot{z}_{sl} - c_B \dot{z}_{sl}\right)dt \tag{5.17}$$

$$h = 0 \tag{5.18}$$

Preload can be the inverse of the normal force,

$$F_l = \bar{F}_n \tag{5.19}$$

$$= \frac{1}{2\pi}\int_{-\pi}^{\pi} F_n d\omega t \tag{5.20}$$

$$= \frac{1}{2\pi}\int_{-\pi}^{\pi} (k_n h) d\omega t \tag{5.21}$$

$$= \frac{k_n}{\pi}\int_0^{\pi}\left(\hat{z}_{st,r}\left(\omega t + \sin(\omega t)\right)\right)d\omega t \tag{5.22}$$

Inter-mittant contact of wave

$$F_l = \frac{k_n}{\pi}\int_0^{\pi}\left(\hat{z}_{st,r}\cos(\omega t) + \hat{z}_{st,r}\right)d\omega t \tag{5.23}$$

$$= \frac{k_n}{\pi}\int_0^{\pi}\left(\hat{z}_{st,r}\left(1 + \cos(\omega t)\right)\right)d\omega t \tag{5.24}$$

$$= \frac{k_n}{\pi}\hat{z}_{st,r}\left[\omega t + \sin(\omega t)\right]_0^{\pi} \tag{5.25}$$

$$F_l = \hat{z}_{st,r} \frac{\pi}{4} EL \tag{5.26}$$

$$\hat{z}_{st,r} = \frac{F_l}{k_n} \tag{5.27}$$

$$F_l = \hat{z}_{st,r} k_n \tag{5.28}$$

$$F_l = \hat{z}_{st,r} \frac{\pi}{4} EL \tag{5.29}$$

$\dot{x}_{st}$ are the tangential wave vibration velocity from the bottom and top stator while $\dot{x}_{sl}$ is the velocity of the shaft. The sliding velocity v_{rb} is $\dot{x}_{st} - \dot{x}_{sl}$ and v_{rt} is $\dot{x}_{st} - \dot{x}_{sl}$.

Tangential displacement of the shaft can be given by,

$$\dot{x}_{sl} = \frac{1}{m} \int \left(F_{t,\mathrm{B}} + F_{t,\mathrm{T}} \right) dt \tag{5.30}$$

The tangential force applied from bottom stator is

$$F_{t,B} = \mu_d F_{n,B} sign(\dot{x}_{st} - \dot{x}_{sl}) \tag{5.31}$$

The tangential force applied from top stator is

$$F_{t,T} = \mu_d F_{n,T} sign(\dot{x}_{st} - \dot{x}_{sl}) \tag{5.32}$$

The tangential wave vibration velocity from top and bottom stator

$$\dot{x}_{st} = \hat{x}_{st} \omega \cos(\omega t) \tag{5.33}$$

5.2 Finite Element Simulation of DFD SAW Motor

Finite element simulation of the DFD SAW motor is carried out in COMSOL Multiphysics using coupling of piezoelectric and solid mechanics modules is shown in Figure 5. 5.

Table 5. 1: Parameters used for FE simulation of the cylindrical shaft

Parameter	symbol	value	Units
Frequency applied	f	8.3165	MHz
Preload	F_n	0.1199	N
Young's modulus shaft	E_1	169	GPa
Young's modulus stator	E_2	172	GPa
Poisson's ratio shaft	ν_1	0.3	
Poisson's ratio Stator	ν_2	0.345	
Radius of shaft	R	100	µm
Length	ln	400	µm
Voltage applied	V	100	V
Wavelength	λ	400	µm

Mass of the shaft	m	0.4	µg
Static coefficient of friction	μ_s	0.45	
Dynamic coefficient of friction	μ_d	0.15	

Parameters involved in solving the SAW motor structure for translational motion is given in Table 5. 1. The table gives the information about young's modulus and Poisson's ratio of both the shaft and stator material. While it provides the information regarding the size and structure of each equipment involved in constructing the SAW motor. The application of the preload to the device keeps the shaft in high contact with the stators.

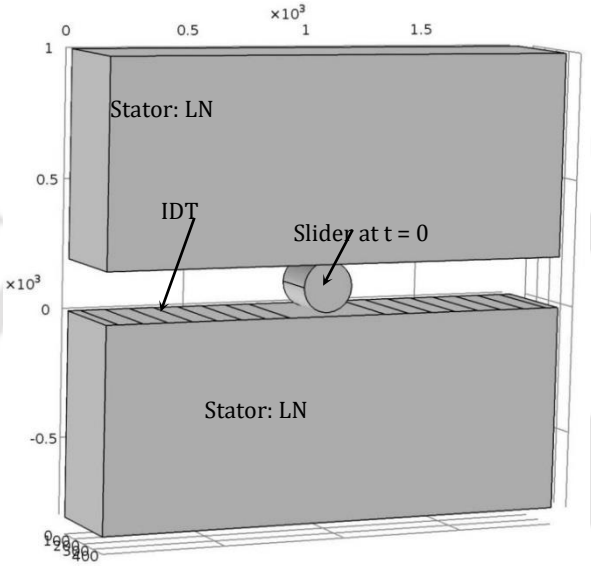

Figure 5. 5: Geometry of DFD SAW motor with cylindrical shaft used in the simulation.

The analysis starts with taking the device in the3D module of the Multiphysics software. Initially, the dimensions of the stator are declared to make the device.

5.2.1 Creating the geometry of SAW motor

The 3D plane geometry of a delay line made by placing array of 4 IDT electrodes of aperture 400 µm (1 λ), width 100 µm (¼ λ) and thickness 0.2 µm on a LN substrate of width 400 µm (1 λ), length 2000 µm (5 λ) and height 800 µm (2 λ). The device is provided with a perfect matching layer to avoid reflections at the edges. A silicon (Si) shaft of length 400 µm and diameter of 200 µm is placed in the active region as shown in Figure 5. 5.

The properties of LN such as elastic coefficients, coupling coefficients, relative permittivity and material density are adapted from [84]. Aluminium is used for IDTs as it is lightweight and highly conductive. The material used for the shaft is Si. Table 5. 1 presents the list of parameters of shaft and stator used for simulating the device.

5.2.2 Multiphysics settings

The domain settings for the device is made by stating the stator as a piezoelectric element and IDTs and shaft are linear elements. Rayleigh wave reflection is absorbed through the PML boundary where each absorbing domain is set with the equation $\beta=1/(\pi*f)$, where β is absorbing condition and f is the frequency applied to generation of the wave.

The boundary settings in FE simulation are as follows. The bottom of the stator is fixed while the ends are terminated with perfect matching layers to avoid reflections. The Periodic boundary condition is applied to the aperture. The shaft and stator are defined as contact pair. The boundaries of the shaft are set free. Swept meshing was applied for all the domains.

The entire SAW motor system has to be divided into a number of individual subsystems before an analysis is carried out to understand the behaviour of the system [58]. Each basic units of the subsystems are called finite elements, which should neither overlap nor have gaps between each other. In order to solve the model, swept meshing was done for all the domains [60]. In this type of meshing a 3D device can be analysed properly, by making layer by layer mashing as shown in Figure 5. 6.

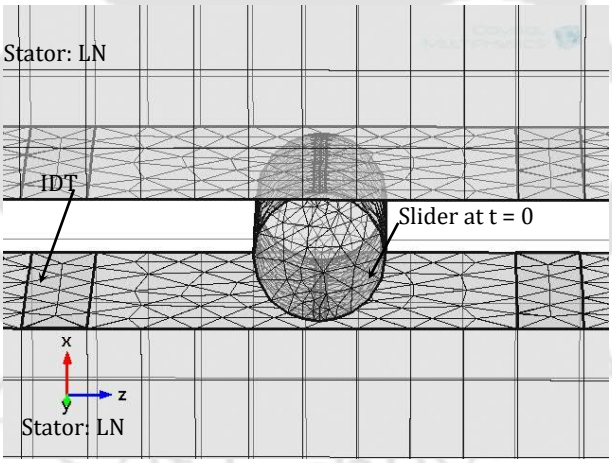

Figure 5. 6: FE model of the SAW motor with the cylinder as shaft after mesh.

5.2.3 Simulation of DFD SAW motor

The preload is applied to the shaft to increase friction at the contact surface with the stator. As the generated Rayleigh SAW wave passes under the shaft, it makes a frictional contact with the bottom surface of the shaft. At the contact position, the wave puts frictional force on the shaft to move in the direction of the motion of the point on the surface of the stator. The normal and tangential displacements of the point on the surface of the stator are on

average 3 nm and 8 nm respectively. The combination of the components of motion of the point makes the shaft to be drawn in the desired direction.

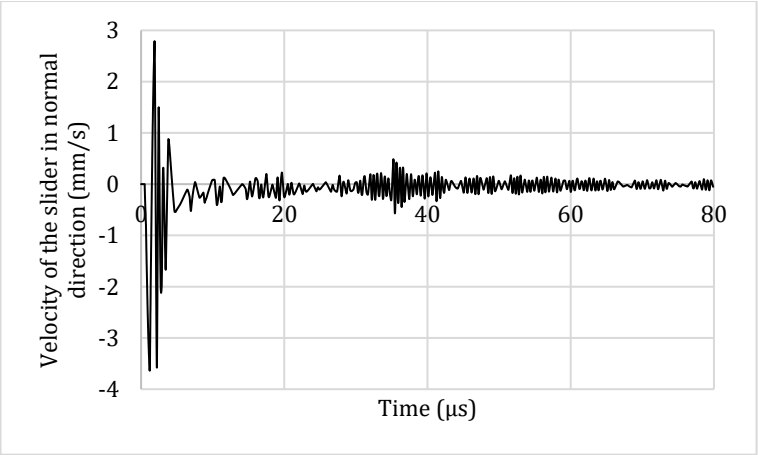

Figure 5. 7: Graph showing the velocity of the shaft in the normal direction.

Initially the shaft shows oscillation in the normal direction and the oscillation diminishes at the end of 5 μs as shown in Figure 5. 7.

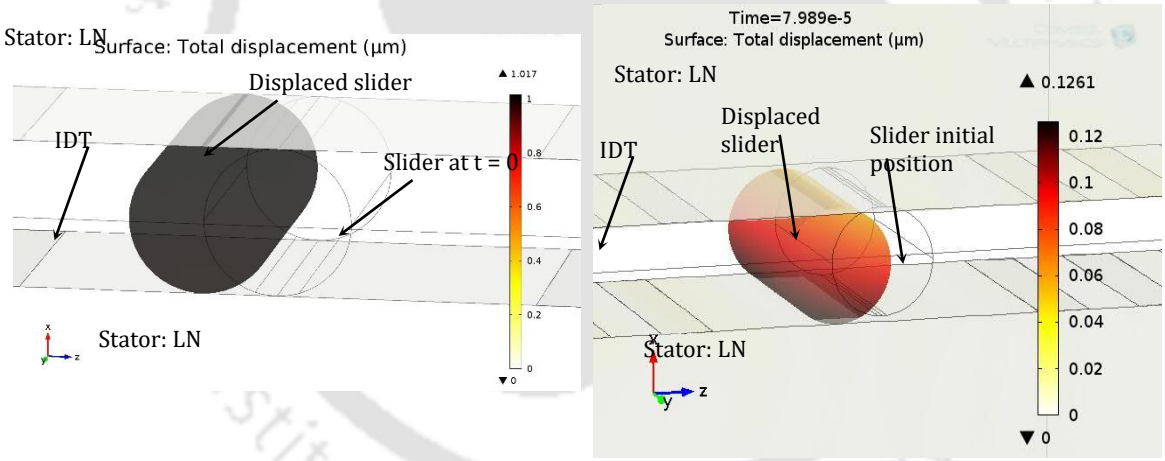

Figure 5. 8: FE simulated picture of translational displacement of the cylindrical shaft.

This frictional force on the shaft drives the shaft in the direction opposite to the direction of propagation of SAW as shown in Figure 5. 8.

The cylindrical shaft is displaced 90 nm in 80 μs as shown in Figure 5. 9. The displacement of the shaft is smooth as seen in the plot. Hence the movement results in translational motion of the shaft in one axis i.e. -*x*-axis as shown in the simulated results in Figure 5. 9. If the excitation switched to IDTs on the other side, the movable object will start moving in the opposite direction i.e. in *x*-direction.

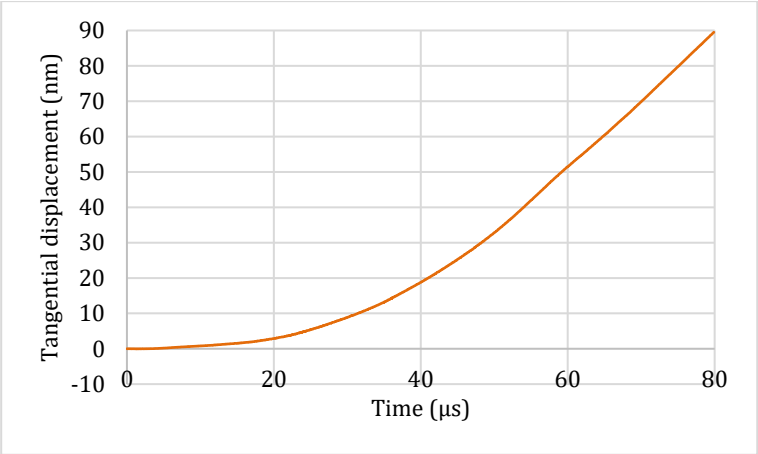

Figure 5. 9: Graph showing the tangential displacement of the cylindrical shaft.

Hence, the shaft is able to make a motion in both positive and negative of *x*-axis which is the translational motion with a dual degree of freedom. The velocity of the shaft increases and saturates to 1.15 mm/s in 80 μs. The Figure 5. 10 shows that the shaft makes high contact pressure on the surfaces of the stators, visible as a line mark at the contact area.

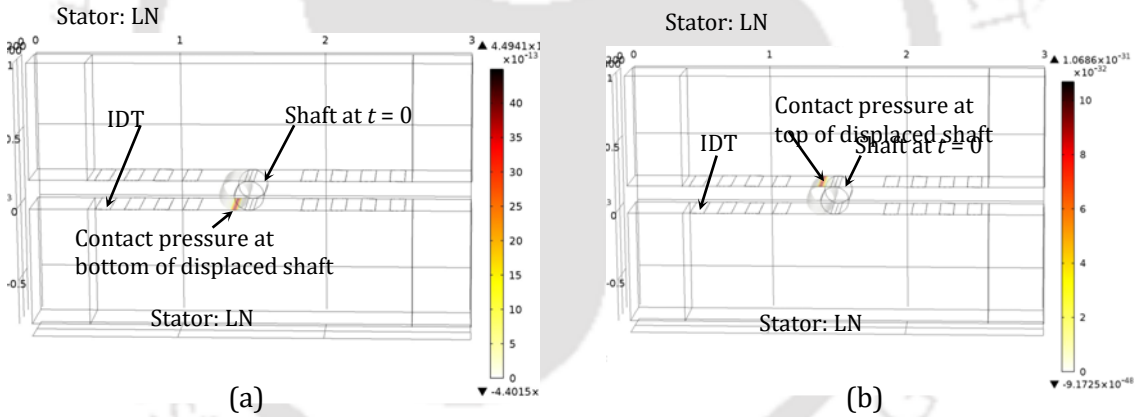

Figure 5. 10: FE simulated picture for contact pressure generated at (a) bottom contact and (b) top contact of the shaft.

5.3 Rotational Motion of Cylindrical Shaft

This section deals with the rotational motion of the cylindrical shaft of the DFD SAW motor. When a voltage is applied to the IDTs placed crosswise on the surface of the top and bottom piezoelectric stator then the SAW will propagate in opposite direction i.e. both the piezoelectric stators faces to each other. So the particles present at the surface of both the substrate will make a motion towards the reverse direction that will result in elliptical motions are now moving in two different directions. One will make a motion in a clockwise direction whereas the other will make an anticlockwise motion. For making the cylinder to

rotate, it is necessary to transmit energy from the waves into the cylinder. To make sure that this transmission is efficient it is necessary that the wave tops have sufficient grip on the cylinder, therefore, a pre-load force is needed. When the pre-load force, which is applied on the cylinder, is increased, the elastic deformation of the waves and cylinder will also increase. The tangential component of motion of these particles is in the upper part of the trajectory in opposite direction with respect to the lower part as shown in Figure 5. 11. When a pre-load force is too large, the cylinder will make contact with the particles that are in the lower part of their trajectory. The energy transmitted by these contacts will add up negatively to the total energy, which can prevent the cylinder to rotate. Seemingly, there is an optimum in the applied force on the cylinder, so the points contacting the shaft will start moving in opposite direction which will put pressure on shaft line contact to move in

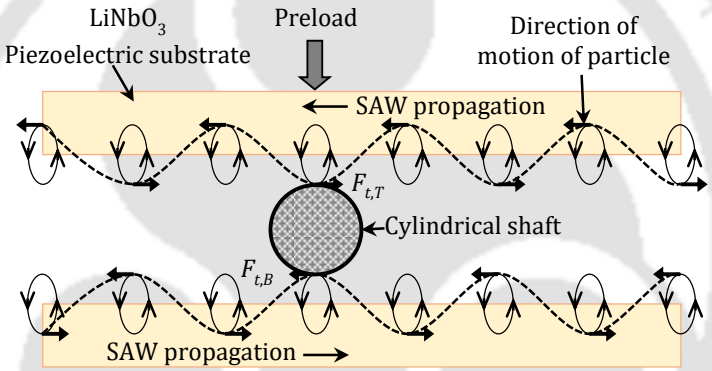

Figure 5. 11: Schematic diagram of DFD SAW motor with cylindrical shaft loaded on SAW making a rotational motion.

opposite direction on two different lines.

The particles present on the surface of the stators starts dragging in their respective direction which helps the cylindrical shaft to start rotating either in clockwise or anticlockwise direction. Hence in this situation also the shaft will start rotating in either direction depending on the application of the power supply to the IDTs. The whole mechanism of the wave which pushes to the cylindrical shaft can be diagrammatically shown in Figure 5. 11 which results in rotational motion of the cylinder.

When a phase difference voltage is applied to the IDTs present at two opposite directions then the shaft starts rotating at its own centre of the axis. If the IDTs present at the left side of the bottom substrate and the IDTs present at right side of the top substrate will be activated, then it will make clockwise direction rotational motion. If the other crosswise

side IDTs will be activated, then the shaft will start moving in the reverse direction i.e. in an anticlockwise direction. With this, the shaft is able to make a motion in both clockwise and anticlockwise direction, which is the rotational motion with a dual degree of freedom.

5.3.1 Cylinder-stator Contact

5.3.1.1 Hertzian Contact Theory

In order to move the shaft due to the waves propagating on the stator, it is essential to press the shaft and stator with an appropriate force against each other. This will also be the case for the cylinder-stator configuration. It will be necessary to have some kind of preload on the cylinder so that the Rayleighwaves have enough grip to make it rotate. The contact theory from Hertz [73] tells us that a line-shaped contact (preload F = 0 N) becomes a rectangularly shaped contact when the value of the preload increases [73]. The Hertzian laws are only valid when the preload force is not too large and the formation of such contact area is only due to elastic deformation.

The cylinder-stator contact will be rectangular shaped. For calculating the width of this contact,

$$a = \sqrt{\frac{4F_l R}{\pi E L}} \tag{5.34}$$

In this formula, 'a' is half the width of the contact area. F_l is the force between the cylinder and stator. The length of the contact surface is described by L, and R is the radius of the cylinder. The variable E is dependent on two material properties of the stator and the cylinder.

A cylinder-plane contact is not the best approach for modelling this configuration, hence it needs to go for a cylinder-cylinder contact i.e. if the waves propagating through the stator are viewed as cylinders. Secondly, what should be the radius of the cylinder representing a wave? For this calculation, the Rayleighwaves are approximated by a sine function, with the same amplitude and wavelength. The radius of the real cylinder will be about 1 to 5 cm. That means that because of the considerable difference in size, it is reasonable to view the contact configuration as a cylinder-plane contact.

The contact area will increase when the preload force on the cylinder is increased. The length of this area is assumed constant and therefore the increase is caused by the increasing width of the contact area. Equation (5.35) gives the relation between the preload force and the size of half the width of the contact area. The pressure between the stator and

cylinder has not the same value in every region of the contact area. The pressure will be at a maximum in the middle and will decrease toward the edges of the contact area. The relation between the preload force and the pressure is given in formula [73],

$$F_l = \frac{\pi a^2 E}{4R} \tag{5.35}$$

$F_l$is the preload force on the cylinder per length unit. As in Equation (5.34), R represents the value of the distance from the middle of the contact area.

The maximum value of the pressure is at x is zero. To calculate the maximum pressure, Equation (5.35) can be rewritten as Maximum Pressure

$$P_{\max} = \frac{2F}{\pi a L} = \sqrt{\frac{FE}{\pi RL}} \tag{5.36}$$

The reason why the maximum contact pressure is of interest is that by this pressure it is possible to compare different cylinders with shafts, which has been used in successful experiments [95]. The maximum pressure depends on the preload force, material parameters and geometry of the contact surface. The maximum pressure increases with increasing preload force. This can be explained by the fact that the preload force per length unit 'F_l' will increase linear and the half-width-contact area 'a' will increase proportionally to a rootfunction with an increasing preload force.

5.3.1.2 Roughness

The cylinder-stator contact has another important issue that has to be taken into account. It is the fact that the surfaces of the cylinder and the stator are not perfectly smooth. The stator has a roughness of 6-7 nm as shown in Figure 5. 12 (which is small) and the cylinder roughness depends on the material used and how successful this material can be smoothened for example silicon as shown in Figure 5. 13.

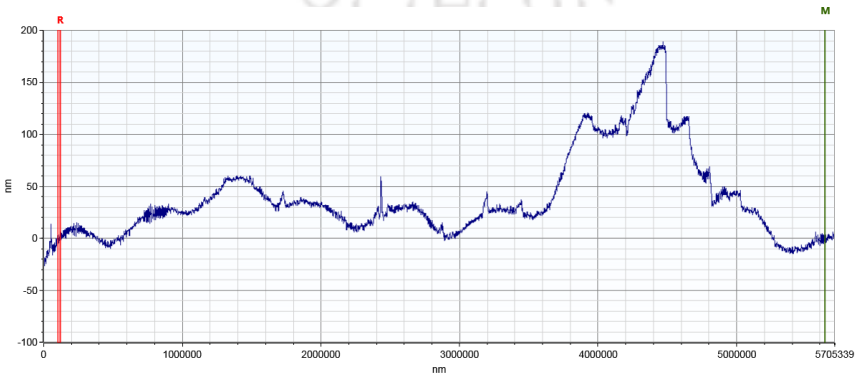

Figure 5. 12: Schematic roughness profile of the LN substrate.

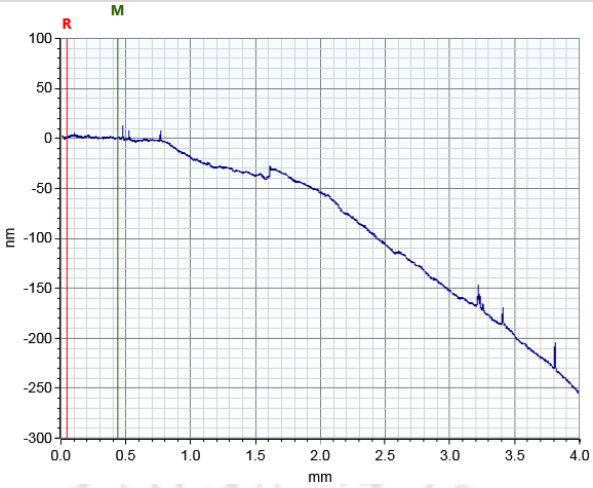

Figure 5. 13: Schematic roughness profile of the silicon shaft.

The roughness of a material can be defined as in equation [104]

$$R_q = \sqrt{\frac{1}{L}\sum_{x=0}^{x=L} z_x^2 dx} \tag{5.37}$$

$R_q$is the r.m.s. the value of the roughness, $z_x$the locale roughness height at distance x, calculated with respect to a line which direction is the same as that of the macro surface. This line is called the centre-line-average because it is the average of the roughness over a distance L. This is graphically shown in figure 5.31.

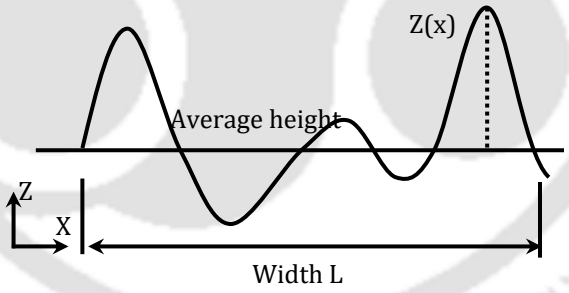

Figure 5. 14: Microscopic surface profile of the LN stator [105].

The cylinder and stator will not make contact over the whole width of the calculated contact- area due to the roughness of the materials, as shown in Figure 5. 15. When the force of the preload is increased, there will be more microscopic contact areas.

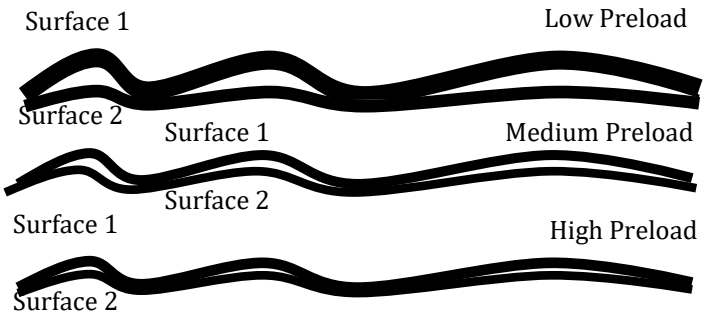

Figure 5. 15:Microscopic surface contacts with increasing preload.

To have a good transition of the energy propagating in the waves to the cylinder it is important to have sufficient microscopic surface contacts. Therefore, it is necessary to have a preload force large enough to create these contacts. The preload must not be too large to overcome continuous contact between the cylinder and the elliptical motion of the waves.

In the configuration with the shaft, the surface was covered with contact shaft, to prevent a squeeze film of air between shaft and stator. The goal is that the contact shaft will make a proper and defined contact with the upper part of the wave but no contact with the lower part. For this to happen, it seems crucial that the contact shaft has a roughness smaller than half the waves amplitude.

The height of the contact shaft is 2 mm and the waves have an amplitude of 20 nm (peak-peak). When the preload is too small only a small amount of the contact balls will make sufficient contact with the wave and therefore the traction force is too small to move the shaft. On the other hand, if the preload is too large it may be possible that some of the contact balls will also make contact with the lower part of the Rayleighwaves. Because of the elliptical motion of a particle in this wave in Figure 5. 11, the contribution of such a contact will be negative compared with the force produced by the contacts on the upper part of the wave. This effect will also be present if the roughness of the contact balls exceeds a certain value. Even with no preload force, this roughness can be the cause of contact areas between the wavevalley and cylinder. Therefore, it is essential to be able to give an estimation of this roughness.

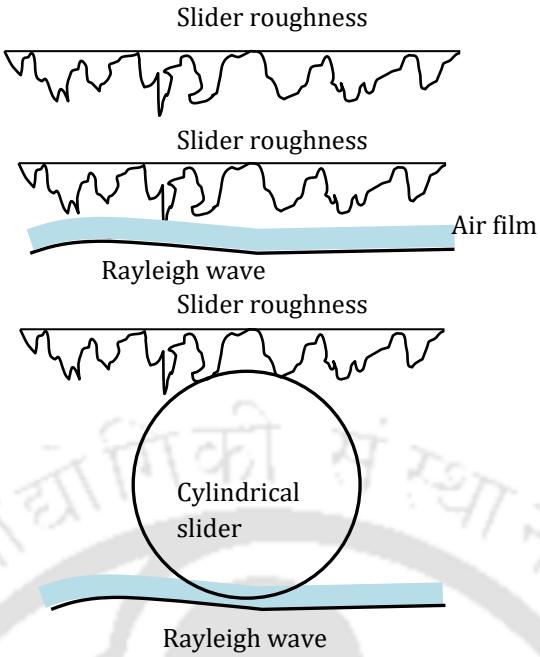

Figure 5. 16: (a) The shaft with roughness (b) The shaft on a Rayleigh-wave; Due to the air film, there is no contact over the whole wavelength (c) Contact balls make the contact more defined.

The mechanism explained above makes it that the preload has an optimum value, depending on a criterion. This optimum is related to the optimum contact pressure. The contact pressure depends on the number and shape of the contact shaft on the surface of the stator, the wave amplitude and the material properties.

5.4 Finite Element simulation of the rotational motion of the cylindrical shaft

Finite element simulation of the DFD SAW motor is carried out in COMSOL Multiphysics using coupling of piezoelectric and solid mechanics modules is shown in Figure 5. 17. Parameters involved in solving the SAW motor structure for rotational motion is given in Table 5. 1. The table gives the information about young's modulus and Poisson's ratio of both the shaft and stator material. While it provides the information regarding the size and structure of each equipment involved in constructing the SAW motor. The application of the preload to the device keeps the shaft in high contact with the stators. The analysis starts with taking the device in the3D module of the Multiphysics software. Initially, the dimensions of the stator are declared to make the device.

5.4.1 Creating the geometry of SAW motor

The 3D plane geometry of a delay line made by using a LN substrate of width 400 μm (1 λ), length 3200 μm (8 λ) and height 800 μm (2 λ). The array of 4 IDT electrodes of aperture 400 μm (1 λ), width 100 μm (¼ λ) and thickness 0.2 μm placed on the LN substrate. The device is provided with a perfect matching layer to avoid reflections at the edges. A silicon (Si) shaft of length 400 μm and diameter of 200 μm is placed in the active region as shown in Figure 5. 17. The properties of LN such as elastic coefficients, coupling coefficients, relative permittivity and material density are adapted from [84]. Aluminium is used for IDTs as it is lightweight and highly conductive.

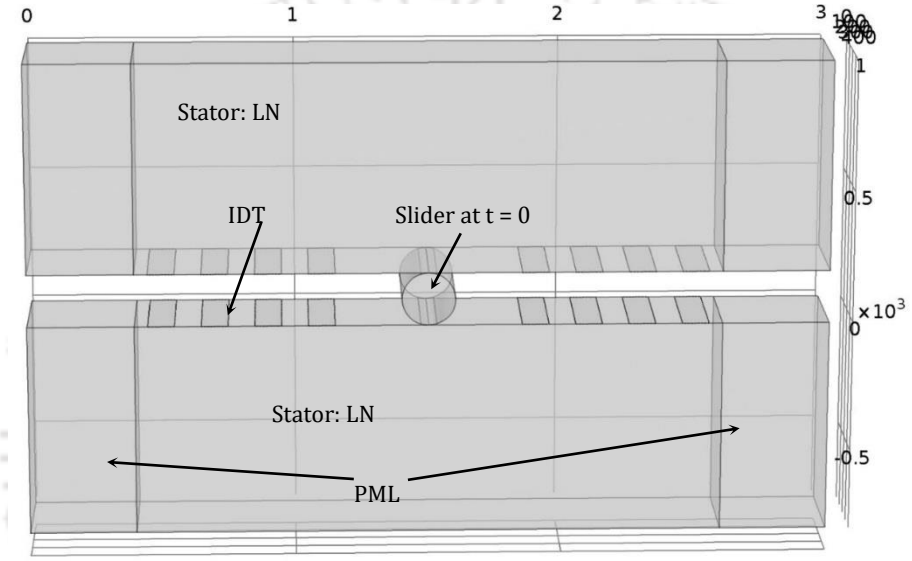

Figure 5. 17: Geometry of DFD SAW motor with cylindrical shaft used in the simulation.

5.4.2 Multiphysics settings

For the domain settings of the device, the same procedure is adopted as per section 5.2.2. The entire SAW motor system has to be divided into a number of individual subsystems before an analysis is carried out to understand the behaviour of the system [58]. Each basic units of the subsystems are called finite elements, which should neither overlap nor have gaps between each other. In order to solve the model, swept meshing was done for all the domains [60]. In this type of meshing a 3D device can be analysed properly, by making layer by layer mashing as shown in Figure 5. 6.

5.4.3 Simulation of DFD SAW motor

With the application of 100 V to the IDTs present at the crosswise side of the stators of both the bottom and top stators, the SAW is generated and propagated towards each other.

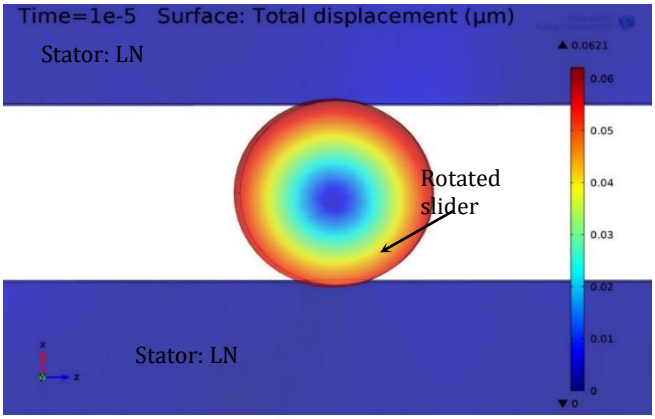

Figure 5. 18: Surface profile of the FE simulated structure of the rotational DFD SAW motor

The cylindrical shaft makes a rotational motion as shown in Figure 5. 19. Two points from the shaft, each from two sides is taken for an account to observe the rotational motion. The observation shows the shaft is making the rotation to its centre of the axis.

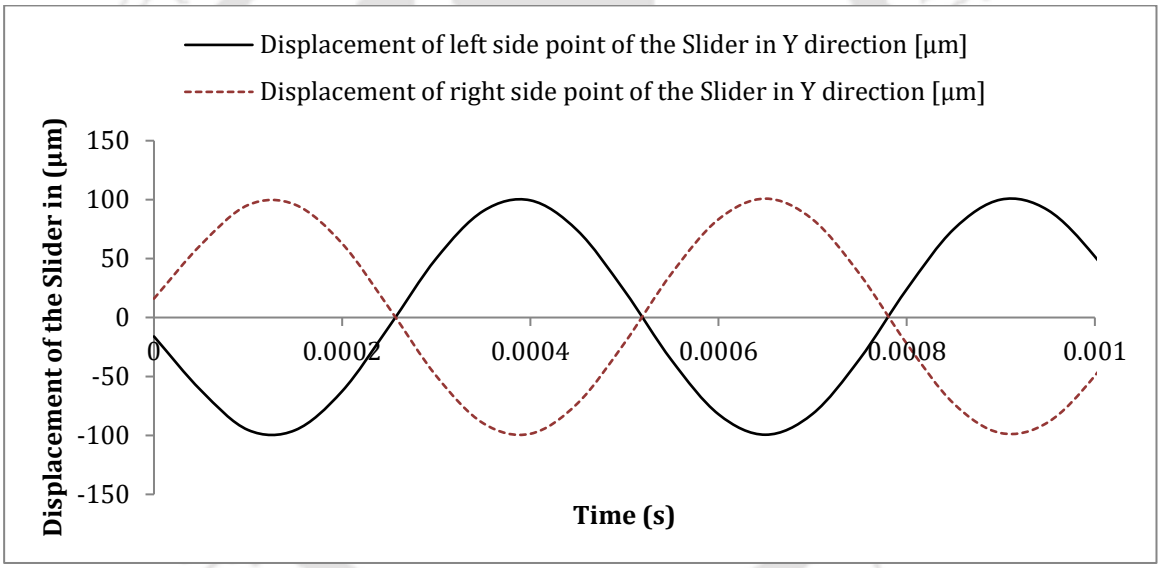

Figure 5. 19: Graph representing the rotational motion of the cylindrical shaft of DFD SAW motor.

The translational velocity of the cylindrical shaft is shown in Figure 5. 20. Two points from the shaft, each from two sides is taken for an account to observe the translational velocity of 1 mm/s. The observation shows the angular velocity of the shaft is

$$\Omega = \frac{V_{max}}{R} = \frac{1\ mm/s}{100\ \mu m} = \frac{1\ mm/s}{0.1\ mm} = 10\ {}^{1}/_{s}$$

So the rotor is making $\omega = {}^{10}/_{2\pi} = 1.6$ rotations per second.

Hence the shaft is making 1.6 rotation per second to its centre of axis.

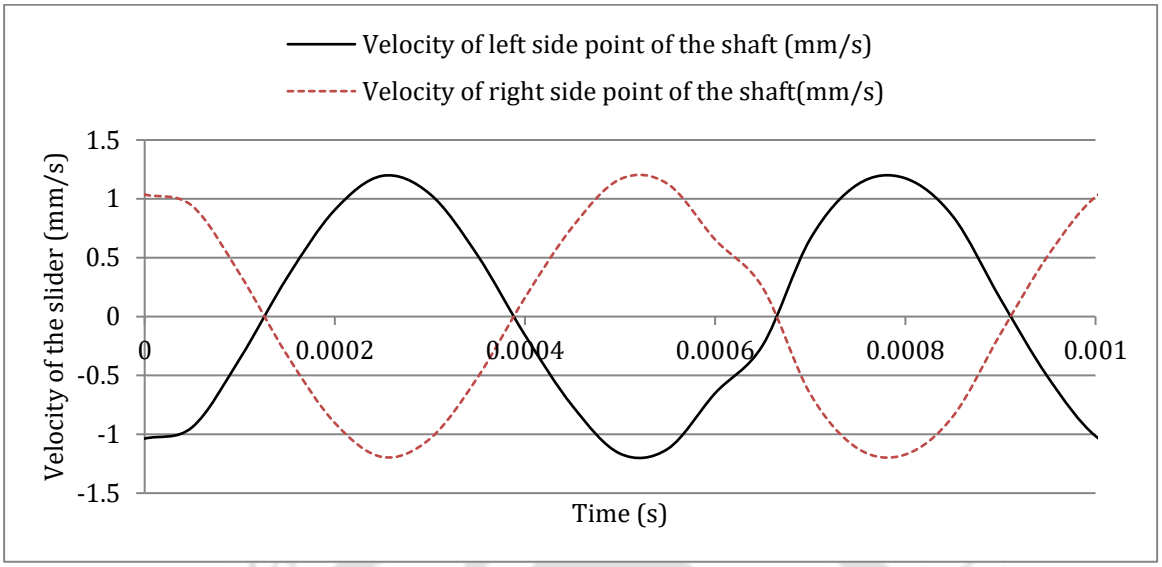

Figure 5. 20: Graph representing the rotational velocity of the cylindrical shaft of DFD SAW motor.

5.5 Rotational motion of the cylindrical shaft with trench on the surface of the stator

In the previous section, the study of rotational motion is carried out by the cylindrical shaft. But the shaft used to slide a little in addition to the rotational motion. In order to avoid the sliding of the shaft, a trench is introduced at the surface of the stator to hold the cylinder with a proper contact. So the points contacting the shaft will start moving in opposite direction which will put pressure on the shaft and the line contact moves in opposite direction in two different directions as shown in Figure 5. 21.

Table 5. 2: Parameters used for FE simulation of the cylindrical shaft

Parameter	symbol	value	Units
Frequency	f	8.28	MHz
Preload	F_n	5	mN
Young's modulus shaft	E_1	169	GPa
Young's modulus stator	E_2	172	GPa
Poisson's ratio shaft	ν_1	0.3	
Poisson's ratio stator	ν_2	0.345	
Radius of shaft	R	250	µm
Voltage	V	100	V
Wavelength	λ	400	µm
Length	ln	400	µm
Mass of the shaft	m	0.4	µg
Static coefficient of friction	μ_s	0.45	
Dynamic coefficient of friction	μ_d	0.15	

When a voltage is applied to the IDTs placed crosswise on the surface of the top and bottom piezoelectric stator then the SAW will propagate in opposite direction i.e. both the piezoelectric stators faces to each other. So the elements present at the surface of both the substrate will make a motion towards a different direction that will result in elliptical motions are now moving in two different directions. One will make a motion in a clockwise direction whereas the other will make an anticlockwise motion. So the particles present on the surface of the stators starts dragging in their respective direction which helps the cylindrical shaft to start rotating either in clockwise or anticlockwise direction. Hence in this situation also the shaft will start rotating in either direction depending on the application of the power supply. The whole mechanism of the wave which pushes to the cylindrical shaft can be diagrammatically shown in Figure 5. 23. It will result in rotational motion of the cylinder. When a phase difference voltage is applied to the IDTs present at two opposite directions then the shaft starts rotating at its own centre of the axis. The rotational motion is shown as per the Figure 5. 23.

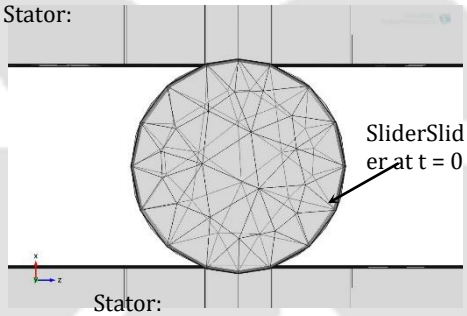

Figure 5. 21: FE simulation model of the rotational SAW motor with cylindrical shaft after mesh.

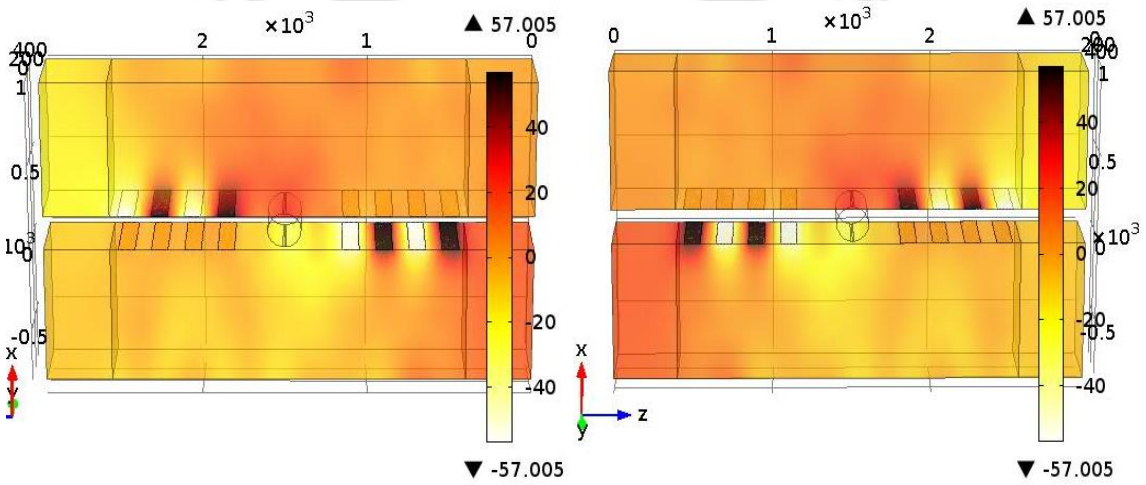

Figure 5. 22: FE simulated picture for SAW motor showing the applied electric potential.

The Figure 5. 22 shows FE simulated picture for SAW motor showing the applied electric potential. If the IDTs present at the left side of the bottom substrate and the IDTs present at right side of the top substrate will be activated then it will make clockwise direction rotational motion shown the simulated results in Figure 5. 23.

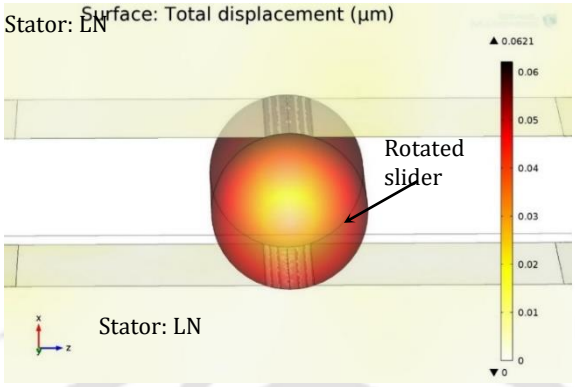

Figure 5. 23: Surface profile of FE simulated for SAW motor showing the rotational motion of the shaft.

If the other crosswise side IDTs will be activated, then the shaft will start moving in the reverse direction i.e. in an anticlockwise direction. Hence, the shaft is able to make a motion in both clockwise and anticlockwise direction, which is the rotational motion with a dual degree of freedom.

As per the literature [95], the minimum voltage applied for the stators to move the slider is 30 $V_{p\text{-}p}$. So a voltage of 100 V is applied to the IDTs present at crosswise of the top and bottom stators. The graph in Figure 5. 24, presents the motion of the shaft in translational direction with the help of three points taken on the surface of the shaft at the end of 70 µs.

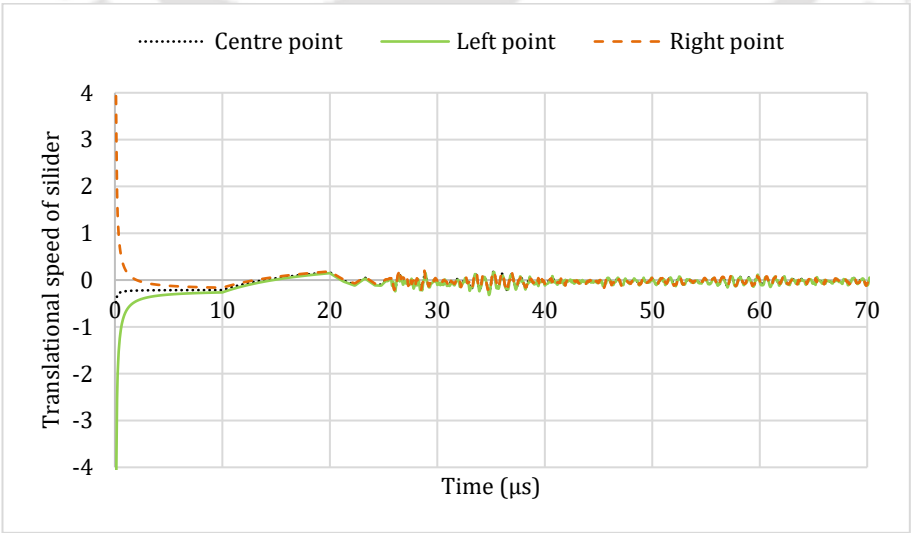

Figure 5. 24: Graph representing the translational speed of shaft as very small with the time progresses.

As per the Figure 5. 25, three different points viz. center, left, and right point present on the surface of the shaft is taken to observe the motion of the cylindrical shaft. The graph shows the displacement of a single cycle of the motion of the shaft as rotational one.

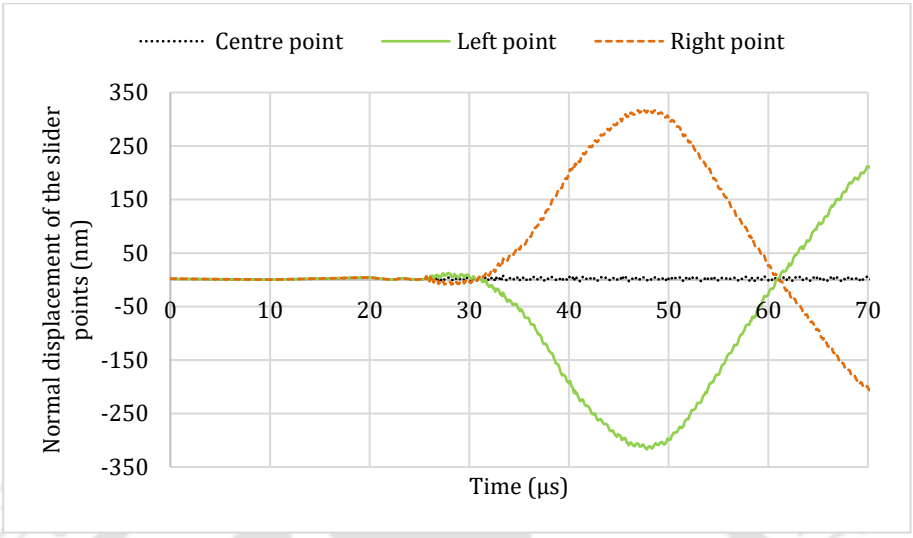

Figure 5. 25: Graph representing the rotational motion of the shaft.

Hence only the rotational motion will occur without the presence of any translational motion of the cylindrical shaft.

The Figure 5. 26 shows the generation of contact pressure from the shaft on the surface of the stator. Figure 5. 26 (a) and (b) shows the line contact pressure of the shaft at its bottom side and top side, which comes in contact with the surface of the stator respectively.

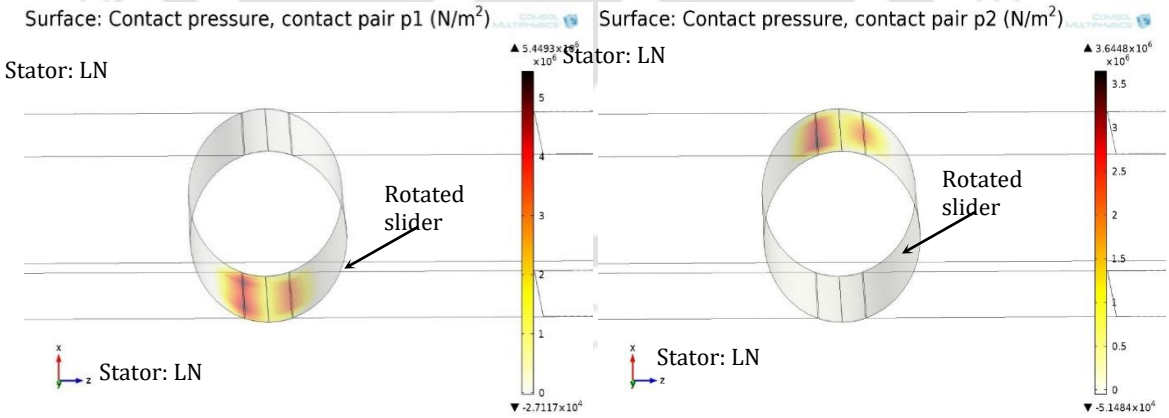

(a) (b)

Figure 5. 26: Surface profile of the FE simulated for SAW motor showing the contact pressure at (a) bottom and (b) the top surface of the shaft.

5.6 Control of the DFD SAW Motor

The Figure 5. 27 shows the schematic circuit diagram of different combinations to activate the IDTs for achieving different types of motion of the shaft of the SAW motor.

The SW1 is the combination of activation of IDT 2 and IDT 4, which results in the translational motion of shaft towards right side direction or towards these two IDTs. The SW2 is the combination of activation of IDT 1 and IDT 3, which results in the translational motion of shaft towards left side direction or towards these two IDTs. The SW3 is the combination of activation of IDT 1 and IDT 4, which results in the rotational motion of shaft in clockwise motion. The SW4 is the combination of activation of IDT 2 and IDT 3, which results in the rotational motion of shaft in anticlockwise motion.

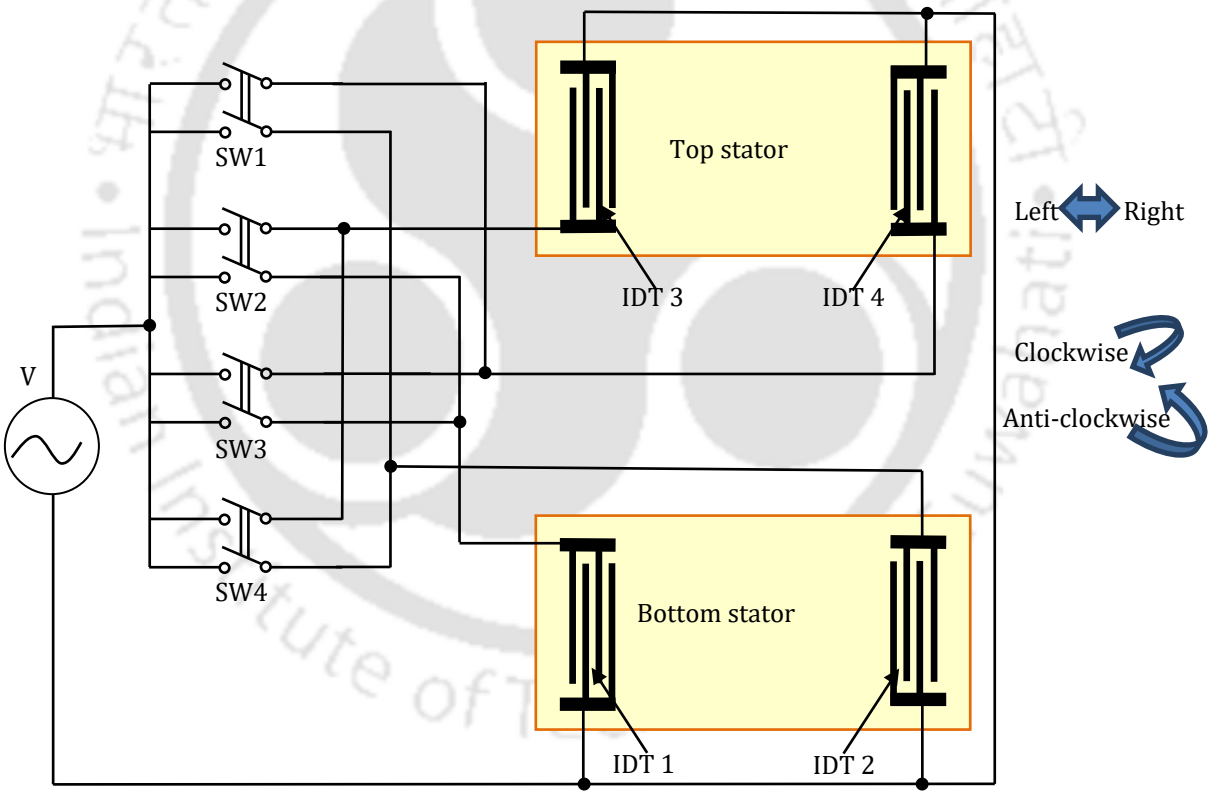

Figure 5. 27: Schematic of the controller for the rotational motion of the cylindrical shaft.

5.7 Summary

This chapter dealt with a dual friction-drive SAW motor using a cylindrical shaft as slider/rotor. The modelling of the contact mechanics between the piezoelectric stator and a cylindrical shaft is carried out to get the parameters such as contact pressure, required

preload and motion of the shaft. Simultaneously the preload plays a distinguished role to decide the friction force between stator and shaft and taking different samples of preload correspond to different coefficient of friction, it is found to be 5 mN. The proposed DFD SAW motor is analysed with the help of finite element simulation using COMSOL Multiphysics for the translational motion. In FE simulation, various aspects are discussed like domain settings, boundary settings, material constants and finally the time domain analysis. It follows the same configuration as a cuboid shaft for the translational motion of the shaft. The DFD SAW motor with cylindrical shaft can make a translational motion at a low amplitude of 12 nm and high frequency of 8.28 MHz Rayleigh wave. The FE simulation was carried out to realise the rotational motion of the shaft, where the activation of IDT combinations is in crosswise. The time domain results of the FE simulation provide the rotational motion of the shaft. During a simple configuration of the DFD SAW motor the cylindrical shaft gives a result of a little translational motion in addition to the expected rotational motion. To avoid the translational motion and achieve only rotational motion, a trench is made on the surface of the stators. Finally, the control circuit is introduced to activate the required IDTs for the desired motion of the shaft, for either translational or rotational motion. So that the activation of IDTs makes the shaft to move in a particular direction in clockwise and anticlockwise direction. It is concluded that a balanced condition of both frictional force and preload is necessary with respect to the deformation of the wave for the smooth motion of the motor. Hence, the summary provides all the necessary details of the device, which are discussed in the chapter.

6

Fabrication of the Dual Friction-drive SAW Motor

The mathematical modelling and FE simulation of the proposed DFD SAW motors with a cuboid slider having projections are presented in chapter 4. While Chapter 5 presents the mathematical modelling and FE simulation of the proposed DFD SAW motor with cylindrical shaft where translational, as well as rotational motion of the slider, is observed. The SAW motors based on the proposed DFD technique are fabricated and experiments are carried out to validate the results of simulation of DFD SAW motors presented in Chapter 4 and 5. This chapter describes the design process and fabrication steps of proposed devices.

6.1 Fabrication of SAW Devices for DFD Motors

Conventionally SAW devices are fabricated using photolithographic patterning techniques used in the semiconductor industry [27]. Usually, IDTs are patterned using UV lithography and aluminium (Al) metal is deposited on the surface of the piezosubstrate using thermal evaporation and followed by an etching process to remove unwanted Al [106]. We have fabricated several SAW delay line devices for the stators operating at different resonance frequencies at Centre for Excellence in Nano Science and Engineering, Indian Institute of Science, Bangalore under Indian Nanoelectronics User Program (INUP).

6.1.1 Fabrication of IDT using UV photolithography process

The basic steps involved in the fabrication of IDT on piezo-substrate using UV photolithography are as follows. Layout designs, mask generation, metal deposition over the clean wafer, UV photolithography, pattern development, etching, and wafer dicing [27].

Two processes are commonly used to pattern IDTs on wafers *viz* etching and lift-off. Though both are used for fabricating SAW devices, the lift-off is more suitable to develop IDT structure of feature size less than 5 μm. In this work, a lift-off process is adopted.

6.1.2 Design methods of interdigital transducers (IDT)

The SAW Delay line device is composed of two sets of comb-structured interdigitated fingers fabricated at the two ends on a piezoelectric substrate. When one of the IDTs is excited by an electrical signal, the mechanical wave is generated due to converse piezoelectric effect [27]. The dimensions of IDTs are either adopted from the published literature or are designed using conventional methods of designing SAW devices [33], [53], [107]. SAW devices are designed to obtain the desired resonance frequency and minimum insertion loss. Impulse response method has been used to model the SAW device [108]. This technique model the piezoelectric, mechanical and electrical behaviours of a SAW device as shown in Figure 6. 1. The model assumes that the aperture is constant and that the metallization ratio between the fingers and spaces is 0.5 [53]. The aperture is found by

continuously adjusting the IDT impedance to 50 ohm. Since most test equipment has an input and output impedance of 50 ohm, hence that is the value chosen for the design of IDT.

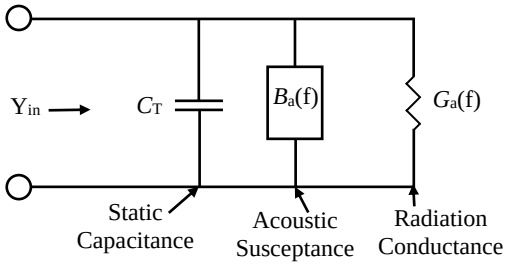

Figure 6. 1: Electrical equivalent input admittance of a surface wave transducer (Hartman, [68])

For single IDT, the frequency response is shaped by the *sync* function and calculated by [68],

$$|H(f)| = 2k\sqrt{(C_s f_0)}N_p \frac{\sin(X)}{X} e^{\frac{-j2\pi fN_p}{2f_0}} \tag{6.1}$$

f is the frequency, f_0 is the centre or synchronous frequency, $N_p$is the number of finger pairs in the IDT, k is the piezoelectric coupling coefficient, C_s is the capacitance of a finger pair per unit length.

Variable X can be written as

$$X = N_p \pi \frac{(f - f_0)}{f_0} \tag{6.2}$$

Centre frequency $f_0$can be found by,

$$f_0 = \frac{(f_r + f_a)}{2} \tag{6.3}$$

$f_r$is the frequency at resonance and f_a is the frequency at anti-resonance of the piezoelectric substrate. The real part of the input admittance is called the conductance and can be written as sinc function,

$$G_a(f) = 8k^2 C_s W_a f_0 N_p^2 \left|\frac{\sin(X)}{X}\right|^2 \tag{6.4}$$

where W_a is the aperture of the electrode. The imaginary part of the input admittance is called as acoustic susceptance. The acoustic susceptance is found by taking the Hilbert transform [108] of the radiation conductance found as shown in Figure 6. 2 and Figure 6. 3 from the equation,

$$B_a(f) = \frac{G_a(f_0)\sin(2X) - 2X}{2X^2} \tag{6.5}$$

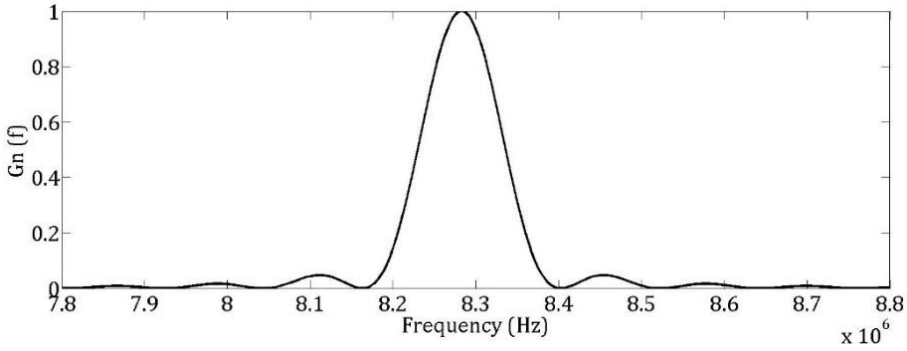

Figure 6. 2: Radiation conductance of the SAW delay line

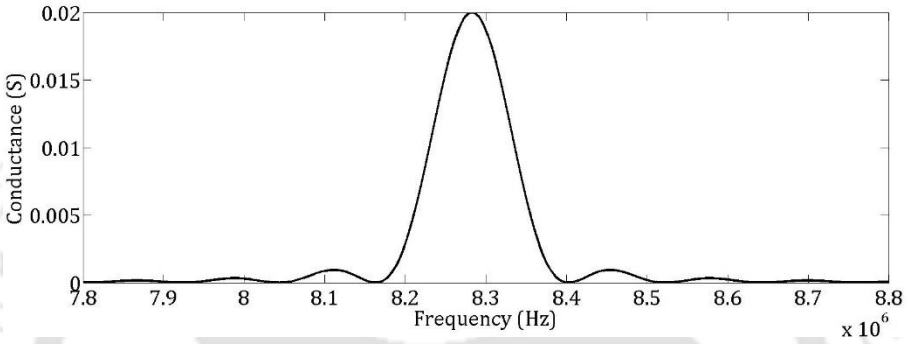

Figure 6. 3: Radiation conductance of the SAW delay line matching with the impedance of 50 ohm

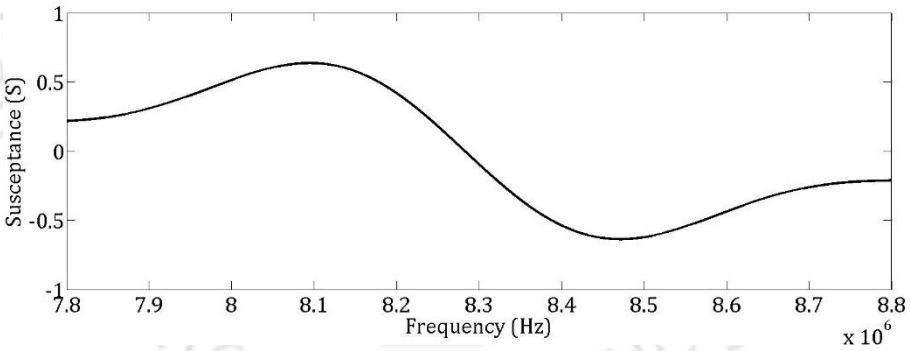

Figure 6. 4: Acoustic susceptance of the SAW delay line

Admittance and Impedance can be calculated from below mathematical equation. The total admittance found by combining the radiation conductance, the acoustic susceptance resulted in Figure 6. 4and the total capacitance. The admittance is given by,

$$Y = G_a + j(2\pi f C_T + B_a) \tag{6.6}$$

Total static capacitance C_T for IDT is found by

$$C_T = N_p C_s W_a \tag{6.7}$$

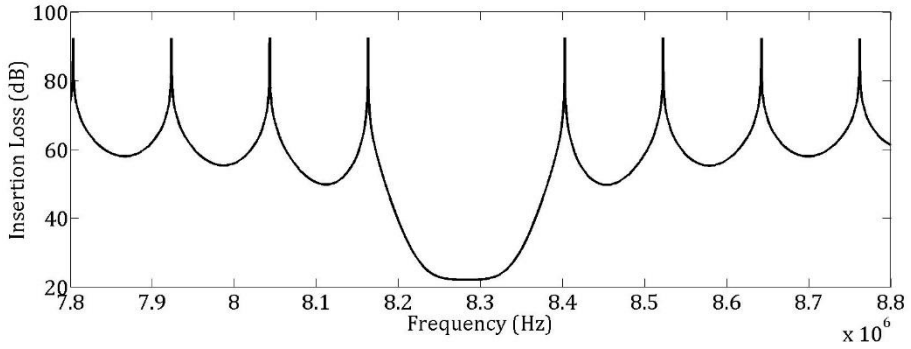

Figure 6. 5: Insertion loss of the SAW delay line

For SAW devices the insertion loss as shown in Figure 6. 5 is a function of frequency and calculated by using conductance, susceptance, and the load resistance R_g as

$$IL(f) = -10\log\left[\frac{2G_a(f)R_g}{(1+G_a(f)R_g)^2+\left[R_g\left(2\pi fC_T+B_a(f)\right)\right]^2}\right] \tag{6.8}$$

The device aperture (W_a) is adjusted to achieve the correct IDT resistance.

$$W_a = \frac{1}{R_{in}}\left(\frac{1}{2f_0C_sN_p}\right)\frac{\left(4k^2N_p\right)}{\left(4k^2N_p\right)2\pi^2} \tag{6.9}$$

$$N_p = round\left(\frac{2}{NBW}f_0\right) \tag{6.10}$$

The aperture is found by continuously adjusting the IDT impedance to 50 ohm. Since most test equipment has an input and output impedance of 50 ohm, hence that is the value chosen for the design of IDT. We have calculated the designing parameters of the IDTs for three different operating frequencies.

6.1.3 Design of the stators and IDTs with various dimensions

The processes involved in the development of interdigital transducers (IDT) over normal and chemically reduced $LiNbO_3$ substrates are summarised as follows:

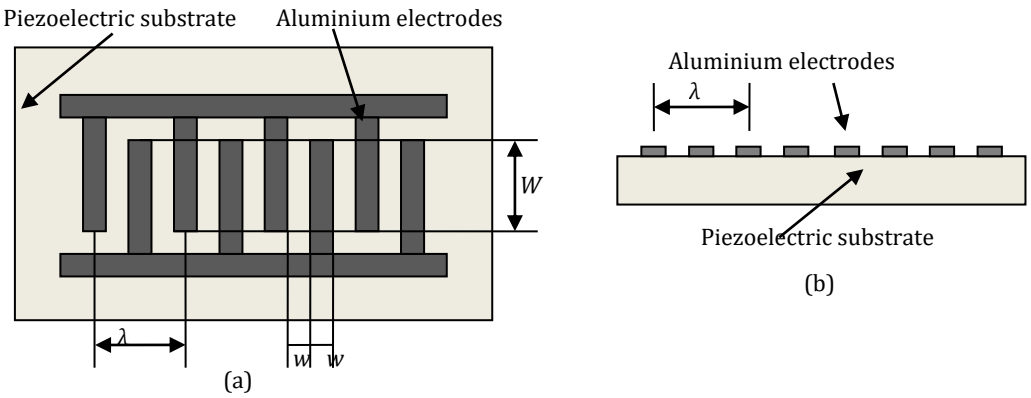

Figure 6. 6: (a) Top view, (b) cross-section view of the comb structured IDT on a piezoelectric substrate.

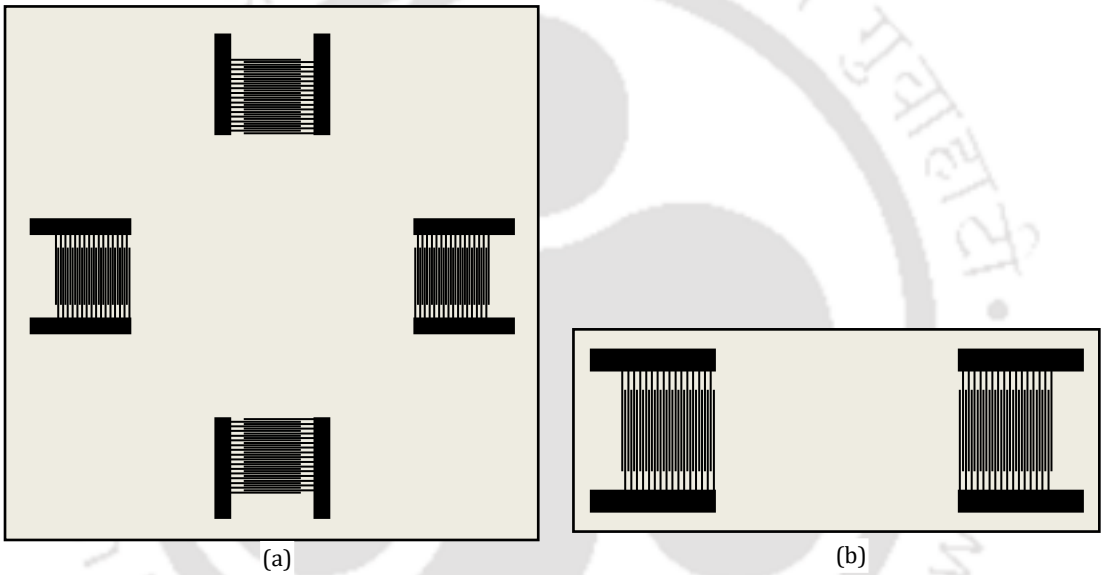

Figure 6. 7: (a)Stator with four sets of IDTs. (b) Stator with two sets of IDTs.

Four stators with dimensions shown in Table 6. 1 are fabricated on $LiNbO_3$ substrates of 0.35 mm thickness.

Table 6. 1: Dimensions of fabricated stators

No.	Dimensions of the stator	Active area	Direction of propagation	Area of each IDT	Frequency
1.	60 mm × 60 mm	30 mm × 30 mm	X, Y	0.1 mm x 9.1 mm	8.62 MHz
2.	12 mm × 48 mm	4 mm × 20 mm	X	0.75 mm x 4 mm	13.2 MHz
3.	20 mm × 60 mm	8 mm × 30 mm	X	0.1 mm x 9.1 mm	8.62 MHz
4.	26 mm × 62 mm	15 mm × 30 mm	X	0.15 mm x 15 mm	6.5 MHz

The parameters of the IDTs obtained for 50-ohm impedance using the design method given above are presented in Table 6. 2.

Table 6. 2: Dimensions of different types of IDTs

Frequency	Finger Width	Wavelength	Aperture	Finger Pairs	Electrode Thickness
13.2 MHz	75 µm	300 µm	3700 µm	30	0.2 µm
8.62 MHz	100 µm	400 µm	9100 µm	21	0.2 µm
6.5 MHz	150 µm	600 µm	15500 µm	20	0.2 µm

6.2 Process Flow for Fabrication of the Devices

In the previous section, the design method for the fabrication of IDTs is presented to estimate the aperture and number of fingers of each IDT for desired operating frequency and impedance. The fabrication of the proposed device goes through the following stages.

I. Layout design for a mask using CleWin software[109]:

The optimised structures to be patterned over the substrate are to be graphically designed using CleWin software.

II. Mask writing:

Mask for the IDT is to be written on chrome plates using the mask writer.

III. Fabrication steps:

Various steps involved in the fabrication of IDT over LiNbO3 substrate are briefly described below. Major steps involved in the fabrication process are graphically presented in Figure 6. 8. The fabrication process flow for making the IDT (a) PMMA film deposited, (b) IDE mask followed by UV exposed, (c) Aluminium (Al) thin film deposition, (d) Structure of IDT after removal of PMMA.

To start the fabrication of Interdigital transducers IDTs on the Lithium niobate $LiNbO_3$ piezoelectric wafer, the wafer needs to go under cleaning process carried out at wet bench. After cleaning of the wafer, it goes under Lithography for photoresist coating. As the wafer is developed after lithography, it needs to measure the structures developed on the wafer with the help of an optical microscope. Then the wafer needs to be deposited uniformly by Aluminium (Al) material on the surface of it. This deposition can be done by e-beam evaporation or thermal evaporation method. In this case, it is tried with both the processes. After the deposition of Al material, the wafer goes throughlift-off process. This lift-off process is done by placing the wafer inside acetone and giving an ultrasonic bath if needed. Then $LiNbO_3$ wafer was taken for measurement of dimensions of the electrodes by an optical microscope.

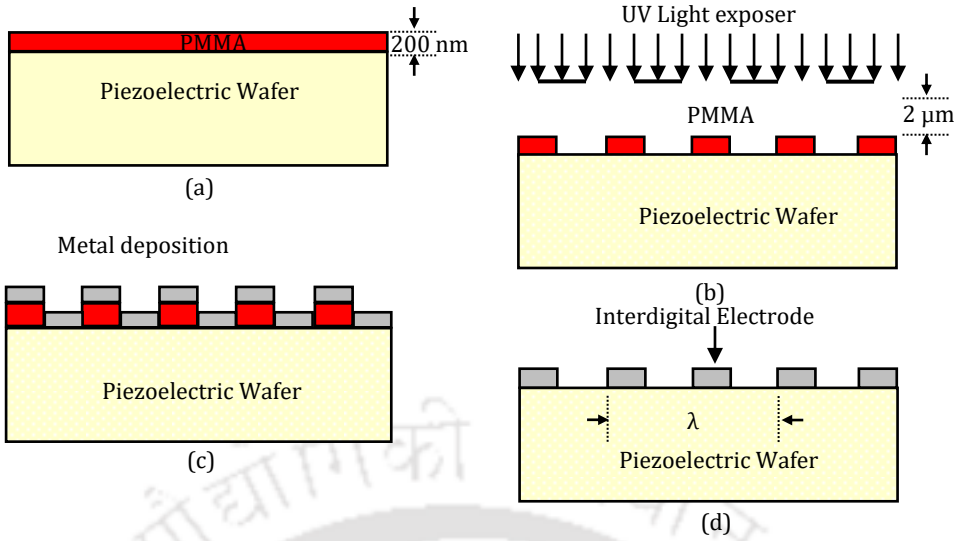

Figure 6. 8: The fabrication process flow for making the IDT(a) PMMA film deposited, (b) IDE mask followed by UV exposed, (c) Aluminium (Al) thin film deposition, (d) Structure of IDT after removal of PMMA.

6.2.1 Layout designing

The structures to be patterned over the $LiNbO_3$ wafer are graphically designed using CleWin software.

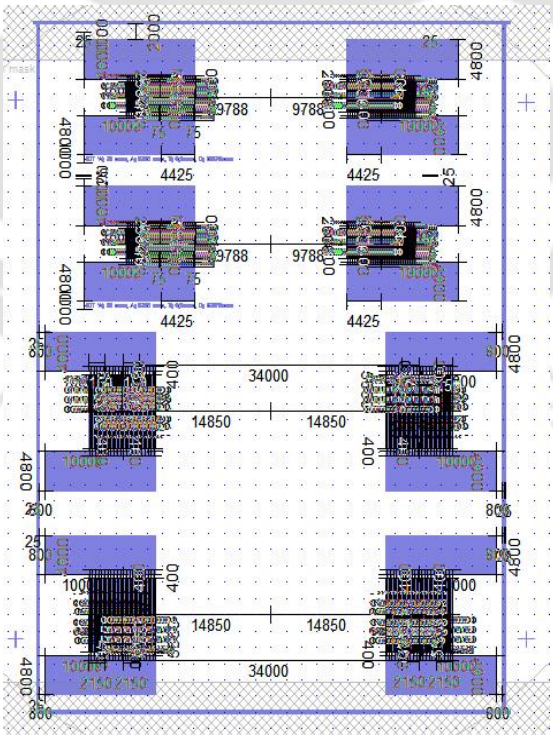

Figure 6. 9: Different dimensions of IDTs (a) Mask with positive, (b) Mask with negative.

The screen shot of IDT design for 4-inch wafer in Figure 6. 9 shows two delay lines with wavelength 300 µm (zoomed in view in Figure 6. 11) and two delay lines with wavelength 400 µm (zoomed in view in Figure 6. 10).

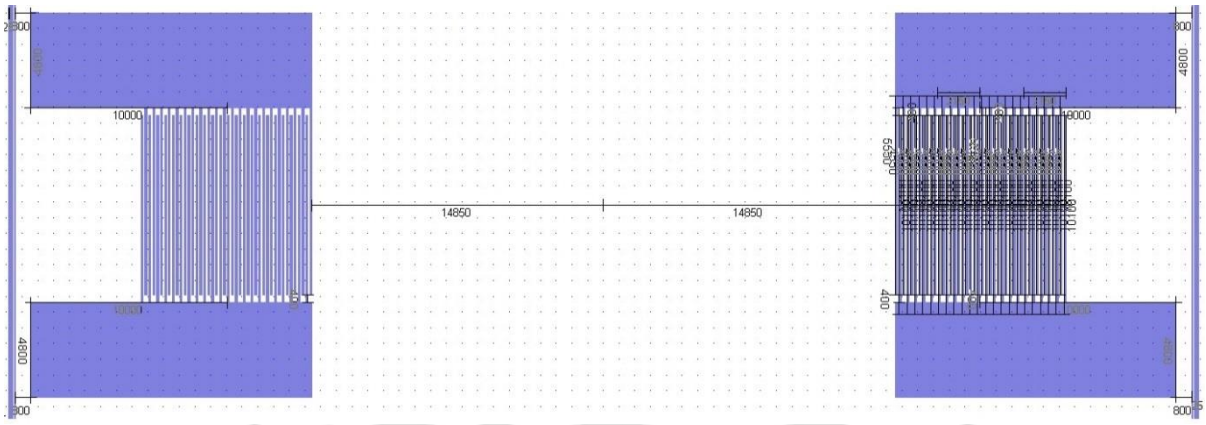

Figure 6. 10: Close up view of a mask designed in CleWin for the delay line of wavelength 400 µm.

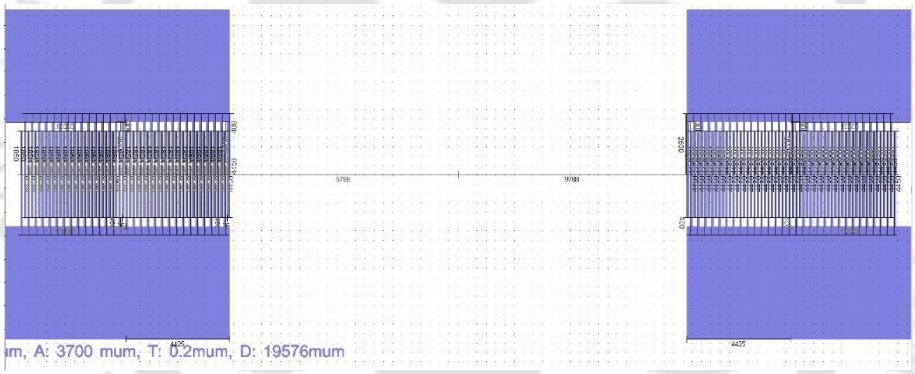

Figure 6. 11: Close up view of a mask designed in CleWin for the delay line of wavelength 300 µm.

6.2.2 Mask writing

The IDT can directly be patterned through laser writing on photoresist covering Al coated LN wafer with high accuracy followed by development and etching. As the IDTs are to be fabricated in a whole 4-inch wafer, the direct laser writing will consume a lot of time. Hence it is decided to pattern the IDT through UV lithography. The mask required for lithography is designed to accommodate a maximum number of delay lines in a 4-inch LN wafer.

Chrome plate masks for UV lithography are written using laser writer Microtech LW – 405. As the minimum dimension of the pattern to be written is of 75 µm, lens 3 of the laser writer is employed. The laser writing process took 14 hours. The chrome plates are developed using MF 26A developer (MicroChem, USA). The exposed chromium is etched

using chrome etchant solution. Chrome etchant solution contains ceric ammonium nitrate $(NH_4)_2Ce(NO_3)_6$ or sulphate $(NH_4)_4Ce(SO_4)_4.2\ H_2O$, with small amounts of HNO_3 [77]. The unwanted photoresist is removed using acetone, followed by piranha cleaning process.

6.2.3 Cleaning of the lithium niobate ($LiNbO_3$) wafer

The cleaning of the substrate is done in order to remove the dust particles, oil, different marks, and grease from the surface of the piezoelectric wafer used for fabrication. The unwanted particles become an obstacle during the lithography process of the structure. The wafer was dipped in Acetone for 10 minutes for cleaning purpose. Isopropyl alcohol (IPA) is used to carry out the further cleaning of the wafer for 2-3 minutes. In general, piranha cleaning[110] is done for removing unwanted particles from the surface of wafers, but as piranha affects the LN wafer and changes its characteristics, it is not advisable to use piranha for cleaning LN wafer. Air blow was given to dry the wafer.

Figure 6. 12: Picture of an LN ($LiNbO_3$) wafer after cleaning.

6.2.4 Lithography for delay line

The cleaned LN wafer is taken for the lithography process. The wafer is again cleaned with acetone and IPA for 2-3 and 1 minute respectively.

6.2.4.1 Soft baking

The spun sample is soft baked by placing it on the hot plate at a temperature of 110°C for 60 s. To avoid wafer getting stuck to the hot plate surface, wipes are placed between the wafer and hot plate.

6.2.4.2 Photoresist coating

The wafer is then placed inside the spin coater. It is ensured that the centre of the wafer is exactly aligned with the spin coater. AZ5214 photoresist (Micro chemicals, GmBH) is dispensed from the bottle and spread all over the wafer by spinning. The wafer is spun at a

speed of 500 rpm for 5 s and followed by 4000 rpm for 40 s. Speed ramp of 500 rpm/s is used. By this method, the photoresist coating of 1 µm thickness over the wafer is achieved.

6.2.4.3 Soft baking

The spun sample is soft baked by placing it on the hot plate at a temperature of 95°C for 60 s. To avoid wafer being stuck to the hot plate surface, wipes are placed between the wafer and hot plate.

6.2.4.4 UV exposure

The positive mask thus prepared is placed in UV mask aligner (EVG 620 Double Sided Mask Aligner) substrate chuck for the UV exposer of the photoresist. The pattern on the mask is transferred to the surface of the wafer through UV exposed with an exposure UV dosage rate of 50 mJ/cm^2. Then the wafer is taken for development to the wet bench.

6.2.4.5 Development of IDT structures

The UV exposed wafer is then dipped in AZ351B (1:4) solution for 30 s. The wafer is taken out from the developer solution once the patterns are identified in the wafer. If the wafer is placed for access time, it will lead to over development and finally end with poor patterns on the wafer. The developed IDT device images are taken and measured through an optical microscope for verification purpose. The pictures of the wafer with IDTs after development are shown in Figure 6.13.

6.2.4.6 Post baking

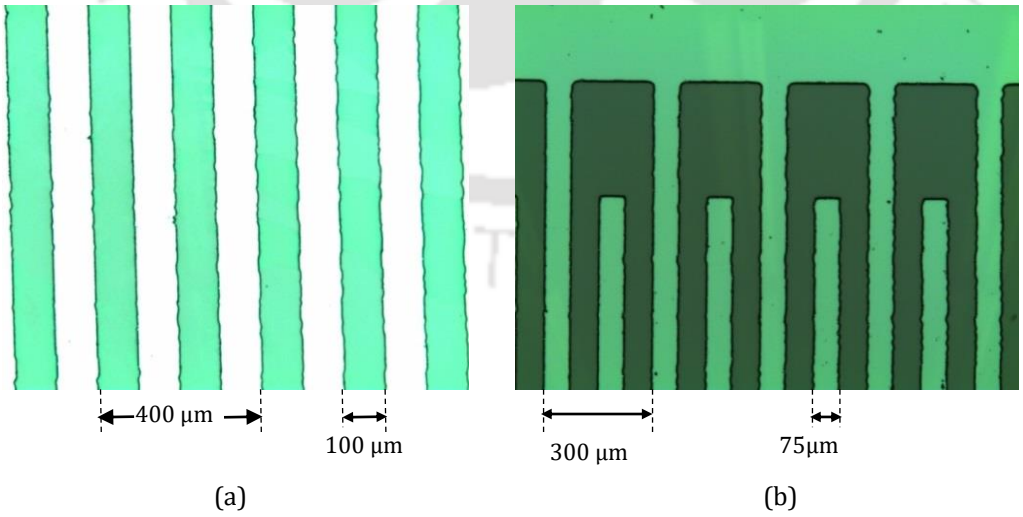

Figure 6.13: Pictures of IDTs taken by digital microscope for finger widths (a) 100 µm and (b) 75 µm after lithography process.

The developed patterns are checked using an optical microscope. The wafer is then hard baked by placing it in a hot plate at a temperature of 110°C for 1 minute.

6.2.5 Aluminium metal deposition on LN wafer

Al metal is usually deposited using two methods, viz. E-beam evaporation and thermal evaporation.

6.2.5.1 Al metal deposition using E-beam evaporation

After cleaning the LN wafer, Al metal of a thickness of 150 nm is coated over the wafer using E-beam evaporator coating system using AlEBI recipe. Where the deposition pressure was 1.5e-6 Torr while base pressure was 1.69e-6 Torr maintaining the temperature at 30° C. The details of E-beam process are given in Table 6. 3.

Table 6. 3: Recipe for depositing Al material on LN substrate

State	Time (minute)	Power Percentage (%)	Rate of Deposition (Å /s)	Current Consumed (mA)	Voltage (kV)	Pressure (Torr)
Rise 1	2:50	5.80	-	70	6.99	2.08×10^{-6}
Soak 1	5.30	10.00	-	132	6.99	2.41×10^{-6}
Rise 2	9.20	16.53	-	230	6.99	1.53×10^{-6}
Soak 2	11.30	20.00	-	279	6.99	1.52×10^{-6}
Deposit	13.00	22.04	5.06	314	6.99	1.67×10^{-6}
	15:10	22.19	5.04	314	6.99	1.58×10^{-6}
	16:10	22.45	5.14	317	6.99	1.55×10^{-6}

Total Run time: 3:15 (HH:mm) Total deposition time: 18 minute

6.2.5.2 Al metal deposition using thermal evaporation

After cleaning the LN wafer, Al metal of a thickness of 200 nm is coated over the wafer using thermal evaporator coating system. The pressure generated inside the chamber is 2.7×10^{-3} mTorr while maintaining the temperature at 21° C. The initial vacuum for 10 minutes then high vacuum for 1 hour with a deposition rate of 1.2 Å/s.

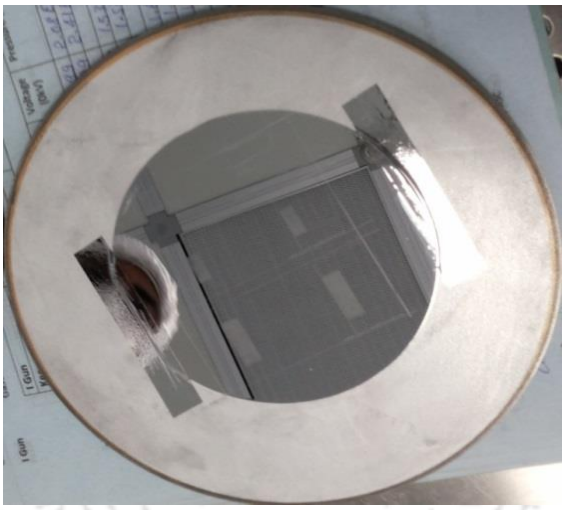

Figure 6. 14: Picture of an LN wafer after Al deposition

6.2.6 Lift-off process

After Al deposition, the wafer is dipped in Acetone for 3 hrs at the wet bench for lift off. An ultrasonic bath was given to the wafer for 5 minutes for cleaning. Then the wafer was cleaned with water and given an air blow and dried. Pictures of IDTs taken by digital microscope after the lift-off process for finger widths of 75 µm, 100 µm, 150 µm are shown in Figure 6. 15, Figure 6. 16, and Figure 6. 17, respectively.

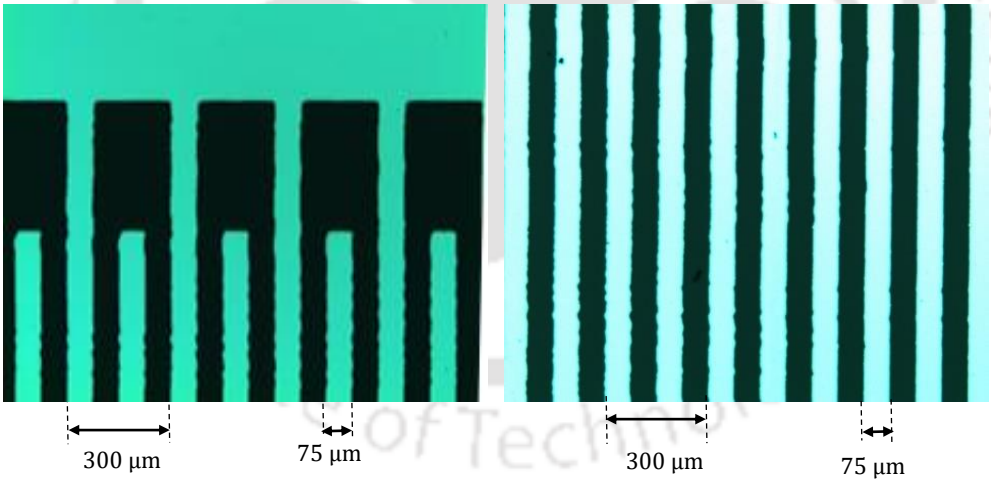

Figure 6. 15: Pictures of IDT with a finger width of 75 µm taken by digital microscope after the lift-off process.

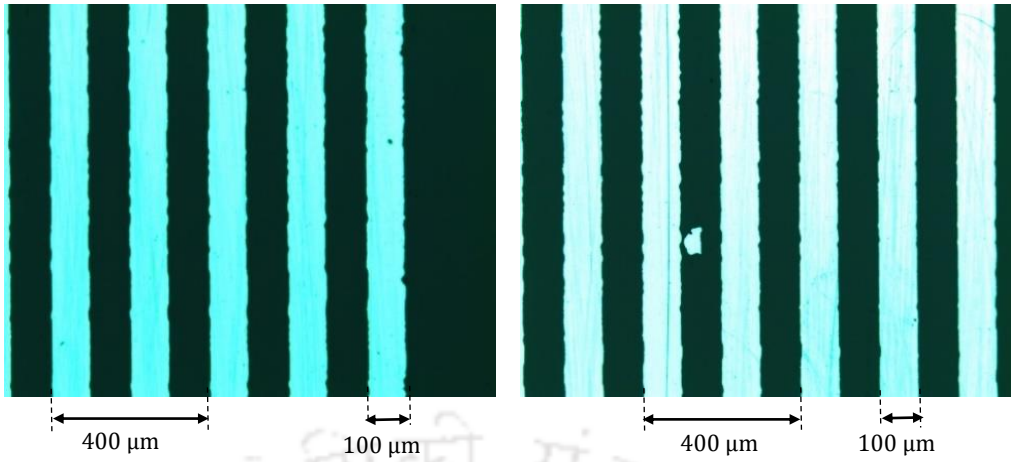

Figure 6. 16: Pictures of IDT with a finger width of 100 µm taken by digital microscope after the lift-off process.

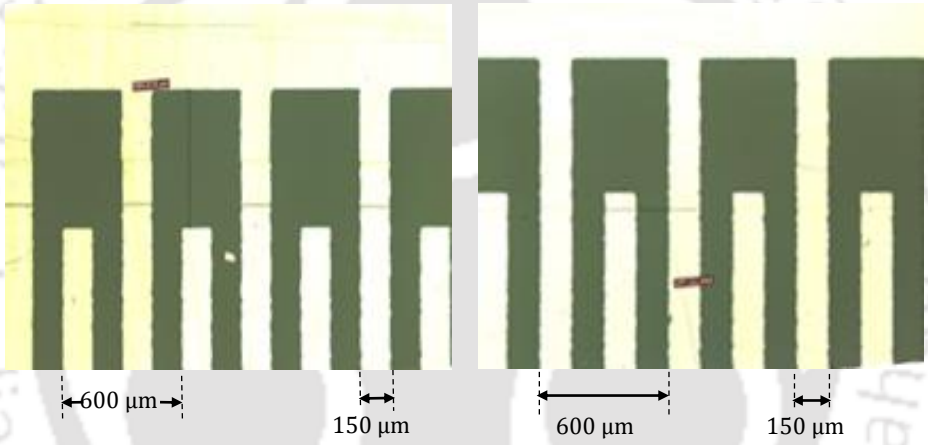

Figure 6. 17: Pictures of IDT with a finger width of 150 µm taken by digital microscope after the lift-off process.

6.2.7 Cleaning the wafer

After lift-off process, the device needs to be cleaned properly with the help of DI water. Finally, the pellets are dried and dehydrated by heating them to a temperature of 120°C. This pellets cleaning method improves the adhesion of Al on the surface of the wafer. The dimensions of fabricated IDT are measured through an optical microscope.

(a) (b)

Figure 6. 18: Pictures of fabricated delay line devices on (a) LN, and (b) chemically reduced LN wafers

6.3 Process Flow for Fabrication of Slider

Sliders of various dimensions are made from the silicon substrate and an array of cylindrical/cubical projections is etched on the surface of each slider. The processes involved in the development of a square shape slider with cylindrical projections are summarised as follows. Fabrication Steps: The steps involved in the fabrication process are graphically shown in Figure 6. 19.

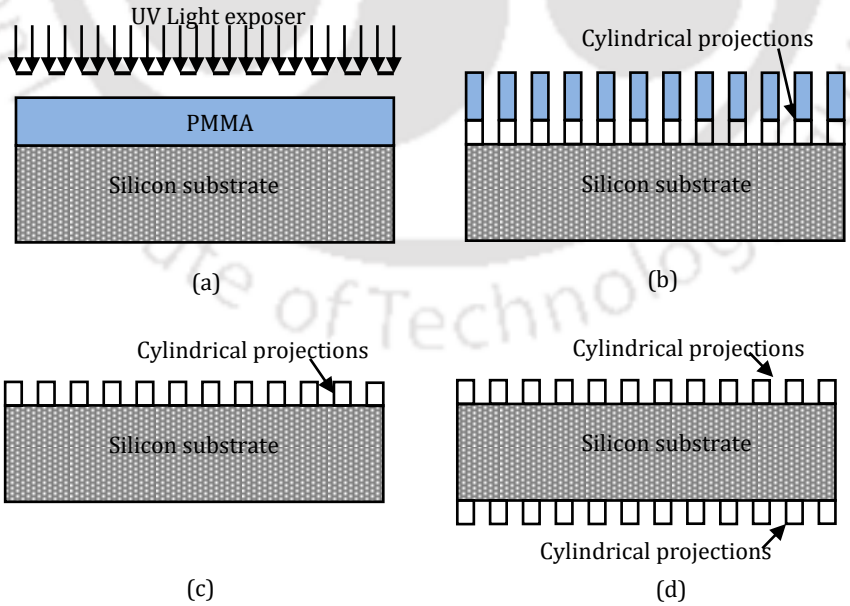

Figure 6. 19: Fabrication flow process for slider with projections
(a) Photoresist coating over UV exposed, (b) Photoresist coating over UV exposed,
(c) Slider with one side projection, (d) Slider with both side projections

Designing of Slider: The dimension of the slider in length × width × height is 4 mm x 4 mm x 0.6 mm, and having various the dimensions of cylindrical projections such as diameter × pitch gap × height is 40 μm × 40 μm × 2 μm, 80 μm × 80 μm × 2 μm, and 40 μm × 80 μm × 2 μm.

Designing Layout for Mask using CleWin software: The optimised structures to be patterned over the substrate are to be graphically designed using CleWin software. While mask for the cylinders is to be written using the mask writing facility.

6.3.1 Design of slider

In Section 6.2, fabrication of delay lines with three different wavelengths is explained. As discussed in Chapter 4, projections on the surface of the sliders are necessary to avoid sticking problems. The spacing between the projections is designed so that the wavelength of the delay line is an integer multiple of centre-to-centre distance (pitch) in the array of projections [74]. The specifications of different types of sliders fabricated are given in Table 6. 4.

Table 6. 4: Dimension of Cylindrical projections

Sl. No.	Diameter	Pitch	Height
1	40 μm	40 μm	2 μm
2	50 μm	300 μm	2 μm

One wafer is processed with the projections given in Table 6. 4 on one side of the wafer. The sliders with projections on both the sides are fabricated on a wafer prepared by bonding two wafers and the mask for projections is transferred by aligning through mask aligner.

6.3.1.1 Layout designing

The structures to be patterned over the Si wafer are graphically designed using CleWin software. The screen shots of IDT designs for 4 inches wafer are shown in Figure 6. 20 (a) and (b). Figure 6. 22 (c) shows the magnified view of the layout.

6.3.1.2 Mask writing

The mask writing process is as explained in Section 6.2.2.

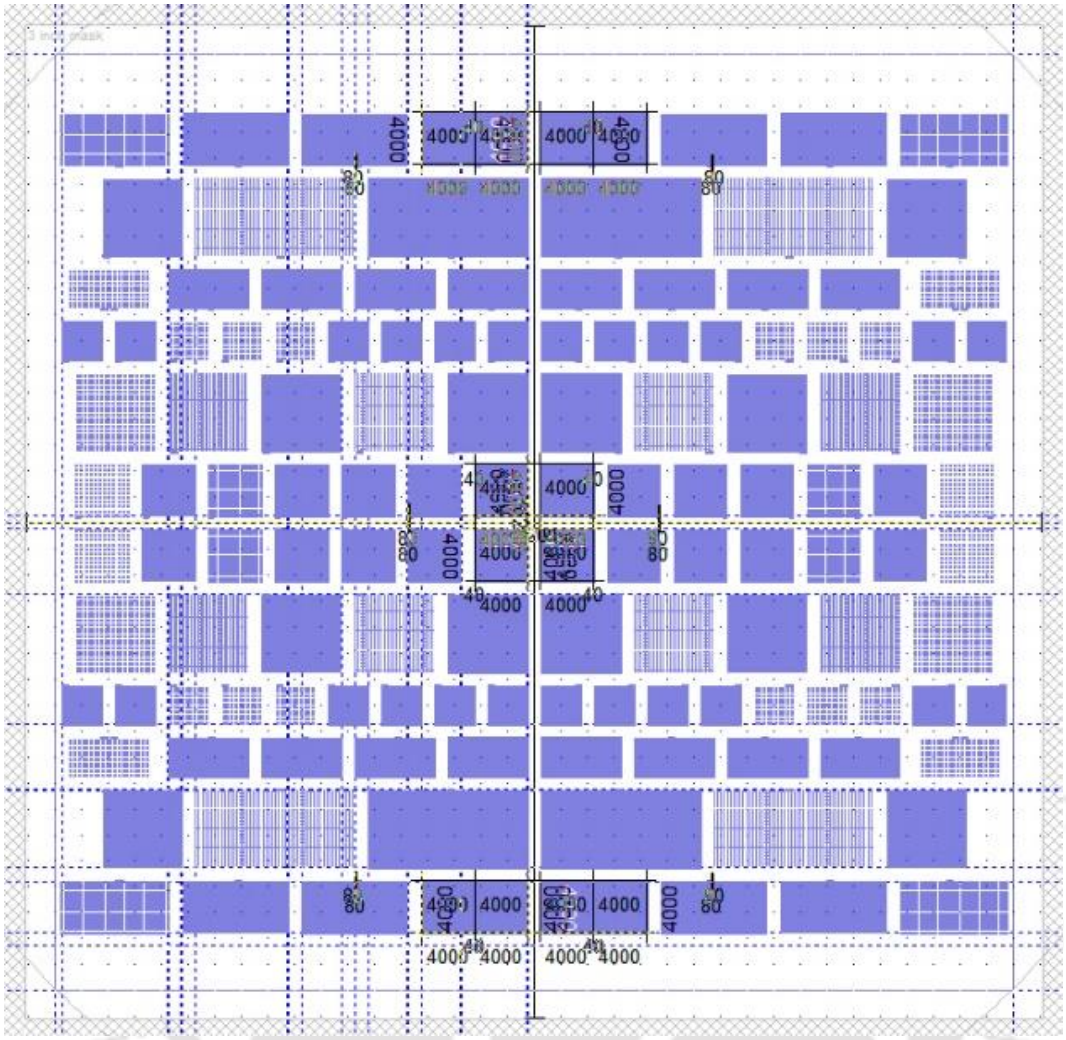

Figure 6. 20: positive mask designed for the variously shaped sliders in CleWin.

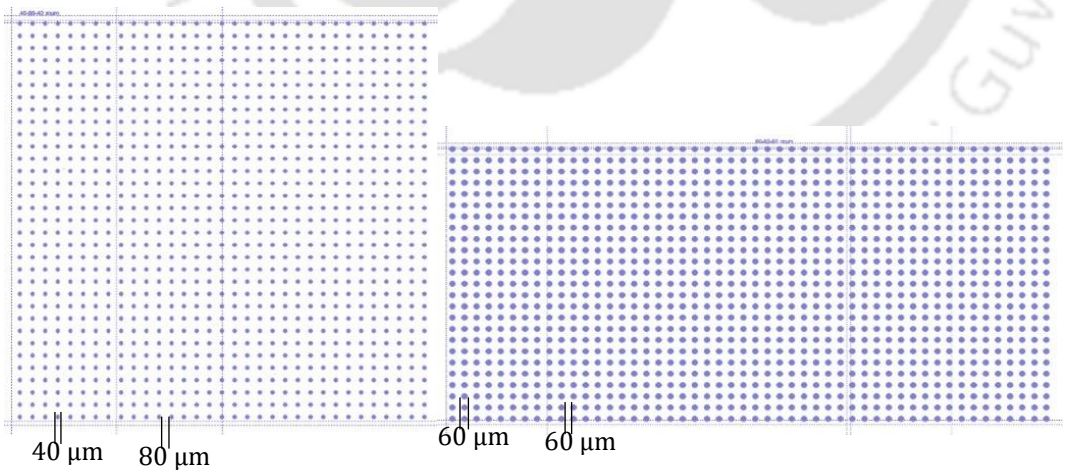

Figure 6. 21: positive mask designed for the slider having projections of (a) 40-80-40 µm, (b) 60-60-60 µm in CleWin.

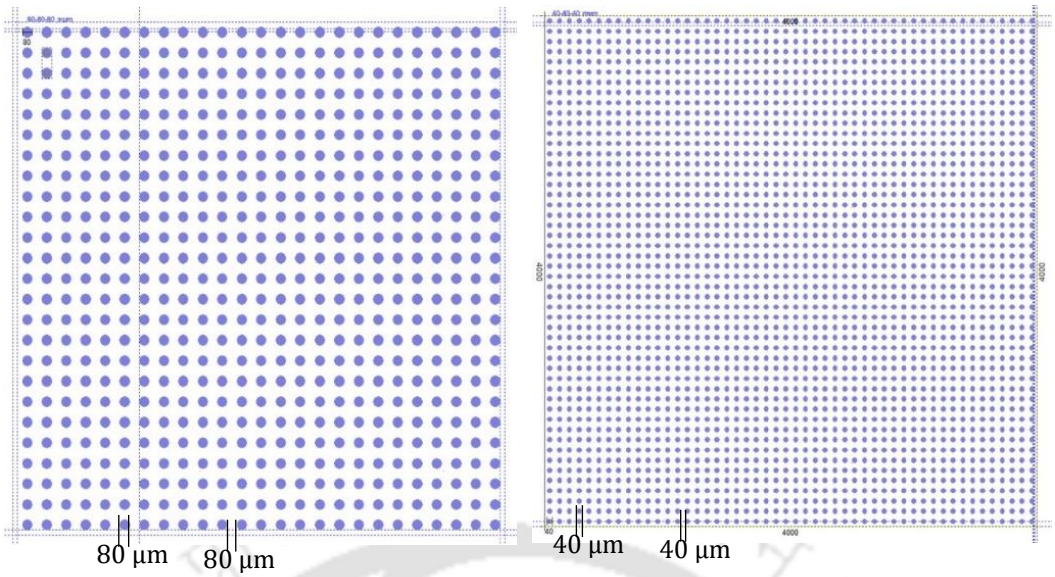

Figure 6. 22: positive mask designed for the slider having projections of (a) 80-80-80 µm, (b) 40-40-40 µm in CleWin.

As the projections on the Si are to be fabricated in both front i.e. mirror polished surface of Si and for projections on both side of the surface need to fabricate on the back side i.e. rough side of the Si on a whole 4/6-inch wafer.

6.3.2 Cleaning of the silicon wafer

The fabrication of sliders is carried out on 6 inches and 4-inch wafers. The cleaning of the substrate is done in order to remove the dust particles, oil, different marks, and grease from the fabricating surface of the silicon wafer. Si wafer is cleaned by dipping into Piranha (H_2SO_4:H_2O_2) with a ratio of (9:1) solution for 10 minutes. Then Si is dipped in HF (HF:H_2O) with a ratio of (1:50) for 5 minutes. To clean rest part of Si, it is dipped into DI water for a2-3 minute. Air blow is given to dry the wafer. The cleaned Si wafer is shown in Figure 6. 23.

Figure 6. 23: Picture of Si wafer after wet bench cleaning process.

6.3.3 Bonding recipe

To get a thicker Si wafer for making projections on both the sides, two 6-inch Si wafers are bonded together using AVG bonder. The bonder works on Van der Waal bonding technique. The two Si wafers are placed with polished surfaces together and heated to 450°C for 25 minutes at a pressure of 5×10^{-2} Torr. Then the temperature is increased to 460°C for 30 minutes. Then cooling is done at a temperature of 60°C for 15 minutes. The picture is shown in Figure 6. 24 (a) is after the bonding process. The total process took 4 hr 30 minutes to execute. The recipe for bonding of two Si wafers is given in Table 6.5.

Table 6. 5: Recipe for bonding two silicon wafers

Bonding Command	Parameter 1	Parameter 2
Heating top/bot	450°C	0.00.00
Pump on	High Vacuum	
Wait	Pressure	5×10^{-2}Torr
Wait	Temp bottom	440°C
Wait	Temp top	440°C
Flags out	All	
Wait	Time	0.00.00
Piston down	1500 N	0.00.00
Heating top/bot	460°C	0.25.00
Wait	Time	0.30.00
Piston up	-	-
Vent on	-	-
Cooling	60°C	0.15.00
Wait	Time	0.20.00

6.3.4 Annealing the bonded Si wafer

The bonded wafer needs to go for annealing after the bonding process to strengthen the bonding in Si. Bonded Si wafer is kept for annealing at temperature 1000°C for a time period of 4 hours. The real bonding time works only for 60 minute, but due to temperature ramp-up and ramp-down, it takes nearly 4 hours to complete the process. The picture of Si wafer shown in Figure 6. 24 (b) is after annealing.

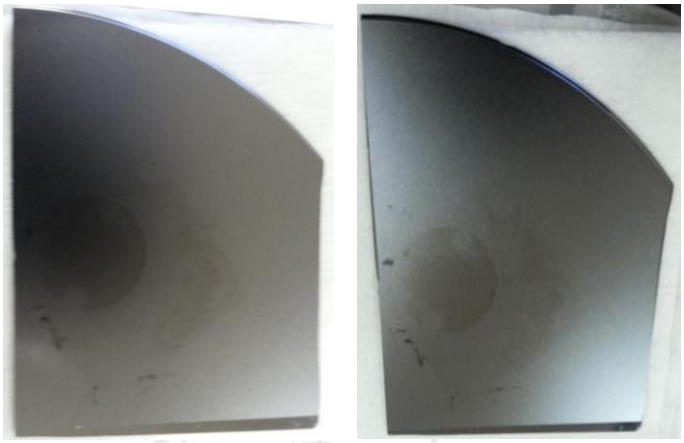

(a) (b)

Figure 6. 24: Picture of a Si wafer (a) after bonding (b) after Annealing.

6.3.5 Lithography for slider

After annealing is over, the bonded Si wafer is taken for the lithography process.

6.3.5.1 Cleaning bonded Si

The Si wafer is cleaned before it is taken for the lithography process. The wafer is cleaned with acetone and IPA for 2-3 and 1 minute, respectively.

6.3.5.2 Soft baking

The spun sample is soft baked by placing it on a hot plate at a temperature of 110°C for 60 s.

6.3.5.3 Photoresist coating

The wafer is then placed inside the spin coater. It is ensured that the centre of the wafer is exactly aligned with the spin coater. Photoresist AZ nLOF 2070 is dispensed from the bottle and spread all over the wafer. The wafer is spun at a speed of 500 rpm/s for 5 s and followed by 4000 rpm/s for 40 s. By this method, the photoresist coating thickness of about 1 μm is achieved over the wafer.

6.3.5.4 Soft baking

The spun sample is soft baked by placing it on the hot plate at a temp. of 95°C for 60 s.

6.3.5.5 UV exposure

The positive mask thus prepared is placed in UV mask aligner (EVG 620 Double Sided Mask Aligner) substrate chuck for the UV exposer of the photoresist. The pattern on the mask is transferred to the surface of the wafer through UV exposed with an exposure UV dosage rate of 65 mJ/cm^2. For double side development, a thorough alignment of the pattern is carried out. The wafer is taken for development to wet bench.

6.3.5.6 Development of projection patterns

The pattern is developed for 30 s in MF-26A for 18 s. The wafer is taken out from the developer solution once the patterns are identified in the wafer. If the wafer is placed for excess time it will lead to over development and finally end with poor patterns on the wafer. The images of developed projections are taken and measured through an optical microscope for verification as shown in Figure 6. 25.

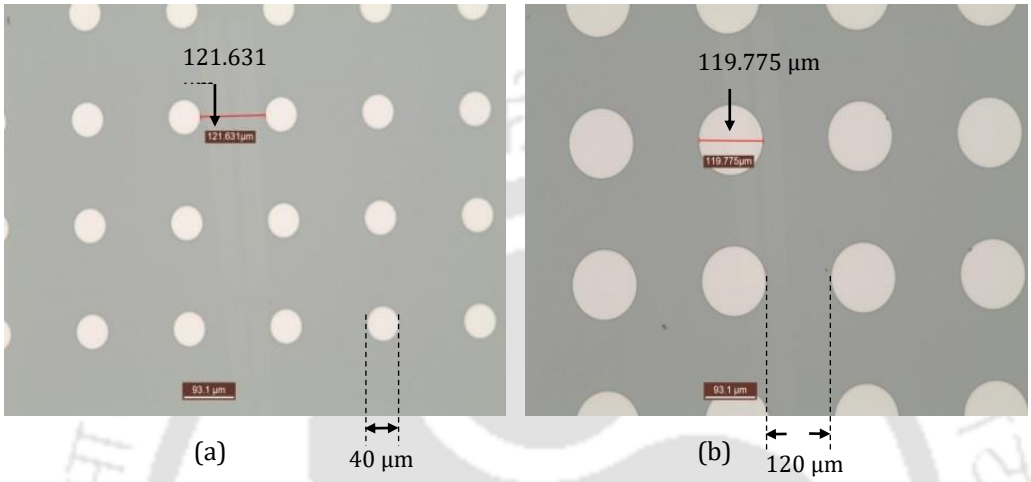

Figure 6. 25: Pictures taken by Digital Microscope of projections on the surface of Si wafer after lithography process for dimension of (a) 40 µm diameter and 160 µm pitch (b) 120 µm diameter and 240 µm pitch.

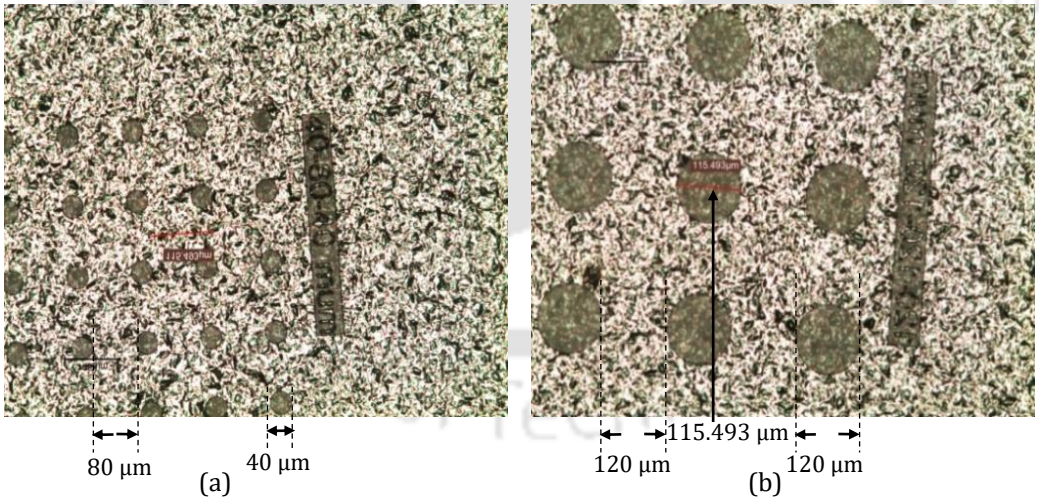

Figure 6. 26: Pictures taken by Digital Microscope of projections on the surface of bonded Si wafer after lithography process for dimension of (a) 40 µm diameter and 120 µm pitch (b) 120 µm diameter and 240 µm pitch.

6.3.6 Dry etching for slider

The plain and bonded silicon wafers are taken for dry etching. It needs 2 minutes for etching of 2 µm thick Si. The parameters used for etching are ICP power 1200 W and RF power 150 W. Gases used are 1st gas C4F8 at 90 SCCM and 2nd gas SF6 at 50 SCCM. The temperature of

the chamber is 15°C and pressure inside the chamber is 16 mTorr. For single sided Si wafer, ashing is done as a part of the cleaning process. But ashing is not applicable for bonded silicon wafers. The device structures are examined with the help of optical microscope shown in Figure 6. 27.

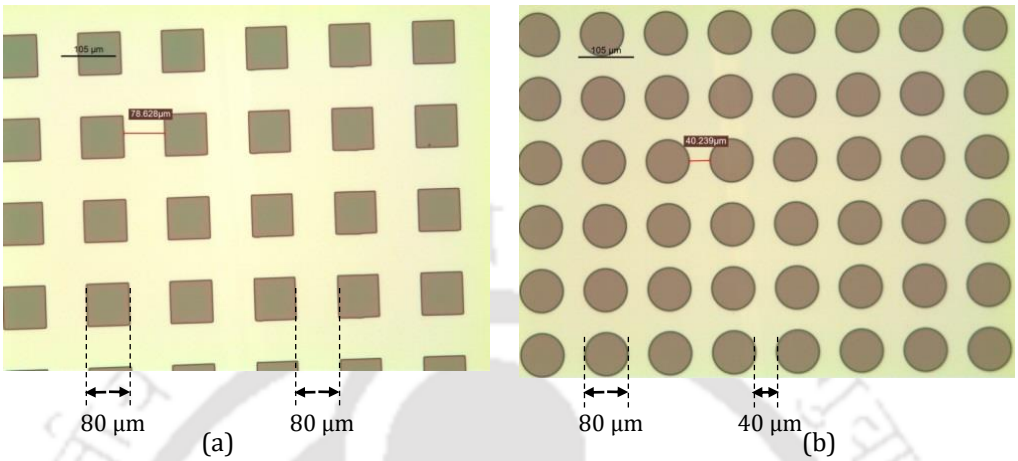

Figure 6. 27: Pictures taken by digital microscope of projections on the surface of Si after etching for thedimension of (a) 80 µm × 80 µm and 160 µm pitch, (b) 80 µm diameter and 120 µm pitch.

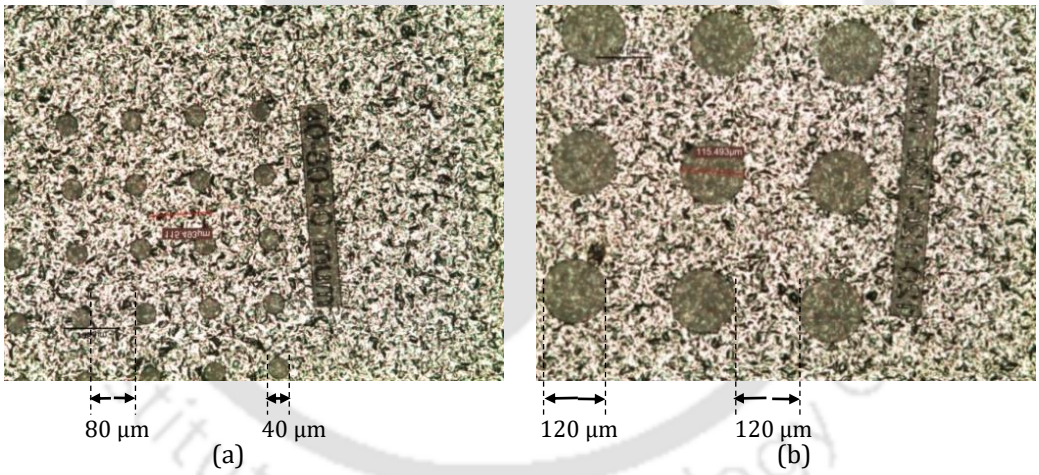

Figure 6. 28: Pictures taken by digital microscope of projections on the surface of bonded Si wafer after etching for dimension of (a) 40 µm diameter and 120 µm pitch, (b) 120 µm diameter and 240 µm pitch.

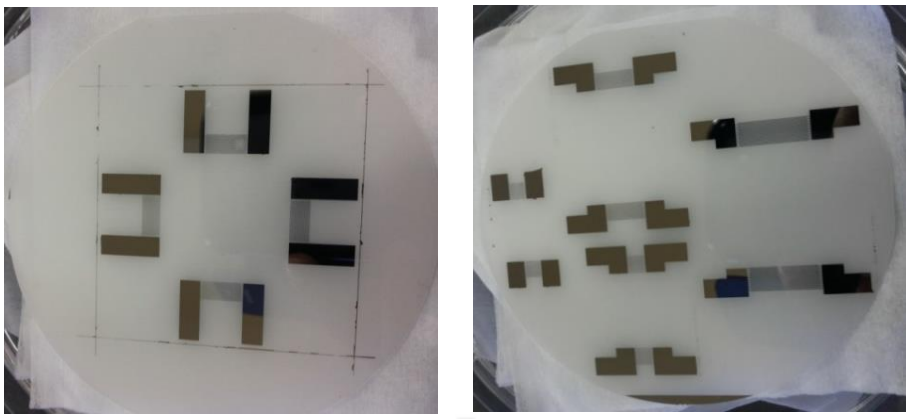

(a) (b)

Figure 6. 29: Final picture of fully developed IDTs on the LN substrate. (a) IDTs fabricated at four sides of the rectangular substrate, (b) delay lines of 300 µm, 400 µm, and 600 µm wavelength.

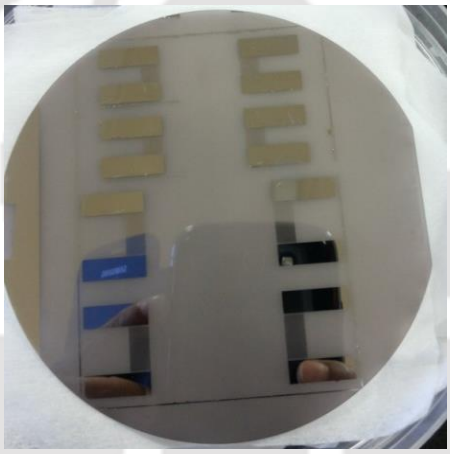

Figure 6. 30: Final picture of fully developed delay lines of 300 µm and 400 µm wavelength on black LN substrate.

6.4 Dicing of the Devices

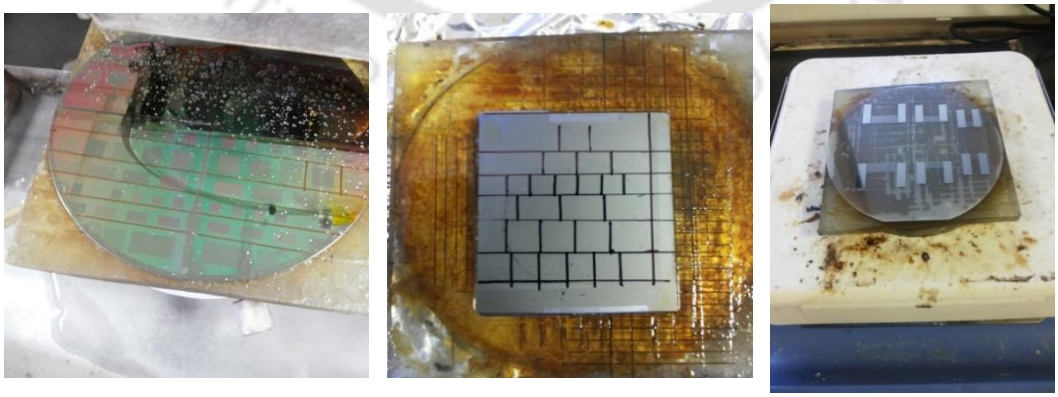

Figure 6. 31: LN substrates with a fabricated delay line and Si wafers with fabricated cylindrical projections are attached to the dicing tool for the separation process.

To separate the devices after fabrication, wafers undergo dicing process. Wafers are attached to the dicing tool with the help of wax as shown in Figure 6. 31. The wafers are attached to the tool, in order to avoid any type of disturbance during the dicing process.

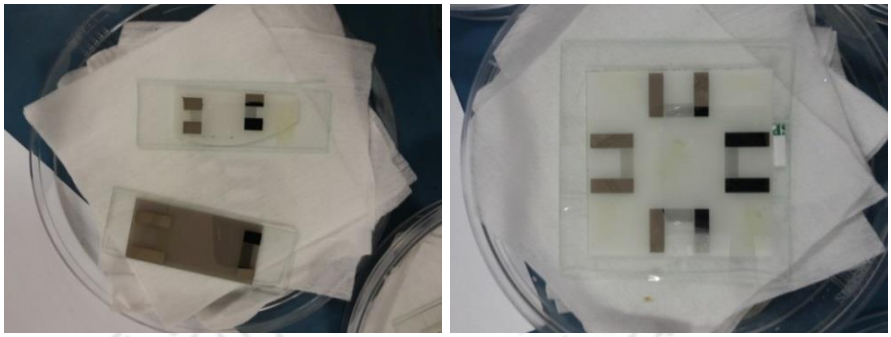

Figure 6. 32: Final picture of fully developed delay lines on the LN substrate after dicing and attaching to the glass substrate to protect from damage, (a) IDTs fabricated at two sides of the substrate, (b) delay line of 400 µm wavelength.

After the dicing process, the delay lines on the LN substrate are attached to the glass substrate to avoid damage.

6.5 Wire Bonding of the Delay Line Devices

Aluminium wire is connected from a bond pad of the delay line to the circuit board through wire bonding as shown in Figure 6. 33.

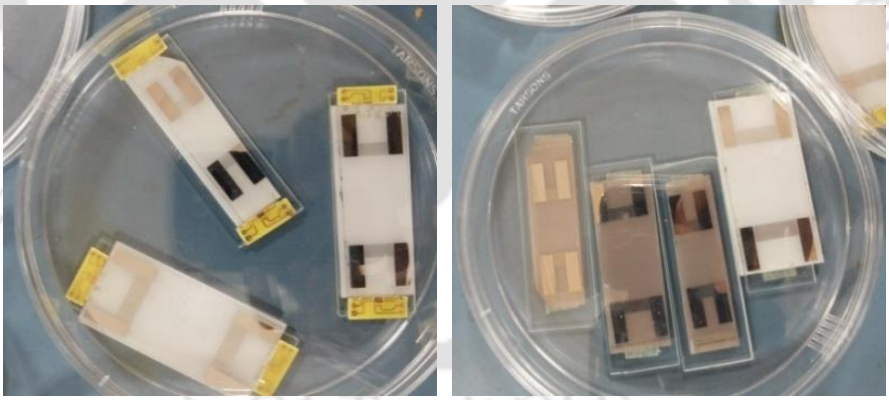

Figure 6. 33: Delay lines are displayed after wire bonding is carried out using wire bonder.

As bonded wire is not sufficient to connect with external point, silver epoxy was used to connect hard bond with the bond pad as shown in Figure 6. 34.

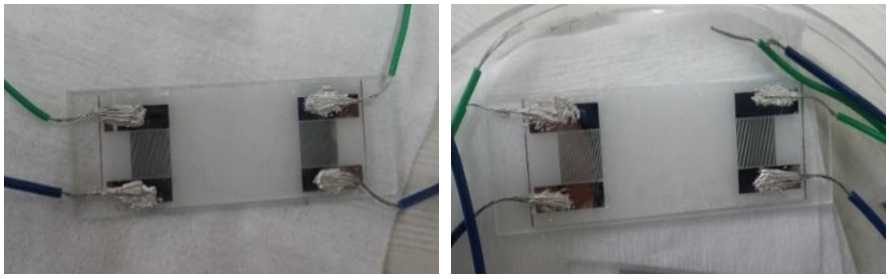

Figure 6. 34. Delay lines are displayed after wire bonding is carried out using silver epoxy.

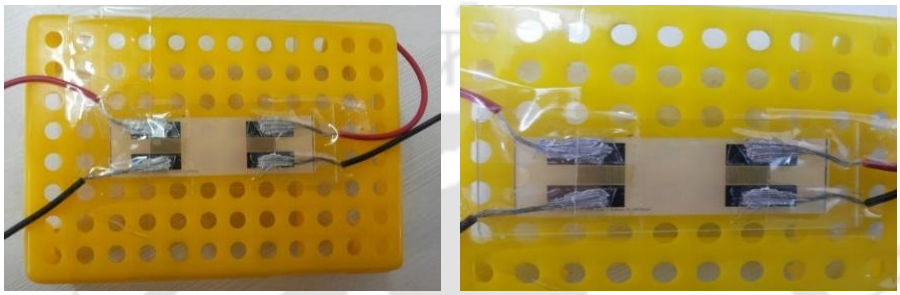

Figure 6. 35: Delay lines are displayed after fixing on the supporting base.

6.6 Summary

In this chapter, the components required for assembling the DFD SAW motor are fabricated. Initially, the processes for the fabrication of stator and slider are proposed. The parameters required for fabrication of the devices are optimised through mathematical modelling and Matlab simulation. Then the fabrication of the device is carried out in clean room fabrication facility. Finally, the fabricated devices are separated by dicing and the electrical connection is provided through wire bonding and silver epoxy. Thus the devices are ready for testing and SAW motor demonstration.

7

Characterization and Experimental Validation of the SAW Motor

This chapter of the thesis describes the assembling, experiments and measurements carried out on the fabricated SAW devices. The details about the fabrication of the devices are given in chapter 6. The measurements of the resonance frequency, output electric potential, and other characteristics of the SAW devices with IDT are performed using a network analyser (Agilent E8361A & Agilent 8753ES), a signal generator (Agilent 33120A) and oscilloscope (Yokogawa DL9040). The resonance frequency of the SAW devices with IDT fabricated on LN and cylindrical projections on Si is measured from the S_{11} parameter of the device. The output electric potential of a SAW delay line with IDT fabricated on LN material is measured using the oscilloscope for an input from the signal generator.

7.1 Characterization of Stator

The stator for the experiment is made of a 128° rotated Y-cut X-propagation $LiNb0_3$ piezoelectric wafer. Two IDTs (interdigital transducers) were arranged on 4 inches' wafer. The IDT pitch was 300 μm and the electrodes strip width was 75 μm. The electrode strip was 22 pairs for each transducer. The driving frequency was 13.50 MHz.

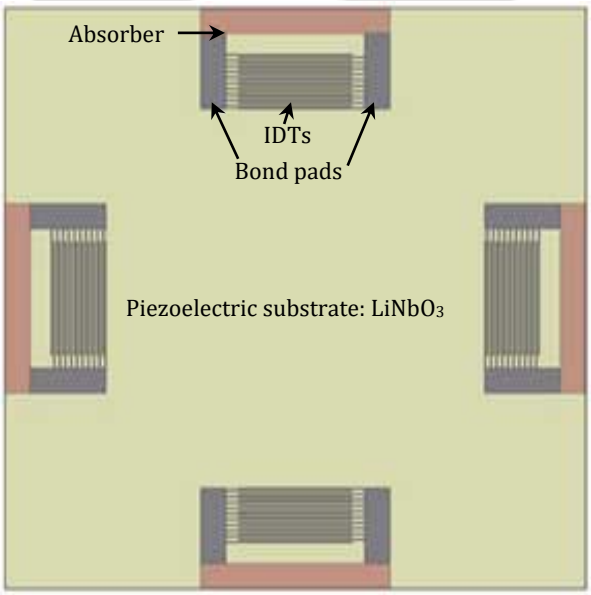

Figure 7. 1: Schematic diagram of a rectangular stator showing four IDTs fabricated on the surface of a piezoelectric substrate at the midpoint of each side followed by the SAW absorber.

The Figure 7. 1 shows a stator having four IDTs fabricated on the surface of a piezoelectric substrate, one comb-shaped IDT each placed at the midpoint of each side of the rectangular stator. Figure 7. 2 shows a stator having two IDTs fabricated on the surface of a piezoelectric substrate, one comb-shaped IDT each placed at the end side of the stator while the absorbers are placed in both the cases followed by the IDTs to avoid edge-reflections.

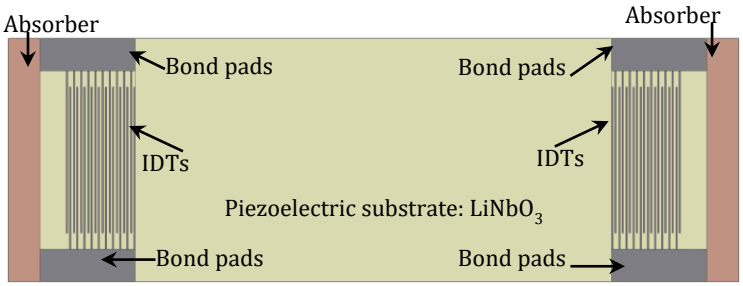

Figure 7. 2: Schematic diagram of a stator showing two IDTs fabricated on the surface of a piezoelectric substrate at two side ends followed by the SAW absorber.

The stator surface has a roughness in nanometers and has a great impact when calculating the contact mechanics between the stator and slider. The roughness of the surface fabricated device is measured with the help of Dektak surface profiler at IISc Bangalore and found to be around 5 nm shown as in Figure 7. 3.

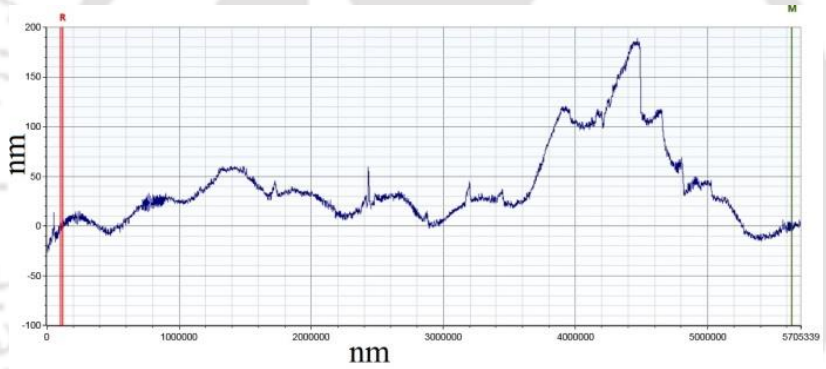

Figure 7. 3: The surface profile of LN stator after the IDT fabrication process, measured by DekTak surface profiler.

7.2 Measurement Setup and Results of the Delay Line Testing

This section describes the measurement setup and characteristics of the SAW devices. The measurement setup comprises a metal enclosure coated with Al thin foil, Bayonet Neil connector (BNC) for signal connection, copper wires connecting the IDT and BNC inside the enclosure as shown in Figure 7. 4. Though the IDT is designed for delay line SAW device, the following experiments on the measurement of S_{11} parameter use only one port of the device. While measuring S_{12} parameter both sides of the delay line is used.

Figure 7. 4: The set up showing network analyser for testing the device.

The fabrication of IDT on LN wafer is described in section 6.1.1. The operation of a SAW delay line using the IDT is verified in the laboratory. The resonance frequency (f_r) of the SAW device with IDT is determined from the S_{11} parameter obtained using network analyser Agilent E8361A. The measurement setup is shown in the picture in Figure 7. 4. The RF probe of pitch length of 50 μm is used

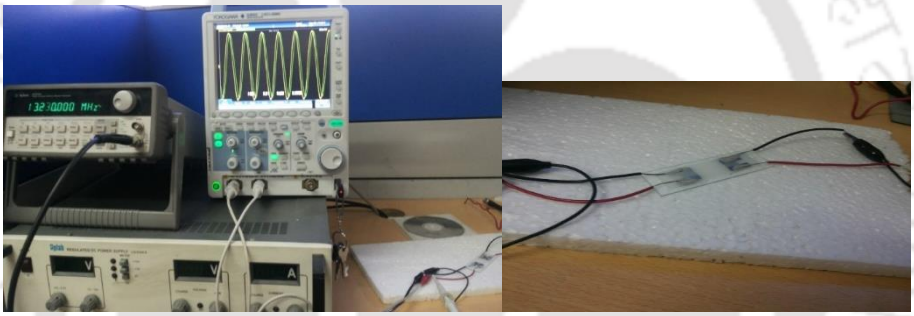

Figure 7. 5: The testing setup for the delay line containing the signal generator of max 15 MHz and voltage 10 $V_{p\text{-}p}$, oscilloscope and the delay line.

7.2.1 Testing of delay line of different wavelength

During the measurement of anS_{11} parameter, the probe of the network analyser is connected to the bond pads of the delay line. The scattering parameter S_{11} is found to be a straight line at 0 dB. Subsequently, an S_{11} parameter of the delay line meant for 13 MHz fabricated on Y–X LN stator is measured using a network analyser (Agilent 8753ES). The response of the device in terms of log magnitude of S_{11} is shown in Figure 7. 6. It can be seen from Figure 7. 6 the measured resonance frequency of the fabricated device is around 12.84 MHz and has input return loss of -100.6 dB.

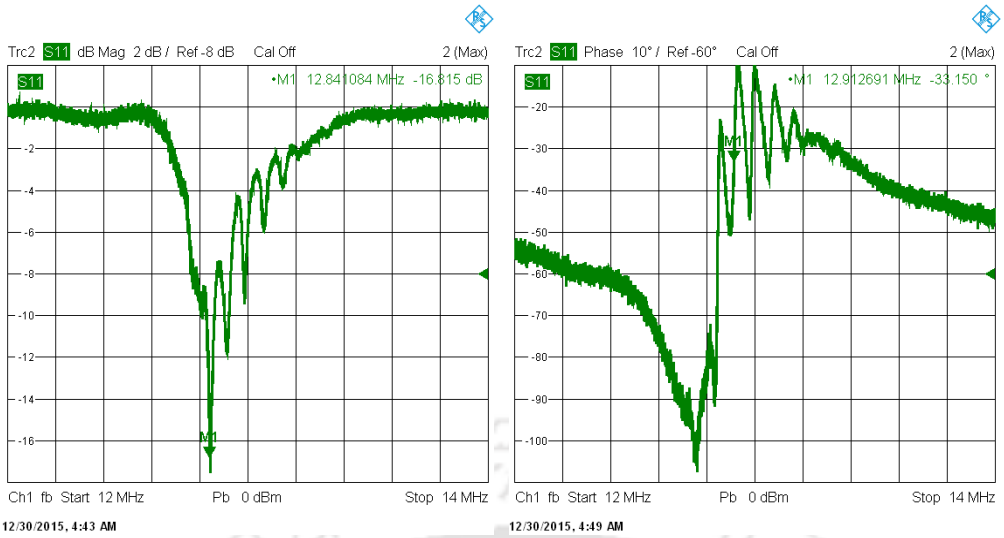

(a) (b)

Figure 7. 6: S_{11}parameter of the SAW delay line using IDT of λ of 300 µm fabricated on LN stator showing (a) conductance (b) susceptance.

The plot of S_{12} in Figure 7. 7shows that the resonance frequency of the device is 12.84 MHz with a return loss of –10.998 dB at the resonance frequency. The pictures are taken from the screen shot of the S_{11} parameter obtained on the network analyser.

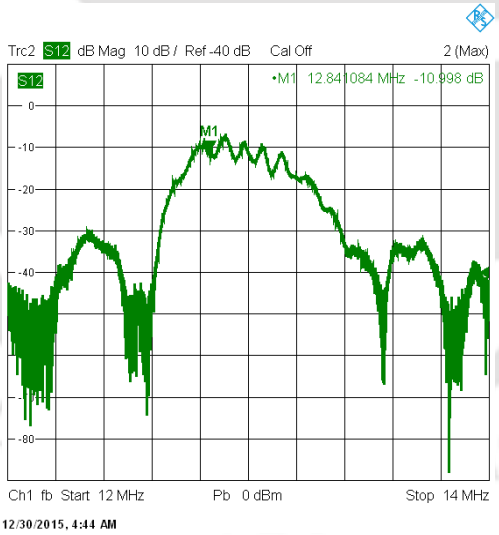

Figure 7. 7: S_{12} parameter of the delay line showing magnitude.

As the measured S11 parameter of the delay line shows not properly matched, matching circuits are designed to get the maximum output. The values for the components used to design the matching circuit are taken from the previously measured delay line parameters and implemented to design the circuit [111] as shown in Figure 7. 8. Z_S is the input power supply from network analyser and at Z_L the delay line is connected to measure at the output from the device. The corresponding matching circuit is made as shown in Figure 7. 9.

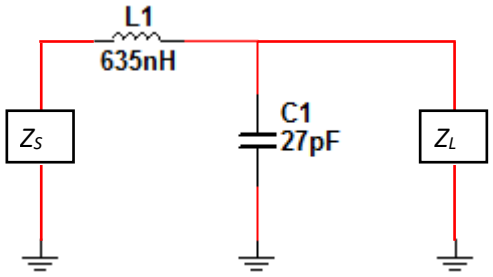

Figure 7. 8: Designed matching circuits.

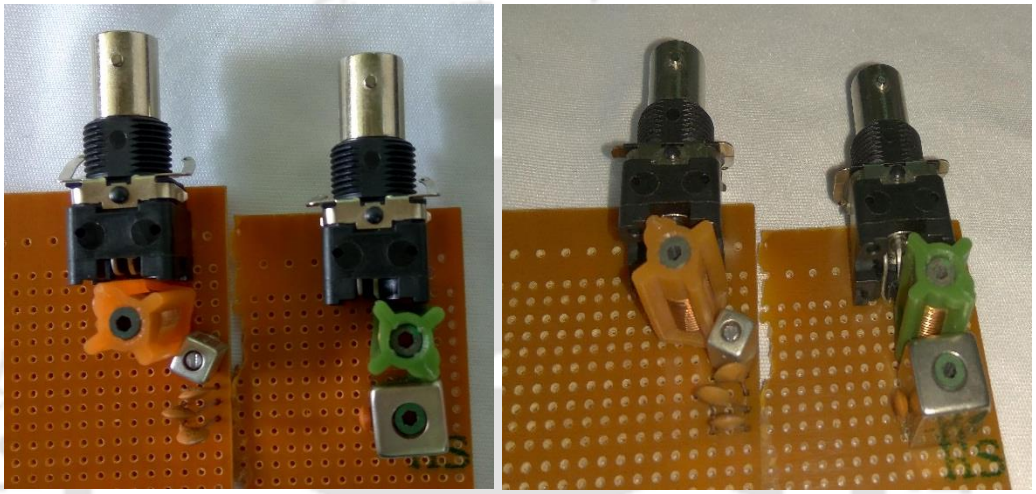

Figure 7. 9: Designed matching circuits.

The Figure 7. 10 shows the measured result of the same delay line measured with the matching circuit.

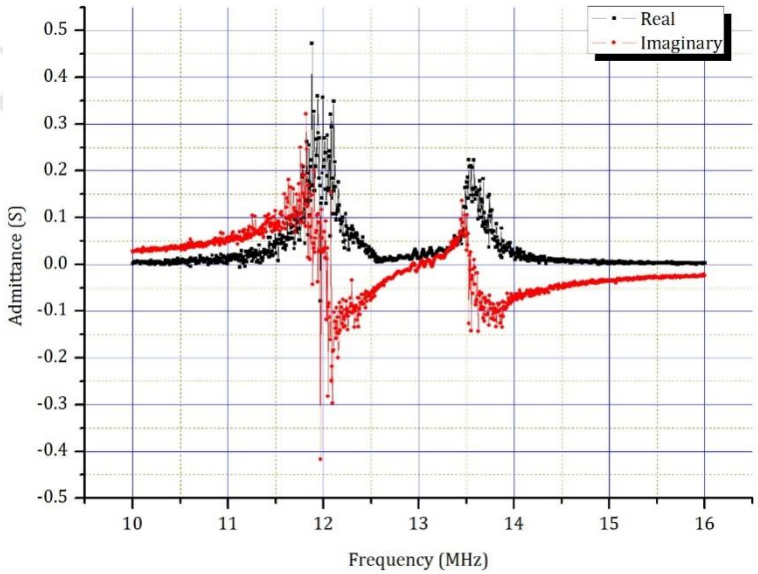

Figure 7. 10: S_{11} parameter of the delay line showing magnitude after matching circuit is added.

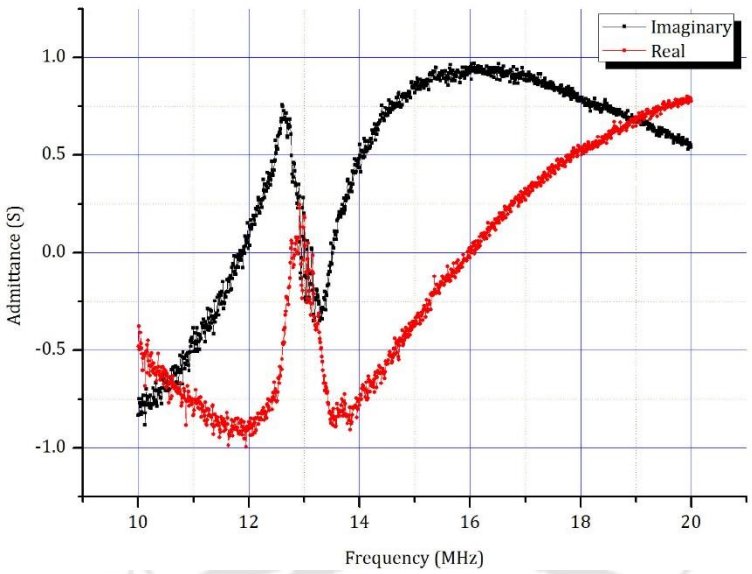

Figure 7. 11: S_{11} parameter of the delay line showing magnitude.

7.3 Characterization of the Slider

Slider with a uniform array of projections on its contact surfaces is preferably made of at least one material selected from semiconductor, ceramic, metal and polymer, and has one slot each at two sides of the slider for connecting a slider that drives the load. The projections on the two sides of the slider should have the identical pattern and the opposite projections should have a common axis. The cross-section of the projections can be circular, square, rectangular, or any other suitable shape. Figure 7. 12 shows the cuboidal slider having an array of projections with a circular cross-section and Figure 7. 13 shows the cuboidal slider having an array of projections with square cross-section on both the contact surfaces.

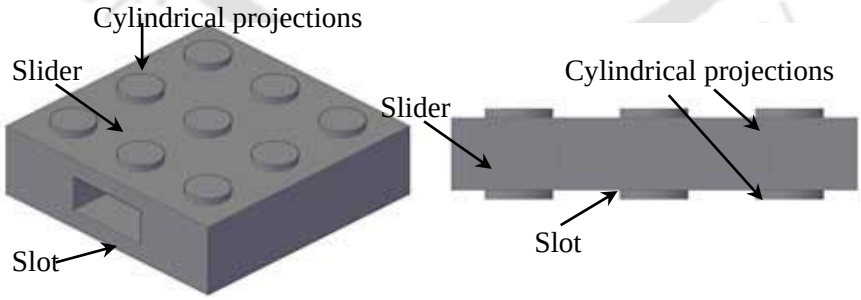

Figure 7. 12: Schematic of aslider having projections of circular cross-sections on both contact surfaces.

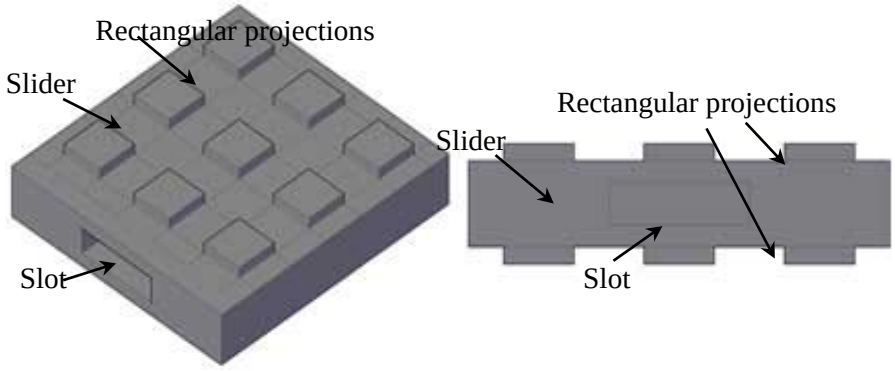

Figure 7. 13: Schematic of a slider having projections of square cross-sections on both contact surfaces.

The surface profile of the silicon wafer on the polished side is measured with the help of DekTak surface profiler. It varies maximum up to 5 nm in height on the surface of the polished side of the Si wafer. Hence the projections on the surfaces were done with a height of 2 μm.

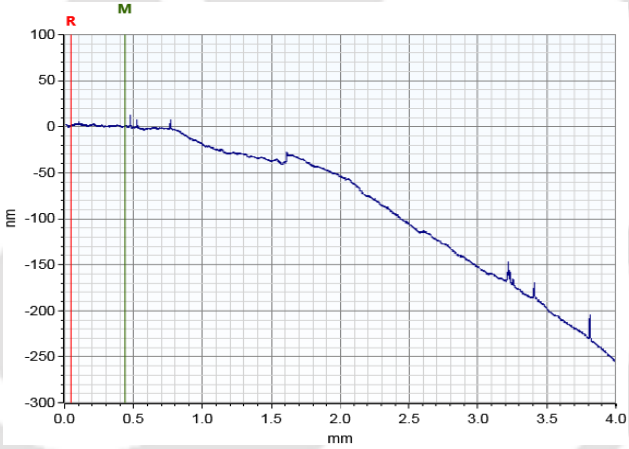

Figure 7. 14: The surface profile of polished side of Si, measured by DekTak surface profiler.

The surface of the polished side of the silicon is measured to know the surface roughness through DekTak surface profiler as shown in Figure 7. 14.

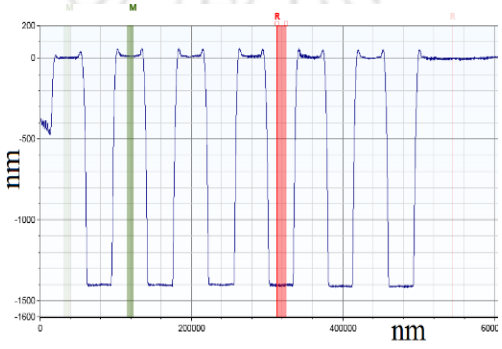

Figure 7. 15: The depth of the cylindrical projection on polished side of Si, measured by DekTak surface profiler

The height of the projection on the polished side of the silicon is measured through the DekTak instrument and subsequent measurement is given in Figure 7. 15. The roughness of the Silicon wafer at the back side is measured with the help of DekTak surface profiler as shown in Figure 7. 16. It varies up to 4 µm in amplitude on the surface of the polished side of the silicon wafer. Hence the projections on the surfaces were done with a height of 4 µm.

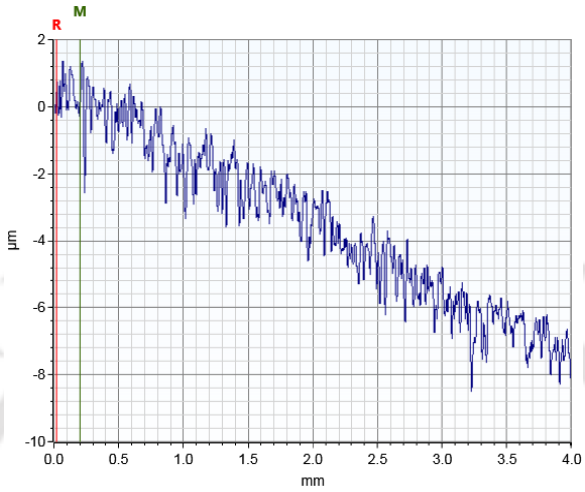

Figure 7. 16. The surface profile of rough side of Si, measured by DekTak surface profiler.

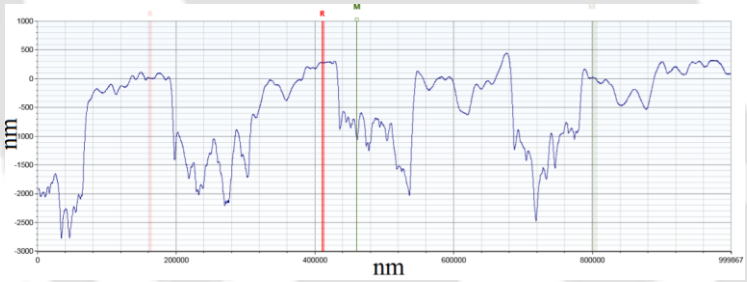

Figure 7. 17. The height of the cylindrical projections on bonded Si substrate, measured by DekTak surface profiler.

The height of the projection on the rough side of the silicon is measured through the DekTak instrument and subsequent measurement is given in Figure 7. 17.

7.3 Experimental Set-up for the SAW Motor

The delay line devices, after verifying their characteristics, are assembled for testing of the proposed principle of the DFD SAW motor.

7.3.1 Assembling and Testing of a Stator

The stator was a rectangular plate of 128° rotated Y-cut X-propagating LN substrate which had IDTs fabricated at both ends. The dimensions of the stator were 60 × 13.6 × 0.35 mm^3. The IDTs were fabricated by the lithography followed by thermal evaporation deposition of

Al. The dimensions of the IDTs were 300 μm in pitch, 75 μm in electrode strip width and gap, and 4.5 mm in the aperture. The IDTs were composed of 30 electrode strip pairs and the resonance frequency for the Rayleigh wave propagation about 13 MHz. The stator of SAW motor is prepared by attaching the delay line device on a glass substrate to provide support and avoid damage. The stator was placed on a 10-mm-thick glass substrate, so the frictional surface of the slider was visible. Sticky tapes were attached as acoustic absorbers [112] to the outside of the driving IDT and to the other side of the IDT so as to prevent reflection waves, which was intended for the accurate measurement of the friction/ contact dynamics between the slider and the travelling Rayleigh wave [113].

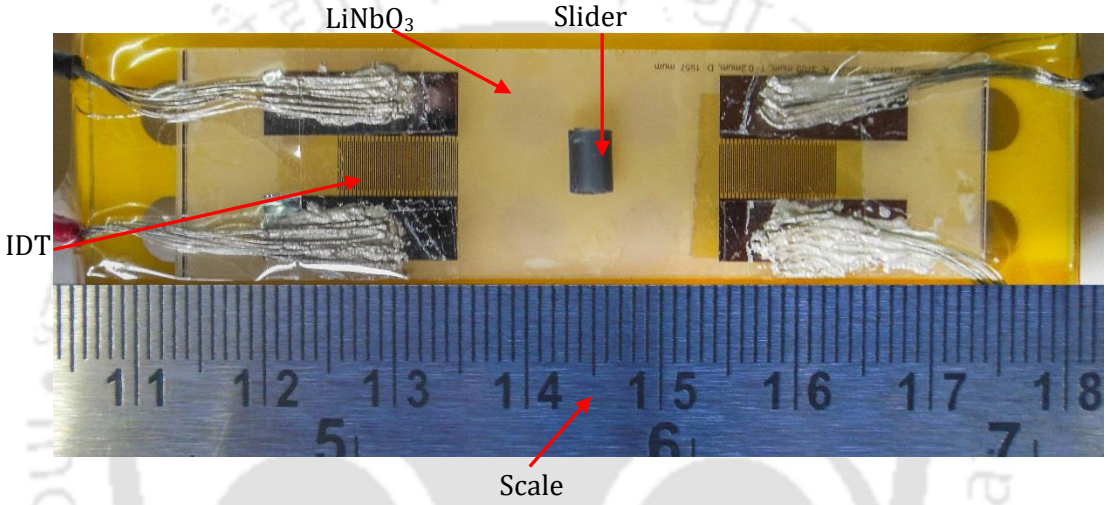

Figure 7.18: Photo of SAW motor set up showing the stator and the slider.

A cylindrical slider is placed at the active region of the delay line of the stator. The glass substrate and the stator were fixed to a basement block by a steel jig that had a glued rubber plate at the contact area with the stator. The basement block had a 120 × 80 mm^2 observation window underneath the track of the slider. The photograph of the SAW motor setup with the upper stator removed is depicted in Figure 7.18. Initially, the test is carried out on a single stator by placing a liquid droplet in the active region of the delay line, and the liquid droplet is found displaced after applying power supply to the IDT.

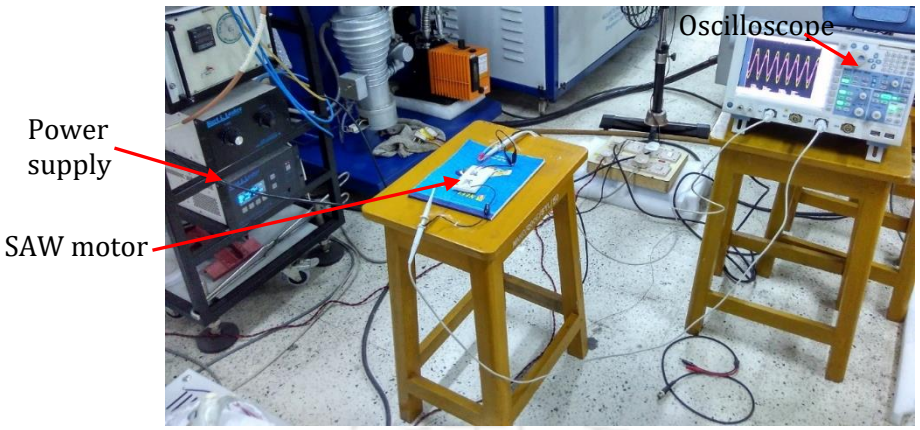

Figure 7. 19: The setup of the SAW motor showing the power supply connected to oscilloscope and the device.

The liquid is placed over the surface of the stator, where the cylinder is placed. We thus supposed that the measured displacement signals were mainly derived from the displacements of the slider. Once the power is switched on, the liquid makes a motion in the direction of wave propagation, the same way the slider also starts moving. This setup and the motion of the slider is captured through the digital video camera. Subsequently, a slider placed with a liquid drop in the active region of the delay line is also displaced. The displacement of the slider data is retrieved from the video and processed to get the displacement of the slider. With 100 V continuous wave excitation, the slider is observed to cover a distance of 16 mm at the end of 0.8 s. The normal direction vibration amplitude of the surface particle was 16 nanometer at a driving voltage of 100V. Because of the elasticity of the materials, the contact area of the slider ball is finite. The arrangement for the dual frictiondrive motor is shown in Figure 7. 19.

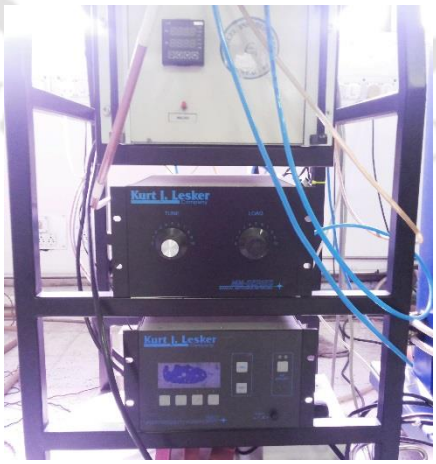

Figure 7. 20: The RF power source used for testing the device.

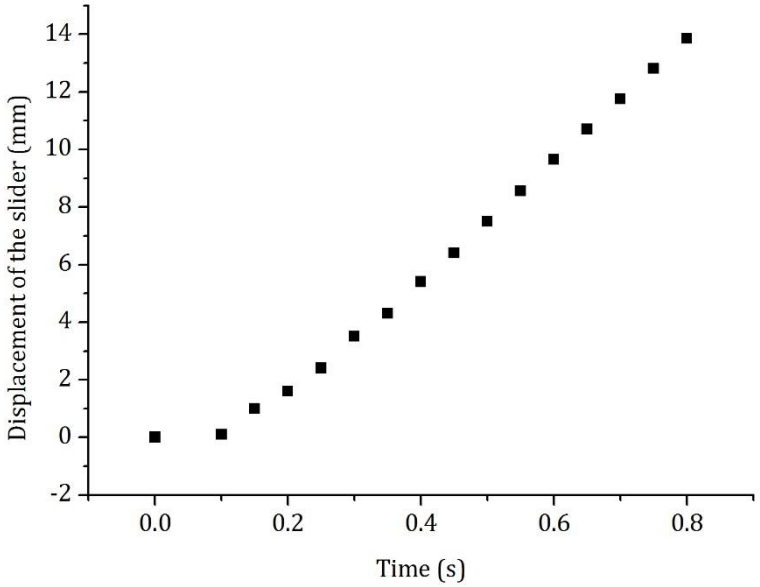

Figure 7. 21: Displacement of slider observed in single side stator.

The contact radius is able to evaluate with the Hertz contact theorem approximately. The actual contact radius was several micrometer at most when the steel ball sliders were put on the stator with attractive force by the neodymium permanent magnet. It should be pointed out that the deformation is almost same order with the stator vibration deformation. The displacement of the slider is 16 mm at the end of 0.8 s as shown by plotting the graph Figure 7. 21. While the velocity of the slider is about 20 mm/s as per the plotted graph Figure 7. 22.

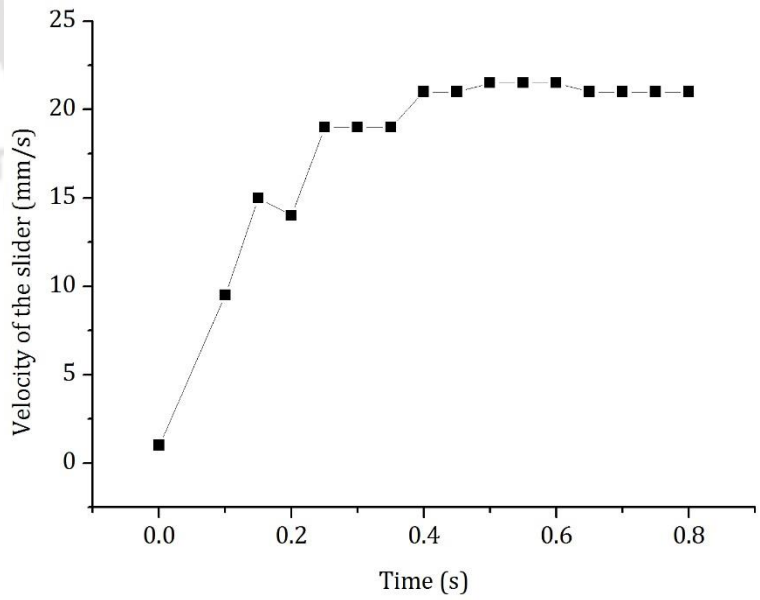

Figure 7. 22: Velocity of slider observed in single side stator.

7.3.2 Assembly of DFD SAW motor

Two identical stators are placed facing each other with a gap using two spacers at the ends while holding a cylindrical slider tightly between them in the active region with help of four screws as shown in Figure 7. 23.

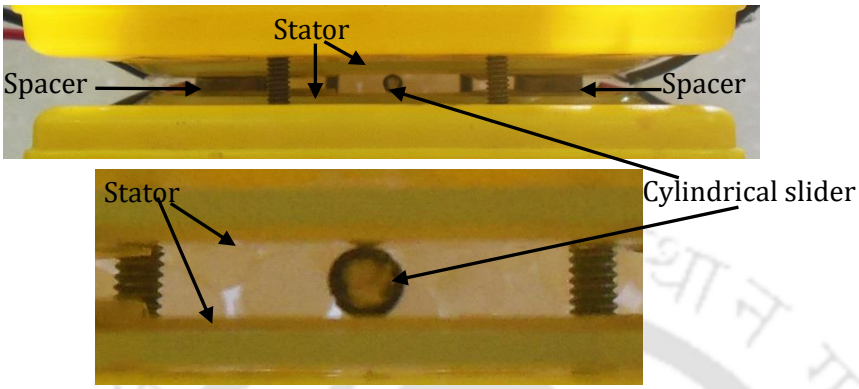

Figure 7. 23: Picture of the DFD SAW motor where the slider is placed between the two stators.

The spacers are made of anon-metallic material to keep a gap that equivalent of the height of the slider placed. The four metallic screws are placed at the corners of the base to complete the arrangement and can be adjusted to provide the desired preload. Electrical connections to the bond pads of the IDTs are provided through the silver epoxy. The silver epoxy is pasted over the bond pads with wire in the ratio of 1:1 epoxy and adhesive respectively. The matching circuits are connected to the extended wire from IDTs as shown in Figure 7. 24. The RF signal generator for supplying the required signal at the resonance frequency is connected to the matching circuits so that the power supply to the IDTs can be provided through the matching circuits to the IDTs as shown in Figure 7. 25. This completes the assembly of the experimental DFD SAW motor.

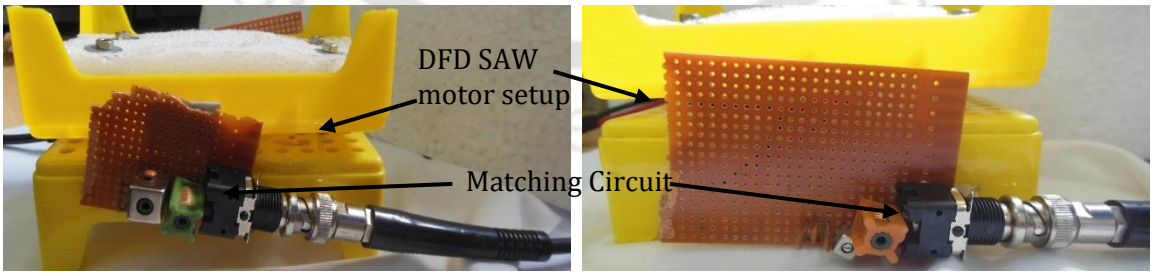

Figure 7. 24: Picture of the DFD SAW motor connected with matching circuit.

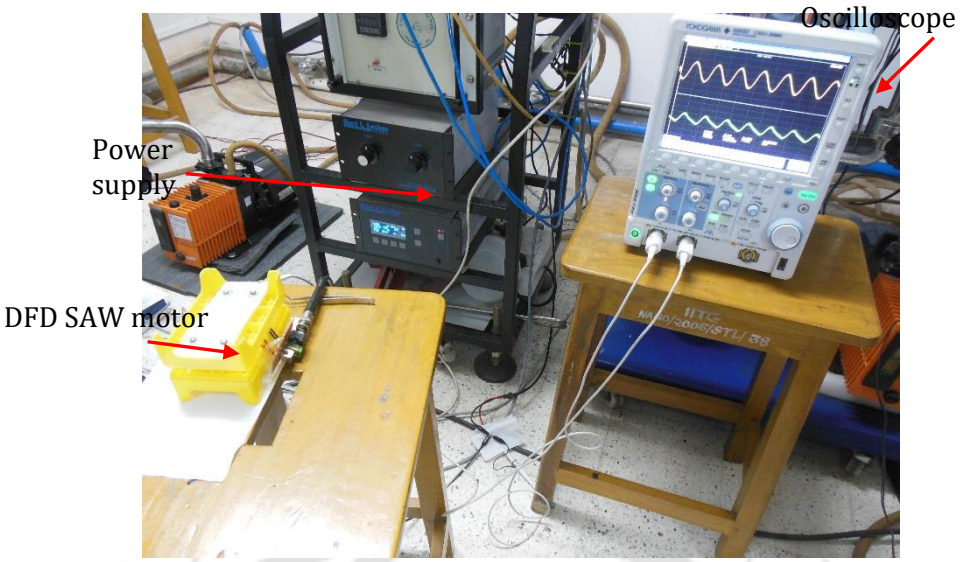

Figure 7. 25: Picture of the DFD SAW motor connected with RF power source and the Oscilloscope.

7.3.3 Testing of DFD SAW motor

When continuous wave excitation of 100 V at the resonance frequency is applied to IDTs of the left side from the top and bottom stators of the motor, while the IDTs at the right side of the stator are connected to the oscilloscope measuring the RF signal. To accomplish the motion of the slider, need to setup the assembly in such manner that the preload will be equivalent to the required one. The preload is adjusted through the four screws available at corners of the holding base. Since the two stators are kept facing each other, for the SAW travelling in a +X direction, the particles at the surface of the stator make anticlockwise elliptical motion and for the SAW travelling in –X direction the particles at the surface of the stator make anticlockwise elliptical motion.

Figure 7. 26: Picture of the input and output side signal from the delay line.

So the slider is dragged both from the top and bottom stator into a single direction i.e. towards the activated IDTs. The applied preload generates high frictional force on the shaft in –X direction at both the contact points and the shaft performs translational motion towards the activated IDTs.

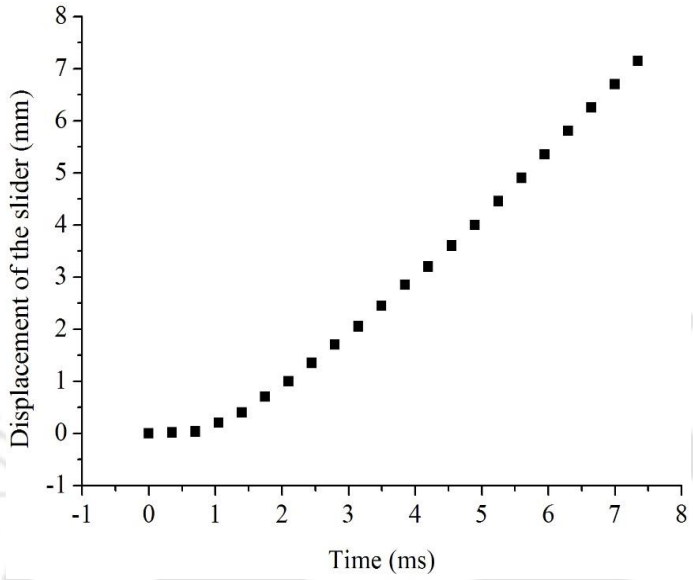

Figure 7. 27: Displacement of theslider in thedouble side.

With the application of the power supply, the slider makes a motion towards the activated IDTs and the motion of the slider is recorded by a digital video camera. The slider is displaced by 15 mm in 0.4 s towards the excited IDTs. When the IDTs on the other side are excited the motion of the slider is reversed.

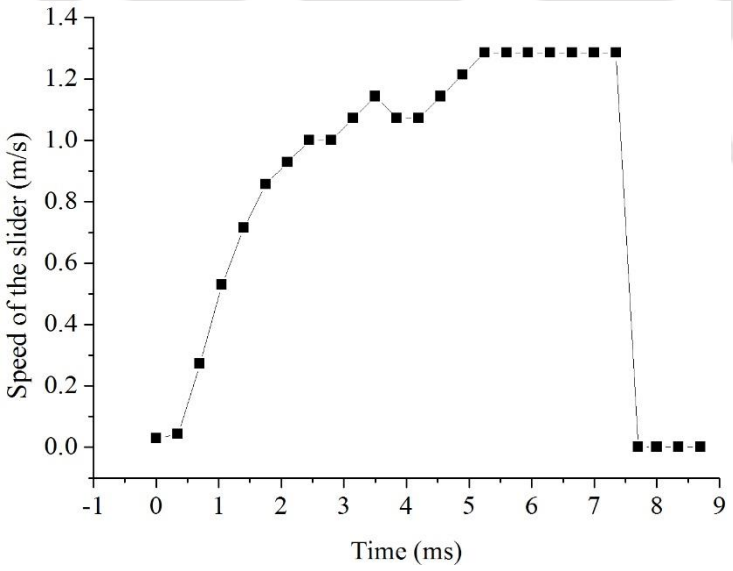

Figure 7. 28: Velocity of theslider in thedouble side.

The displacement of the slider is 15 mm at the end of 0.4 s as shown by plotting the graph Figure 7. 27. While the velocity of the slider is about 1.3 m/s as per the plotted graph Figure 7. 28. As compared to the single side the velocity of the slider in dual friction drive is high.

7.3.4 Rotational motion

To observe the motion of slider as a rotational way, the assembly of the SAW motor is arranged as per the proposed one. Two identical stators are placed facing each other with a gap using two spacers at the ends while holding a cylindrical shaft tightly between them in the active region with help of four screws as shown in Figure 7. 29. The spacers are made of anon-metallic material to keep a gap that equivalent of the height of the slider placed. The four metallic screws are placed at the corners of the base to complete the arrangement and can be adjusted to provide the desired preload. Electrical connections to the bond pads of the IDTs are provided through the silver epoxy. The matching circuits are connected to the extended wire from IDTs. Now the arrangement of the matching circuit for rotational motion is arranged. The matching circuit is connected to the IDTs located at the left side of the bottom stator and at the right side of the top stator and excited simultaneously. The RF signal generator for supplying the required signal at the resonance frequency is connected to the matching circuits so that the power supply to the IDTs can be provided through the matching circuits to the IDTs as shown in Figure 7. 25. This completes the assembly of the experimental rotational DFD SAW motor.

Since the two stators are kept as a mirror image to each other, for the SAW travelling in a+X direction, the particles at the surface of the stator make anticlockwise elliptical motion and for the SAW travelling in –X direction the particles at the surface of the stator make anticlockwise elliptical motion. As the crosswise placed IDTs of the top and bottom stator are activated, so at one place of the slider is getting one side rotation of clockwise motion. The applied preload generates high frictional force on the shaft in –X direction at both the contact points and the cylindrical shaft performs a rotational motion in a clockwise direction. The cylindrical shaft made a rotation of 1 rev per 0.8 s.

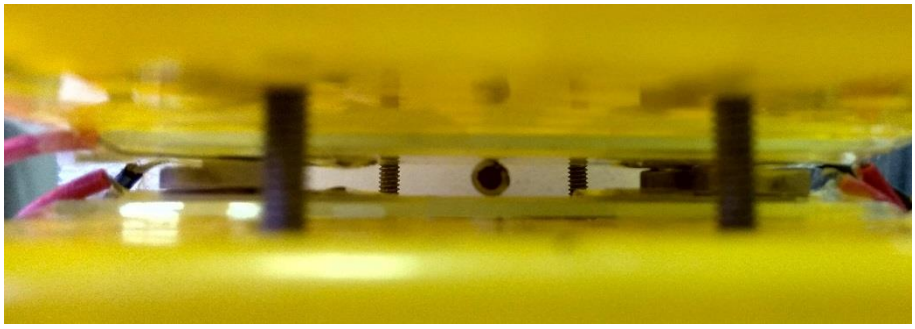

Figure 7. 29: Assembly for the DFD SAW motor for rotational motion.

Similarly, if IDTs on the other side are activated instead of presently activated IDTs, the shaft will perform a rotational motion in the opposite direction i.e. in an anticlockwise direction. Thus the shaft is able to make a rotational motion in both clockwise and anticlockwise directions.

7.3.5 Simultaneous translational and rotational motion

By applying alternate excitations for translational and rotational motions in a time-multiplexing way as described above repeatedly, simultaneous translational and rotational motion is achieved.

7.4 Efficiency calculation of the DFD SAW motor

The efficiency of the proposed SAW motor is calculated as follows by using the procedure mentioned in [114], [115].

The efficiency of the motor $E = \frac{P_{Out}}{P_{In}}$

P_{Out} = Output mechanical power

P_{In} = Input electrical power

$P_{In} = V \times I$

V is the applied voltage and I is applied current.

P_{In} = 100 V × 0.5 A =50 W

$P_{Out} = F \times v$

F is pressure given to the motor and v is the velocity of the motor.

F = 1 N, v = 1.3 m/s

P_{Out} = 1.3 × 1 = 1.3 W

E = (1.3/ 50) = 2.6%

The efficiency of a conventional SAW motor reported in [114] is 2%, while the proposed DFD SAW motor has an efficiency of 2.6%.

7.5 Proposed Assembly for DFD SAW Linear Motor

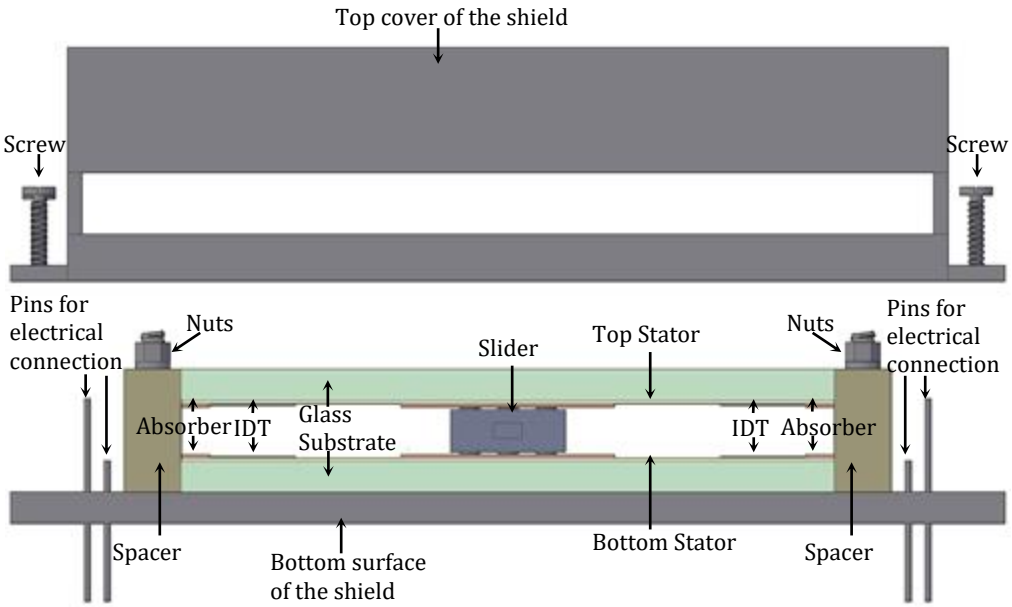

Figure 7. 30: Schematic front view of the assembly of the dual drive SAW linear motor.

The schematic in Figure 7. 30 shows of the motor assembly before the top cover is attached. The assembly of DFD SAW linear motor where SAW is generated on two stators facing each other holding tightly a slider and an outer shield is shown in Figure 7. 31. In the illustrated structure of the present device, the SAW motor comprises two piezoelectric substrates, supported on glass substrates, a movable slider, IDTs, spacers, base with electric connection pins, and top cover with slotted conical disc spring. An outer shield that holds the motor assembly and consists of two parts, the top part has spring to provide preload and slots for slider extension to drive a load, and the bottom part has electric connection pins. The device contains a base having power supply pins, the top cover has slots for attaching the load to the slider, and a slotted disc spring that provides the required preload for generating contact friction force between the slider and the stators after the top cover is fixed to the base. The slider with uniform arrays of projections on both contact surfaces is held tightly between the two piezoelectric substrates on the delay line. Both the stators are aligned with a gap to hold the slider using spacers as shown in Figure 7. 30. The stators are bonded to the glass substrates to protect the stators from damage and provide base support. Specifically designed spacers are fixed at the two sides of the glass substrate to align the stators in all the directions while maintaining the required gap between the two substrates in Y direction, and facialtatting electrical connections to the IDTs through slots and mechanical assembly through screws, and, washers and nuts as shown in the Figure 7. 31. SAW motor is capable of making forward or reverse translational motion in two dimensions.

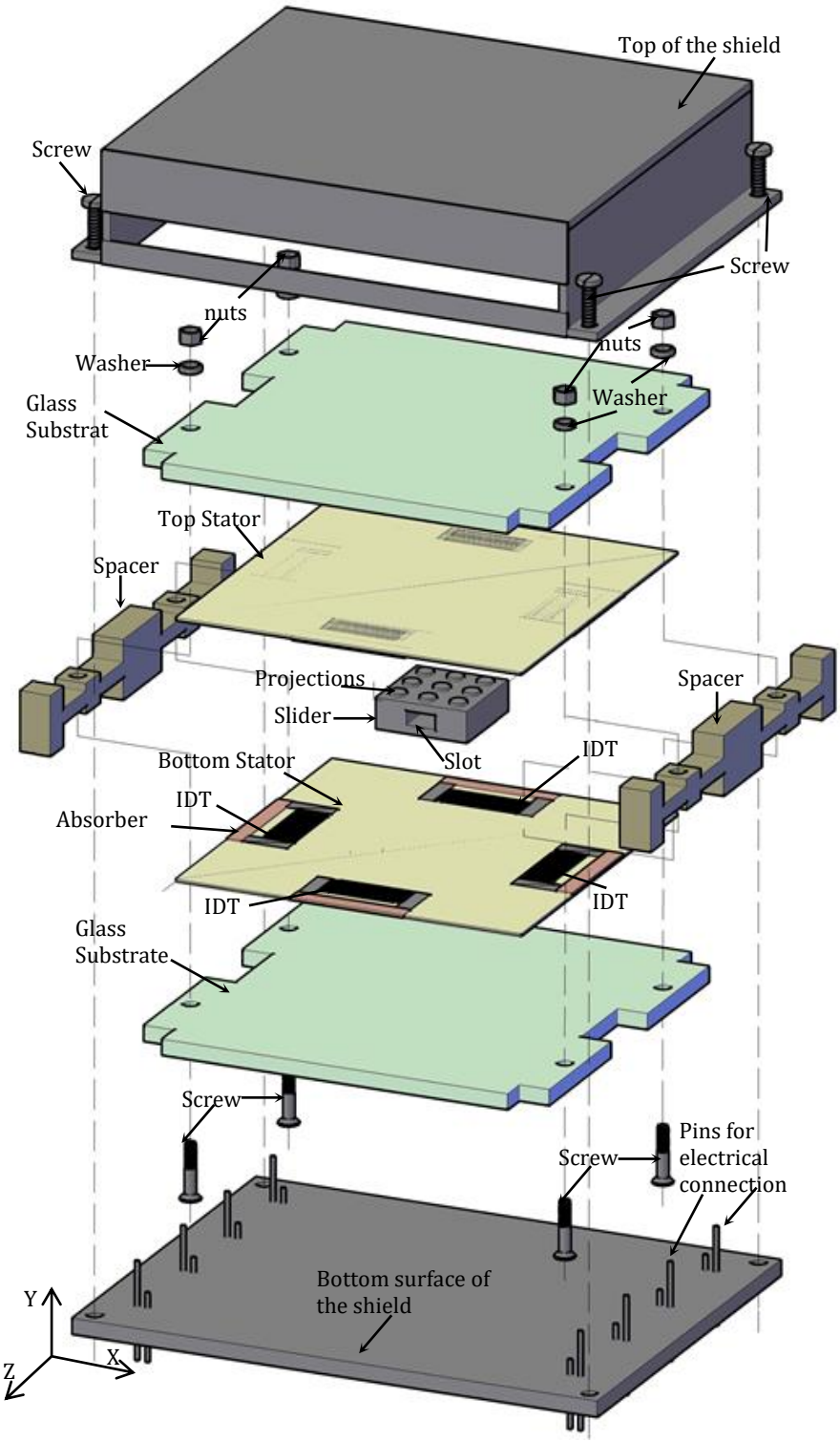

Figure 7. 31: Exploded perspective of the DFD SAW linear motor, showing each component making the complete device.

The bottom part of the outer shield shown in Figure 7. 32 is designed to provide a strong base to the whole SAW motor assembly and hold the power supply pins. External power supply is connected through wires bonded between the bond pads, and electric connection

pins. The bottom part of the outer casing acts as the base of the SAW motor and contains pins for electrical connection.

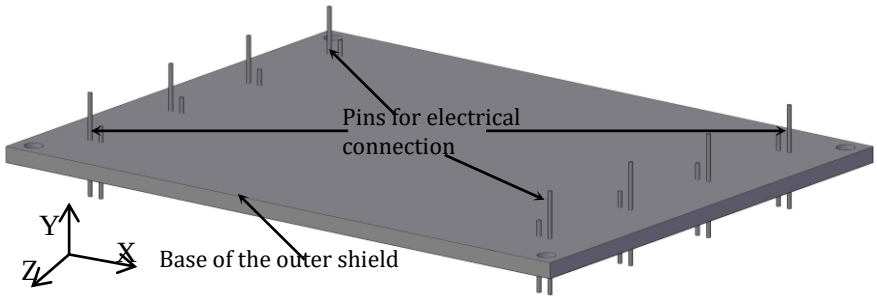

Figure 7. 32: The base of the outer shield showing electric connection pins of the motor.

The top cover of the external shield contains a slotted disc spring at the centre as shown in Figure 7. 33 and provides preload to the slider after the top cover is fixed to the base by the screws, and it completes the packaging of the motor having two degrees of freedom.

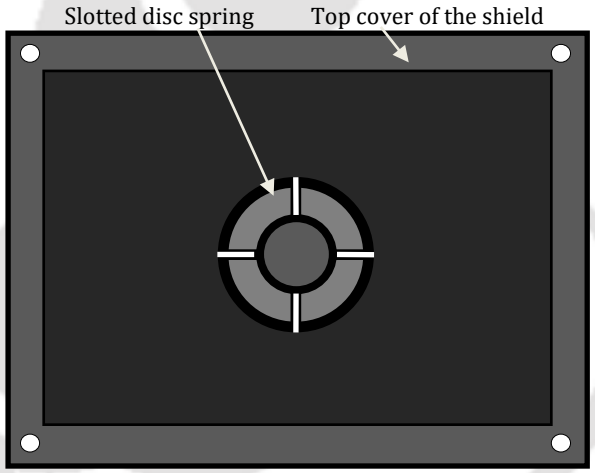

Figure 7. 33: The slotted disc spring attached inside the top cover of the SAW motor.

The outer shield is multipurpose, consisting of a slotted spring [116] attached inside the top cover to provide preload, a slot to attach the extension to the slider and drive a load, and electric connection pins at the base. The top part of the outer casing protects motor assembly and provides the required preload through a slotted spring after fixing the bottom part. The top cover has two slots for accommodating the slider to drive the load. The exploded perspective of DFD SAW linear motor modified for one degree of freedom with the external shield is shown in Figure 7. 34.

7.5.1 Proposed assembly for dual friction-drive SAW linear motor with single degree of freedom

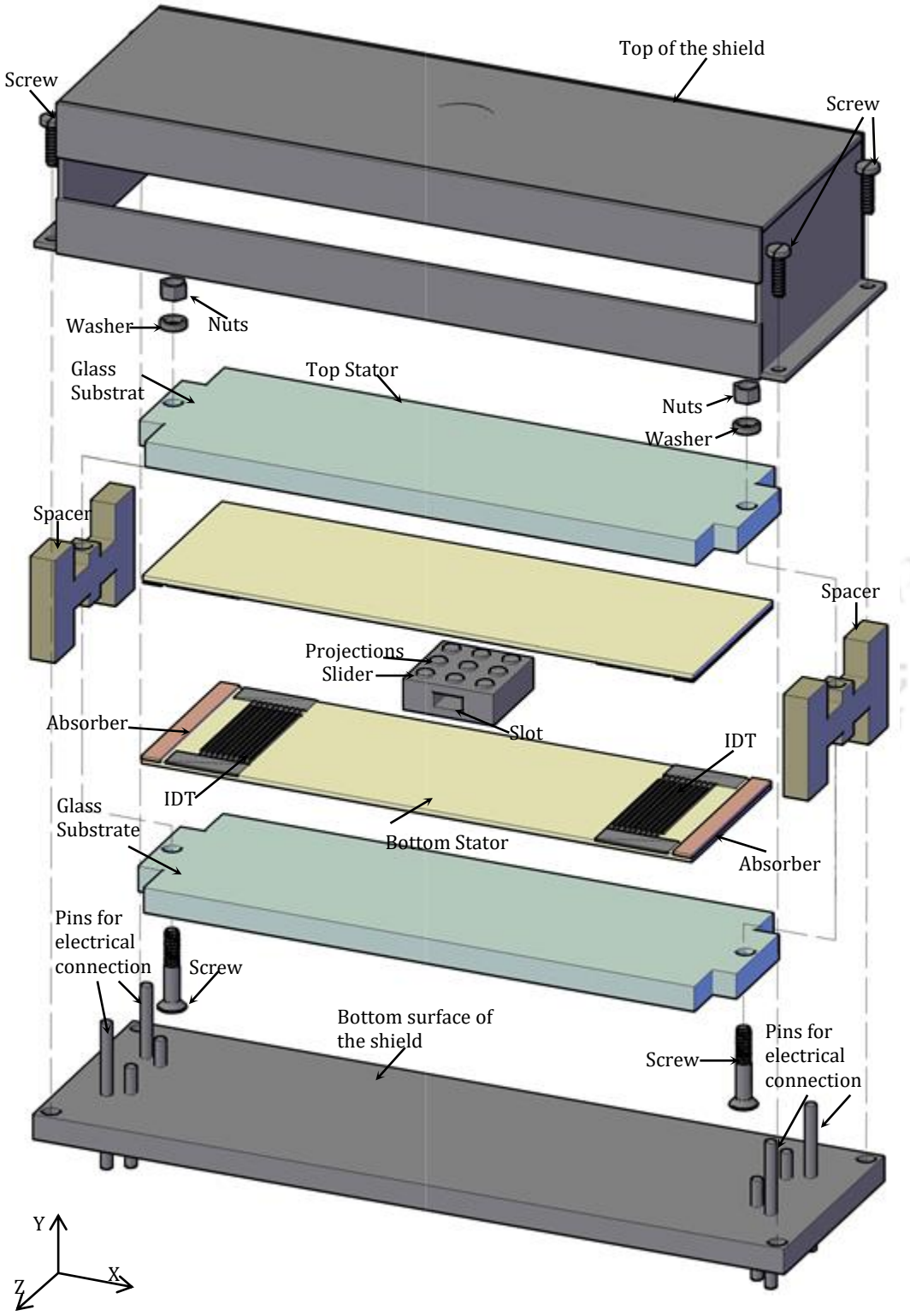

Figure 7. 34: The exploded perspective of DFD SAW linear motor with the forward and backwards motion of the slider.

7.6 Assembly for DFD SAW Motor with Cylindrical Shaft

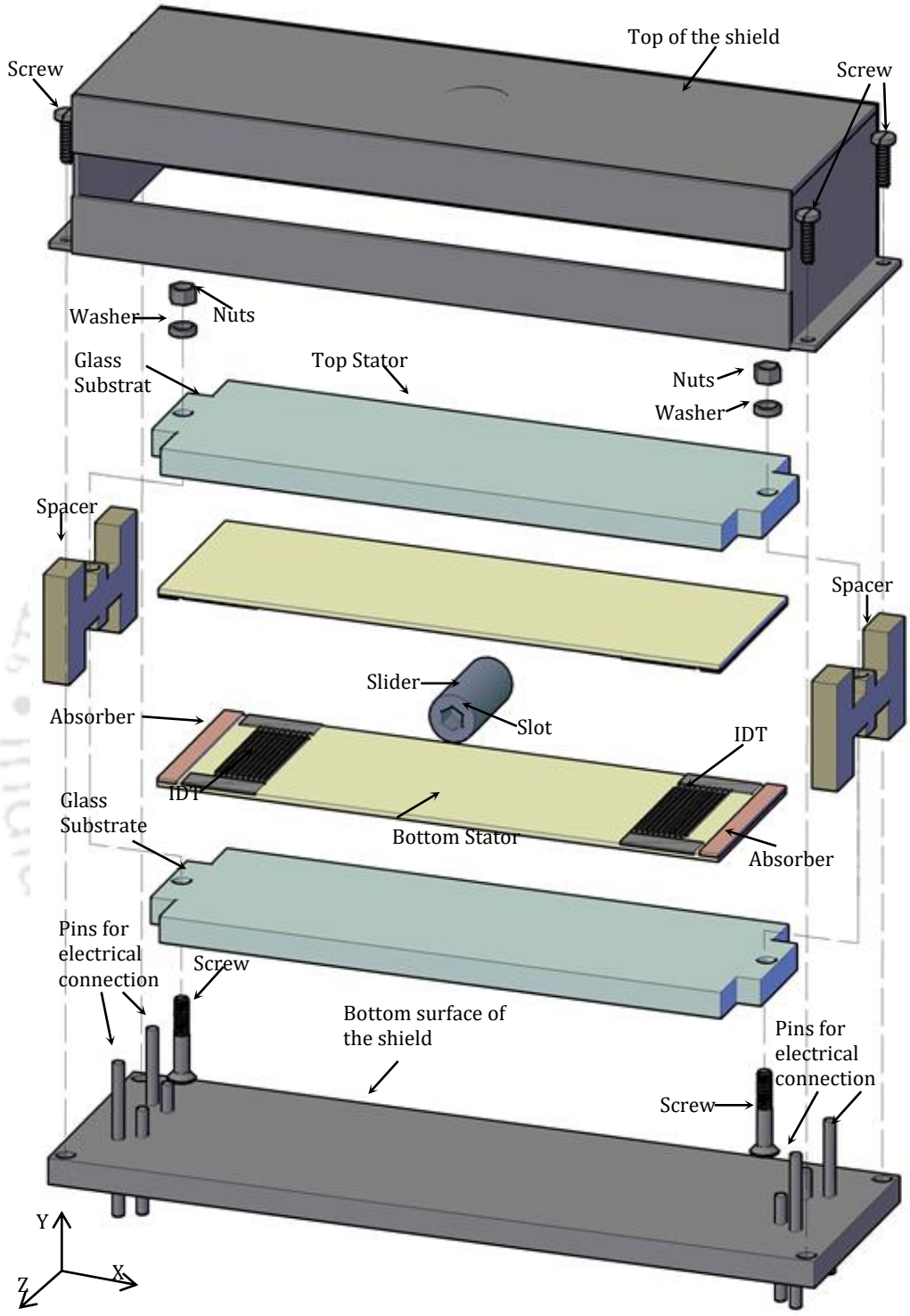

Figure 7. 35: Exploded view of the SAW motor with a cylindrical shaft.

The surface acoustic wave (SAW) motor that can possess translational as well as the rotational motion of a cylindrical shaft using appropriate excitation, and an outer metallic shield having power supply pins and slots for driving an external load as shown in Figure 7. 35. The SAW motor comprises a cylindrical shaft held tightly between two piezoelectric flat

stators facing each other. Additional pressure to increase friction between the shaft and the stators is provided through a slotted conical disc spring attached at the centre of the inner side of the upper part of the metallic casing.

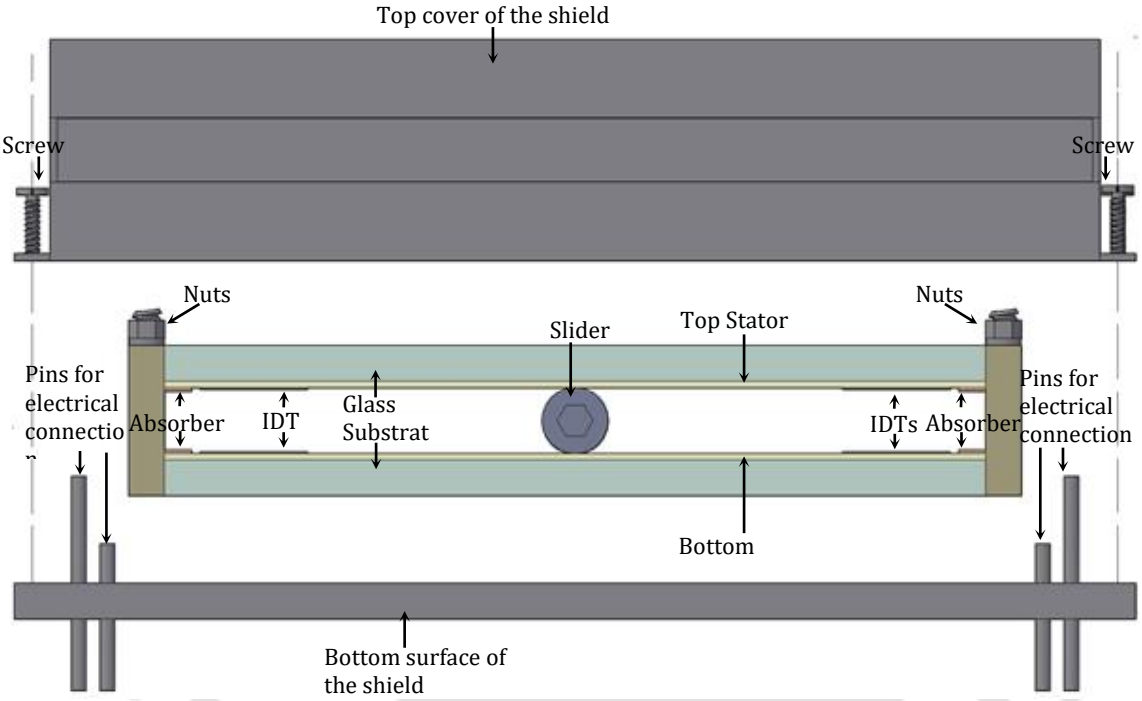

Figure 7. 36: Front view of the SAW motor with a cylindrical shaft.

7.7 Summary

This chapter provides the characterisation and testing results for the proposed fabricated DFD SAW motor. Initially, the fabricated device is characterised with the help of network analyser and AFM. In characterisation part we are able to measure the S – parameters and designed matching circuit get the efficient output from the device while it is concluded that the fabricated delay line is able to process further for testing as SAW motor. In the next part of the chapter, the assembling of the device for single side and DFD SAW motor operation is carried out. Then with the proper arrangement, the testing is done to obtain both translational and rotational motion of the slider. This device to accomplish miniaturisation of these devices including weight and size reduction keeping the output efficiency unharmed through the combination of the linear motor shield. It is capable of protecting the motor with proper assembly of the external metallic casing. This device has applications where a light weight and the efficient motor is required to move the elements such as lenses in camera, mirrors in precision instruments.

8

Conclusion and Future Work

This chapter deals with the conclusion of mathematical modelling and finite element simulation of dual friction drive SAW motor, where a slider is sandwiched between stators. The sandwich structure having block type of slider with and without a uniform array of projections at the contact surface were simulated through COMSOL Multiphysics. Then the Multiphysics simulation of the cylindrical shaft for both translational and rotational motion was carried out, where we achieved the expected mechanical motions of the cylindrical shaft in COMSOL Multiphysics. The motion of the slider with driving external load was also observed by the simulated results. Then the interdigital transducers were designed for fabricating the delay line and mask was done with Clewin software. Then the fabrication the proposed device was carried out at IISc, Bangalore under Indian Nano Users Program (INUP). Some part of the device characterization was carried out using Dektak surface profile measurement of IISc, Bangalore and Atomic force measurement (AFM) of CIF Lab, IIT Guwahati. The device setup is done at Control and Instrumentation Lab., IIT Guwahati. The movement of the slider and cylindrical shaft is remaining for measurement.

8.1 Conclusion

This thesis focuses on the modelling, finite element simulation, fabrication, and demonstration of the surface acoustic wave (SAW) motors based on the proposed dual friction-drive (DFD) technique which leads to substantial reduction in the size and weight of conventional SAW motors. The proposed technique gets rid of the heavy and bulky lubricated guide rails used in the conventional motors by replacing the guide rail with an additional stator so that the slider is driven from both top and bottom sides simultaneously. Using a cylindrical slider rotational motion has also been achieved.

Initially, modelling of single point contact is presented and the parameters like force, preload and contact length are derived. It is followed by modelling of multiple points contact normally prevalent in the case of sliders having projections. The modelling is extended for the proposed DFD technique using the cuboid slider with projections (multiple points contact) and using the cylindrical slider (line contact). Finite element simulations for conventional and proposed DFD SAW motors are carried out in COMSOL Multiphysics. Initially, the conventional SAW motors with spherical and cuboid sliders are simulated. The SAW motor based on DFD technique is simulated for cuboid sliders without projections and with different shapes of projections. The simulation for SAW motor using cylindrical slider ascertains both translational and rotational motions.

The stators for different operating frequencies are designed and fabricated using microfabrication facility. A large number of cuboid sliders having projections of different shapes and spacing using silicon substrate are fabricated. All the fabricated devices are

characterised and tested. The stators are arranged in DFD assembly and tested for both translational and rotational motion of sliders. The experimental observation is captured through the digital video camera to determine the displacement of the slider.

8.2 Future Work

The scope of the thesis includes the introduction of a significantly compact and lightweight SAW motor by employing dual friction-drive (DFD) technique, mathematical modelling, finite element simulation, fabrication of the device, and experimental verification of the proposed DFD technique. The following works are suggested before the proposed technique to be implemented in commercial motors.

Fabrication and packaging of DFD SAW motor: The SAW motors may be fabricated and packaged as described in the exploded views given in Chapter 7. The associated power control circuit may be designed to control the direction of motion of the slider/ shaft.

Load driving capacity: The load driving capacity may be experimentally evaluated with different voltage excitations after the fabrication of the DFD SAW motors.

Estimate step size: The step size for the slider may be estimated through experimental results with different voltage excitations.

9

Appendix

Appendix A

A. Important Substrate Materials Used in SAW Sensor Applications

Important substrate materials used in SAW sensor application are shown in Table A.1 [1], [3], and [80]

Table A.1. Important substrate materials used in SAW sensors

Substrate	Propagation	K^2 (%)	Acoustic velocity (m/s)
ST- quartz	X	1.89	3158
Y- quartz	X	1.1	3159
Y- $LiNbO_3$	Z	4.5	3488
Y -128° $LiNbO_3$	X	5.3	3992
77.5° Y- $LiTaO_3$	X	1.6	3379
36° Y- $LiTaO_3$	X	5	4160
Langasite	-	3.2	2742
100-011 GaAs	-	0.7	2864
Y-60° CdS	-	-	1702
ZnO	-	-	2639

Appendix B

B. Matrix Technique for Crystal Axes Rotation to given Euler Angles

It is important to rotate the crystal axes according to given Euler angles viz., ϕ, θ, and ψ rotated along x_1, x_2 and x_3 axis and align them with the required Cartesian coordinate axes. During such rotations, the stiffness matrix ($\mathbf{C}^E$), piezoelectric matrix (e) and dielectric matrix ($\boldsymbol{\varepsilon}$) of the material also gets transformed accordingly. A very efficient matrix technique has been developed for this purpose by W. L. Bond [29]. If the directional vector written as $\vec{r} = (x_1, x_2, x_3)$, then the directional vector is written in terms of crystal axes: $\tilde{r}$ may be found using a coordinate transformation matrix a, and bond matrix M_b. The rotated stiffness ($\tilde{\mathbf{C}}^E$), piezoelectric constant ($\tilde{\mathbf{e}}$), and permittivity matrix ($\tilde{\boldsymbol{\varepsilon}}$) can be obtained using the following equations

$$\tilde{r} = \mathbf{a}.\vec{r}$$

$$\tilde{\mathbf{C}}^{\mathbf{E}} = \mathbf{M}.\, C^E.\mathbf{M}'$$

$$\tilde{\mathbf{e}} = \mathbf{a}.\,\mathbf{e}.\,\mathbf{M}'$$

$$\tilde{\boldsymbol{\varepsilon}} = \mathbf{a}.\,\boldsymbol{\varepsilon}.\,\mathbf{a}$$

where the coordinate transform matrix a rotating around x_3, x_2 and x_1 (in the given order)as below

$$\mathbf{a} = \begin{pmatrix} a_{11} & a_{12} & a_{13} \\ a_{21} & a_{22} & a_{23} \\ a_{31} & a_{32} & a_{33} \end{pmatrix}$$

$$= \begin{pmatrix} \cos(\phi)\cos(\theta) & \sin(\phi)\cos(\theta) & -\sin(\theta) \\ \cos(\phi)\cos(\theta)\sin(\psi) - \sin(\phi)\cos(\psi) & \cos(\phi)\cos(\psi) + \sin(\phi)\sin(\theta)\sin(\psi) & \cos(\theta)\sin(\psi) \\ \cos(\phi)\sin(\theta)\cos(\psi) + \sin(\phi)\sin(\psi) & \sin(\phi)\sin(\theta)\cos(\psi) + \cos(\phi)\sin(\psi) & \cos(\theta)\cos(\psi) \end{pmatrix}$$

The bond matrix M_b is as given below

$$\mathbf{M_b} = \begin{pmatrix} a_{11}^2 & a_{12}^2 & a_{13}^2 & 2a_{12}a_{13} & 2a_{13}a_{12} & 2a_{11}a_{12} \\ a_{21}^2 & a_{22}^2 & a_{23}^2 & 2a_{22}a_{23} & 2a_{23}a_{21} & 2a_{21}a_{22} \\ a_{31}^2 & a_{32}^2 & a_{33}^2 & 2a_{32}a_{33} & 2a_{33}a_{31} & 2a_{31}a_{32} \\ a_{23}a_{31} & a_{22}a_{31} & a_{23}a_{33} & a_{22}a_{11} + a_{23}a_{32} & a_{21}a_{33} + a_{23}a_{31} & a_{22}a_{31} + a_{21}a_{32} \\ a_{23}a_{31} & a_{22}a_{12} & a_{33}a_{13} & a_{12}a_{33} + a_{13}a_{32} & a_{13}a_{31} + a_{11}a_{33} & a_{11}a_{32} + a_{12}a_{21} \\ a_{11}a_{21} & a_{12}a_{22} & a_{13}a_{23} & a_{12}a_{23} + a_{13}a_{22} & a_{13}a_{21} + a_{11}a_{23} & a_{11}a_{22} + a_{12}a_{21} \end{pmatrix}$$

Appendix C

C. Material Constants of Lithium Niobate

Material constants of Lithium Niobate used in the thesis are taken from [43]. The constants for X-cut Y - $LiNbO_3$ and Y-cut Z- $LiNbO_3$ are given in section C.1 and C. 2, respectively.

C. 1Material constants of Y cut Z - $LiNbO_3$

Density (ρ) = 4675 kg/m^3

$$\text{Stiffness, } \mathbf{C}^E = \begin{pmatrix} 20.3 & 5.3 & 7.5 & 0.9 & 0 & 0 \\ 5.3 & 20.3 & 7.5 & -0.9 & 0 & 0 \\ 7.5 & 7.5 & 24.5 & 0 & 0 & 0 \\ 0.9 & -0.9 & 0 & 6.0 & 0 & 0 \\ 0 & 0 & 0 & 0 & 6.0 & 0.9 \\ 0 & 0 & 0 & 0 & 0.9 & 7.5 \end{pmatrix} \times 10^{10}\,\text{N/m}^2$$

$$\text{Piezoelectric constant , } \mathbf{e} = \begin{pmatrix} 0.0 & 0.0 & 0.0 & 0.0 & 3.7 & -2.5 \\ -2.5 & 2.5 & 0.0 & 3.7 & 0.0 & 0.0 \\ 0.2 & 0.2 & 1.3 & 0.0 & 0.0 & 0.0 \end{pmatrix} \text{C/m}^2$$

$$\text{Permittivity , } \boldsymbol{\varepsilon} = \begin{pmatrix} 44 & 0 & 0 \\ 0 & 44 & 0 \\ 0 & 0 & 29 \end{pmatrix}$$

C. 2 Material constants of Y-cut Z - $LiNbO_3$

Density (ρ) = 4675 kg/m^3

$$\text{Stiffness, } \mathbf{C}^E = \begin{pmatrix} 24.24 & 7.52 & 7.52 & 0 & 0 & 0 \\ 7.52 & 20.3 & 5.73 & 0 & 8.5 & 0 \\ 7.52 & 5.73 & 20.3 & 0 & -8.5 & 0 \\ 0 & 0 & 0 & 7.52 & 0 & 8.5 \\ 0 & 8.5 & -8.5 & 0 & 5.95 & 0 \\ 0 & 0 & 0 & 8.5 & 0 & 5.95 \end{pmatrix} \times 10^{10}\,\text{N/m}^2$$

$$\text{Piezoelectric constant , } \mathbf{e} = \begin{pmatrix} 1.3 & 0.23 & 0.23 & 0 & 0 & 0 \\ 0 & 0 & 0.0 & -2.5 & 0 & 3.7 \\ 0 & -2.5 & 2.5 & 0 & 3.7 & 0 \end{pmatrix} \text{C/m}^2$$

$$\text{Permittivity , } \boldsymbol{\varepsilon} = \begin{pmatrix} 28.7 & 0 & 0 \\ 0 & 85.2 & 0 \\ 0 & 0 & 85.2 \end{pmatrix}$$

Material properties and tensor transformation

Appendix C

Following are the material properties taken from Auld [91].

Lithium Niobate – Density ρs = 4700 kg/m^3

Lithium Tantalate – Density ρs = 7450 kg/m^3

Piezoelectric constant , $\mathbf{e} = \begin{pmatrix} 0 & 0 & 0 & 0 & e_{x5} & -e_{y2} \\ -e_{y2} & e_{y2} & 0 & e_{x5} & 0 & 0 \\ e_{z1} & e_{z1} & e_{z3} & 0 & 0 & 0 \end{pmatrix}$ C/m^2

Lithium Niobate – Trig. *3m* $ex5 = 3.7$, $ey2 = 2.5$, $ez1 = 0.2$, $ez3 = 1.3$.

Lithium Tantalate – Trig. *3m* $ex5 = 2.6$, $ey2 = 1.6$, $ez1 = 0.0$, $ez3 = 1.9$.

Trigonal *3m*

Stiffness, $\mathbf{C}^E = \begin{pmatrix} c_{11} & c_{12} & c_{13} & c_{14} & 0 & 0 \\ c_{12} & c_{11} & c_{13} & -c_{14} & 0 & 0 \\ c_{13} & c_3 & c_{33} & 0 & 0 & 0 \\ c_{14} & -c_4 & 0 & c_{44} & 0 & 0 \\ 0 & 0 & 0 & 0 & c_{44} & c_{14} \\ 0 & 0 & 0 & 0 & c_{14} & \frac{1}{2}(c_{11} - c_{12}) \end{pmatrix}$ N/m^2

Lithium Niobate – Trig. *3m* $c11 = 20.3 \times 1010$, $c33 = 24.5 \times 1010$, $c44 = 6.0 \times 1010$, $c12 = 5.3 \times 1010$, $c13 = 7.5 \times 1010$, $c14 = 0.9 \times 1010$.

Lithium Tantalate – Trig. *3m* $c11 = 23.3 \times 1010$, $c33 = 27.5 \times 1010$, $c44 = 9.4 \times 1010$, $c12 = 4.7 \times 1010$, $c13 = 8.0 \times 1010$, $c14 = -1.1 \times 1010$.

Trigonal *3m*

Permittivity , $\boldsymbol{\varepsilon} = \begin{pmatrix} \varepsilon_{xx}^S & 0 & 0 \\ 0 & \varepsilon_{yy}^S & 0 \\ 0 & 0 & \varepsilon_{zz}^S \end{pmatrix}$

Lithium Niobate – Trig. *3m* $Sxx = 44 \times 8.854 \times 10^{-12}$, $Szz = 29 \times 8.854 \times 10^{-12}$.

Lithium Tantalate – Trig. *3m* $Sxx = 41 \times 8.854 \times 10^{-12}$, $Szz = 43 \times 8.854 \times 10^{-12}$.

Appendix C

The material properties need to be transformed to the correct orientation for actual use. The bond transformation principle is used here [91]. A first rank tensor has 31 components (displacement), a second rank tensor has 32 components (stress/strain), a third rank tensor has 33 components (piezoelectric stress constants), and a fourth rank tensor has 34 components (elastic stiffness constants). The transformation for first, Material properties and tensor transformation 163 second, third, and fourth rank tensors are

First rank tensor (vector) $[\zeta] = [a][\zeta]$, (E.4)

Second rank tensor [] = $[a][]/[a]$, (E.5)

Third rank tensor $[e] = [a][e][M]$, (E.6)

Fourth rank tensor $[c] = [M][T][M]$, (E.7)

where $[a]$ is a transformation matrix, and $[M]$ is the bond transformation matrix. A zero rank tensor is a scalar quantity. For transformation in orthogonal Cartesian coordinates, we have the following:

$$[a_z] = \begin{pmatrix} \cos\theta & \sin\theta & 0 \\ -\sin\theta & \cos\theta & 0 \\ 0 & 0 & 1 \end{pmatrix}$$

$$[a_y] = \begin{pmatrix} \cos\theta & 0 & \sin\theta \\ 0 & 1 & 0 \\ -\sin\theta & 0 & \cos\theta \end{pmatrix}$$

$$[a_z] = \begin{pmatrix} \cos\theta & \sin\theta & 0 \\ -\sin\theta & \cos\theta & 0 \\ 0 & 0 & 1 \end{pmatrix}$$

$$[M] = \begin{pmatrix} a_{xx}^2 & a_{xy}^2 & a_{xz}^2 & 2a_{xy}a_{xz} & 2a_{xz}a_{xx} & 2a_{xx}a_{xy} \\ a_{yx}^2 & a_{yy}^2 & a_{yz}^2 & 2a_{yy}a_{yz} & 2a_{yz}a_{yx} & 2a_{yx}a_{yy} \\ a_{zx}^2 & a_{zy}^2 & a_{zz}^2 & 2a_{zy}a_{zz} & 2a_{zz}a_{zx} & 2a_{zx}a_{zy} \\ a_{yx}a_{zx} & a_{yy}a_{zy} & a_{yz}a_{zz} & a_{yy}a_{zz}+a_{yz}a_{zy} & a_{yx}a_{zz}+a_{yz}a_{zx} & a_{yy}a_{zx}+a_{yx}a_{zy} \\ a_{zx}a_{xx} & a_{zy}a_{xy} & a_{zz}a_{xz} & a_{xy}a_{zz}+a_{xz}a_{zy} & a_{xz}a_{zx}+a_{xx}a_{zz} & a_{xx}a_{zy}+a_{xy}a_{zx} \\ a_{xx}a_{yx} & a_{xy}a_{yy} & a_{xz}a_{yz} & a_{xy}a_{yz}+a_{xz}a_{yy} & a_{xz}a_{yx}+a_{xx}a_{yz} & a_{xx}a_{yy}+a_{xy}a_{yx} \end{pmatrix}$$

Appendix C

$$[M]=\begin{pmatrix} a_{xx}^2 & a_{xy}^2 & a_{xz}^2 & 2a_{xy}a_{xz} & 2a_{xz}a_{xx} & 2a_{xx}a_{xy} \\ a_{yx}^2 & a_{yy}^2 & a_{yz}^2 & 2a_{yy}a_{yz} & 2a_{yz}a_{yx} & 2a_{yx}a_{yy} \\ a_{zx}^2 & a_{zy}^2 & a_{zz}^2 & 2a_{zy}a_{zz} & 2a_{zz}a_{zx} & 2a_{zx}a_{zy} \\ a_{yx}a_{zx} & a_{yy}a_{zy} & a_{yz}a_{zz} & a_{yy}a_{zz}+a_{yz}a_{zy} & a_{yx}a_{zz}+a_{yz}a_{zx} & a_{yy}a_{zx}+a_{yx}a_{zy} \\ a_{zx}a_{xx} & a_{zy}a_{xy} & a_{zz}a_{xz} & a_{xy}a_{zz}+a_{xz}a_{zy} & a_{xz}a_{zx}+a_{xx}a_{zz} & a_{xx}a_{zy}+a_{xy}a_{zx} \\ a_{xx}a_{yx} & a_{xy}a_{yy} & a_{xz}a_{yz} & a_{xy}a_{yz}+a_{xz}a_{yy} & a_{xz}a_{yx}+a_{xx}a_{yz} & a_{xx}a_{yy}+a_{xy}a_{yx} \end{pmatrix}$$

The transformed piezoelectric constant *ekij*, dielectric constant *Sik* and elastic stiffness constant *cE ijkl* for 128° YX lithium niobate (LiNbO3, LN) are

$$\text{Piezoelectric constant , } \mathbf{e}=\begin{pmatrix} 0 & 0 & 0 & 0 & 4.46 & 0.4 \\ -1.77 & 4.46 & -1.59 & 0.12 & 0 & 0 \\ 1.68 & -2.67 & 2.4 & 0.59 & 0 & 0 \end{pmatrix} \text{C/m}^2$$

$$\text{Permittivity , } \boldsymbol{\varepsilon}=\begin{pmatrix} 44 & 0 & 0 \\ 0 & 37.9 & -7.81 \\ 0 & -7.81 & 34 \end{pmatrix}\frac{F}{m}$$

$$\text{Stiffness, } \mathbf{C}^E=\begin{pmatrix} 24.3 & 7.23 & 6.02 & 1.07 & 0 & 0 \\ 7.23 & 19.4 & 9.06 & 0.89 & 0 & 0 \\ 6.02 & 9.06 & 22.03 & 0.81 & 0 & 0 \\ 1.07 & 0.89 & 0.81 & 7.49 & 0 & 0 \\ 0 & 0 & 0 & 0 & 5.63 & -0.44 \\ 0 & 0 & 0 & 8.5 & -0.44 & 7.6 \end{pmatrix}\times 10^{10}\,\text{N/m}^2$$

D. Absorbing Boundary Conditions

In order to avoid reflection of waves from the boundaries or edges of the SAW devices, absorbing boundary conditions are applied in the FEM simulations. The influence of wave reflections from boundaries can be reduced by assuming critical damping along the boundaries [38].This can be achieved by employing suitable values for Rayleigh damping coefficients in the COMSOL Multiphysics software [33].In Rayleigh damping model, the Rayleigh damping matrix Z is a linear combination of mass matrix and stiffness matrix as given as $\xi = A_{dM} M + B_{dk} k$

where the mass proportional damping parameter (A_{dM}) and stiffness proportional damping parameter (B_{dk}) are damping coefficients and they are related to damping ratio (ξ) as

$$\xi = \frac{A_{dM} + B_{dk}\omega^2}{2\omega}$$

Absorbing boundary can be achieved by assuming critical damping, $\xi = 1$ and $A_{dm} = 0$ then $B_{dk} = 1/\pi.f$.

Appendix E

MATLAB Program

For determining the Material Co-efficient of Lithium Niobate

Elastic and piezoelectric constants of lithium niobate from ultrasonic velocity measurements

```
p=38*(pi/180);
 %ELASTICITY STIFFNESS MATRIX PROVIDED

c=      [       20.3    5.3     7.5     0.9     0       0;
                5.3     20.3    7.5     -0.9    0       0;
                7.5     7.5     24.5    0       0       0;
                0.9     -0.9    0       6       0       0;
                0       0       0       0       6       0.9 ;
                0       0       0       0       0.9     7.5];
a11=1;
a12=0;
a13=0;
a21=0;
a22= cos(p);
a23= sin(p);
a31=0;
a32=-sin(p);
a33= cos(p);

a=[a11      a12     a13;
  a21       a22     a23;
  a31       a32     a33] ;
M=
 [a11^2         a12^2   a13^2   2*a12*a13        2*a11*a13       2*a11*a12;
  a21^2   a22^2   a23^2   2*a22*a23        2*a21*a23       2*a21*a22;
  a31^2   a32^2   a33^2   2*a32*a33        2*a31*a33       2*a31*a32;
  a21*a31 a22*a32 a23*a33 a22*a33+a32*a23 a21*a33+a31*a23
a31*a22+a21*a32;
  a11*a31 a12*a32 a13*a33 a12*a33+a32*a13 a31*a13+a11*a33
a11*a32+a31*a12;
```

Appendix E

```
  a11*a21  a12*a22   a13*a23   a12*a23+a22*a13   a21*a13+a11*a23
a11*a22+a12*a21];
%PIEZO MATRIX PROVIDED
 S= [0          -2.5          0.2;
  0            2.5          0.2;
  0            0           1.3;
  0            3.7          0;
  3.7          0            0;
 -2.5          0            0];

%RELATIVE PERMITIVITY MATRIX PROVIDED

eps= [44         0                0;
    0            44           0;
    0            0            29];
%transform the co-ordinates for the piezo matrix
% TRASFORMED RESLT
 %ELASTICITY STIFFNESS
 stiff1= M*c*M';
  stif = stiff1.*10^10
  % PIEZO MATRIX
   S1=a*S'*M'
   % RELATIVE PERMITIVITY
eps1=a*eps*a'
```

10

Bibliography

Bibliography

[1] J. G. Korvink and O. Paul, *MEMS : A Practical Guide to Design , Analysis , and Edited by*, First Edit. New York: Springer, 2006.

[2] S. E. Lyshevski, *MEMS AND NEMS Systems, Devices, and Structures*, First Edit. New York: CRC Press, 2002.

[3] M. Gad-el-Hak, *The MEMS Handbook*, First Edit. New York: CRC Press, 2002.

[4] J. W. Gardner, V. K. Varadan, and O. O. Awadelkarim, *Microsensors, MEMS, and Smart Devices*, First Edit. England: John Wiley & Sons Publication, 2001.

[5] M. Exchange, "What is MEMS technology," *Retrieved Jan 2014*, pp. 1–4, 2014.

[6] H. Janocha, *Actuators Basics and Applications*, First Edit. Berlin: Springer, 2004.

[7] Wikipedia, "Actuator," *Wikipedia*. Wikipedia, pp. 1–4, 2015.

[8] A. L. W. Williams and W. J. Brown, "Piezoelectric motor," US2439499, 1948.

[9] V. Lavrinenko and M. Nekrasov, "Electrical Motor," 1965.

[10] K. Spanner and B. Koc, "Piezoelectric Motors, an Overview," *MDPI*, 2016.

[11] V. Wischnewskiy, L. Gultajeva, I. Kartashev, and V. Lavrinenko, "Piezoelectric motor," 1976.

[12] K. Uchino, K. Kato, M. Imaizumi, and M. Tohda, "Ultrasonic Linear Motors Using Piezoelectric Actuators," *J. Japan Ceram.*, vol. 96, no. 12, pp. 1131–1136, 1988.

[13] B. Koc, P. Bouchilloux, and K. Uchino, "Piezoelectric Micromotor Using a Metal-Ceramic Composite Structure," *IEEE Trans. Ultrason. Ferroelectr. Freq. Control*, vol. 47, no. 4, pp. 836–43, Jan. 2000.

[14] Sadayuki Ueha and M. Kurosawa, "Ultrasonic motors," in *IEEE Ultrasonics Symposium*, 1988, pp. 519–522.

[15] C. Zhao, *Ultrasonic Motors Technologies and Applications*, First Edit. Nanjing, China: Springer, 2011.

[16] S. Ueha, "Present Stae of Art Ultrasonic Motors," *Jpn. J. Appl. Phys.*, vol. 28, pp. 3–6, 1988.

[17] R. M. Moroney, R. M. White, and R. T. Howe, "Ultrasonic Micromotors: Physics and Applications," in *Proceedings of the IEEE*, 1990, pp. 182–187.

[18] T. Takano, Y. Tomikawa, T. Ogasawara, S. Sugawara, and M. Konno, "Ultrasonic Motor using piezoelectric ceramic multi mode vibrators," in *Proceedings on Ultrasonic Electronics*, 1987.

[19] H. V. Barth, "Ultrasonic magnetic surface finisher," US 3771939, 1973.

[20] T. Wakai, M. Kuribayashi, and T. Higuchi, "Transducer for an Ultrasonic Linear Motor with Flexible Driving Part," in *IEEE Ultrasonics Symposium*, 1998, pp. 683–686.

[21] M. K. Kurosawa, O. Kodaira, Y. Tsuchitoi, and T. Higuchi, "Transducer for high speed and large thrust ultrasonic linear motor using two sandwich-type vibrators," *IEEE Trans. Ultrason. Ferroelectr. Freq. Control*, vol. 45, no. 5, pp. 1188–1195, 1998.

[22] T. Sashida, "Motor device utilizing ultrasonic oscillation," 4,562,374, 1985.

[23] M. Kurosawa and S. Ueha, "Hybrid Transducer Type Ultrasonic Motor," *IEEE Trans. Ultrason. Ferroelectr. Freq. Control*, vol. 38, no. 2, pp. 89–92, 1991.

[24] C. Campbell, *Surface Acoustic Wave Devices and Their Signal processing Applications*, First Edit. Boston: Academic Press INC, 1989.

[25] C. C. W. Ruppel and T. A. Fieldly, *Advances in Surface Acoustic Wave Technology, Systems and Applications (Vol. I)*. World Scientific Publishing Co. Pte. Ltd., 2001.

[26] T. Shigematsu, M. K. Kurosawa, and K. Asai, "Nanometer stepping drives of surface acoustic wave motor," *IEEE Trans. Ultrason. Ferroelectr. Freq. Control*, vol. 50, no. 4, pp. 376–385, 2003.

[27] D. Royer and E. Dieulesaint, *Elastic waves in solids: Generation, Acousto-optic Interaction, Applications (Vol. II)*, First Edit. New York: Springer, 1999.

[28] D. Morgan, *Surface Acoustic Wave Filters With Applications to Electronic Communications and Signal Processing*, Second Edi. Oxford: Elsevier Academics Press, 2007.

[29] T. Shigematsu and M. K. Kurosawa, "Friction Drive of an SAW Motor. Part III : Modeling," *IEEE Trans. Ultrason. Ferroelectr. Freq. Control*, vol. 55, no. 10, pp. 2266–2276, 2008.

[30] B. A. Auld, *Acoustic Fields and Waves in Solids (Vol. II)*, First Edit. Canada: John Wiley & Sons Publication, 1973.

[31] D. S. Ballantine, R. M. White, S. I. Martin, A. I. Ricco, E. T. Zellers, G. C. Frye, and H. Wohltjen, *Acoustic Waves Sensors theory, design, and physico–chemical Applications*, First Edit. New York: Academic Press, 1997.

[32] D. Royer and E. Dieulesaint, *Elastic waves in solids: Free and Guided Propagation (Vol. I)*, First Edit. Northampton, England: Springer, 1996.

[33] M. Thompson, *Surface-Launched Acoustic Wave Sensors : Chemical Sensing And Thin-Film Characterization*. John Wiley & Sons Publication, 1997.
[34] K. Hashimoto, *Surface Acoustic Wave Devices in Telecommunications Modelling and Simulation*, First. Chiba, Japan: Springer, 2000.
[35] D. Royer, *Elastic waves in solids1*. France: Springer, 1996.
[36] T. Morita, M. K. Kurosawa, and T. Higuchi, "Simulation of Surface Acoustic Wave Motor with Spherical Slider," *IEEE Trans. Ultrason. Ferroelectr. Freq. Control*, vol. 46, no. 4, pp. 929–934, 1999.
[37] N. Osakabe, M. Kurosawa, T. Higuchi, and O. Shinoura, "Surface acoustic wave linear motor using silicon slider," in *Proceedings of the IEEE*, 1998, pp. 390–395.
[38] A. V. Mamishev, K. Sundara-Rajan, F. Yang, Y. Du, and M. Zahn, "Interdigital Sensors and Transducers," in *Proceedings of the IEEE*, 2004, vol. 92, no. 5, pp. 808–845.
[39] K. Uchino, *Advanced Piezoelectric Materials Science and Technology*. Oxford: Woodhead Publishing Limited, 2010.
[40] M. K. Kurosawa, M. Takashashi, and T. Higuchi, "Ultrasonic Linear motor using Surface Acoustic Waves," *IEEE Trans. Ultrason. Ferroelectr. Freq. Control*, vol. 43, no. 5, pp. 901–906, 1996.
[41] M. K. Kurosawa, M. Chiba, and T. Higuchi, "Evaluation of a surface acoustic wave motor with a multi-contact-point slider," *Smart Mater. Struct.*, vol. 7, no. 3, pp. 305–311, Jun. 1998.
[42] T. Shigematsu, M. K. Kurosawa, and K. Asai, "Sub-nanometer stepping drive of surface acoustic wave motor," in *Proceedings of the IEEE*, 2003, vol. 2, pp. 299–302.
[43] L. P. Cheng, G. M. Zhang, S. Y. Zhang, J. Yu, and X. J. Shui, "Miniaturization of surface acoustic waves rotary motor.," *Elsevier Ultrason.*, vol. 39, no. 8, pp. 591–4, Jun. 2002.
[44] P. J. Feenstra, P. C. Breedveld, M. M. P. . Vermeulen, and F. G. P. Peeters, "Modelling and Experimental Validation of a Linear Surface Acoustic Wave Motor Prototype," in *Proceedings of Mechatronics*, 2002, no. June, pp. 24–26.
[45] G. M. Zhang, L. P. Cheng, S. Zhang, J. Yu, and X. Shui, "Surface acoustic wave rotation motor," *Electron. Lett.*, vol. 36, no. 16, pp. 1437–1438, 2000.
[46] A. Sano, Y. Matsui, and S. Shiokawa, "A new manipulator based on surface acoustic wave streaming," in *IEEE Ultrasonics Symposium*, 1997, pp. 467–470.
[47] Y. Fujii, H. Kotani, T. Masaya, and T. Mizuno, "Surface Acoustic Wave Linear Motor Using Segment-Structured Diamond-Like Carbon Films on Contact Surface," pp. 2543–2546, 2007.
[48] H. Gu, D. Ma, S. Zhang, L. Cheng, and X. Shui, "Theoretical analysis of non contact linear motors driven by surface acoustic waves," in *Proceedings of the IEEE*, 2008, pp. 3–6.
[49] K. Sakano, M. K. Kurosawa, and T. Shigematsu, "Surface Acoustic Wave Motor with Flat Plane Slider," in *Proceedings of the IEEE*, 2008, pp. 243–248.
[50] K. Sakano, M. K. Kurosawa, and T. Shigematsu, "Driving Characteristics of a Surface Acoustic Wave Motor using a Flat-Plane Slider," *Adv. Robot.*, vol. 24, no. May 2012, pp. 1407–1421, 2010.
[51] D. Royer and E. Dieulesaint, *Elastic waves in solids II*, First. New York: Springer, 1999.
[52] V. Plessky and J. Koskela, "Coupling-of-modes analysis of saw devices," *Journal, Int. Electron. High Speed Electron. Syst.*, pp. 1–81, 2000.
[53] T. T. Wu, S. M. Wang, Y. Y. Chen, T. Y. Wu, P. Z. Chang, L. S. Huang, C. L. Wang, C. W. Wu, and C. K. Lee, "Inverse Determination of Coupling of Modes Parameters of Surface Acoustic Wave Resonators," *Jpn. J. Appl. Phys.*, vol. 41, no. 11, pp. 6610–6615, 2002.
[54] W. R. Smith, H. M. Gerard, J. H. Collins, T. M. Reeder, and H. J. Shaw, "Analysis of Interdigital Surface Wave Transducers by Use of an Equivalent Wave Circuit Model," *IEEE Trans. Microw. Theory Tech.*, vol. MTT-17, no. 10, pp. 856–864, 1969.
[55] A. A. Vives, *Piezoelectric Transducers and Applications*, Second Edi. Spain: Springer-Verlag Berlin Heidelberg, 2008.
[56] G. S. Kino, "Acoustoelectric Interactions in Acoustic- Surface-Wave Devices," *Proc. IEEE*, p. 27, 1976.
[57] V. K. Varadan, K. J. Vinoy, and S. Gopalakrishnan, *Smart Material Systems and MEMS : Design and Development Methodologies*, First Edit. England: John Wiley & Sons Publication, 2006.
[58] D. S. H. Lo, *Finite Element Mesh Generation*, First Edit. New York: CRC Press, 2015.
[59] F. L. Matthews, G. A. O. Davies, D. Hitchings, and C. Soutis, *Finite element modelling of composite materials and and structures*, First Edit. New York: Woodhead Publishing Limited, 2003.
[60] C. Multiphysics and M. Guide, "COMSOL Multiphysics Modeling Guide," *COMSOL Multiphysics*,

p. 348, 2005.
[61] R. Lerch, “Simulation of piezoelectric devices by two-and-three-dimensional finite elements,” *IEEE Trans. Ultrason. Ferroelectr. Freq. Control*, vol. 37, no. 2, p. 15, 1990.
[62] S. Rahman, M. Kataoka, C. H. W. Barnes, and H. P. Langtangen, “Numerical investigation of a piezoelectric surface acoustic wave interaction with a one-dimensional channel,” *Phys. Rev. B*, vol. 74, pp. 1–8, 2006.
[63] M. Z. Atashbar, B. J. Bazuin, M. Simpeh, and S. Krishnamurthy, “3D FE simulation of H2 SAW gas sensor,” *Sensors Actuators B. Chem.*, vol. 112, pp. 213–218, 2005.
[64] S. J. S. J. Ippolito, K. Kalantar-zadeh, D. A. D. A. Powell, and W. Wlodarski, “A 3-dimensional finite element approach for simulating acoustic wave propagation in layered SAW devices,” in *IEEE Ultrasonics Symposium*, 2003, vol. 0, no. c, pp. 303–306.
[65] X. Wang and G. Xu, “Numerical Study of the Effects of Film Properties to the Mass Sensitivity of Surface Acoustic Wave Sensors,” in *Proceedings of the IEEE*, 2005, pp. 442–448.
[66] A. C. Tikka and D. Abbott, “Finite Element Modelling of SAW Correlator,” *Proc. SPIE BioMEMS Nanotechnol. III*, vol. 6799, pp. 1–9, 2007.
[67] Z. C. Feng and C. Chicone, “A delay differential equation model for surface acoustic wave sensors,” *Sensors Actuators A. Phys.*, vol. 104, pp. 171–178, 2003.
[68] C. S. Hartmann, D. T. Jr. Bell, and R. C. Rosenfeld, “Impulse Model Design of Acoustic Surface-Wave Filters,” *IEEE Trans. Microw. Theory Tech.*, vol. 21, no. 4, p. 14, 1973.
[69] J. Koskela, V. P. Plessky, and M. M. Salomaa, “SAW/LSAW COM parameter extraction from computer experiments with harmonic admittance of a periodic array of electrodes,” *IEEE Trans. Ultrason. Ferroelectr. Freq. Control*, vol. 46, no. 4, pp. 806–816, 1999.
[70] N. Ramakrishnan, A. K. Namdeo, H. B. Nemade, and R. Paily, “Simplified Model for FEM Simulation of SAW Delay Line Sensor,” *Eng. Prpcedia*, vol. 41, pp. 1022–1027, 2012.
[71] Y. L. Rao, “Nanostructure Enhanced Surface Acoustic Love Wave Devices for Biosensing Applications,” 2008.
[72] W. Richard, H. M. Gerard, J. H. Collins, M. Reeder, and H. J. Shaw, “Design of Surface Wave Delay Lines with Interdigital Transducers,” *IEEE Trans. Microw. Theory Tech.*, vol. 17, no. 11, p. 9, 1969.
[73] K. L. Johnson, *Contact Mechanics*, First Edit. Cambridge: Cambridge University Press, 1985.
[74] P. J. Feenstra, “Modeling and Control of Surface Acoustic Wave Motors,” University of Twente, 2005.
[75] K. Asai and M. K. Kurosawa, “Simulation Model of Surface Acoustic Wave Motor Considering Tangential Rigidity,” *Electron. Commun. Japan*, vol. 87, no. 2, pp. 54–66, Feb. 2003.
[76] T. Shigematsu and M. K. Kurosawa, “Friction Drive of an SAW Motor. Part I : Measurements,” *IEEE Trans. Ultrason. Ferroelectr. Freq. Control*, vol. 55, no. 9, pp. 2005–2015, 2008.
[77] H. Hertz, “On the Contact of Elastic Solids,” *Misc. Pap. (Journal fur die reine und Angew. Math.*, vol. 92, pp. 146–162, 1881.
[78] Lord Rayleigh, “On the contact of Elastic Solids,” no. 92, pp. 156–171, 1881.
[79] M. Zhu, “Contact Analysis and Mathematical Modeling of Traveling Wave Ultrasonic Motors,” *IEEE Trans. Ultrason. Ferroelectr. Freq. Control*, vol. 51, no. 6, pp. 668–679, 2004.
[80] P. J. Feenstra and P. C. Breedveld, “Contact Behavior of a Surface Acoustic Wave Motor,” p. 7500, 1994.
[81] M. K. Kurosawa and T. Shigematsu, “Friction Drive Simulation of a SAW Motor with Slider Surface Texture Variation,” *Adv. Sci. Technol.*, vol. 54, pp. 366–371, 2008.
[82] P. J. Feenstra and P. C. Breedveld, “Analysis of a surface acoustic wave motor,” in *IEEE Ultrasonics Symposium*, 2003, pp. 1133–1136.
[83] K. K. Wong, *Propeties of lithium niobate*. London: INSPEC, The Institution of Electrical Engineers, 2002.
[84] T. M. Kwang, “Surface Acoustic Wave Microfluidic Actuation,” Monash University, 2009.
[85] C. Multiphysics, “COMSOL: Modeling Guide,” *COMSOL Multiphysics*, 2008.
[86] M. Takahashi, M. Kurosawa, and T. Higuchi, “Direct frictional driven surface acoustic wave motor,” in *The 8th International Conference on Solid-State Sensors and Actuators, and Eurosensors IX*, 1995, pp. 3–6.
[87] B. Behera, H. B. Nemade, and S. Trivedi, “Modelling and Finite Element Simulation of a Surface Acoustic Wave driven Linear Motor,” in *12th International Conference on Vibration Problems*, 2015, vol. 144, pp. 1411–1418.
[88] COMSOL Multiphysics, *COMSOL Multiphysics User’s Guide*. US: COMSOL 4.3a, 2012.
[89] T. Shigematsu and M. K. Kurosawa, “Friction drive of an SAW motor. Part IV: Physics of

contact," *IEEE Trans. Ultrason. Ferroelectr. Freq. Control*, vol. 55, no. 10, pp. 2277–87, Oct. 2008.
[90] T. Maeno and D. B. Bogy, "Effect of the hydrodynamic bearing on rotor/stator contact in a ring-type ultrasonic motor.," *IEEE Trans. Ultrason. Ferroelectr. Freq. Control*, vol. 39, no. 6, pp. 675–82, Jan. 1992.
[91] M. Kuribayashi Kurosawa, M. Takahashi, T. Higuchi, M. T. Minoru Kuribayashi Kurosawa, and T. IIiguchi, "Elastic Contact Conditions to Optimize Friction Drive of Surface Acoustic Wave Motor," *IEEE Trans. Ultrason. Ferroelectr. Freq. Control*, vol. 45, no. 5, pp. 1229–1237, Jan. 1998.
[92] M. Kurosawa, M. Takahashi, and T. Higuchi, "Optimum Pre-load of Surface Acoustic Wave Motor," in *IEEE Ultrasonics Symposium*, 1996, pp. 369–372.
[93] T. Shigematsu, M. K. Kurosawa, and K. Asai, "Nano Meter Stepping Drive of Surface Acoustic Wave Motor," in *Proceedings of the IEEE*, 2001, pp. 495–500.
[94] M. Kurosawa, M. Takahashi, and T. Higuchi, "An Ultrasonic X-Y Stage using 10 MHz Surface Acoustic Wave," in *IEEE Ultrasonics Symposium*, 1994, pp. 535–538.
[95] M. K. Kurosawa, H. Itoh, K. Asai, M. Takasaki, and T. Hipchi, "Optimization of Slider Contact Face Geometry for Surface Acoustic Wave Motor," in *Proceedings of the IEEE*, 2001, vol. 0, pp. 252–255.
[96] T. Shigematsu and M. K. Kurosawa, "Friction Drive of an SAW Motor. Part II : Analyses," *IEEE Trans. Ultrason. Ferroelectr. Freq. Control*, vol. 55, no. 8, pp. 2005–2015, 2008.
[97] T. Shigematsu and M. K. Kurosawa, "Friction drive modeling of SAW motor using classical theory of contact mechanics," in *International Conference on New Actuators*, 2006, no. June, pp. 14–16.
[98] M. K. Kurosawa and T. Shigematsu, "Friction drive simulation of a surface acoustic wave motor," in *Ens'07*, 2007, no. December, pp. 3–4.
[99] B. Behera, H. Nemade, and Shyam Trivedi, "Modelling and Finite Element Simulation of a Dual Friction-drive SAW Motor using Flat Slider," in *IEEE Ultrasonics Symposium*, 2016, pp. 1–5.
[100] Roditi, "Lithium Niobate Wafers - Free of Pyro-Electric Effect," 2013.
[101] G. B. Dorjin and I. G. Simakov, "Acoustic study of adsorbed liquid layers," *Acoust. Phys.*, vol. 48, no. 4, pp. 436–440, 2002.
[102] H. Tian and T. Matsudaira, "The Role of Relative Humidity, Surface Roughness and Liquid Build-Up on Static Friction Behavior of the Head/Disk Interface," *Trans. ASME*, vol. 115, no. 1, p. 28, 1993.
[103] T. Shigematsu and M. K. Kurosawa, "Friction Drive of an SAW Motor. Part V : Design Criteria," *IEEE Trans. Ultrason. Ferroelectr. Freq. Control*, vol. 55, no. 10, pp. 2288–2297, 2008.
[104] E. P. Degarmo, J. T. Black, R. A. Kohser, and B. E. Klamecki, *Materials and Process in Manufacturing*, Ninth Edit. Wiley and Sons, 2003.
[105] Wikipedia and F. Wikipedia, "Surface roughness," in *Wikipedia*, 2015, pp. 1–6.
[106] M. Gad-el-Hak, *MEMS Design and Fabrication*, Second Edi. New York: Taylor & Francis, 2006.
[107] M. Cole, G. Sehra, J. W. Gardner, S. Member, and V. K. Varadan, "Development of Smart Tongue Devices for Measurement of Liquid Properties," *IEEE Sens. J.*, vol. 4, no. 5, pp. 543–550, 2004.
[108] W. C. Wilson and G. M. Atkinson, "Mixed Modeling of a SAW Delay Line using VHDL," in *Proceedings of the IEEE*, 2006, pp. 34–39.
[109] CleWin, "CleWin," *CleWin*, 2002. [Online]. Available: http://www.wieweb.com/ns6/index.html.
[110] Moran Mirabal, "Piranha Cleaning," 2014.
[111] Leivre.com, "Impedance Matching Network Designer," 2016. [Online]. Available: http://leleivre.com/rf_lcmatch.html.
[112] H. Li, Y. Tian, Y. Ke, and S. He, "Analysis of Rayleigh Surface Acoustic Waves Propagation on Piezoelectric Phononic Crystal with 3-D Finite Element Model Perpendicular to the wave," in *Proceedings of IEEE*, 2014, pp. 2533–2536.
[113] Lord Rayleigh, "On Waves Propagated along the Plane Surface of an Elastic Solid," *Misc. Pap.*, vol. November, no. 12, pp. 4–11, 1885.
[114] S. E. Motor, "Calculation of Efficiency of Motor," *Simple Electric Motor*, 2017. .
[115] K. Asai and M. K. Kurosawa, "Surface acoustic wave motor using an energy circulation driving method," in *IEEE Ultrasonics Symposium*, 2001, vol. 1, pp. 525–529.
[116] H. Metalcraft, "Slotted Belleville Type Conical Disc Spring Washer," *HK Metalcraft*, 2012. [Online]. Available: http://www.hkmetalcraft.com/Products/Washers/SlottedBellevilleSpringWashers.shtml.

List of Publications Related to Thesis

Patents:

1. B. Behera and H. B. Nemade, "Dual Drive Surface Acoustic Wave Motor and the Package," 878/KOL/2014, 2014, India.
2. B. Behera and H. B. Nemade, "Dual Drive Surface Acoustic Wave Linear Motor and the Package," 978/KOL/2014, 2014, India.

Journals*:*

1. B. Behera, H, B. Nemade, "Modelling and finite element simulation of a surface acoustic wave driven linear motor," published in Elsevier- Procedia Engineering, 144 (2016) 1411 – 1418.
2. B. Behera, H. B. Nemade, "Finite element simulation of a SAW motor driven by dual friction," published in Elsevier- Materials Today Proceeding, 2017.
3. B. Behera, H. B. Nemade, "Investigating Translational Motion of a Dual Friction-drive Surface Acoustic Wave Motor through Modelling and Finite Element Simulation," Submitted to SAGE Journals- Simulation: Transactions of the Society for Modelling and Simulation International.

Conferences:

1. B. Behera, H. B. Nemade, and S. Trivedi, "Modelling and finite element simulation of a dual friction-drive SAW motor using flat slider," in *IEEE IUS 2016*, Tours, France on 18th - 21st Sep. 2016.
2. B. Behera, H. B. Nemade, "Finite element simulation of a SAW motor driven by dual friction," *ICEMS 2016*, JNU Jaipur, India, and 17th -19th Mar. 2016.
3. B. Behera, H. B. Nemade, "Modelling and finite element simulation of a surface acoustic wave driven linear motor," in *12th ICOVP 2015*, IIT Guwahati, India, 14th -17th Dec. 2015.
4. B. Behera, H. B. Nemade, and S. Trivedi, "Finite Element Simulation of a Surface Acoustic Wave driven Linear Motor using COMSOL Multiphysics," in *COMSOL Conference*, pp. 1–4, 29th - 30th Oct. 2015.
5. B. Behera and H. B. Nemade, "Optimizing Preload and Coefficient of Friction for Surface Acoustic Wave Linear Motor," *5th Int. 26th All India Manuf. Technol. Des. Res. Conf.*, no. AIMTDR, pp. 1–6, 12th -14th Dec. 2014.
6. B. Behera and H. B. Nemade, "Simulation of Piezoelectric SAW Motor using COMSOL Multiphysics," in *COMSOL Conference*, pp. 1–5, 13th -14th Nov. 2014.